

**Luminescence enhancement of phosphors
by doping with silver**

by

**Abd Ellateef Abbass
(MSc)**

A thesis submitted in fulfilment of the requirements for the degree

PHILOSOPHIAE DOCTOR

in the

Faculty of Natural and Agricultural Sciences

Department of Physics

at the

University of the Free State

Promoter: Prof. R. E. Kroon

Co-promoter: Prof. H. C. Swart

October 2015

Acknowledgements

In pursuit of this academic endeavour I feel that I have been especially fortunate as inspiration, guidance, direction, co-operation, love and care all came in my way in abundance and it seems almost an impossible task for me to acknowledge the same in adequate terms.

Firstly, I wish to thank my supervisor **Prof. R. E. Kroon** for his kind advice, incessant support, patient guidance and hours spent in reviewing my papers and this thesis.

I would like to express my thanks and sincere gratitude to my co-supervisor **Prof. H. C. Swart**, head of research group in the Physics Department for his strong support, encouragement, inspiration and constructive criticism throughout my research work.

I extend my sincere thanks to **Dr Liza Coetsee** for measuring XPS and Auger spectra and **Dr Mart-Mari Biggs** for measuring TOF-SIMS and helping me with FTIR and UV-vis measurements.

I also accord my thanks to **Dr Shaun Cronjé** for technical assistance and ordering equipment and **Dr Pat van Heerden** for help with computer issues.

I accord my thanks to all staff members of the Department of Physics and postgraduate students, specially, to **Prof. Koos Terblans**, head of the Physics Department, **Prof. Pieter Meintjes** and **Prof. Martin Ntwaeaborwa** for their support.

I am also thankful to **Prof. Pieter van Wyk**, **Dr Chantel Swart** and **Ms Hanlie Grobler** at the University of the Free State Centre for Microscopy and **Prof. Mike Lee** and **Dr**

Arno Janse van Vuuren at the Nelson Mandela Metropolitan University for assisting with the TEM measurements.

My special thanks to my officemate **Dr Raphael Nyenge**, for the hours he spent patiently correcting my many mistakes, making helpful suggestions, and also for keeping me going when I needed encouragement.

I would like to take this opportunity to thank all my colleagues in **phosphor group** at the University of the Free State for their good discussions, especially **Dr Mubarak Yagoub, Dr Abdelrhman Yousif Mohmmmed Ahmed, Dr Hassan Abdelhalim Abdallah Seed Ahmed, Dr Vinod Kumar** and **Dr Rasha Jafar**.

I also sincerely thank **Ms Karen Cronje** and **Mrs Yolandie Fick** for being so helpful to me during my study period.

Last but not least, I would express my sincere gratitude to my parents, my brothers and sisters and my beloved wife for their encouragement and support throughout, which always inspired me. To my lovely kids: Mohammed, Rugd thank you for your love.

Thank you all
Abd Ellateef Abbass

Abstract

Phosphor materials doped with noble metals have attracted considerable attention for the past fifty years due to their possible applications in lighting and solar cells with improved efficiency, biology, lasers and novel display technologies. Active research has recently been focused on the interaction between noble metal nanoparticles and rare-earth ions in different phosphor hosts, with the aim of luminescence enhancement. Much attention has been paid to silver nanoparticles due to their strong absorption of electromagnetic radiation, resulting from localized surface plasmon resonance which can enhance the incident electric field by about two orders of magnitude. Although some reports have been published in regard to phosphors doped with silver, there is still room to better understand the interaction between silver and phosphors and to boost the efficiency of such phosphors.

In this work, three different types of materials, namely amorphous silica, bismuth silicate and zinc oxide were used as hosts for silver and terbium. These hosts were selected due to their good physical properties and particularly because they have the appropriate refractive index, which is one of the main parameters required to control the plasmon absorption band for plasmonic enhancement. Doped and undoped amorphous silica and bismuth silicate were successfully prepared by the sol-gel method, while zinc oxide was prepared by the combustion method. The sources of the dopants used in this work were silver nitrate and terbium nitrate. The prepared phosphor powders were investigated by many techniques in order to apply appropriate conditions for phosphor enhancement. The structure, morphology and particle size were investigated by X-ray diffraction and transmission electron microscopy. Reflectance and absorption band of localized surface plasmon resonance were measured using a ultraviolet-visible spectrophotometer. X-ray photoelectron spectroscopy was used to investigate the composition of the phosphors, while optical properties were investigated using a fluorescence spectrophotometer having a xenon lamp or by exciting samples with a helium-cadmium laser.

Firstly, doped and undoped amorphous silica was synthesized by the sol-gel method. The photoluminescence properties of amorphous silica doped only with silver as a function of annealing temperature were investigated in detail. The obtained results showed that the addition of silver after annealing at low temperature (500 °C) enhanced the luminescence associated with oxygen deficiency centres of the amorphous silica host, which is attributed to the formation of silver oxide. Increasing the annealing temperature to 1000 °C introduced new optically active centres in the amorphous silica. These new emission bands were related to excess oxygen due to decomposition of the silver oxide at high temperature. The additional luminescence band changed the blue emission from pure amorphous silica to near white light from the silver doped material suggesting that the silver doped silica system may be suitable for solid state lighting applications. The stability of this phosphor under ultraviolet irradiation was also investigated.

To study the effect of addition of silver on the terbium luminescence, both terbium (5 mol%) and different silver concentrations were incorporated into amorphous silica using the sol-gel method. The obtained results showed significant enhancement of the terbium emission when 1 mol% silver was added after annealing at 500 °C. In previous works, the enhancement of rare-earth ion emission in the presence of silver was assigned to two possibilities, namely plasmonic enhancement associated with silver nanoparticles or energy transfer associated with silver ions. This work shows a third possibility, namely that enhancement of the rare-earth (e.g. terbium) emission is due to energy transfer from defects of the host material to the terbium ions, where the addition of silver influences the silica host defects.

Secondly, powder samples of doped and undoped zinc oxide were successfully prepared by the combustion method. The photoluminescence properties of zinc oxide doped only with silver were studied in detail. More than a two fold increase in the intensity of near band edge emission of undoped zinc oxide was observed in the presence of silver nanoparticles. A new mechanism due to interaction between silver nanoparticles and zinc oxide has been proposed as being responsible for the enhancement of near band edge emission which is different from previous reports.

In other samples, zinc oxide was doped with both terbium and silver. The addition of 1 mol% silver to the 5 mol% terbium doped zinc oxide system caused significant quenching on the terbium emission intensity instead of enhancement. The quenching effect is attributed to radiative energy transfer from terbium ions to silver nanoparticles (re-absorption) and was studied by means of spectral overlap and lifetime measurements. In the previous reports, researchers focused only on enhancement as a beneficial effect and considered quenching as a deleterious effect. In this work, the obtained results showed that the absorption of energy by silver nanoparticles (acting as energy acceptors) can also be beneficial in biological and polymer applications where local heating is desired i.e. photothermal applications. Another novelty of this work is that one can use the down-converting phosphor properties (containing, for example, rare-earth ions) as effective method to indirectly couple a laser to the plasmon resonance wavelength of metal nanoparticles without the need to change the particle size or shape of the nanoparticles, which requires special synthesis methods.

Thirdly, bismuth silicate was synthesized using the sol-gel method and successfully doped with only terbium or silver, or co-doped with both. A simple way to select a suitable host material, when doped with any rare-earth ion and incorporated with silver nanoparticles, to cause overlap between an excitation band of the rare-earth ions and the localized surface plasmon resonance of the metallic nanoparticles in order to study possible plasmonic enhancement is presented using Mie theory calculations. Luminescence properties of the terbium doped bismuth silicate containing silver nanoparticles were explored in detail and an enhancement of the emission from the terbium ions at 545 nm when excited at 485 nm of about two and a half times is attributed to amplification of the electric field associated with the localized surface plasmon resonance of the silver nanoparticles. A particular novelty of the present work is the use of a crystalline host instead of an amorphous host to study plasmonic enhancement as in previous studies.

Keywords and acronyms

Keywords

phosphor, silica, zinc oxide, bismuth silicate, sol-gel method, combustion method, Mie theory, metallic nanoparticle, metal enhanced fluorescence, plasmonic enhancement, localized surface plasmon resonance, defect luminescence, energy transfer, silver, terbium.

Acronyms

AES	Auger electron spectroscopy
CCD	Charged coupled device
CCT	Colour correlated temperature
CIE	Commission Internationale de l'Eclairage
CTS	Charge-transfer state
EELS	Electron energy loss spectroscopy
EDS	Energy dispersive X-ray spectroscopy
ESCA	Electron spectroscopy for chemical analysis
ET	Energy transfer
FTIR	Fourier transform infrared (spectroscopy)
FWHM	Full-width-at-half-maximum
ICDD	International centre for diffraction data
LED	Light emitting diode
LSP	Localized surface plasmon
LSPR	Localized surface plasmon resonance
NBE	Near band edge
NIR	Near-infrared

NP	Nanoparticle
ODC	Oxygen deficiency centre
PDF	Powder diffraction file
PL	Photoluminescence
PMT	Photomultiplier tube
pcW-LED	Phosphor converted white light emitting diode
RE	Rare-earth
SP	Surface plasmon
SPP	Surface plasmon polariton
TEM	Transmission electron microscopy
TEOS	Tetraethoxysilane
TMOS	Tetramethoxysilane
UV	Ultraviolet
UV-vis	Ultraviolet-visible
W-LED	White light emitting diode
XPS	X-ray photoelectron spectroscopy
XRD	X-ray diffraction

Table of Contents

Acknowledgements	i
Abstract.....	iii
Keywords and acronyms	vi
Table of contents	viii

Chapter 1

Introduction

1.1 Overview	1
1.2 Problem statement	3
1.3 Research objectives.....	4
1.3.1 General objective	4
1.3.2 Specific objectives	4
1.4 Thesis layout	5
1.5 References	5

Chapter 2

Phosphors

2.1 Introduction.....	8
2.2 Fundamentals of phosphors.....	8
2.3 Applications of phosphors.....	10
2.4 Lanthanides	11
2.4.1 Lanthanide excitation processes	14
2.4.1.1 <i>4f-4f</i> transitions	14
2.4.1.2 <i>4f-5d</i> transitions.....	14
2.4.1.3 Charge-transfer state transitions.....	15

2.4.2 Some luminescent centres	15
2.4.2.1 Terbium ions.....	15
2.4.2.2 Silver ions.....	16
2.5 Energy transfer mechanisms	17
2.5.1 Radiative energy transfer.....	19
2.5.2 Non-radiative energy transfer	19
2.6 Preparation methods of phosphors	20
2.6.1 Sol-gel method	20
2.6.2 Combustion method.....	22
2.7 Structure of phosphor hosts.....	24
2.7.1 Silica (SiO ₂).....	24
2.7.2 Zinc oxide (ZnO).....	27
2.7.3 Bismuth silicate (Bi ₄ Si ₃ O ₁₂)	29
2.8 References	30

Chapter 3

Plasmons and plasmonic enhancement

3.1 Introduction.....	35
3.2 Plasmon types	35
3.2.1 Bulk plasmons	35
3.2.2 Surface plasmons	36
3.3 Localized surface plasmon resonance and Mie theory	38
3.3.1 Quasistatic approximation model.....	39
3.3.2 Electrodynamics model	40
3.4 Silver as a good plasmonic material	41
3.5 Tuning of the localized surface plasmon resonance.....	45
3.5.1 Influence of nanoparticle size	45
3.5.2 Influence of nanoparticle shape.....	46

3.5.3 Influence of dielectric constant of the environment.....	48
3.6 Plasmon decay	49
3.7 Metal-enhanced fluorescence.....	50
3.8 References	53

Chapter 4

Experimental research techniques

4.1 Introduction.....	58
4.2 X-ray diffraction	58
4.2.1 Generation of X-rays	59
4.2.2 Bragg's law	60
4.2.3 X-ray diffractometer.....	61
4.3 Ultraviolet-visible spectroscopy	63
4.3.1 Basic theory	64
4.3.2 Sample preparation	65
4.3.2.1 Solution phase.....	65
4.3.2.2 Solid phase	65
4.3.3 Determination of the energy band gap.....	65
4.3.3.1 Energy band gap from absorption spectra.....	65
4.3.3.2 Energy band gap from reflectance spectra.....	66
4.3.4 Instrumentation.....	66
4.4 Transmission electron microscopy	68
4.4.1 Elastic Scattering	70
4.4.1.1 Bright field and dark field images.....	70
4.4.1.2 Diffraction patterns	71
4.4.2 Inelastic Scattering.....	71
4.4.3 Energy dispersive X-ray spectroscopy	72
4.4.4 Instrumentation.....	72

4.5 Fourier transform infrared spectroscopy	73
4.5.1 Physical principles	74
4.5.2 Sample preparation	75
4.5.3 Instrumentation.....	76
4.6 Photoluminescence spectroscopy	78
4.7 X-ray photoelectron spectroscopy	80
4.7.1 Basic theory	81
4.7.2 Instrumentation.....	84
4.7.3 Interpretation of spectra	85
4.8 References	87

Chapter 5

White luminescence from sol-gel silica doped with silver

5.1 Introduction.....	90
5.2 Experimental	91
5.3 Results and discussion	92
5.4 Conclusion	102
5.5 References	103

Chapter 6

Effect of Ag nanoparticles on the luminescence of Tb doped sol-gel silica

6.1 Introduction.....	107
6.2 Experimental	108
6.3 Results and discussion	109
6.3.1 Structural and morphological characterization.....	109
6.3.2 Optical characterization.....	111
6.4 Conclusion	113
6.5 References	114

Chapter 7

Effect of silver ions on the energy transfer from host defects to Tb ions in sol-gel silica glass

7.1 Introduction.....	116
7.2 Experimental	117
7.3 Results and discussion	118
7.4 Conclusion	127
7.5 References	127

Chapter 8

Non-plasmonic enhancement of the near band edge luminescence from ZnO using Ag nanoparticles

8.1 Introduction.....	130
8.2 Experimental	132
8.3 Results and discussion	133
8.4 Conclusion	140
8.5 References	141

Chapter 9

Use of ZnO:Tb down-conversion phosphor for Ag nanoparticle plasmon absorption using a He-Cd ultraviolet laser

9.1 Introduction.....	145
9.2 Experimental	146
9.3 Results and discussion	147
9.4 Conclusion	154
9.5 References	154

Chapter 10

Enhanced terbium emission due to plasmonic silver nanoparticles in bismuth silicate

10.1 Introduction.....	157
10.2 Experimental	158
10.3 Results and discussion	160
10.4 Conclusion	169
10.5 References	169

Chapter 11

Summary and future work

11.1 Summary.....	172
11.2 Future work.....	174

Appendix A

Publications	176
Conference presentations	177

Chapter 1

Introduction

1.1 Overview

Nowadays, phosphors with low cost and high efficiency are required due to increasing concern on consuming energy. Consequently, the amount of research in this field has increased rapidly in varied areas of research in the past fifty years. Among luminescent materials, rare-earth (RE) ions are well-known due to their unique luminescent properties. RE ions can emit in a wide range of the electromagnetic spectrum which make them a good candidate in many applications such as solid state lasers, optical communications, sensing and display systems etc. [1], and recently have found an application in photodynamic therapy of cancer [2].

On the other hand, some other phosphors such as ZnO and SiO₂ have become more and more popular in the last decade. ZnO is well-known for having good physical properties over most other semiconductor materials. Due to its wide band gap (3.37 eV) and large exciton binding energy (60 meV) at room temperature [3, 4], ZnO plays an important role in developing optoelectronic devices. Moreover, ZnO has attracted considerable attention as a low-cost and environmentally-friendly photonic material and can be easily synthesised in different forms e.g. nanoparticles (NPs), nanorods, nano-disks, nano-cubes, etc. [4]. Recently, ZnO has been used in the medical field because of its biocompatibility, biodegradability and non-toxicity. SiO₂ is a potential candidate material for optoelectronic applications because it is an environmental friendly, low cost and easy to fabricate material with good thermal and chemical stability.

The effective extraction of light from phosphors has attracted a major attention [5]. Some significant improvements in phosphor efficiency have been made by modifying the excitation rate by co-doping by different activators such as RE and transition metal ions [6]. However, the absorption cross-section of RE ions is very small, since the $4f-4f$

transitions are theoretically forbidden due to the parity selection rule. Consequently, the RE ions cannot be effectively excited directly by ultraviolet (UV) light. As a result different approaches, namely charge-transfer state (CTS) absorption, *f-d* absorption and host absorption, have been used to enhance the excitation rate of RE ions [7, 8]. In a different way, for other phosphors such as ZnO [9-11] and SiO₂ [12] doping with different impurities has also become a strategy for enhancing or modifying their optical properties.

Recently, active research has focused on noble metal doped phosphors with the aim of enhancement [7, 11, 13]. Special attention has been given to Ag NPs due to their good optical properties associated with the so-called surface plasmons (SPs). NPs are defined as particles having sizes in the range of 1-100 nm, and sometimes several hundreds of nanometres are considered. The most important characteristics of NPs are their high surface area to volume ratio. Due to these properties, NPs exhibit specific physical and chemical properties which are different from their bulk forms [14]. The most attractive property of these nanostructures is electromagnetic resonances due to collective oscillations of the free electrons (conduction electrons) which are termed SPs [13]. SPs can exist in various metals, most importantly in noble metals such as Ag and Au. Actually, there are two types of SPs, namely localized SPs (LSP) and SP polaritons (SPPs). This work will mostly be concerned with the former, defined as the collective excitation of the conduction band free electrons associated with the small metal NPs [7]. The resonance modes occur when the frequency of the charge oscillation in NPs match the frequency of the incident light, and a very strong electric field around metal NPs is created. This occurs in metal NPs in the size range about 10-100 nm and results in amplification of the electric field near the particle surfaces. This field has a spatial range in the order of 10-50 nm and is strongly dependent on NP size, shape, and local dielectric environment [15].

It is well known that in order to enhance the luminescence efficiency of phosphors by noble metal NPs, there should be an optimum distance between the NPs and the emitters. If the distance between them is very small, non-radiative energy transfer (ET) from the

emitter to the NP can occur and therefore quenching is observed. If the emitter is located within 10-50 nm [15], then enhancement of the emitter may be observed. At large separations quenching of the emitters can again be observed due to re-absorption of light by Ag NPs (radiative ET). It has been reported that to effectively enhance luminescence efficiency from the emitters, a narrow linewidth LSP resonance (LSPR) absorption band and spectral overlap between this LSPR absorption band and the excitation or emission band of the emitters are required [16]. It worth noting that Ag doped in a phosphor can exist in different forms namely, Ag ions (e.g. single Ag^+ , Ag^+-Ag^+ pairs, $(\text{Ag}^+)_2$, $(\text{Ag}_2)^+$ or more generally in the form of $(\text{Ag}_n)^{m+}$), small Ag clusters (less than about 5 nm in size) or Ag NPs (Ag^0 , from about 5-100 nm in size) [17]. It is well known that the enhancement or quenching of emitters in the presence of Ag^+ ions is assigned to ET while the enhancement of emitters in the presence of Ag NPs is attributed to local field enhancement associated with LSPR. Due to the very short lifetime of the plasmons, ET from Ag NPs to RE ions is not expected [13]. However, there is still lack of information about the nature of interaction between the phosphor and Ag, making prediction of the enhancement and quenching of phosphors in the presence of Ag challenging. Understanding the interaction mechanism between the Ag and phosphors is needed for the luminescence enhancement of phosphors.

In this study, the effect of doping Ag on the luminescence of Tb^{3+} ions in an amorphous host (SiO_2) and crystalline hosts (ZnO and $\text{Bi}_4\text{Si}_3\text{O}_{12}$) has been investigated. The influence of the addition of Ag on the emission from ZnO and SiO_2 also has been studied. New mechanisms of interaction between Ag and phosphors have been proposed, which suggest an additional complexity in understanding the enhancement, quenching and broadening of the emission from phosphors in the presence of Ag.

1.2 Problem statement

Lanthanide ions (e.g., Tb^{3+}) can exhibit three types of excitation transitions, namely $4f-4f$ transitions, $4f-5d$ transitions, and CTS transitions. $4f-4f$ transitions are very important in many applications such as solid state lasers, optical communications, sensing and display

systems and will be the focus of this work. They involve transitions of electrons between the different energy levels of the $4f$ orbital of the same lanthanide ion. These transitions are in theory forbidden by the parity selection rule. However, when the lanthanides are introduced into asymmetric solid hosts, the parity selection rule is relaxed due to interactions with the host crystal field. These interactions slightly increase the probability of these transitions (i.e. increase the absorption cross-section) [18]. Due to the low probabilities of these transitions the fluorescence lifetimes may be as long as several milliseconds. Although the probabilities of these transitions are increased due to interactions with crystal field, they are still very weak with narrow emissions, prompting a need for methods of enhancing their luminescence. In general, in order to increase the efficiency of phosphors, the excitation rate and radiative rate should be enhanced. Noble metal NPs are a good candidate for this purpose due to strong local electric fields associated with LSPR. Therefore, noble metal NPs incorporated in a phosphor are expected to enhance its efficiency.

1.3 Research Objectives

1.3.1 General Objective

The main objective of the work is to enhance luminescence from phosphors by adding Ag as well as the study of the interaction mechanism between phosphors and Ag in both cases of luminescence enhancement and quenching.

1.3.2 Specific Objectives

- To synthesize SiO_2 and $\text{Bi}_4\text{Si}_3\text{O}_{12}$ with and without dopants (Tb and/or Ag) using the sol-gel method.
- To synthesize undoped and Tb and/or Ag doped ZnO using the combustion method.
- To determine the structure of the pure hosts with X-ray diffraction (XRD).
- To incorporate Ag into SiO_2 , $\text{Bi}_4\text{Si}_3\text{O}_{12}$ and ZnO hosts and study the formation of Ag NPs as the function of annealing temperature using XRD, ultraviolet-visible (UV-vis) spectroscopy, transmission electron microscopy (TEM), Auger emission spectroscopy (AES) and X-ray photoelectron spectroscopy (XPS) techniques.

- To study the effect of Ag doping on the luminescence from SiO₂ and ZnO using photoluminescence (PL) techniques.
- To incorporate Ag and Tb ions into SiO₂, Bi₄Si₃O₁₂ and ZnO hosts and investigate the effect of doping Ag on the PL properties of Tb ions for different annealing temperatures.
- To formulate luminescence mechanisms for the emission of SiO₂:Ag, ZnO:Ag, SiO₂:Tb,Ag, ZnO:Tb,Ag and Bi₄Si₃O₁₂:Tb,Ag.

1.4 Thesis layout

[Chapter 1](#) provides a general information and aim of this study. A brief background on the fundamental of phosphors and their applications, properties of lanthanides, ET mechanisms and preparation methods of phosphors are given in [chapter 2](#). In [chapter 3](#) a literature survey of the theoretical propositions and the main concepts behind NP LSPR and the principles of plasmonic enhancement of fluorescence are discussed. The experimental techniques adopted to realize our objective are described in detail in [chapter 4](#). The effects of Ag ions and Ag NPs on the luminescence properties of sol-gel SiO₂ is reported in [chapter 5](#), while [chapter 6](#) discusses the effect of the Ag NPs on the luminescent properties of Tb ions in this host. [Chapter 7](#) presents the effect of Ag ions on the ET from host defects to Tb ions in sol-gel SiO₂ glass. The enhancement of near band edge (NBE) emission of ZnO due to the addition of Ag NPs is presented in [chapter 8](#). In [chapter 9](#) the use of down-conversion properties of Tb³⁺ ions to indirectly couple a laser to the LSPR wavelength of metal NPs is investigated. [Chapter 10](#) presents the enhancement of Tb emission due to plasmonic Ag NPs in Bi₄Si₃O₁₂. Finally, a conclusion and suggestions for future work are given in [chapter 11](#).

1.5 References

[1] K. Ogasawara, S. Watanabe, H. T. Oyshima and M. G. Brik, First-principles calculations of 4fⁿ-4fⁿ⁻¹-5d transition spectra, In: Handbook on the Physics and Chemistry

of Rare Earths, edited by K. A. Gschneidner Jr., J. G. Bünzli and V. K. Pecharsky, *Elsevier*, North-Holland, volume **37** (2007) (511 pages).

[2] S. Derom, A. Berthelot, A. Pillonnet, O. Benamara, A. M. Jurdyc, C. Girard and G. Colas des Francs, Metal enhanced fluorescence in rare earth doped plasmonic core-shell nanoparticles, *Nanotechnology* **24** (2013) 1-14.

[3] G. L. Kabongo, G. H. Mhlongo, T. Malwela, B. M. Mothudi, K. T. Hillie and M. S. Dhlamini, Microstructural and photoluminescence properties of sol-gel derived Tb³⁺ doped ZnO nanocrystals, *J. Alloys Compd.* **591** (2014) 156-163.

[4] M. A. Moghri Moazzen, S. M. Borghei and F. Taleshi, Change in the morphology of ZnO nanoparticles upon changing the reactant concentration, *Appl. Nanosci.* **3** (2013) 295-302.

[5] W. L. Barnes, A. Dereux and T. W. Ebbesen, Surface plasmon subwavelength optics, *Nature* **424** (2003) 824-830.

[6] C. H. Seagera and D. R. Tallant, Interactions of excited activators in rare earth and transition metal doped phosphors and their role in low energy cathodoluminescence, *J. Appl. Phys.* **91** (2002) 153-165.

[7] A. E. Abbass, H. C. Swart, R. E. Kroon, Effect of silver ions on the energy transfer from host defects to Tb ions in sol-gel silica glass, *J. Lumin.* **160** (2015) 22-26.

[8] J. J. Li, R. F. Wei, X. Y. Liu and H. Guo, Enhanced luminescence via energy transfer from Ag⁺ to RE ions (Dy³⁺, Sm³⁺, Tb³⁺) in glasses, *Opt. Express* **20** (2012) 10122 - 10127.

[9] P. Krongarrom, S. T. Rattanachan, and T. Fangsuwannarak, ZnO Doped with Bismuth in case of In-Phase Behavior for Solar Cell Application, *Eng. J.* **16** (2012) 59-70.

[10] F. Xian, X. Li, Effect of Nd doping level on optical and structural properties of ZnO:Nd thin films synthesized by the sol-gel route, *Opt. Laser Techn.* **45** (2013) 508-512.

[11] H. Y. Lin, C. L. Cheng, Y. Y. Chou, L. L. Huang and Y. F. Chen, Enhancement of band gap emission stimulated by defect loss, *Opt. Express* **14** (2006) 2372-2379.

- [12] M. A. Villegas, M. A. Garcia , J. Llopis and J. M. Fernández Navarro, Optical Spectroscopy of Hybrid Sol-Gel Coatings Doped with Noble Metals, *J. Sol-Gel Sci. Technol.* **11**(1998) 251-265.
- [13] O. L. Malta, P. A. Santa-Cruz, G. F. Desa and F. Auzel, Fluorescence enhancement induced by the presence of small silver particles in Eu^{3+} doped materials, *J. Lumin.* **33** (1985) 261-272.
- [14] N. Sui, Y. Duan, X. Jiao and D. Chen, Large-Scale Preparation and Catalytic Properties of One-Dimensional α/β - MnO_2 Nanostructures, *J. Phys. Chem. C* **113** (2009) 8560-8565.
- [15] A. J. Haes, C. L. Haynes, A. D. McFarland, G. C. Schatz, R. P. Van Duyne and S. Zou, Plasmonic Materials for Surface-Enhanced Sensing and Spectroscopy, *MRS Bull.* **30** (2005) 368-375.
- [16] Y. Chen, K. Munechika and D. S. Ginger, Dependence of Fluorescence Intensity on the Spectral Overlap between Fluorophores and Plasmon Resonant Single Silver Nanoparticles, *Nano Lett.* **7** (2007) 690-696.
- [17] S. Lai, Z. Yang, J. Liao, J. Li, B. Shao, J. Qiu and Z. Song, Investigation on existing states and photoluminescence property of silver in the SiO_2 three-dimensionally ordered macroporous materials, *RSC Adv.* **4** (2014) 33607-33613.
- [18] J. H. Van Vleck, The puzzle of rare-earth spectra in solids, *J. Phys. Chem.* **41** (1937) 67-80.

Chapter 2

Phosphors

2.1 Introduction

This chapter consists of six sections. Basic information about the fundamentals of phosphors and their application is given in [sections 2.2 and 2.3](#), respectively. [Section 2.4](#) presented the main properties of lanthanides. The theory and types of energy transfer (ET) are reported in [section 2.5](#). Details of the preparation methods of our phosphors are discussed in [section 2.6](#). Finally, the structure of the SiO_2 , ZnO and $\text{Bi}_4\text{Si}_3\text{O}_{12}$ has been presented in [section 2.7](#).

2.2 Fundamentals of phosphors

Luminescent materials, also known as phosphors, can emit light when they are excited with incident radiation. Phosphors may either be in the powder or thin film form with specific requirements on particle size distribution and morphology. Usually, phosphor nanoparticles (NPs) of high quality are required, since the quantum efficiencies are relatively higher in nanophosphors due to the fact that NPs do not scatter light [\[1\]](#). The emission from phosphors usually falls into the visible range but could also be in ultraviolet (UV) or near-infrared (NIR). A phosphor is composed of a host and one or more dopants (activators) with the amount ranging from parts per million to a few mole percent (see [figure 2.1](#)). In generally, a host with good optical, mechanical and thermal properties is required. Although there is a big difference between crystalline and amorphous host properties, both of them have been used for phosphors. The selection of host depends on the applications.

The luminescence properties of phosphors can be determined either by the host or activators [\[2\]](#). An activator is an impurity ion that gives desired emission when

incorporated into the matrix. In some cases, when the activator shows a weak absorption (e.g., $4f-4f$ transition in the rare-earth (RE) ions, because the optical transition is forbidden), a second type of impurities (sensitizers) can be used. The sensitizer absorbs energy from the primary excitation source and therefore transfers the energy to the activator (see [figure 2.1](#)). The ET will be discussed in more detail in [section 2.5](#). It is worthwhile to note that in the case of a narrow band gap host, the optical absorption can also take place by the host lattice itself (band absorption) and the energy can be transferred to the activator ions i.e. in this case the host can act as sensitizer.

According to the excitation mechanism, the luminescence can be classified into different types, namely photoluminescence (PL), cathodoluminescence, electroluminescence, etc., which are excited by photons, electrons, passage of electric current (or a strong electric field) respectively [[3](#), [4](#)]. In addition to classification by excitation, two other terms are also often used and are related to the decay time: fluorescence and phosphorescence [[4](#)] (see [figure 2.1](#)). Phosphorescence refers to an emission of a relatively longer decay time ranging from a few microseconds up to several milliseconds, while fluorescence exhibit an emission of short decay time, about 10^{-9} to 10^{-7} s. According to quantum mechanical theory, in a fluorescence event the electron transition occurs to singlet excited state where the electron does not change its spin direction. However, for a phosphorescence event, under appropriate conditions an electron could change its spin and create a triplet excited state (see [figure 2.1](#)). The transitions from these triplet states to the ground state are forbidden by the selection rules and subsequently, this process requires a longer time until the electron spin flips back.

A phosphor is commonly represented by a formula such as $\text{SiO}_2:\text{Tb}^{3+}$ (1.0 mol%), where SiO_2 indicates the matrix, Tb^{3+} indicates the activator while the percentage value (1.0 mol%) represents the amount of Tb (activator) that was incorporated per mole of the matrix. In the case where more than one activator is used, a comma is used to separate them, for example $\text{SiO}_2:\text{Tb}^{3+},\text{Ag}$.

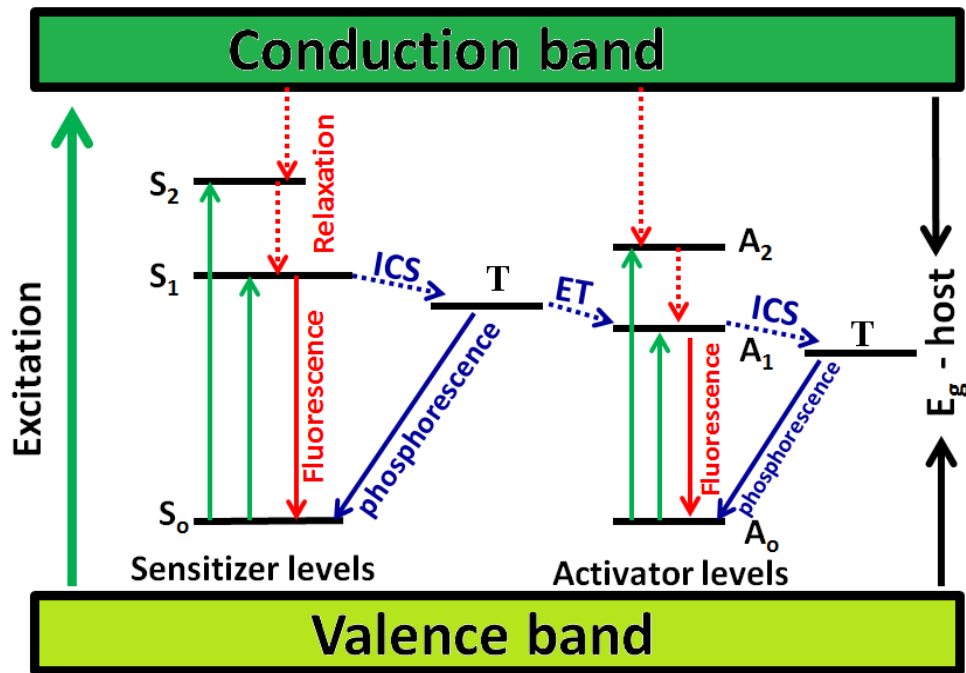


Figure 2.1: Energy level diagram of the activators and sensitizers in a solid host. S_0 , S_1 , S_2 , A_0 , A_1 and A_2 represent the singlet energy levels of the activators and sensitizers while T represents the triplet state. ICS refers to intersystem crossing “spin-forbidden singlet-triplet transition” whereas the ET stands for energy transfer.

2.3 Applications of phosphors

Phosphors have found wide application today in many fields (see figure 2.2). Major additional applications are in emissive displays and fluorescent lamps [2, 5], e.g. electroluminescent displays, vacuum fluorescent displays, plasma displays, and field emission displays [3]. Other classical applications include amplifiers in optical communication [6], lasers [7], X-ray detector systems [8] and scintillators [9]. Recently phosphors have found new areas of applications such as solar cells [1, 10] and white light emitting diodes (W-LEDs) [1, 11].

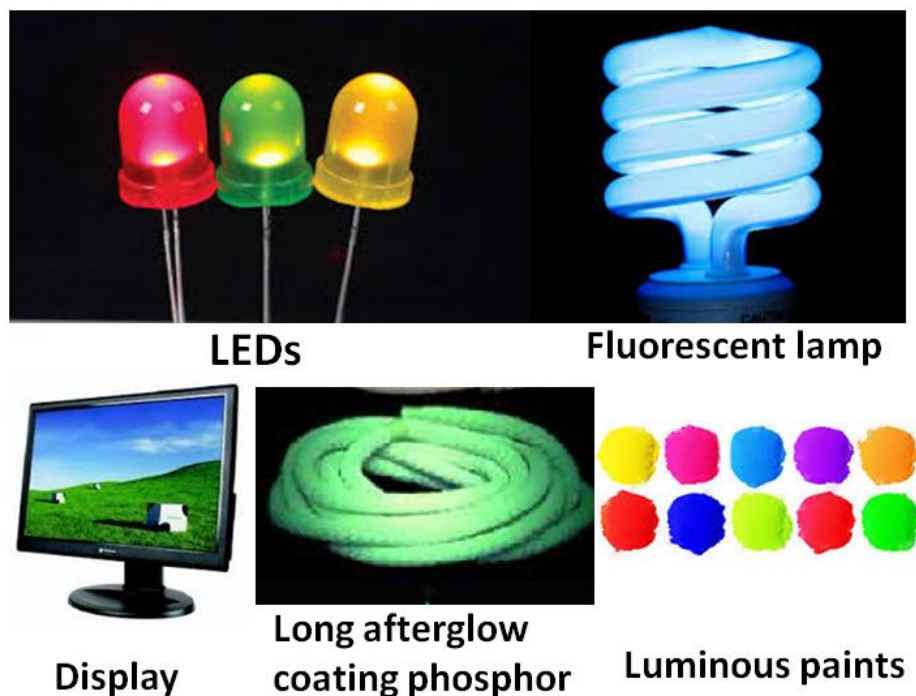


Figure 2.2: Some phosphor applications.

2.4 Lanthanides

The lanthanides are the group of fifteen elements in the periodic table from atomic numbers 57-71. It is worth noting that when scandium (Sc, $Z = 21$) and yttrium (Y, $Z = 39$) are included, they form the RE elements (yellow colour in [figure 2.3](#)). Lanthanides are known to have unique luminescent properties and they emit in a wide range of wavelengths, including UV, visible and NIR regions, which makes them good candidates for many applications, including lasers, lighting and scintillators [\[12\]](#). For instance, Tb^{3+} , Sm^{3+} , Eu^{3+} , and Tm^{3+} emit green, orange, red and blue light, respectively. Nd^{3+} , Er^{3+} and Yb^{3+} are well-known to have an emission in NIR region, but other lanthanide ions such as Pr^{3+} , Sm^{3+} , Dy^{3+} , Ho^{3+} , and Tm^{3+} also show transitions in the NIR region.

1 H																	2 He
3 Li	4 Be											5 B	6 C	7 N	8 O	9 F	10 Ne
11 Na	12 Mg											13 Al	14 Si	15 P	16 S	17 Cl	18 Ar
19 K	20 Ca	21 Sc	22 Ti	23 V	24 Cr	25 Mn	26 Fe	27 Co	28 Ni	29 Cu	30 Zn	31 Ga	32 Ge	33 As	34 Se	35 Br	36 Kr
37 Rb	38 Sr	39 Y	40 Zr	41 Nb	42 Mo	43 Tc	44 Ru	45 Rh	46 Pd	47 Ag	48 Cd	49 In	50 Sn	51 Sb	52 Te	53 I	54 Xe
55 Cs	56 Ba	57 La	72 Hf	73 Ta	74 W	75 Re	76 Os	77 Ir	78 Pt	79 Au	80 Hg	81 Tl	82 Pb	83 Bi	84 Po	85 At	86 Rn
87 Fr	88 Ra	89 Ac	104 Rf	105 Db	106 Sg	107 Bh	108 Hs	109 Mt	110 Ds	111 Rg	112 Uub						
		58 Ce	59 Pr	60 Nd	61 Pm	62 Sm	63 Eu	64 Gd	65 Tb	66 Dy	67 Ho	68 Er	69 Tm	70 Yb	71 Lu		
		90 Th	91 Pa	92 U	93 Np	94 Pu	95 Am	96 Cm	97 Bk	98 Cf	99 Es	100 Fm	101 Md	102 No	103 Lr		

Figure 2.3: The periodic table of elements. The lanthanides (together with Sc and Y) are highlighted in yellow, the actinides in grey.

Most of the lanthanides exhibit a trivalent (3+) oxidation state which is the most stable. Due to the presence of an empty, half-full or full $4f$ shell, other stable oxidation states also occur, such as tetravalent (e.g. Ce^{4+}) and divalent (e.g. Eu^{2+}). The $4f$ electrons of lanthanides are well shielded from the surroundings by filled $5s$ and $5p$ orbitals. Therefore, the optical transitions within the $4f$ orbitals are hardly affected by the surroundings (ligands) or crystal electric field. As the result of shielding, the emission transitions from lanthanides exhibit typically very narrow lines in luminescence and absorption spectra because they have almost retained their atomic character [2]. Moreover, $4f$ - $4f$ transitions are theoretically forbidden by the parity rule which leads to long life time of the excited state of lanthanides [2, 13]. The energy levels of $4f$ electrons of the trivalent RE ions have been investigated by Dieke *et al.* [14] (see figure 2.4). A Dieke diagram was determined theoretically and experimentally by considering the optical spectra of individual ions incorporated in $LaCl_3$ crystals host. Due to the good shielding of the $4f$ electron shell from the environment, the diagram is applicable to ions

in almost any host lattice. Therefore this diagram can be used to identify the possible energy level transitions of all lanthanides.

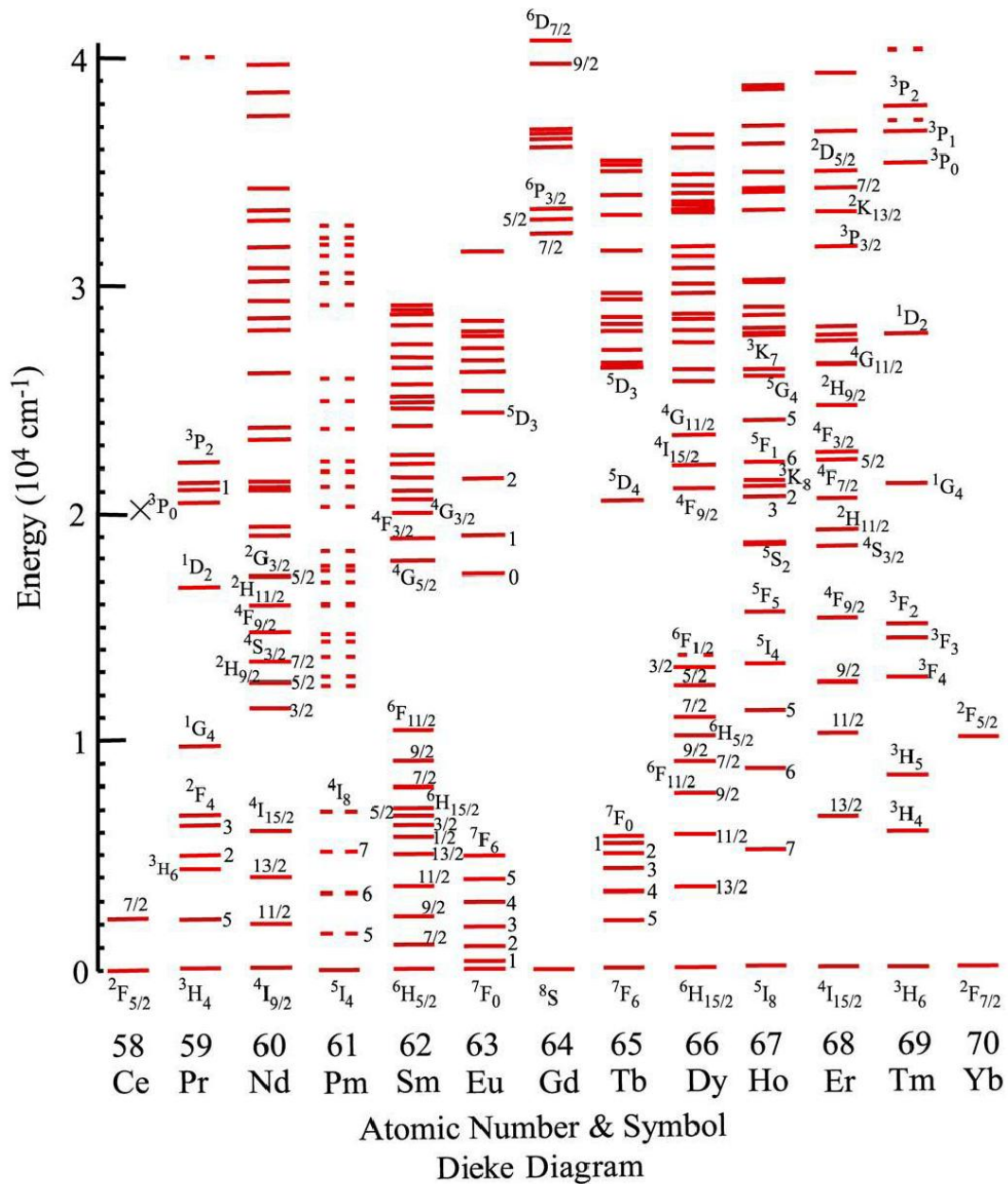


Figure 2.4: Dieke diagram showing the energy levels of the trivalent lanthanides [12].

2.4.1 Lanthanide excitation processes

Lanthanide ions can exhibit three types of excitation transitions, namely $4f-4f$, $4f-5d$ and charge-transfer state transitions. The details about these excitation transitions will be discussed below.

2.4.1.1 $4f-4f$ transitions

The $4f-4f$ transitions are very important in many applications (e.g., lasers, lighting and scintillators) and will be the focus in this work. The $4f$ electrons exhibit transitions between different energy levels of the $4f$ orbitals of the same lanthanide ion. The electric-dipole $4f-4f$ transitions are in theory forbidden by the parity selection rule. However, this rule can be relaxed when the lanthanides are introduced into asymmetric solid hosts. The interactions with the host material slightly increase the probability of such transitions. This is due to the mixing of the $4f$ wave functions of the ion with a small amount of opposite parity wave functions of the host which causes intra-configurational $4f$ transitions to gain some intensity [15], but the corresponding emission bands usually remain weak and narrow. Consequently, researchers use different approaches, namely $f-d$ absorption (see section 2.4.1.2), charge-transfer state absorption (see section 2.4.1.3) and host absorption, to enhance the excitation efficiencies of RE ions. Recently, plasmonic metal NPs have been used due to strong local electric field (plasmonic effect discussed in chapter 3).

2.4.1.2 $4f-5d$ transitions

Unlike $4f-4f$ transitions, $4f-5d$ transitions are allowed and therefore give more emission intensity than $4f-4f$ transitions [1]. In $4f-5d$ transitions, one of the $4f$ electrons is excited to a $5d$ orbital of higher energy. Due to the interaction of the $5d$ electrons with the surrounding ligand ions, the bonding strength changes upon $4f-5d$ excitation (the d electrons contribute in the chemical bonding), resulting in broad absorption and emission bands [2], and this is typically observed in Ce^{3+} ions ($4f^1$ configuration). For this reason the $4f-5d$ excitation strongly depends on the host properties (particularly crystal field) and therefore varies over the spectral range of the blue and UV region [1].

Therefore, using noble metal NPs to enhance the $4f$ - $5d$ excitation is not a good proposition.

2.4.1.3 Charge-transfer state transitions

In this transition mechanism, the $2p$ electrons from the neighbouring anions (e.g. oxygen in oxides) are transferred to a $4f$ orbital [3]. These charge-transfer state (CTS) transitions are allowed and result in intense and broad absorptions. They may occur between the lanthanide dopant and a host ion or between the host ions themselves [16]. For instance, a Eu^{3+} ion ($4f^6$) needs one additional electron to reach the half filled configuration. Thus $2p$ electrons from surrounding anions can easily transfer to the $4f$ orbital of Eu^{3+} .

2.4.2 Some luminescent centres

2.4.2.1 Terbium ions

The trivalent Tb^{3+} ion is one of the most investigated RE ions during the past decade [12, 17]. Due to its promising properties, Tb^{3+} is used as dopant for many solid-state devices such as light emitting diodes (LEDs), fluorescent lamps and television screens. Under UV excitation, the Tb^{3+} ions in SiO_2 produced during this study show narrow emission lines in both green spectral region at 490, 544, 587 and 623 nm due to $^5\text{D}_4 \rightarrow ^7\text{F}_J$ ($J = 6, 5, 4, 3$) transitions and the blue spectral region at 380, 415, 438, 460, 478 nm due to $^5\text{D}_3 \rightarrow ^7\text{F}_J$ ($J = 6, 5, 4, 3, 2$) transitions, respectively (see figure 2.5, the band around 478 nm is not resolved due to its overlap with much stronger emission band around 490 nm). The most intense transition occurs in the green region and corresponds to $^5\text{D}_4 \rightarrow ^7\text{F}_5$ which is located around 544 nm while in the blue region the intense transition is strongly depended on the host and the concentration of Tb^{3+} . It is also important to note that the intensity ratio of the green emission to the blue emission depends mainly on the Tb^{3+} concentration. At high concentration the electrons from $^5\text{D}_3$ level non-radiatively decay to the lower energy level of $^5\text{D}_4$ through cross relaxation, therefore quenching the blue emission. The cross relaxation actually occurs between two identical ions or molecule (e.g. Tb^{3+}) when a first ion is primarily in an excited state exchanges energy with the second ion that was initially in ground state, which in turn leads to simultaneously change both ions to excited state.

Tb³⁺ ions exhibit two excitation regions: one is due to the *f-d* excitation band which is located below 300 nm. The other one is due to *f-f* excitation band located between 300-500 nm (figure 2.5(a)). Figure 2.5(b) shows the corresponding absorption and emission of Tb³⁺ ions in silica glass.

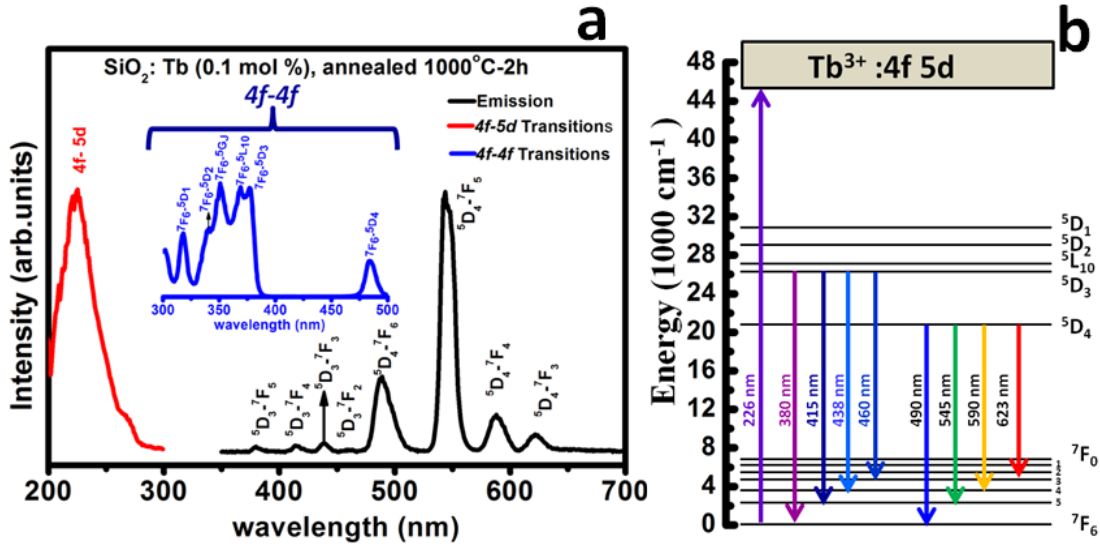


Figure 2.5: (a) The excitation and emission of 0.1 mol% Tb³⁺ doped SiO₂ (b) schematic energy level diagram.

2.4.2.2 Silver ions

Silver ions (Ag⁺) are well-known to have photoluminescence emission in crystal and glassy matrices [18-20]. The Ag atom has a core ground state electron configuration of [Kr] 4d¹⁰5s¹. If the electron in the 5s orbital is lost, resulting in a Ag ion (Ag⁺) with electron configuration of [Kr]4d¹⁰, then the origin of the luminescence is owing to electronic transitions between the 4d¹⁰ ground state (¹S₀) and some levels (excited states) of the 4d⁹5s¹ configuration. These transitions are theoretically forbidden in free ions due to the parity rule, but when introduced into a matrix they partially become allowed due to the coupling with lattice vibration of the odd parity. The Russell-Saunders states arising from the 4d⁹5s¹ configuration are split into different energy levels (³D₃, ³D₂, ³D₁ and ¹D₂ in order of increasing energy) by spin-orbit coupling and by the crystal field induced by

the surrounding ligands [19]. The transitions from 3D_J ($J = 3, 2, 1$) to ground state 1S_0 are spin forbidden while the transitions from 1D_2 to ground state 1S_0 are spin allowed [18]. The transitions ${}^3D_J-{}^1S_0$ ($J = 3, 2, 1$) exhibit emission in the long wavelength (e.g. blue and green) while the ${}^1D_2-{}^1S_0$ transition gives emission in the short wavelength (e.g. violet) [18].

It is well known that when Ag ions are incorporated into glass matrices at low temperature, they occur in different form such as Ag^+ , $(Ag^+)_2$ and $(Ag_2)^+$ or generally in the form of $(Ag_n)^{m+}$ [21]. The excitation and emission bands of these ions are observed in the UV and visible spectral ranges and can exhibit considerable shift depending on the composition and structure of glasses. It is worth noting that the overlap between two different Ag species (e.g., Ag^+-Ag^+) can also shift the excitation and emission bands [20]. For instance, the lowest excited electronic states of the isolated Ag ion in most glasses fall at 39163 cm^{-1} (255.34 nm) (3D_3), 40741 cm^{-1} (245.45 nm) (3D_2), 43739 cm^{-1} (228.63 nm) (3D_1) and 46046 cm^{-1} (217.17 nm) (1D_2) [19]. Details about excitation and emission of some Ag species in different glasses can be found in chapter 5.

2.5 Energy transfer mechanisms

ET is a physical phenomenon that occurs between two luminescent centres separated by a distance R (see figure 2.6 (a)). An excited donor (D) can transfer its energy to another centre called an acceptor (A), either radiatively by emitting a photon (re-absorption), or non-radiatively. The non-radiative ET can take place by either inducing a dipole in the neighbouring acceptors (Förster-type), or by electron-exchange (Dexter-type). It is worthwhile to note that the ET can occur between a pair of identical centres (homotransfer), i.e. $Tb^{3+}-Tb^{3+}$ or between two different centres (heterotransfer), i.e. Ag^+-Tb^{3+} . Although the nature of Förster and Dexter types of ET is different, they require overlap between the emission spectrum of the donor and the excitation spectrum of the acceptor. Figure 2.6 (b) explains the steps of ET from donor to acceptor.

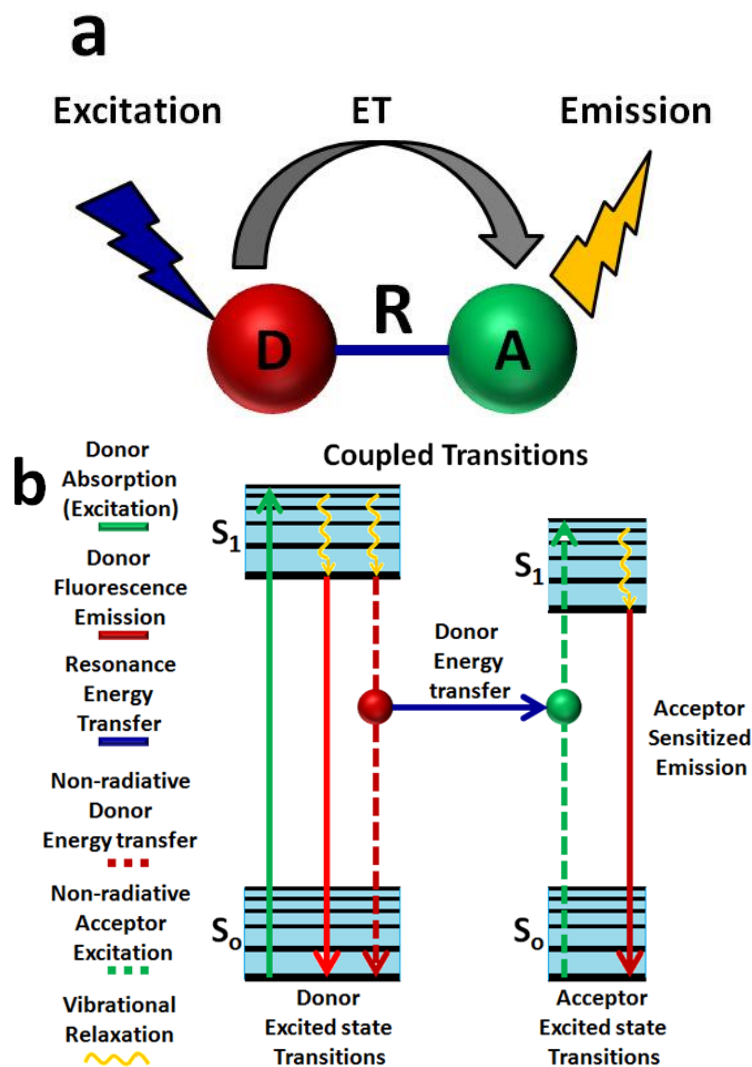
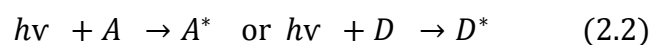


Figure 2.6: (a) Illustration of ET phenomenon (b) Jablonski diagram illustrating coupled transitions between donor emission and acceptor absorbance in fluorescence resonance ET. Absorption and emission transitions are represented by straight vertical arrows (green and red respectively), while vibrational relaxation is indicated by wavy yellow arrows. The coupled transitions are drawn with dashed lines. The phenomenon of ET is illustrated by a blue arrow [22].

2.5.1 Radiative energy transfer

Radiative ET occurs when a real photon emitted by donor D is re-absorbed by an acceptor A (or D) and is observed when the average distance between D and A (or D) is larger than the wavelength of light emitted by the donor. The radiative ET mechanism is represented by [equations 2.1 and 2.2](#):



where D^* and A^* are the excited donor and acceptor, respectively. $h\nu$ refers to the photon energy emitted by the donor.

This type of ET does not require any interaction between the donors and acceptors, but it depends only on the spectral overlap and the concentration. In case of heterotransfer the fluorescence decay of the donor remains unchanged while in case of homotransfer the fluorescence decays more slowly as a result of successive re-absorptions and re-emissions [\[23\]](#).

2.5.2 Non-radiative energy transfer

Unlike radiative transfer, the non-radiative ET occurs without emission of real photons by the donor and requires some interaction between the donor and acceptor. However, non-radiative ET can result from different interaction mechanisms, involving Coulombic interaction or intermolecular orbital overlap. The Coulombic interactions are composed of long-range dipole-dipole interactions (Förster type) and short-range multi-polar interactions, while intermolecular orbital overlap include electron exchange (Dexter type) and charge resonance interactions which are only short range (see [figure 2.7](#)).

Förster and Dexter types are very important and extensively studied in phosphors. Förster type is more sensitive at shorter distances (1-10 nm) whereas the Dexter type dominates at very close distances (< 1 nm) where the wave functions of the donor and acceptor start

overlapping allowing for electron exchange. For more details about ET, the reader is recommended to consult the references [23, 24].

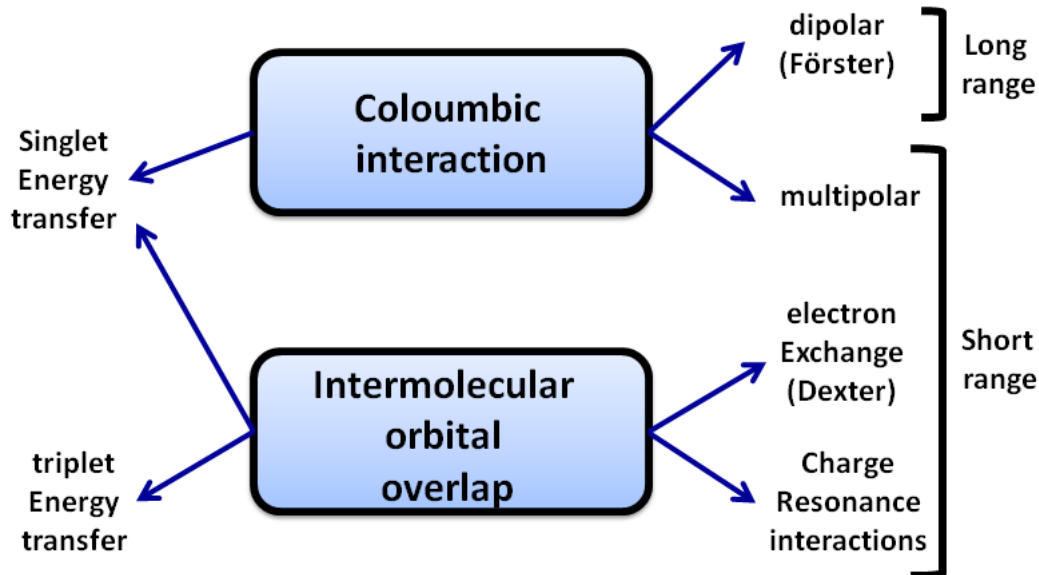


Figure 2.7: Types of interactions involved in non-radiative ET mechanisms. Adapted from [23].

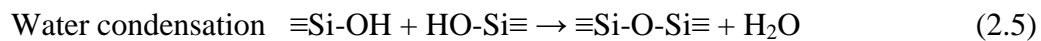
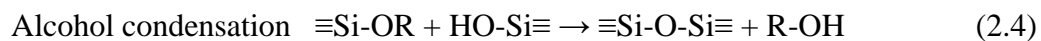
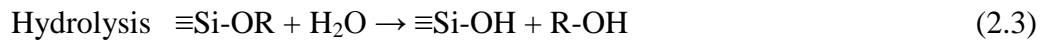
2.6 Preparation methods of phosphors

Many methods of preparing phosphors have been used such as combustion, sol-gel, solid state reaction, hydrothermal, microwave process, spray pyrolysis and precipitation method. Phosphors with low cost and high efficiency require simple synthesis methods at low temperature to produce a homogenous distribution of dopant and small particle size. Combustion and sol-gel methods are a good choice because they both meet the mentioned requirements.

2.6.1 Sol-gel method

The sol-gel process is a wet chemical technique widely used in the fields of ceramics and glassy materials at relatively low temperatures [25]. This method involves formation of a *sol* (colloidal suspension of small particles suspended in a liquid) and subsequent crosslinking to form a viscous *gel*. Through this technique, highly reactive compounds are used as initial precursors. The most common starting precursors used are generally

metal alkoxides $M(OR)_x$, where M is a metal (e.g. Zr, Ti, Fe, Ni) or a transition metal (e.g. Si, Sn) atom and R is an alkyl group (e.g. methanol, ethanol, propanol, etc.). The most widely metal alkoxide compounds used in the sol-gel method are $Si(OR)_4$, such as tetramethoxysilane (TMOS) and tetraethoxysilane (TEOS). In our case TEOS is used. These precursors are normally mixed with polar solvents such as alcohol or water, which facilitate the two primary reactions of hydrolysis and condensation. These two reactions (with two possibilities for the condensation reaction) are [17]:



In the hydrolysis reaction the alkoxide group (-OR) is replaced by a hydroxyl group (-OH) as shown in equation 2.3. The condensation can take place by either two silanols ($\equiv Si-OH$) (equation 2.5) or between a silanol and an alkoxy group ($\equiv Si-OR$) (equation 2.4) to form a bridging siloxane group ($\equiv Si-O-Si\equiv$). The number of this group increases by allowing time for polycondensation and the network of silica is ultimately formed. Compared to other metal alkoxides, it is well-known that the kinetics for the hydrolysis of $Si(OR)_4$ compounds require several days for completion. Consequently, some catalysts are generally added to the mixture such as acids (e.g. HCl, HNO_3) or bases (e.g., KOH, amines, NH_3). However, changing the reaction rate using the pH, $[H_2O/M(OR)_n]$ molar ratio, and catalyst may force the completion of hydrolysis prior to condensation, which greatly affects the physical properties of the final product [26].

A drying process is necessary to remove unwanted solvents trapped in the network, which is typically accompanied by a significant shrinkage and densification. Further thermal treatment (sintering) is also required to form dense glass or ceramic and to enhance structural stability and mechanical properties.

Compared to other traditional methods, the sol-gel method offers several advantages, including low processing temperature, high purity, higher concentrations of dopants (e.g., RE^{3+}) is possible, high homogeneity of samples and relatively low cost. Figure 2.8 shows typical processing steps for sol-gel preparation of amorphous silica particles (SiO_2). In this study the molar ratio of 1:5:10 for TEOS:ethanol:water was used.

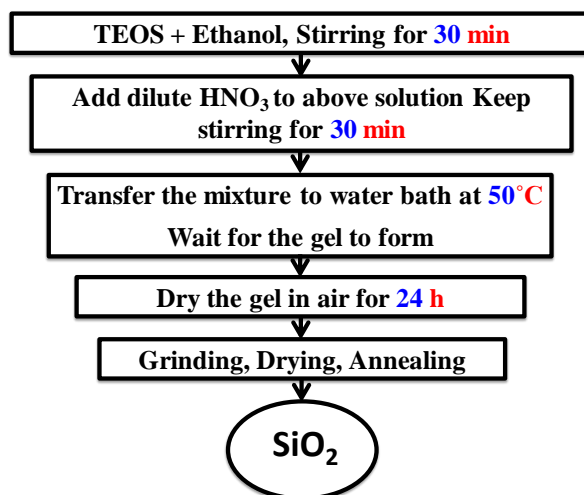
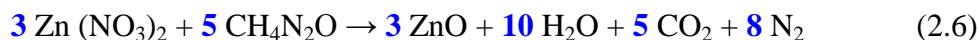


Figure 2.8: Schematic diagram for preparation of amorphous SiO_2 powder by sol-gel method.

2.6.2 Combustion method

Combustion is defined as rapid oxidation generating heat, or both light and heat in the case of fast oxidation [27]. This method has been extensively used to produce industrially useful materials [28]. It is known as a versatile, simple and fast process, which offers effective synthesis of a variety of nanomaterials. The most important features that make the combustion method useful to prepare a phosphor are the formation and crystallization of as prepared phosphors without need of annealing process. This process involves a self-sustained reaction in homogeneous solution of different oxidizers (e.g., metal nitrates) and fuels (e.g., urea, glycine, hydrazides). Stoichiometric compositions of the metal nitrates (oxidizers) and fuels (urea) can be calculated using the total oxidizing and

reducing valencies of the components which serve as numerical coefficients for stoichiometric balance, so that the equivalent ratio is unity and the energy released by the combustion is at a maximum [29]. Equation 2.6 is an example of a stoichiometric combustion reaction of zinc nitrate ($\text{Zn}(\text{NO}_3)_2 \cdot 4\text{H}_2\text{O}$) and urea ($\text{CO}(\text{NH}_2)_2$) to form zinc oxide (ZnO):



The N_2 , CO_2 and H_2O are released during the reaction and no residuals are left in the final product. Figure 2.9 is a schematic diagram for the preparation of nanocrystalline zinc oxide powders by the combustion process.

In typical reaction, initially, the mixture (metal nitrates and fuel) boils and undergoes dehydration followed by decomposition with the generation of large amounts of gases (oxides of nitrogen and carbon) and flames after about 5 minutes, resulting in a product that appears as porous foam filling the capacity of the container.

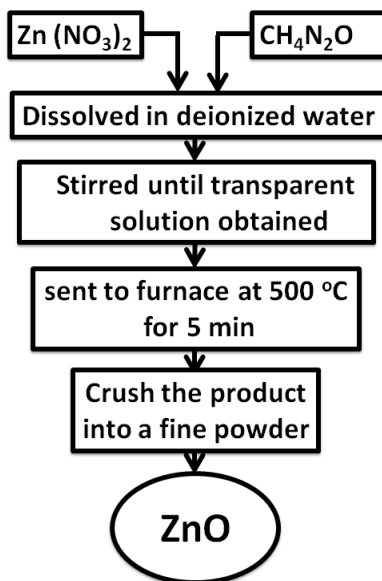


Figure 2.9: Schematic diagram for preparation of nanocrystalline ZnO powder by combustion method.

2.7 Structure of phosphor hosts

In this study we have used amorphous SiO_2 and crystalline $\text{Bi}_4\text{Si}_3\text{O}_{12}$ and ZnO as hosts for both Tb^{3+} ions and Ag due to their good physical properties. Of particular interest is that they have appropriate refractive index to shift the localized surface plasmon resonance (LSPR) absorption band associated with Ag NPs to overlap with one of the Tb^{3+} ions absorption bands for plasmonic enhancement. Details about these hosts are given below.

2.7.1 Silica (SiO_2)

Sol-gel derived silica (SiO_2) is well known as a good host material for RE ions due to its good physical and chemical stability, its excellent optical properties and the fact that it is inexpensive and easy to fabricate. It has potential technological applications in many fields such as lighting, catalysts, sensors, solar energy collectors, fibre optics, waveguides, electronics, vacuum systems, and furnace windows [26, 30].

Amorphous silica may crystallize into several crystalline forms (polymorphs) under different conditions of temperature and pressure, namely quartz, coesite, stishovite, cristobalite, tridymite [30]. The most common are quartz, cristobalite and tridymite [31]. Except the stishovite form, all other forms have the same tetrahedral framework structure (SiO_4), but a distinct crystal structure. The Si atom is surrounded by four O atoms to form a tetrahedral SiO_4 unit and each tetrahedron corner is shared with another tetrahedron to form the silica framework (see figure 2.10 (a)). The distance of the Si-O bonds is ranging between 0.152 nm to 0.169 nm while the tetrahedral O-Si-O bond angle is 109.18° [32]. Each oxygen anion in the silica network is bonded to two silicon cations (Si-O-Si) with bond angle ranging from 120° to 180° , depending on the phase (see figure 2.10 (b)).

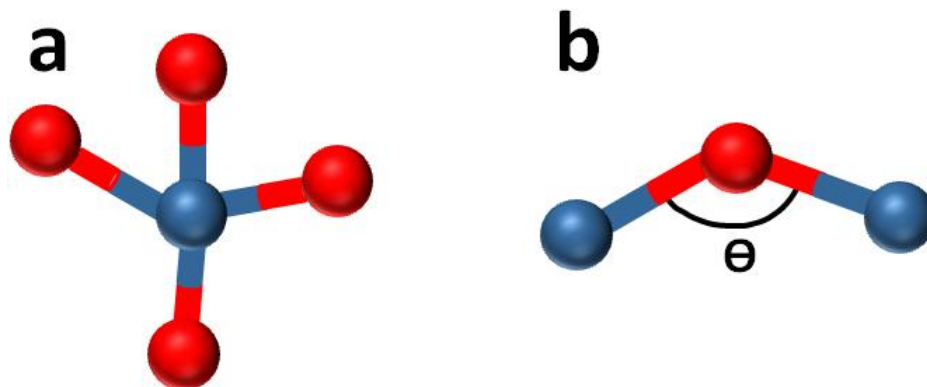


Figure 2.10: (a) SiO_4 structural unit of most forms of SiO_2 , showing tetrahedral coordination. (b) Si-O-Si bonding configuration with Si-O-Si bond angle Θ varying from 120° to 180° depending on the form of SiO_2 . Adapted from [32].

To understand the structure difference between quartz, amorphous silica and the cristobalite phase of silica, X-ray diffraction (XRD) patterns and Fourier transform infrared (FTIR) spectra of these phases are given in figure 2.11. The XRD (figure 2.11(a)) shows clear differences between these phases. The sample annealed at 1200°C show only broad hump around 21° indicate glassy silica with a high degree of randomness and when annealed at 1500°C is converted to cristobalite phase as confirmed by the Powder Diffraction File (PDF) 00-039-1425. The natural quartz showed different XRD lines compare to the amorphous and cristobalite phase which indicate that quartz has its own structure. Moreover, the FTIR spectra of figure 2.11(b) also show differences between the three phases which can be used as fingerprint to differentiate between them. There are four common peaks for these phases related to Si-O-Si vibration modes which appear in all samples indicating the formation of the silica network. Of interest is that there is small variation in the peak position of these peaks compared to the amorphous phase. The shift is correlated with changes in silica structure, especially changes in Si-O-Si bond angle (figure 2.10 (b)) [33].

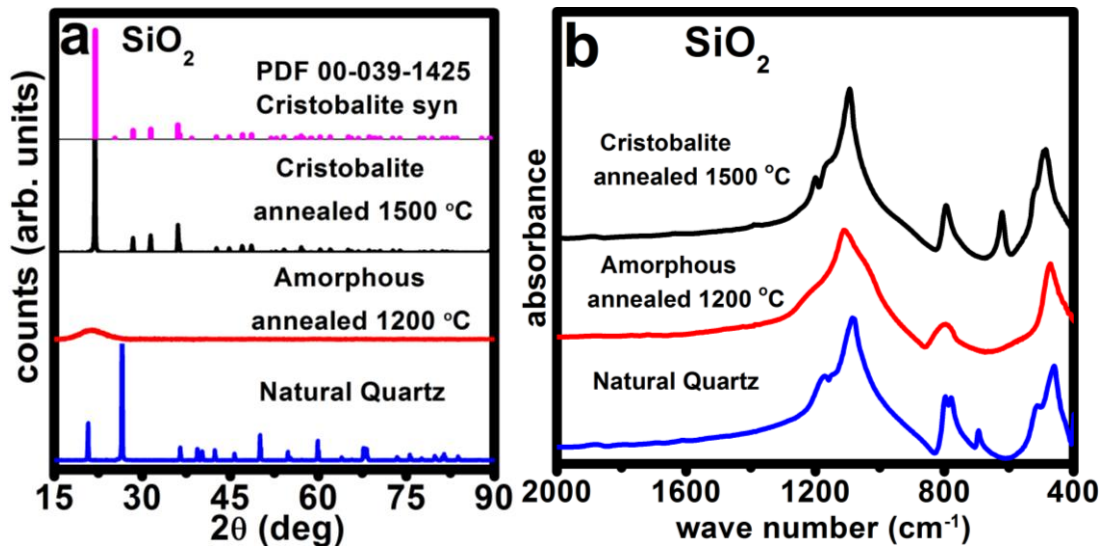


Figure 2.11: (a) XRD (b) FTIR of different phases of SiO₂.

Theoretically, from the silica phase diagram (figure 2.12), at normal pressure trigonal α -quartz will transform into hexagonal β -quartz at 573 °C, upon further heating the quartz will transform into hexagonal β -tridymite at 870 °C. Heating β -tridymite at 1470 °C gives cubic β -cristobalite and at 1705 °C β -cristobalite finally melts [30].

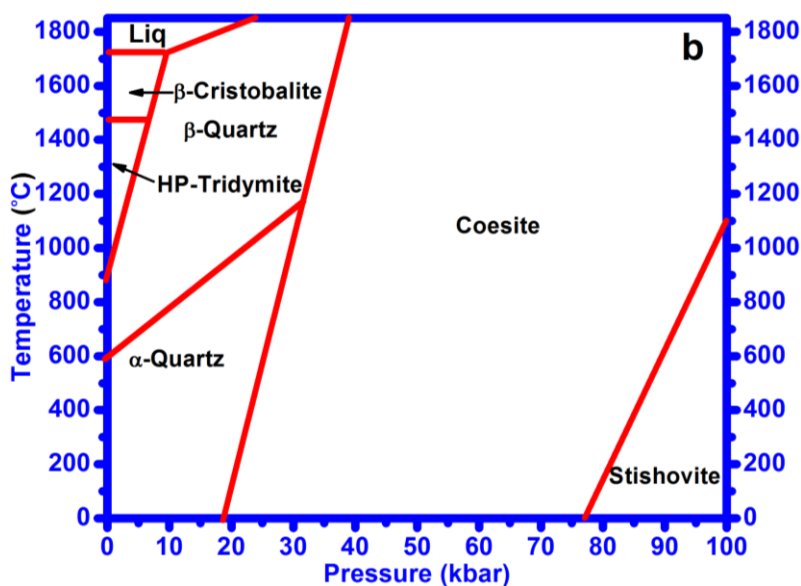


Figure 2.12: Phase diagram for SiO₂. Adapted from [30].

Despite this, when silica glass is heated up it will simply turn into β -cristobalite [34] because the structure of amorphous silica is similar to the liquid phase. To confirm that experimentally, silica glass was prepared by the sol-gel method and annealed in different temperature (1200 °C and 1500 °C). Both samples were characterized by XRD and FTIR. Figure 2.11(a) shows XRD patterns which confirm the transition of amorphous silica directly to β -cristobalite (PDF 00-039-1425) when heated up to 1500 °C at a heating rate of 0.2 °C/min.

2.7.2 Zinc oxide (ZnO)

Zinc oxide (ZnO) is a chemical compound found naturally in the mineral called zincite. It is a binary compound semiconductor belonging to the group II-VI with a wide energy band gap (3.37 eV) and a large exciton binding energy of 60 meV at room temperature [35]. ZnO powder has attracted much attention in the past fifty years due to its intriguing properties such as dielectric, piezoelectric, pyroelectric, semiconducting, acousto-optic, optical, electro-optical, nonlinear optical, photo-electro-chemical and electrical properties [36]. Due to exceptional luminescent properties in the UV and visible region, ZnO has found many applications particularly in optoelectronic devices [35]. Moreover, ZnO is known as an attractive host lattice for several dopants (luminescence centres) and show versatile applications.

ZnO crystallizes into different forms, namely zinc blende (B3), wurtzite (B4) and rocksalt (B1) as schematically shown in figure 2.13. B1, B3, and B4 indicate the Strukturbericht designations for the three phases [37]. In the cubic zinc blende and hexagonal wurtzite structure, each anion is surrounded by four cations at the corners of a tetrahedron and vice versa, while the cubic rocksalt phase is crystallized in the well known NaCl structure (figure 2.13(a)). Among these structures, wurtzite is the thermodynamically stable phase under ambient conditions while zinc blende and rocksalt can be stabilized only by growth on cubic substrates and at relatively high pressures, respectively [37].

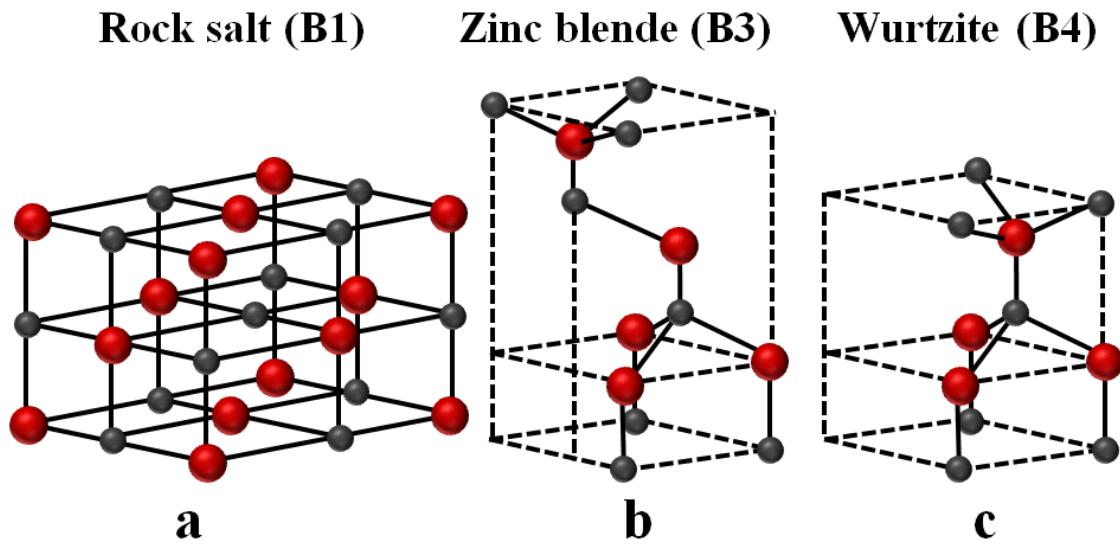


Figure 2.13: Schematic representation of ZnO crystal structures: (a) cubic rocksalt (B1), (b) cubic zinc blende (B3), and (c) wurtzite (B4). Red and grey spheres denote Zn and O atoms, respectively. Adapted from [37].

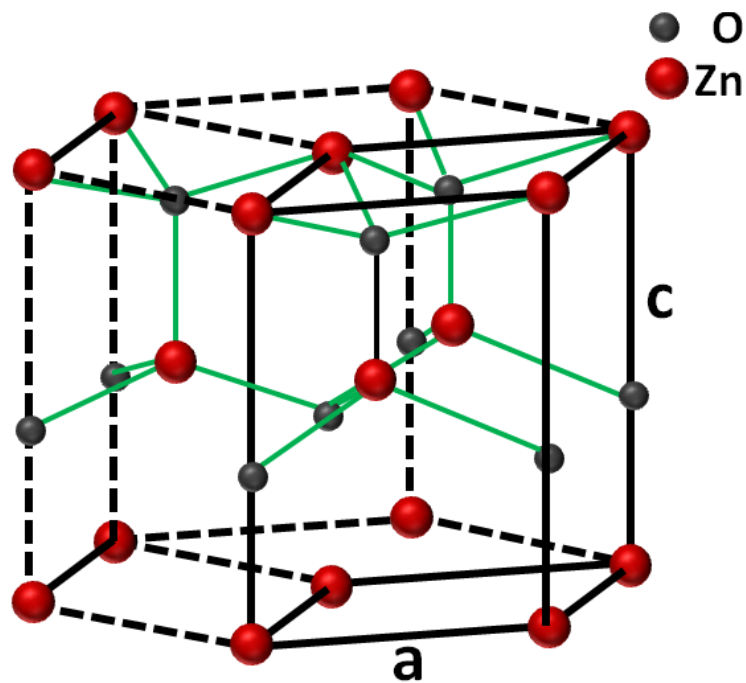


Figure 2.14: Unit cell of the wurtzite structure of ZnO. Adapted from [38].

Figure 2.14 shows the hexagonal unit cell of the wurtzite structure which has two lattice parameters a and c . In an ideal wurtzite structure the ratio of these parameters is $c/a = \sqrt{8/3} = 1.633$ and experimentally it varies from 1.593 to 1.601 [39]. The hexagonal wurtzite structure of ZnO belongs to the space group C_{6v}^4 in the Schoenflies notation and $P6_3mc$ in the Hermann-Mauguin notation [37].

2.7.3 Bismuth silicate ($\text{Bi}_4\text{Si}_3\text{O}_{12}$)

Bismuth-based oxides have attracted much attention in science due to their good optical and electrical properties, which make them attractive in many applications [40]. Among bismuth-based oxides, bismuth silicate $\text{Bi}_4\text{Si}_3\text{O}_{12}$ has excellent physical, chemical and mechanical properties such as a high refractive index, high nonlinearity index, high mechanical strength, chemical inertness and a fast response to optical signals [41]. Moreover, $\text{Bi}_4\text{Si}_3\text{O}_{12}$ is well known as a new fast scintillation material which is used in high energy physics, computed tomography and dosimetry [42]. Recently, $\text{Bi}_4\text{Si}_3\text{O}_{12}$ has been used as a host for some RE ions for lasing and lighting applications [43, 45].

Bismuth silicate may crystallize into different phases, namely Bi_2SiO_5 , $\text{Bi}_{12}\text{SiO}_{20}$ and $\text{Bi}_4\text{Si}_3\text{O}_{12}$ depending on the thermal treatment. The most stable phases are Bi_2SiO_5 and $\text{Bi}_4\text{Si}_3\text{O}_{12}$ [41], which have different structures and space groups, namely orthorhombic ($Cmc2_1$) for Bi_2SiO_5 and cubic ($\bar{I}43d$) for $\text{Bi}_4\text{Si}_3\text{O}_{12}$.

In the $\text{Bi}_4\text{Si}_3\text{O}_{12}$ structure the Si^{4+} cations with the local symmetry S_4 are coordinated tetrahedrally by four O^{2-} anions [SiO_4] while the Bi^{3+} ions occupy a special 16-fold position of the C_3 symmetry and are coordinated by six oxygen atoms in the form of [BiO_6] octahedrons in three dimensions (figure 2.15) [45]. Figure 2.15 shows the cubic unit cell of $\text{Bi}_4\text{Si}_3\text{O}_{12}$ which was generated using the Diamond programme [46].

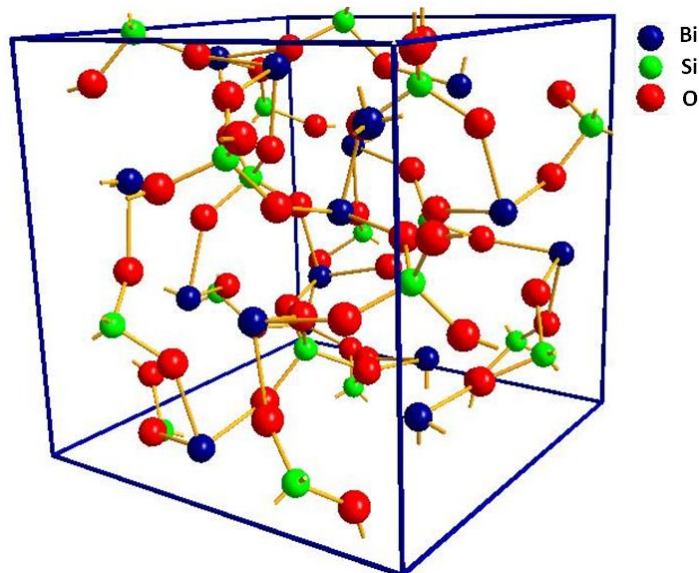


Figure 2.15: Unit cell of $\text{Bi}_4\text{Si}_3\text{O}_{12}$ structure generated using Diamond programme.

2.8 References

- [1] H. A. Höpfe, Recent developments in the field of inorganic phosphors, *Angew. Chem. Int. Ed.* **48** (2009) 3572-3582.
- [2] C. R. Ronda, T. Jüstel and H. Nikol, Rare earth phosphors: fundamentals and applications, *J. Alloys Compd.* **275-277** (1998) 669-676.
- [3] S. Shionoya and *et al.*, Phosphor handbook, edited by W. M. Yen, *Taylor & Francis Group*, USA, 2nd ed. (2007) (46 pages).
- [4] C. Feldmann, T. Jüstel, C. R. Ronda and P. J. Schmidt, Inorganic Luminescent Materials: 100 Years of Research and Application, *Adv. Funct. Mater.* **13** (2003) 511-516.
- [5] A. K. Levine and F. C. Palilla, A new highly efficient Red-emitting cathodoluminescent phosphor ($\text{YVO}_4:\text{Eu}$) for color Television, *Appl. Phys. Lett.* **5** (1964) 118-120.
- [6] S. Tanabe, Optical transitions of rare earth ions for amplifiers: how the local structure works in glass, *J. Non-Cryst. Solids* **259** (1999) 1-9.

- [7] M. H. Huang, S. Mao, H. Feick, H. Yan, Y. Wu, H. Kind, E. Weber, R. Russo and P. Yang, Room-temperature ultraviolet nanowire nanolasers, *Science*, **292** (2001) 1897-1899.
- [8] J. Zhang, Z. Hao, X. Zhang, Y. Luo, X. Ren, X. Wang and J. Zhang, Color tunable phosphorescence in $KY_3F_{10}:Tb^{3+}$ for X-ray or cathode-ray tubes, *J. Appl. Phys.* **106** (2009) 034915.
- [9] K. Tanaka, Cathode luminescence of samarium, europium, and gadolinium ion doped scintillator $CdWO_4$ single crystals studied with X-ray photoelectron spectroscopy, *J. Appl. Phys.* **89** (2001) 5449-5453.
- [10] A. Shalava, B. S. Richards and M. A. Green, Luminescent layers for enhanced silicon solar cell performance: Up-conversion, *Sol. Energy Mater. Sol. Cells* **91** (2007) 829-842.
- [11] V. Bachmann, C. Ronda, O. Oeckler, W. Schnick and A. Meijerink, Color Point Tuning for $(Sr,Ca,Ba)Si_2O_2N_2:Eu^{2+}$ for White Light LEDs, *Chem. Mater.* **21** (2009) 316-325.
- [12] K. Ogasawara, S. Watanabe, H. T. Oyshima and M. G. Brik, First-principles calculations of $4f^n-4f^{n-1}-5d$ transition spectra, In: Handbook on the Physics and Chemistry of Rare Earths, edited by K. A. Gschneidner Jr., J. G. Bünzli and V. K. Pecharsky, *Elsevier*, North-Holland, volume **37** (2007) (511pages).
- [13] J. G. Bünzli, Lanthanide-containing luminescent molecular edifices, *J. Alloys Compd.* **408-412** (2006) 934-944.
- [14] G. H. Dieke and H. M. Crosswhite, The Spectra of the Doubly and Triply Ionized Rare Earths, *Appl. Opt.* **2** (1963) 675-686.
- [15] J. H. Van Vleck, The puzzle of rare-earth spectra in solids, *J. Phys. Chem.* **41** (1937) 67-80.
- [16] A. H. Krumpe, P. Boutinaud, E. van der Kolk, P. Dorenbos, Charge Transfer Transitions in the Transition Metal Oxides $ABO_4:Ln^{3+}$ and $APO_4:Ln^{3+}$ ($A = La, Gd, Y, Lu, Sc$; $B = V, Nb, Ta$; $Ln = Lanthanide$), *J. Lumin.* **130** (2010) 1357-1365

- [17] R. K. Verma, K. Kumar and S. B. Rai, Pulsed laser ablation synthesis of silver nanoparticles and their use in fluorescence enhancement of Tb³⁺-doped aluminosilicate glass, *Solid State Commun.* **150** (2010) 1947-1950.
- [18] E. Borsella, G. Battaglin, M. A. Garcia, F. Gonella, P. Mazzoldi, R. Polloni and A. Quaranta, Structural incorporation of silver in soda-lime glass by the ion-exchange process: a photoluminescence spectroscopy study, *Appl. Phys. A* **71** (2000) 125-132.
- [19] E. Borsella, F. Gonella, P. Mazzoldi, A. Quaranta, G. Battaglin and R. Polloni, Spectroscopic investigation of silver in soda-lime glass, *Chem. Phys. Lett.* **284** (1998) 429-434.
- [20] J. Rozra, I. Saini, S. Aggarwal and A. Sharma, Spectroscopic analysis of Ag nanoparticles embedded in glass, *Adv. Mat. Lett.* **4** (2013) 598-604.
- [21] S. Lai, Z. Yang, J. Li, B. Shao, J. Yang, Y. Wang, J. Qiu and Z. Song, Photoluminescence enhancement of Eu³⁺ ions by Ag species in SiO₂ three-dimensionally ordered macroporous materials, *J. Mater. Chem. C* **3** (2015) 7699-7708.
- [22] S. Saini, H. Singh, and B. Bagchi, Fluorescence resonance energy transfer (FRET) in chemistry and biology: Non-Förster distance dependence of the FRET rate, *J. Chem. Sci.* **118** (2006) 23-35.
- [23] B. Valeur, Molecular Fluorescence Principles and Applications, *WILEY-VCH Verlag GmbH*, Germany, (2002) (381 pages).
- [24] C. R. Ronda, Emission and Excitation Mechanisms of Phosphors, In: Luminescence: From Theory to Applications, edited by C. R. Ronda, *WILEY-VCH Verlag GmbH & Co. KGaA*, Weinheim, (2008) 219-260.
- [25] C. J. Brinker, G. W. Scherer, Sol-Gel Science: the Physics and Chemistry of Sol-Gel processing, *Academic Press Inc.*, USA, (1990) (908 pages).
- [26] J. Lin and K. Baerner, Tunable photoluminescence in sol-gel derived silica xerogels, *Mater. Lett.* **46** (2000) 86-92.
- [27] S. R. Turns, An Introduction to Combustion concepts and applications, *The McGraw-Hill Book Companies Inc.*, Singapore, 2nd ed. (2000) (676 pages).

- [28] S. T. Aruna and A. S. Mukasyan, Combustion synthesis and nanomaterials, *Curr. Opin. Solid State Mater. Sci.* **12** (2008) 44-50.
- [29] J. J. Kingsley, K. Suresh, K. C. Patil, Combustion synthesis of fine-particle metal aluminates, *J. Mater. Sci.* **25** (1990) 1305-1312.
- [30] L. P. Davila, S. H. Risbud and J. F. Shackelford, Quartz and Silicas, In: Ceramic and Glass Materials, edited by J. F. Shackelford and R. H. Doremus, *Springer Science+Business Media*, USA, (2008) 71-86.
- [31] M. G. Garnica-Romo, J. González-Hernández, M. A. Hernández-Landaverde, Y. V. Vorobiev, F. Ruiz and J. R. Martínez, Structure of heat-treated sol-gel SiO₂ glasses containing silver, *J. Mater. Res.* **16** (2001) 2007-2012.
- [32] T. Bakos, Defects in amorphous SiO₂: reactions, dynamics and optical properties, *PhD thesis*, Vanderbilt University, USA (2003) 6-59.
- [33] J. W. Hong, FTIR investigation of Amorphous Silica Fibers and Nano-Size Particles, *PhD thesis*, Rensselaer Polytechnic Institute Troy, New York (2003) 1-53.
- [34] The Silica Group: Overview of Silica Polymorphs, [online]. Available from http://www.quartzpage.de/gen_mod.html [Accessed 21 July 2015].
- [35] N. S. Singh, S. D. Singh, S. D. Meetei, Structural and photoluminescence properties of terbium-doped zinc oxide nanoparticles, *Chin. Phys. B* **23** (2014) 058104 (5 pages).
- [36] S. Chu, T. Yan, Characteristics of sol-gel synthesis of ZnO-based powders, *J. Mater. Sci. Lett.* **19** (2000) 349-352.
- [37] H. Morkoç and Ü. Özgür, Zinc Oxide Fundamentals, Materials and Device Technology, *WILEY-VCH Verlag GmbH & Co. KGaA*, Germany (2009) 1-70.
- [38] M. Niskanen, M. Kuisma, O. Cramariuc, V. Golovanov, T. I. Hukka, N. Tkachenko and T. T. Rantala, Porphyrin adsorbed on the (10 $\bar{1}$ 0) surface of the wurtzite structure of ZnO-conformation induced effects on the electron transfer characteristics, *Phys. Chem. Chem. Phys.* **15** (2013) 17408-17418.
- [39] S. Desgreniers, High-density phases of ZnO: Structural and compressive parameters, *Phys. Rev. B* **58** (1998) 14102-14105.

- [40] Z. G. Zhang, X. F. Wang, Q. Q. Tian, Grain orientation distribution and development of grain line in highly ordered $\text{Bi}_4\text{Si}_3\text{O}_{12}$ micro-crystals, *Sci. Sinter.* **42** (2010) 51-59.
- [41] H. W. Guo, X. F. Wang and D. N. Gao, Non-isothermal crystallization kinetics and phase transformation of Bi_2O_3 - SiO_2 glass-ceramics, *Sci. of Sinter.* **43** (2011) 353-362.
- [42] H. Xiea, C. Jia, Y. Jiang, X. Wangb, Synthesis of $\text{Bi}_4\text{Si}_3\text{O}_{12}$ powders by a sol-gel method, *Mater. Chem. Phys.* **133** (2012) 1003-1005.
- [43] A. Lira C., M. O. Ramirez, J. Garcia Solé, U. Caldiño, Photoluminescence of $\text{Bi}_4\text{Si}_3\text{O}_{12}:\text{Er}^{3+}$ crystal excited in the commercial laser diode emission region, *Opt. Mater.* **29** (2007) 605-609.
- [44] Z. Yan , X. Jia-Yue, Z. Ting-Ting, Synthesis and Luminescence Properties of Eu^{3+} -doped $\text{Bi}_4\text{Si}_3\text{O}_{12}$, *J. Inorg. Mater.* **26** (2011) 1341-1345.
- [45] A. A. Kaminskii, S. N. Bagayev, N. V. Kravtsov, S. N. Chekina, Ya. V. Vasiliev, N. I. Ivannikova, K. Ueda, J. Lu, H. J. Eichler, G. M. A. Gad, J. Hanuza, J. Fernandez, and P. Reiche, Spectroscopy and cw Laser Action, Magneto-optics and Nonlinear Optical Frequency Conversion in Ln^{3+} Doped and Undoped $\text{Bi}_4\text{Ge}_3\text{O}_{12}$ and $\text{Bi}_4\text{Si}_3\text{O}_{12}$ Crystals, *Laser Phys.* **11** (2001) 897-918.
- [46] Diamond - Crystal and Molecular Structure Visualization Crystal Impact - Dr. H. Putz & Dr. K. Brandenburg GbR, Kreuzherrenstr. 102, 53227 Bonn, Germany. (<http://www.crystalimpact.com/diamond>).

Chapter 3

Plasmons and plasmonic enhancement

3.1 Introduction

This chapter introduces the main concepts behind nanoparticle (NP) local surface plasmon resonance (LSPR) and the principles of plasmonic enhancement of fluorescence. Details about plasmon types will be given in [section 3.2](#). LSPR will be the focus of this work and the theoretical explanation will be given in [section 3.3](#). [Section 3.4](#) explains why Ag is the best metal for plasmonic applications. The influence of size, shape and dielectric environment on the LSPR frequency will be given in [section 3.5](#). [Section 3.6](#) outlines the mechanism of plasmon damping while [section 3.7](#) explains how metals influence the fluorescence from emitters.

3.2 Plasmon types

Plasmons are an optical phenomenon arising from the collective oscillation of conduction free electrons in metals [\[1-6\]](#). When these metals are exposed to electromagnetic radiation, the Columbic attraction between the electrons and positive ions causes the free electrons to oscillate at their natural frequency, which is called the plasma frequency. Depending on the boundary conditions for the electromagnetic fields, it is commonly accepted to distinguish between two types of plasmons, namely bulk plasmons (BPs) and surface plasmons (SPs). Surface plasmon also exists in two classes, namely SP polaritons (SPPs) and localized SPs (LSPs). Details about these types will be given below.

3.2.1 Bulk plasmons

BPs refers to the collective excitation of the dense electron gas in the bulk of a metal. According to the Drude model, plasmons can be described as a cloud of negatively

charged electrons disturbed from their equilibrium positions against the positive ion cores. The characteristic oscillation frequency (plasma frequency) is given by [7]:

$$\omega_p = \sqrt{N e^2 / \epsilon_0 m_e} \quad (3.1)$$

where N is the conduction electron density, e is the electron charge, m_e is the electron effective mass and ϵ_0 is the vacuum dielectric permittivity. Equation 3.1 shows that the plasma frequency depends only on the free electron density for a particular metal. The electromagnetic radiation of frequency that is below the plasma frequency is reflected because the free electron in the metal would always oscillate so as to cancel out any applied electric field. Above the plasma frequency, the electrons cannot respond quickly enough to screen the applied electric field and the light is instead transmitted. Most of the bulk metals have plasmon frequency with corresponding energy in the order of 5-15 eV [1].

BPs cannot be excited by photons due to the longitudinal nature of plasma oscillations and the transverse nature of photons which are mismatching [1]. The only experimental evidence of BPs is the electron energy loss spectroscopy (EELS) where the electrons interact with thin metal foil. The properties mentioned above make the BPs impractical in photonic applications.

3.2.2 Surface plasmons

Historically, SPs were first observed in 1902 by Wood [8]. Physical interpretation of this phenomenon was initiated by Lord Rayleigh (1907) and further investigation was done by Fano (1941) [8]. The complete explanation of SPs was possible only in 1968 when Otto and in the same year Kretschmann and Raether reported the excitation of SPs [8].

As mentioned earlier, there are two types of SPs, namely LSPs and SPPs. Unlike BPs, SPs can be excited by photons due to the presence of new boundary conditions associated with small size [9]. SPPs are as a result of strong coupling between plasma oscillation and electromagnetic waves (plasmon and photon) at the interface between a metal and a dielectric, or more generally between materials that have an opposite sign of real part of

dielectric permittivity (figure 3.1(a)). Once the SPP is excited, it propagates in the x - and y -directions along the metal-dielectric interface until its energy is lost to either absorption in the metal or scattering into other directions.

In the case of LSPs (figure 3.1(b)), light interacts with particles much smaller than the incident wavelength. Due to the small size of the NPs, light can penetrate a whole particle and force the entire free electron to oscillate in response to the external electric field, with the effect being maximized at a resonance frequency resulting in the LSPR phenomenon [4]. The LSPR frequency for most metals falls into ultraviolet (UV) region, while some of alkali metals and some transition metals such as Cu, Ag, and Au exhibit plasmon frequencies in the visible region.

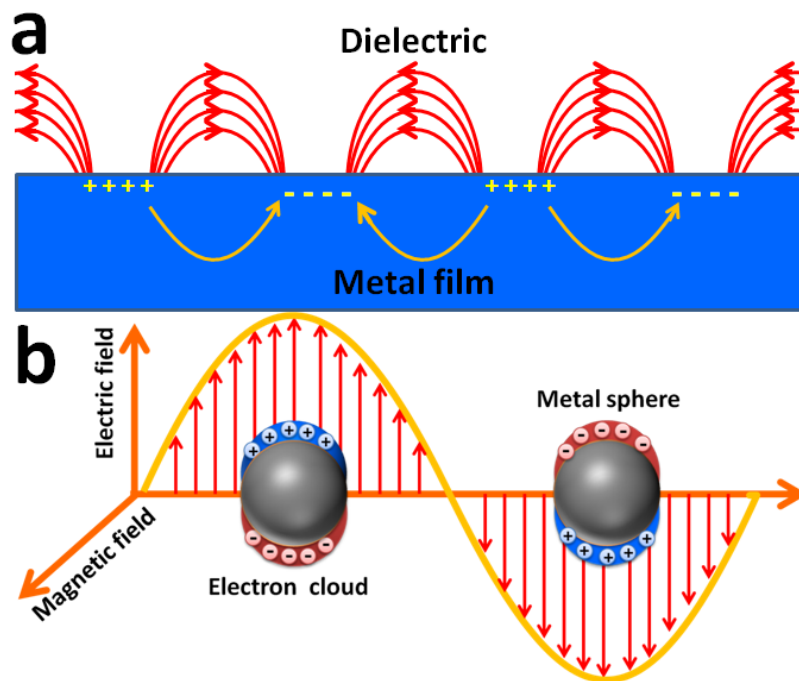


Figure 3.1: Schematic diagrams illustrating (a) SPP and (b) LSP. Adapted from [4].

Both SPPs and LSPs have the same physical origin, which exhibit electromagnetic field localization near the metallic surfaces and significant enhancement with respect to the incident fields. But their appearances are quite different, which in turn leads to different

applications. Recently, SPs has found a way to a wide range of practical applications in physics, chemistry, medicine and biology [10-12].

This work will be concerned only with LSPR and its applications in phosphors. Therefore, the theoretical explanation of LSPR will be discussed in this chapter. Details about SPPs can be found elsewhere [1, 13].

3.3 Localized surface plasmon resonance and Mie theory

In 1904, Maxwell-Garnett [14] explained the colour of glasses containing small metallic particles by developing a theory of effective dielectric constant. The famous scientist Mie (1908) [15] developed an electromagnetic theory of scattering and absorption of light by a spherical particle of arbitrary size, which is now the well-known Mie theory. The general concepts of Mie theory is that, when a metal NPs is exposed to an electromagnetic field, its free electrons start to oscillate, transforming energy from the incident electromagnetic wave into thermal energy in an absorption process. On the other hand, these electrons can also be accelerated, and then they can radiate energy in a scattering process. Therefore, the attenuation of an electromagnetic wave that is interacting with metals i.e. the electromagnetic extinction (C_{ext}) can be expressed by the sum of scattering (C_{sca}) and absorption (C_{abs}):

$$C_{ext} = C_{abs} + C_{sca} \quad (3.2)$$

In general, there are two models that have been demonstrated by Mie theory: firstly, for small spherical particles much smaller than the incident electromagnetic wavelength the interaction is governed by electrostatics rather than electrodynamics. This is often called the quasistatic approximation (only dipole interaction is present). Secondly, for large particles the quasistatic approximation is no longer applied due to significant phase-changes of the driving field over the particle volume and then electrodynamics approach (high modes present. e.g. quadruple, octupole) is required.

3.3.1 Quasistatic approximation model

In this model, the electrodynamics effect of the local-field enhancement, described by the Mie theory, becomes independent of R , where R is the radius of spherical particles. This model is only valid when the NP is significantly smaller compared to the wavelength of the incident light. In this case ($R \ll \lambda$), retardation effects that lead to radiative plasmon (scattering) damping disappear and the extinction cross-section is given by the dipole absorption only. Mie's solution to Maxwell's equations for this quasi-static approximation is represented by [16]:

$$C_{ext} = \frac{9\epsilon^{3/2} V_0}{\lambda} \cdot \frac{\epsilon_2(\lambda)}{[\epsilon_1(\lambda) + 2\epsilon_m]^2 + \epsilon_2(\lambda)^2} \quad (3.3)$$

where $V_0 = \frac{4}{3}\pi R^3$ is the volume of the NPs, λ is the excitation wavelength, ϵ_m is the (real) dielectric function of the medium surrounding the metal NPs and $\epsilon_1(\lambda)$ and $\epsilon_2(\lambda)$ are the real and imaginary parts of the dielectric function of the metal NPs, respectively. The dipole resonance frequency is determined by the condition $\epsilon_1(\lambda) \approx -2\epsilon_m$, provided ϵ_2 is not too large and does not change much in the vicinity of the resonance. In this approximation the wavelength position of the LSPR is independent of the NP size. This model is used when only qualitative information is needed [5], and allows the calculation of the expected absorption spectra of small spherical metal NPs. Figure 3.2 shows the calculated extinction cross-section of small Ag NPs distributed in different hosts, namely amorphous SiO₂ ($\epsilon_m = 2.2$) [17], YAG ($\epsilon_m = 10.6$) [18], Bi₄Si₄O₁₂ ($\epsilon_m = 8.8$) [19] and ZnO ($\epsilon_m = 8.5$) [20]. The dielectric constant of Ag depends on the frequency of the incident electromagnetic wave [21]. Substituting $R = 10$ nm (radius of Ag NPs) and the above data in equation 3.3 gives the results plotted in figure 3.2, which shows the position of LSPR in different hosts. Due to small size compared to the wavelength of the incident light, the position of plasmon excitation does not vary much in this size regime and relatively depends on the dielectric constant of the host (see figure 3.2).

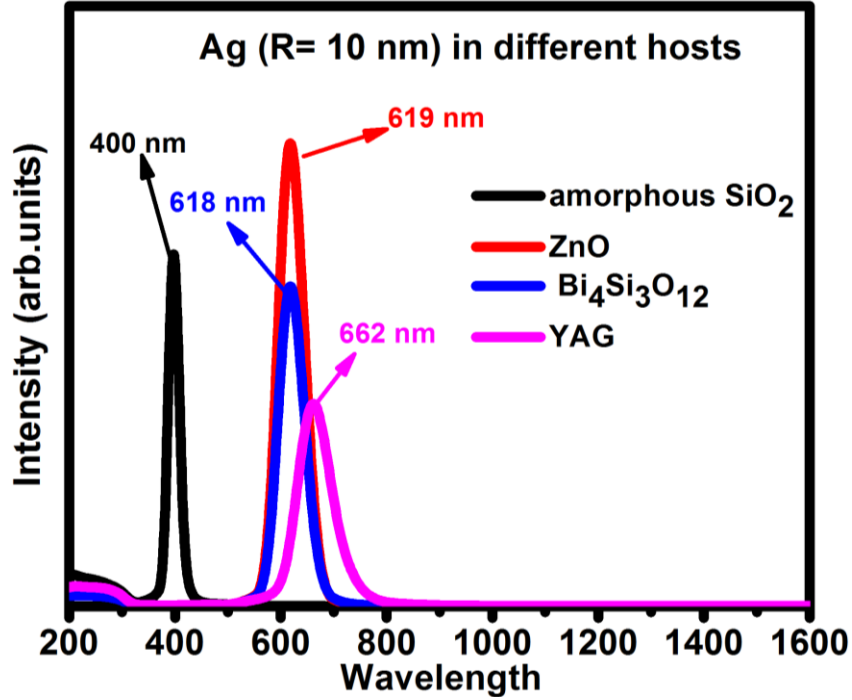


Figure 3.2: Extinction cross-section for a Ag sphere in different hosts.

3.3.2 Electrodynamics model

In this model the dipole approximation is no longer valid. For large particles, the plasmon resonance becomes explicitly dependent on the particle size. The extinction cross-section is dominated by higher-order multipole absorption and scattering and the full Mie theory is required to model the extinction spectra.

Mie solved Maxwell's equations for an incoming plane wave interacting with a spherical particle. The interaction between these waves and large particles leads to electromagnetic fields which may be expanded into multipole contributions and the expansion coefficients can be found by applying the correct boundary conditions at the interface between the metallic NP and its surrounding, leading to [17, 22]:

$$C_{ext} = \frac{\lambda^2}{2\pi} \sum_{n=1}^{\infty} (2n + 1) \text{Re}\{a_n + b_n\} \quad (3.4)$$

Here the parameters a_n and b_n are defined as:

$$a_n = \frac{\psi_n(\beta)\psi_n'(m\beta) - m\psi_n(m\beta)\psi_n'(\beta)}{\xi_n(\beta)\psi_n'(m\beta) - m\psi_n(m\beta)\xi_n'(\beta)} \quad (3.5)$$

$$b_n = \frac{m\psi_n(\beta)\psi_n'(m\beta) - \psi_n(m\beta)\psi_n'(\beta)}{m\xi_n(\beta)\psi_n'(m\beta) - \psi_n(m\beta)\xi_n'(\beta)} \quad (3.6)$$

The size parameter is defined as $\beta = 2\pi R n_m/\lambda$ where λ is the incident wavelength with respect to the vacuum and n_m represents the real refractive index of the surrounding medium and $m = n/n_m$ where n is the complex refractive index of the particle.

These expressions can be solved computationally to produce approximate solutions that provide some information about the effect of size and dielectric constant of the environment on the LSPR frequency. All the numerical calculations used in this work were carried out with the program MiePlot v4.2.11 [23], which is based on the equations 3.4-3.6.

3.4 Silver as a good plasmonic material

Among metals, noble metals are the most often used in plasmonic applications due to their relatively low loss in the visible and near-infrared (NIR) ranges. In fact, most of the experimental work in plasmonics has used either Ag or Au. Metals other than Ag and Au have limited use due to their other disadvantages. For instance, alkali metals have low loss compared to Ag and Au, but in pure elemental form they are very reactive to air and water and are easily oxidized. Therefore, noble metals (e.g. Ag, Au) and others such as Cu and Al are good metals for plasmonic applications. The SP damping of some metals can be described by the quality factor Q given by [6]:

$$Q = \omega(d\varepsilon_r/d\omega)/2(\varepsilon_i)^2 \quad (3.7)$$

where ϵ_r and ϵ_i are the real and imaginary parts of the metal dielectric function respectively, while ω is the frequency of the light. In most plasmonic applications the quality factor Q should be more than 10 [6]. This implies that the higher the quality factor is, the stronger the LSPR. Figure 3.3 shows the quality factors of different metals. As can be seen, Ag has a high quality factor in the spectral range from 300-1200 nm. Al shows high quality factor only in the UV region while Au and Cu exhibit high quality factor in the NIR.

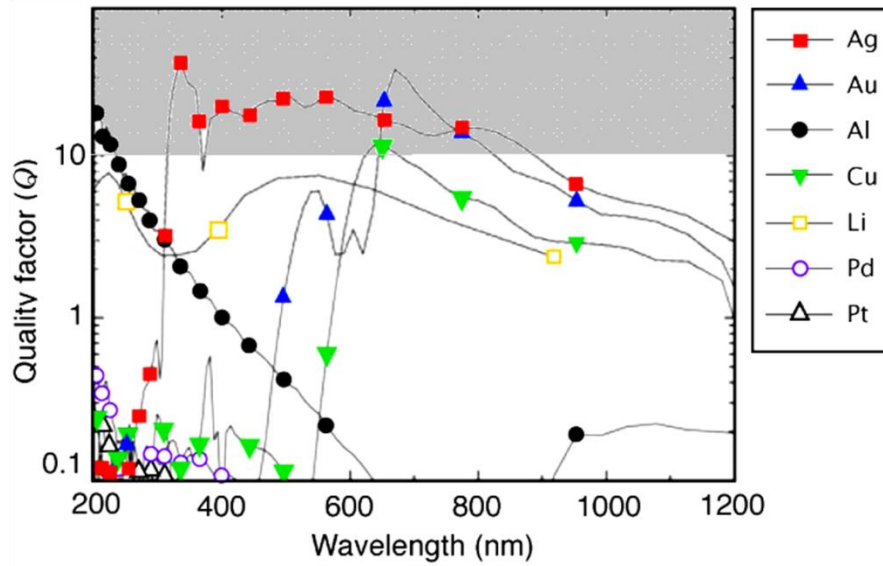


Figure 3.3: The quality factor (Q) of the LSPR for a metal/air interface. A higher Q denotes less damping and a stronger plasmon resonance. The shaded area represents the desired quality factor for plasmonic applications. Adapted from [6].

The dielectric constant data used in figure 3.3 is for bulk metal. It is well known that when the particle size become comparable to the mean free path l_∞ (e.g. 52 nm for Ag), then the collision of the conduction electrons with the NP surface becomes important and the total damping constant as the function of size can be expressed by [24]:

$$\Gamma(R) = \Gamma_\infty + \frac{V_F}{R} \quad (3.8)$$

where Γ_∞ is the damping constant of the bulk metal (0.021 eV for Ag), V_F is the Fermi velocity (1.39×10^6 m/s for Ag) and R is the particle radius. If the free electrons are affected only by the particle size, one can express the dielectric constant of Ag as the function of both ω and R by [24]:

$$\varepsilon(\omega, R) = \varepsilon_\infty(\omega) + \left[\omega_p^2 \left(\frac{1}{\omega^2 + \Gamma_\infty^2} - \frac{1}{\omega^2 + \Gamma(R)^2} \right) \right] + i \left[\frac{\omega_p^2}{\omega} \left(\frac{\Gamma(R)}{\omega^2 + \Gamma(R)^2} - \frac{\Gamma_\infty}{\omega^2 + \Gamma_\infty^2} \right) \right] \quad (3.9)$$

where ω_p is the plasma frequency and $\varepsilon_\infty(\omega)$ is the dielectric constant of the bulk Ag at the frequency ω .

Figure 3.4 shows the effect of particle size on the optical properties of Ag. The real (a) and imaginary (b) parts are plotted against wavelength for different particle size using equations 3.8 and 3.9. As can be seen both parts of the dielectric constant are significantly changed when the particle radius is less than 20 nm and becomes almost equal to the dielectric constant of bulk Ag above 50 nm, in agreement with the fact that when the mean free path of the conduction electron is much less than the particle size, the dielectric constant becomes independent of R .

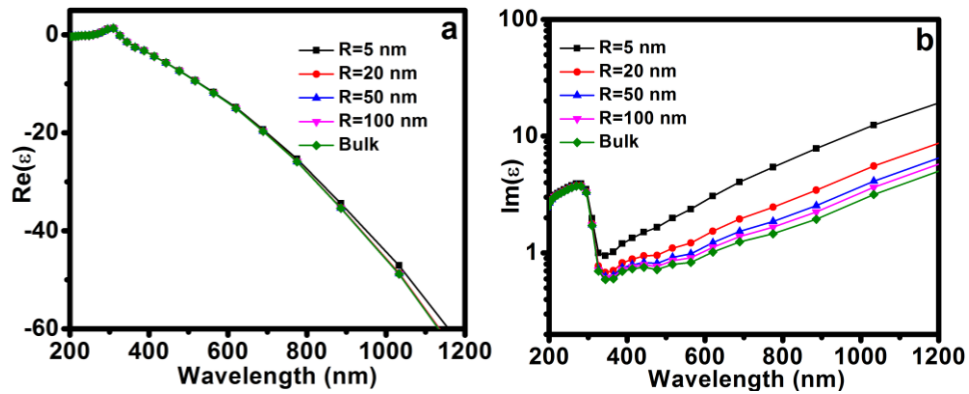


Figure 3.4: Overview of the optical properties of Ag in the range between 200-1200 nm. (a) is the real part and (b) is the imaginary part of dielectric constant of Ag as the function of particle size and for bulk Ag.

To study the effect of particle size on the quality factor of Ag, the quality factor of bulk Ag and of Ag with different sizes as the function of wavelength is plotted as shown in [figure 3.5](#), using [equation 3.7](#) and the dielectric constant data plotted in [figure 3.4](#). It can be seen that the quality factor of Ag depends on the particle size. According to the discussion above, it can be concluded that the best size of Ag NPs for plasmonic enhancement effect should be equal or greater than 20 nm. The detail about the effect of Ag NPs with particle size more than 20 nm on the position of the plasmon absorption band will be discussed in [section 3.5.1](#).

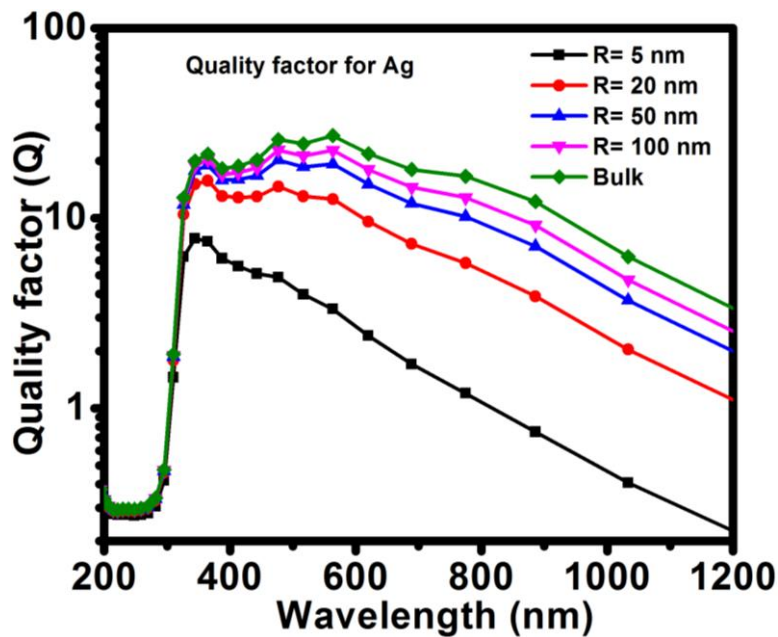


Figure 3.5: The quality factor (Q) of the LSPR for a bulk Ag/air interface compare to Ag with different sizes.

Interband transition in these metals also plays a role in the plasmon damping effect. Ag has stronger plasmon resonance because its interband transition occurs at higher energy (~ 3.8 eV) compared to the LSPR energy (~ 2.9 eV) [25]. Au exhibits LSPR at ~ 530 nm (2.3 eV) which is very close to the interband transition region (2.5 eV) [25]. Cu has the weakest plasmon resonance because this overlaps with the interband transition region

(2.1 eV) [25]. Therefore, according to the discussion above, Ag is the best metal for plasmonic applications in the visible and NIR region.

3.5 Tuning of the localized surface plasmon resonance

As mentioned above, when a metallic NP is irradiated by light, the conduction electrons oscillate coherently in response to the electric field at certain wavelength (plasmon resonance). In fact, the LSPR wavelength depends on three different parameters, namely the size and shape of the NP and the dielectric constant of the environment. Details about these parameters are given below.

3.5.1 Influence of nanoparticle size

The particles with sizes in the range of 1-100 nm are defined as NPs. Actually, there are two different size effects in this particular size regime: intrinsic size effect and extrinsic size effect. Intrinsic size effect (quantum size effect) exists in very small particles (R less than about 5 nm), which lead to significant change in the metal properties due to their discrete energy levels [26]. In this size regime (when the NP may be referred to as a cluster) the classical theory of Mie scattering is no longer valid and the quantum theory is required. As the particle size becomes large, the energy level spacing decreases to a continuous band structure for bulk solid and this is known as extrinsic size effect. In order to study the influence of size effect on the optical properties of a NP, a sphere is chosen for simplicity and NPs with size greater than 5 nm is selected.

For a spherical NP much smaller than the wavelength of light (R between 5 nm and 20 nm) the light can homogeneously polarize the particle, and the interaction is dominated only by the dipole absorption (see figure 3.6(a)). Q_{ext} denotes the extinction efficiency factor which is defined as the ratio of the extinction cross-section to the physical cross-sectional area (πR^2). As the particle size increases, the light can no longer polarize the NPs homogeneously, resulting in high order modes. These higher-order modes peak at higher energies with respect to the dipole peak (higher-order modes peak are indicated by the arrows in figure 3.6). Consequently, the plasmon band red shifts with increasing particle size (see figure 3.6 (b, c and d)). In addition, the electrons in large NPs can be

accelerated and radiate energy in scattering process which becomes dominant for particles large than 30 nm (figure 3.6 (c and d)). Due to this secondary process, the electron experiences energy loss (plasmon decay), shifting the dipole resonance to longer wavelength and broadening the plasmon resonance linewidth (figure 3.6 (c and d)).

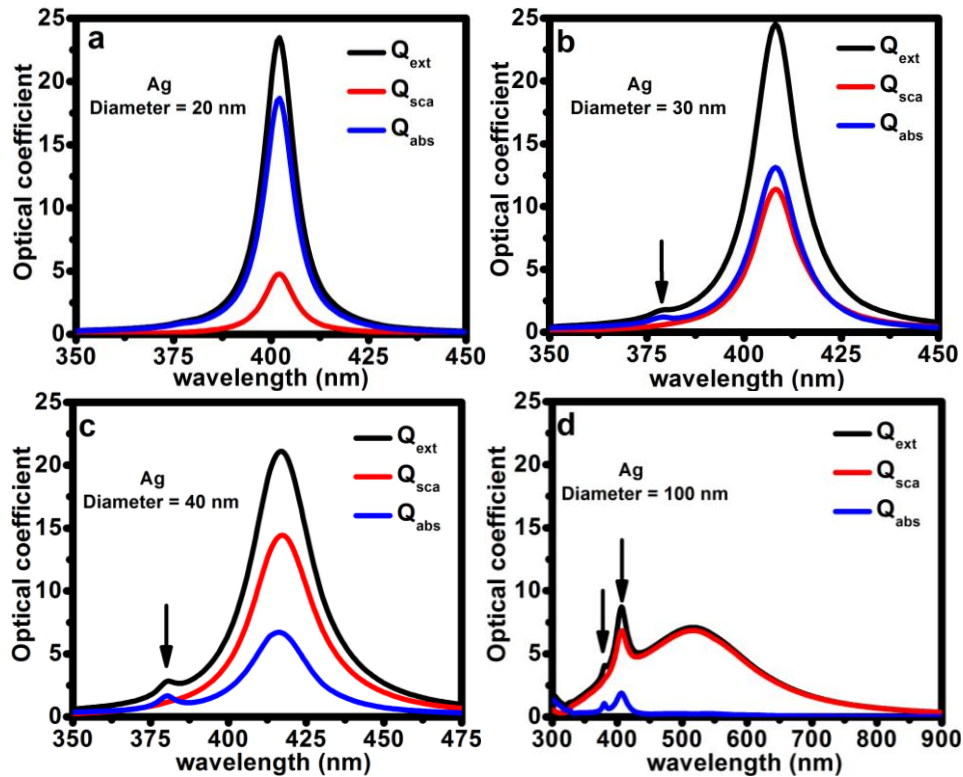


Figure 3.6: Extinction (Q_{ext}), absorption (Q_{abs}) and scattering (Q_{sca}) efficiencies for different sizes of Ag sphere embedded in SiO₂ with refractive index of 1.46 [27], calculated using MiePlot v4.2.11[23].

3.5.2 Influence of nanoparticle shape

Mie theory provides only the exact solutions to the problem of light scattered or absorbed by spherical particles of arbitrary sizes. Later on, Gans extended Mie theory to particles with ellipsoid shape [22]. Further approximation of Mie equations has been developed for other geometries to cover a wide range of arbitrary shapes, resulting in different numerical methods including the discrete dipole approximation [9, 28], the T-matrix

method [29], the multiple multipole method [30], the finite difference time domain method [31] and the modified long wavelength approximation [5].

It is well-known that the plasmon resonance frequency is primarily determined by the surface polarization, which in turn depends on the geometry or shape of NPs. Therefore, any change of this parameter will change the surface polarization and therefore the resonance frequency. For instance, an ellipsoid with three different axes presents three distinct dipole modes even in the quasistatic approximation model, which is different from a sphere with only one dipole mode [32]. Moreover, when the particle size with shapes other than spherical is increased, extra higher modes will be present. Wiley *et al.* [2] calculated the extinction, absorption and scattering spectra for a 40 nm Ag NPs with different shapes using the discrete dipole approximation method (figure 3.7).

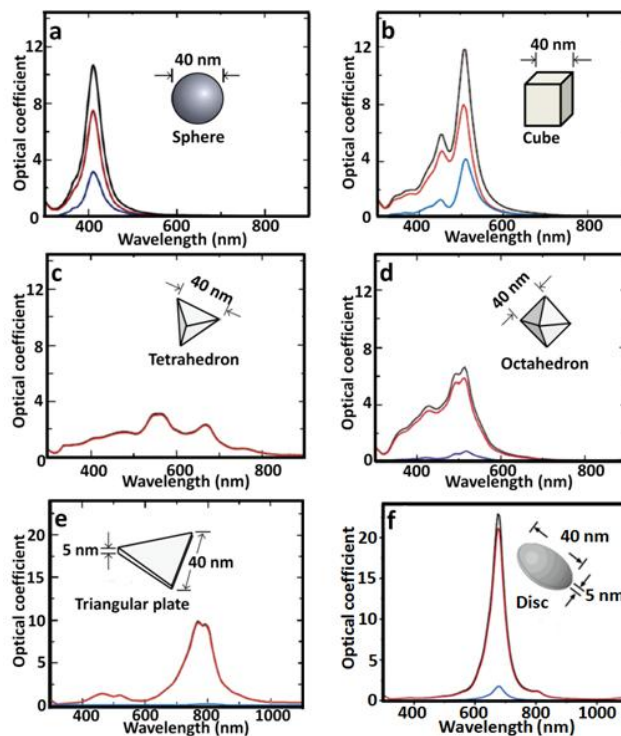


Figure 3.7: The discrete dipole approximation calculation for Ag NPs with different shapes, extinction (black), absorption (red), and scattering (blue) spectra. (a) a sphere, (b) a cube, (c) a tetrahedron, (d) an octahedron, and (e) a triangular plate. Adapted from [2, 9].

Compare of nanospheres, other shapes display red-shifted resonance peaks, which is attributed to the accumulation of surface charges on the particle corners [2]. The distribution of these charges near the corners increases the surface polarization and therefore reduces the restoring force for electron oscillation, resulting in a red-shift of the plasmon resonance peak and the appearance of higher modes (figure 3.7) [2].

3.5.3 Influence of dielectric constant of the environment

Already the effects of the size and shape on the plasmon resonance position have been discussed. The dielectric constant of the environment also plays a role in plasmon shifting effect. According to equation 3.3 (in the dipole approximation regime for a sphere), it is clear that the dielectric constant of the surrounding medium affects the LSPR wavelength of NPs.

An increase in the relative permittivity of the dielectric medium (or particularly the refractive index $n = \epsilon_m^{1/2}$) results in a decrease in the restoring force of electron oscillation and therefore shifts the plasmon resonance towards longer wavelength [1]. Figure 3.8(a) shows the absorption cross-sections for Ag particle with a 20 nm radius embedded in non-absorbing media with refractive index varied from 1.0 to 2.0, calculated using MiePlot v4.2.11 [23]. As it is expected, the plasmon resonance shifts to longer wavelength as the refractive index increases. Figure 3.8(b) shows maximum wavelength (λ_{\max}) of the absorption band of the LSPR associated with Ag NPs as the function of the refractive index of material host extracted from figure 3.8(a). Of interest is that the peak position of LSPR absorption band increases linearly with the local refractive index in agreement with Jensen *et al.* [33]. This data is very useful in case one needs to control the LSPR band for Ag NPs for a particular application. For instance, if the desired absorption band of LSPR is 440 nm then the refractive index of the host material should be 1.7 (see figure 3.8(b)).

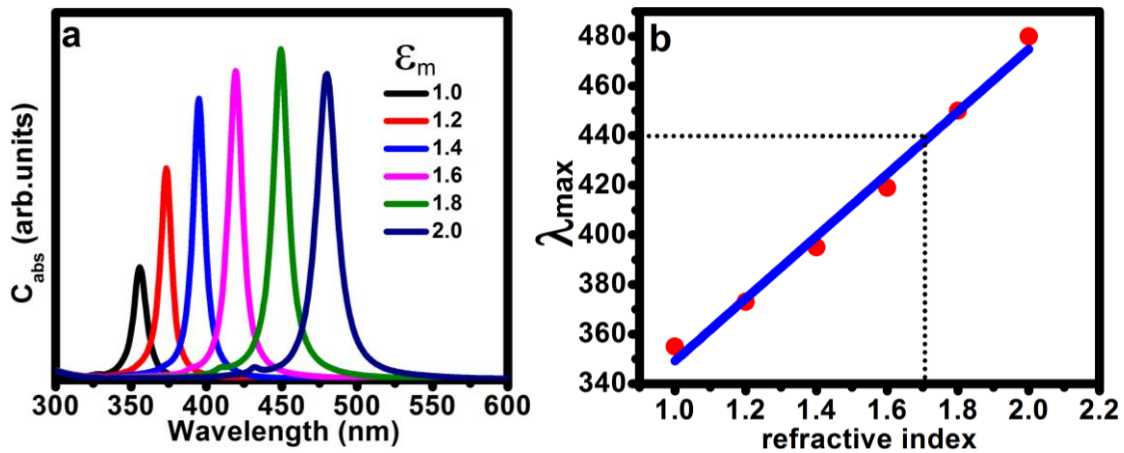


Figure 3.8: (a) Absorption cross-section as a function of wavelength for Ag particles with a 20 nm radius embedded in media with refractive index $n = 1.0$ to $n = 2.0$ calculated using MiePlot v4.2.11. (b) Wavelength corresponding to maximum absorption as a function of refractive index for various materials. The blue line is a fit to act as a guide for the eye.

Other particle shapes have been shown to exhibit a similar dependence on the refractive index. Miller and Lazarides showed that the refractive index sensitivity linearly increases with the peak wavelength, regardless of the NP shape for wavelengths up to 800 nm [34].

3.6 Plasmon decay

When the electromagnetic wave interacts with the metal NPs and excites a plasmon, it can decay on the femtosecond timescale either radiatively or non-radiatively [35, 36] (figure 3.9). Radiative decay results in a scattering process (re-emission of a photon). This process does not lead to heating of the NP, since the entire energy is emitted as photons. Non-radiative decay occurs via excitation of electron-hole pairs either within the conduction band (intraband excitation) or through interband excitations caused by transitions between d bands and the conduction band. Consequently, the excited electrons relax through electron-electron and electron-phonon collisions, and ultimately the energy is converted into heat. It is also worthwhile to note that the d band energy levels of Ag lie

~4 eV below the Fermi energy level, making the interband excitations more unlikely than intraband excitations [36]. The material, size and shape of the particles are very important in determining the type of decay. Nonradiative decay is inversely proportional to the volume of the NP while radiative decay is proportional [36].

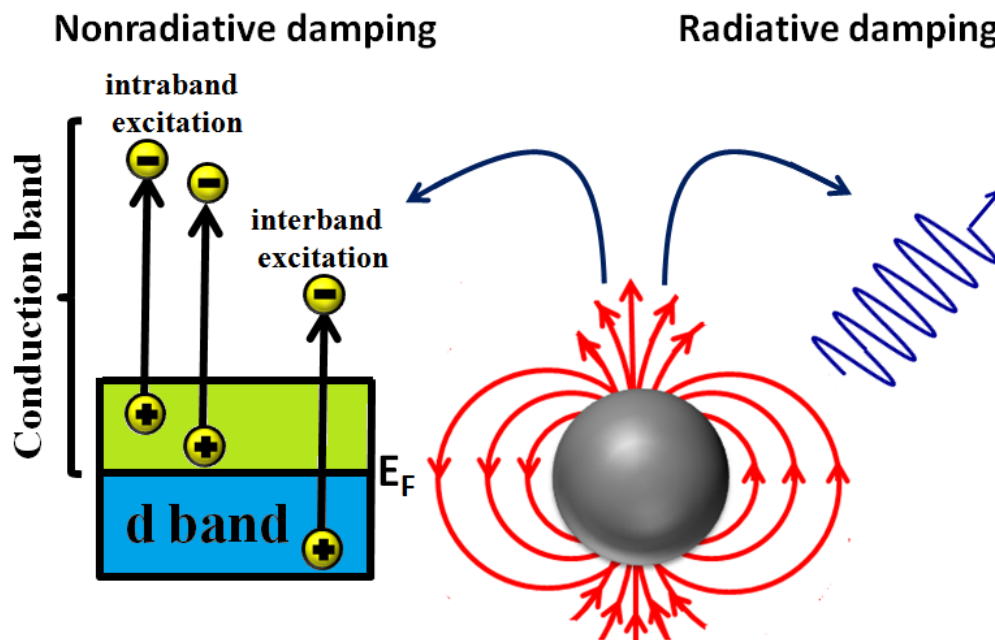


Figure 3.9: Schematic representation of radiative and nonradiative decay of particle plasmons in noble metal NPs.

3.7 Metal-enhanced fluorescence

The optical properties of metals NP have been of interest from a long time ago, since the brilliantly coloured colloids used in stained glass windows in Roman times. Recently, a number of experiments have generated new interest in using metal NPs in phosphors [37-41]. In particular, the enhanced and confined local electric fields occurring near the surface of these NPs when excited at the LSPR can significantly enhance the fluorescence of emitters located near a NP [40, 41]. Metal NPs can affect the luminescence from the closed emitter by two ways. Firstly, enhanced excitation, which in this case the metal NPs can enhance the excitation rate (which strongly depends on the

intensity of the electric field) of the nearby emitter due to modification of the applied electric field, resulting from the excitation of the LSPR. Consequently, emitters in such hot spots absorb more light than in the absence of metal NPs and therefore increases emission efficiency of the emitter. Secondly, the excited-state emitter can couple to the LSPR of the close NP, generating far-field radiation at the emission wavelength, resulting in an increase in the emission intensity which is accompanied by a decrease in emission lifetime [38, 41]. To explain the processes of excitation and emission of fluorescent emitters, Jablonski diagrams for fluorescence in the absence of metal (a) and the metal-emitter interactions (b) are shown in figure 3.10.

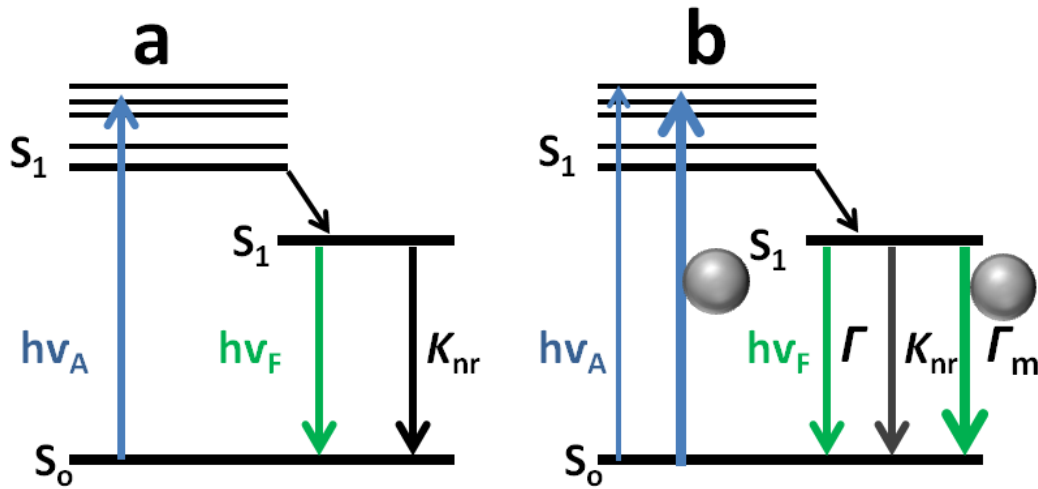


Figure 3.10: Jablonski diagram without (a) and with (b) metal-emitter interactions. The thicker arrows represent enhanced excitation and emission rates. Adapted from [37].

In the absence of metal NPs, the intrinsic quantum yield Q_o and lifetime τ_o of the emitter are given by [38]:

$$Q_o = \Gamma / (\Gamma + k_{nr}) \quad (3.10)$$

$$\tau_o = (\Gamma + k_{nr})^{-1} \quad (3.11)$$

where Γ and k_{nr} are radiative and non-radiative decay rate, respectively. The radiative decay rate Γ is a basic parameter for any given emitter while the non-radiative decay rate k_{nr} is the only parameter that can increase or decrease the quantum yield Q_o . It is clearly seen from [equation 3.10](#) that the quantum yield can be increased by decreasing the non-radiative decay rate. Moreover, the non-radiative decay rate can also play a role by affecting the life time (see [equation 3.11](#)).

In the case when the emitter is located in the vicinity of a metal NP, the radiative decay rate is increased and the quantum yield and lifetime are given by [\[38\]](#):

$$Q_m = (\Gamma + \Gamma_m)/(\Gamma + \Gamma_m + k'_{nr}) \quad (3.12)$$

$$\tau_m = (\Gamma + k'_{nr} + \Gamma_m)^{-1} \quad (3.13)$$

where Γ_m and k'_{nr} are radiative and non-radiative decay rates induced by the metal NP, respectively. It is clear from [equations 3.12](#) and [3.13](#) that an increase in the metal-induced radiative decay rate results in an increased quantum yield and a decrease in lifetime. The decrease in the lifetime means that the emitter will spend less time in the excited state per excitation/emission cycle which in turn leads to improved photostability of the emitter. Therefore, emitters near metal NP, with increased quantum yield and decreased lifetime, can emit considerably more photons per second than those in the absence of metal NP [\[37\]](#).

Although there are different parameters that can influence fluorescence enhancement such as optical properties of metal NPs, the orientation of the emitters, electric field enhancement and the distance between the metal NP and the emitter, the main parameters that have strong effect are the spectral overlap of the resonant plasmon position in the metal NP with excitation/emission spectrum of the emitter and the plasmon resonance linewidth [\[40\]](#). Both these parameters can be manipulated by changing size or shape of the NPs.

On the other hand, the presence of metal NPs in the vicinity of emitters can also quench the fluorescence. These two processes (enhancement and quenching) depend on the distance between the metal particle and the emitter. If the distance is less than 5 nm, then non-radiative energy transfer occurs and this is accompanied by a decrease in the emission lifetime of the emitters [42]. If the distance is in the range of 10-50 nm [43], then the emission enhancement may be observed. At longer distance outside metal NPs field the quenching can be observed due to re-absorption of emitter's emission by metal NPs (radiative transfer) which in this case the emission lifetime remains unchanged [44].

3.8 References

- [1] S. A. Maier, Plasmonics: fundamentals and applications, *Springer Science + Business Media*, USA, (2007) (223 pages).
- [2] B. J. Wiley, S. H. Im, Z. Li, J. McLellan, A. Siekkinen and Y. Xia, Maneuvering the Surface Plasmon Resonance of Silver Nanostructures through Shape-Controlled Synthesis, *J. Phys. Chem. B* **110** (2006) 15666-15675.
- [3] C. L. Haynes, A. D. McFarland, L. L. Zhao, R. P. Van Duyne and G. C. Schatz, Nanoparticle Optics: The Importance of Radiative Dipole Coupling in Two-Dimensional Nanoparticle Arrays, *J. Phys. Chem. B* **107** (2003) 7337-7342.
- [4] K. A. Willets and R. P. Van Duyne, Localized surface plasmon resonance spectroscopy and sensing, *Annu. Rev. Phys. Chem.* **58** (2007) 267-297.
- [5] K. L. Kelly, E. Coronado, L. L. Zhao and G. C. Schatz, The Optical Properties of Metal Nanoparticles: The Influence of Size, Shape, and Dielectric Environment, *J. Phys. Chem. B* **107** (2003) 668-677.
- [6] M. Rycenga, C. M. Cobley, J. Zeng, W. Li, C. H. Moran, Q. Zhang, D. Qin and Y. Xia, Controlling the synthesis and assembly of silver nanostructures for plasmonic applications, *Chem. Rev.* **111** (2011) 3669-3712.
- [7] R. V. Baltz, Plasmons and surface plasmons in bulk metals, metallic clusters, and metallic heterostructures, In: *Spectroscopy and Dynamics of Collective Excitations in*

Solids, edited by B. D. Bartolo and S. Kyrkos, *Springer Science + Business Media*, New York, (1997) 303-338.

[8] A. J. Tudos and R. B. M. Schasfoort, Introduction to Surface Plasmon Resonance, In: Handbook of Surface Plasmon Resonance, edited by R. B. M. Schasfoort and A. J. Tudos, *The Royal Society of Chemistry*, UK (2008) 1-13.

[9] X. Lu, M. Rycenga, S. E. Skrabalak, B. Wiley and Y. Xia, Chemical synthesis of novel plasmonic nanoparticles, *Annu. Rev. Phys. Chem.* **60** (2009) 167-192.

[10] K. Y. Yang, K. C. Choi and C. W. Ahn, Surface plasmon-enhanced energy transfer in an organic light-emitting device structure, *Opt. Express* **17** (2009) 11495-11504.

[11] N. G. Khlebtsova and L. A. Dykmana, Optical properties and biomedical applications of plasmonic nanoparticles, *J. Quant. Spectrosc. Radiat. Transfer* **111** (2010) 1-35.

[12] W. L. Barnes, A. Dereux and T. W. Ebbesen, Surface plasmon subwavelength optics, *Nature* **424** (2003) 824-830.

[13] J. M. Pitarke, V. M. Silkin, E. V. Chulkov and P. M. Echenique, Theory of surface plasmons and surface-plasmon polaritons, *Rep. Prog. Phys.* **70** (2007) 1-87.

[14] J. C. Maxwell Garnett, Colours in Metal Glasses and in Metallic Films, *Phil. Trans. R. Soc. Lond. A* **370** (1904) 385-420.

[15] H. Horvath, Gustav Mie and the scattering and absorption of light by particles: Historic developments and basics, *J. Quant. Spectrosc. Radiat. Transfer* **110** (2009) 787-799.

[16] Y. Hong, Y. MinHuh, D. S. Yoon and J. Yang, Nanobiosensors Based on Localized Surface Plasmon Resonance for Biomarker Detection, *J. Nanomater.* **2012** (2012) 1-13.

[17] W. T. Doyle, Optical properties of a suspension of metal spheres, *Phys. Rev. B* **39** (1989) 9852-9858.

[18] I. Kagomiya, Y. Matsuda, K. Kakimoto and H. Ohsato, Microwave Dielectric Properties of YAG Ceramics, *Ferroelectr.* **387** (2009) 1-6.

[19] H. Xie, F. Li, H. Xi and D. Zhou, Microwave Dielectric Properties of Sol-Gel Processed Bi₄Si₃O₁₂ Ceramics and Single Crystal, *Trans. Ind. Ceram. Soc.* **73** (2015) 1-3.

- [20] J. Yoon, C. Lee and K. Lee, Voltage Enhancement of ZnO Oxide Varistors for Various Y₂O₃ Doping Compositions, *Trans. Electr. Electron. Mater.* **10** (2009) 152-155.
- [21] P. B. Johnson and R. W. Christy, Optical constants of Noble metals, *Phys. Rev. B* **6** (1972) 4370-4379.
- [22] P. K. Jain, K. S. Lee, I. H. El-Sayed and M. A. El-Sayed, Calculated Absorption and Scattering Properties of Gold Nanoparticles of Different Size Shape, and Composition: Applications in Biological Imaging and Biomedicine, *J. Phys. Chem. B* **110** (2006) 7238-7248.
- [23] P. Laven, MiePlot: A Computer Program for Scattering of Light from a Sphere using Mie Theory & the Debye series, [online]. Available from <http://www.philiplaven.com/mieplot.htm>.
- [24] V. Amendola, O. M. Bakr and F. Stellacci, A Study of the Surface Plasmon Resonance of Silver Nanoparticles by the Discrete Dipole Approximation Method: Effect of Shape, Size, Structure, and Assembly, *Plasmonics* **5** (2010) 85-97.
- [25] H. Wang, F. Tam, N. K. Grady and N. J. Halas, Cu Nanoshells: Effects of Interband Transitions on the Nanoparticle Plasmon Resonance, *J. Am. Chem. Soc.* **109** (2005) 18218-18222.
- [26] B. Balamurugan and T. Maruyama, Evidence of an enhanced interband absorption in Au nanoparticles: Size-dependent electronic structure and optical properties, *Appl. Phys. Lett.* **87** (2005) 143105.
- [27] J.-Q. Xi, M. Ojha, W. Cho, J. L. Plawsky, W. N. Gill, Th. Gessmann and E. F. Schubert, Omnidirectional reflector using nanoporous SiO₂ as a low-refractive-index material, *Opt. Lett.* **30** (2005) 1518-1520.
- [28] W. Yang, G. C. Schatz and R. P. Van Duyne, Discrete dipole approximation for calculating extinction and Raman intensities for small particles with arbitrary shapes, *J. Chem. Phys.* **103** (1995) 869-875.
- [29] N. Riefler and T. Wriedt, T-matrix Simulation of Plasmon Resonances of Particles on or Near a Surface, in *Proceedings of PIERS2006*, Cambridge, March 26-29 (2006) 450-454 [ISBN: 1-933077-08-5].

- [30] E. Moreno, D. Erni, C. Hafner and R. Vahldieck, Multiple multipole method with automatic multipole setting applied to the simulation of surface plasmons in metallic nanostructures, *J. Opt. Soc. Am. A* **19** (2002) 101-111.
- [31] R. X. Bian, R. C. Dunn and X. S. Xie, Single molecule emission characteristics in near-field microscopy, *Phys. Rev. Lett.* **75** (1995) 4772-4776.
- [32] C. F. Bohren and D. R. Huffman, Absorption and scattering of light by small particles, *John Wiley & Sons, Inc.*, Canada, (1983) (530 pages).
- [33] T. R. Jensen, M. L. Duval, K. L. Kelly, A. A. Lazarides, G. C. Schatz and R. P. Van Duyne, Nanosphere Lithography: Effect of the External Dielectric Medium on the Surface Plasmon Resonance Spectrum of a Periodic Array of Silver Nanoparticles, *J. Phys. Chem. B* **103** (1999) 9846-9853.
- [34] M. M. Miller and A. A. Lazarides, Sensitivity of Metal Nanoparticle Surface Plasmon Resonance to the Dielectric Environment, *J. Phys. Chem. B* **109** (2005) 21556-21565.
- [35] C. Sönnichsen, T. Franzl, T. Wilk, G. von Plessen, J. Feldmann, Drastic Reduction of Plasmon Damping in Gold Nanorods, *Phys. Rev. Lett.* **88** (2002) 077402 (4 pages).
- [36] C. Clavero, Plasmon-induced hot-electron generation at nanoparticle/metal-oxide interfaces for photovoltaic and photocatalytic devices, *Nature Photon.* **8** (2014) 95-103.
- [37] J. R. Lakowicz, K. Ray, M. Chowdhury, H. Szmanski, Y. Fu, J. Zhang and K. Nowaczyk, Plasmon-controlled fluorescence: a new paradigm in fluorescence spectroscopy, *Analyst* **133** (2008) 1308-1346.
- [38] K. Ray, M. H. Chowdhury, J. Zhang, Y. Fu, H. Szmanski, K. Nowaczyk and J. R. Lakowicz, Plasmon-Controlled Fluorescence Towards High-Sensitivity Optical Sensing, In: *Advances in Biochemical Engineering/Biotechnology*, edited by G. Rao, *Springer-Verlag Berlin Heidelberg*, New York, (2009) 29-72.
- [39] V. A. G. Rivera, S. P. A. Osorio, D. Manzanib, Y. Messaddeq, L.A.O. Nunes and E. Marega Jr., Growth of silver nano-particle embedded in tellurite glass: Interaction between localized surface plasmon resonance and Er^{3+} ions, *Opt. Mater.* **33** (2011) 888-892.

- [40] Y. Chen, K. Munehika and D. S. Ginger, Dependence of Fluorescence Intensity on the Spectral Overlap between Fluorophores and Plasmon Resonant Single Silver Nanoparticles, *Nano Lett.* **7** (2007) 690-696.
- [41] Y. Zhang, A. Dragan and C. D. Geddes, Wavelength Dependence of Metal-Enhanced Fluorescence, *J. Phys. Chem. C* **113** (2009) 12095-12100.
- [42] J. Qi, Y. Xu, F. Huang, L. Chen, Y. Han, B. Xue, S. Zhang, T. Xu, S. Dai and A. Srivastava, Photoluminescence of Ag Nanoparticles and Tm³⁺ Ions in the Bismuth Germanate Glasses for the Blue Light-Excited W-LED, *J. Am. Ceram. Soc.* **97** (2014) 1471-1474.
- [43] A. J. Haes, C. L. Haynes, A. D. McFarland, G. C. Schatz, R. P. Van Duyne and S. Zou, Plasmonic Materials for Surface-Enhanced Sensing and Spectroscopy, *MRS Bull.* **30** (2005).
- [44] L. Rothberg and S. Pan, Plasmon-enhanced radiative rates and applications to organic electronics, In: Metal-enhanced fluorescence, edited By C. D. Geddes, *John Wiley & Sons. Inc.* New Jersey, (2010) 543-570.

Chapter 4

Experimental research techniques

4.1 Introduction

In this chapter, a brief description of the different techniques used in the characterization of powder nano-phosphor doped with Ag is presented. The techniques include X-ray diffraction (XRD), ultraviolet-visible (UV-vis) spectroscopy, transmission electron microscopy (TEM), X-ray photoelectron spectroscopy (XPS), Fourier transform infrared (FTIR) spectroscopy and photoluminescence spectroscopy (PL). A detailed chemical analysis of powder phosphors was determined with XPS. XRD and TEM were used to identify the crystalline phases and sizes of the Ag nanoparticles (NPs). The UV-vis spectroscopy was used to determine the absorption band of localized surface plasmon resonance (LSPR) while FTIR was used to identify chemical group in our phosphor powder.

4.2 X-ray diffraction

X-ray diffraction is one of the most important characterization tools used in solid state chemistry and materials science. This technique had been discovered in 1912 by von Laue [1]. In the beginning, X-ray diffraction was used only for the determination of crystal structure of matter. Later on, other uses for X-ray diffraction were discovered and successfully applied to study physical, chemical and mechanical properties of materials. The common used of this technique is identification of phase, preferential orientation, texture, crystallite size, microstrain and residual stress [2]. Peak positions give information about crystal phases as well as size, shape and translational symmetry of the unit cell. Crystallite size, microstrain and residual stress are determined by peak shapes

and widths while the peak intensities give information about preferential orientation which is determined by calculating the texture coefficient [2].

4.2.1 Generation of X-rays

X-rays are generated when high energetic electrons interact with the inner shell electrons of an atom by inelastic scattering. These energetic electrons can excite inner shell electrons to outer shell orbitals, leaving inner shell vacancies. Then the outer shell electrons fall to inner shell orbitals, and characteristic amounts of energy are emitted as X-ray photons. This energy depends on target element and the type of orbital decay. In a cathode ray tube, X-rays are generated by heating a filament to produce electrons and accelerating them toward a target by applying high voltage. The kinetic energy of the electrons is transformed into electromagnetic energy (X-rays). The fast moving electrons exhibit energy loss, which is converted into a photon to satisfy the law of conservation of energy. As the result, a broad band of continuous radiation is generated which is the so-called Bremsstrahlung or braking radiation (see figure 4.1). The produced X-ray spectra consist of several components; the most common are K_{α} and K_{β} . K_{α} is produced when the upper energy electron (L-shell electron) falls into a vacancy where the lower energy electron (K-shell electron) has been removed (with wavelength 1.54178 Å for Cu) while K_{β} is produced when the upper energy electron (M-shell electron) falls into a vacancy where the lower energy electron (K-shell electron) has been removed (with wavelength 1.39217 Å for Cu). The characteristics of these X-ray spectra can be seen in figure 4.1.

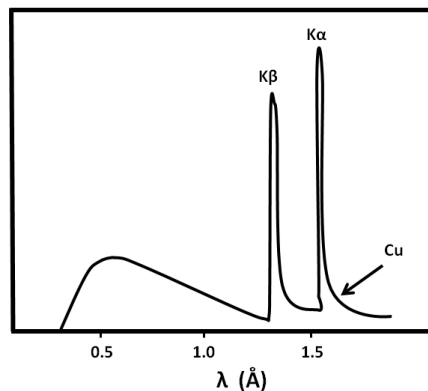


Figure 4.1: Continuous and characteristic X-rays for copper. Adapted from [3].

To produce monochromatic X-rays as required for diffraction, filtering by foils or crystal monochromators is necessary. The proper filter used in case of Cu target is Ni which can be used to filter out the $K\beta$ X-rays as shown in figure 4.2 [1].

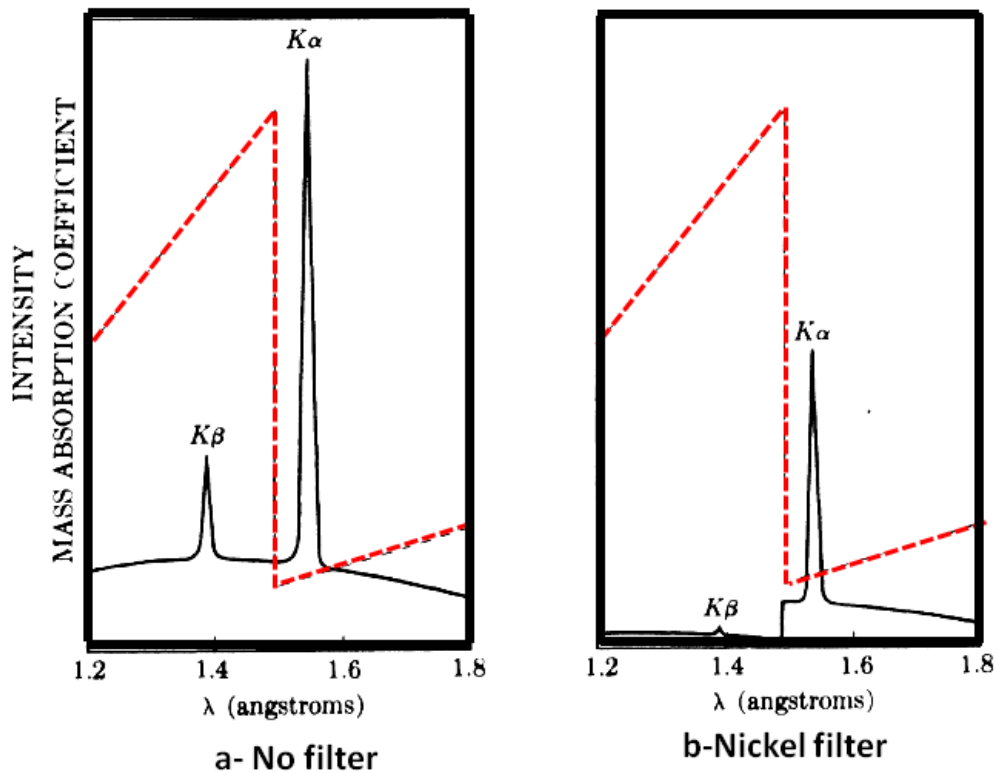


Figure 4.2: Ni filter for Cu X-rays. Adapted from [1].

4.2.2 Bragg's law

The crystals material can diffract X-ray only if the interplanar spacing (d) of the crystal is of the same order as that of the X-ray wavelength. When a crystal is bombarded with X-rays at certain specific wavelengths and incident angles, intense peaks of reflected X-rays are produced. W. L. Bragg explained this result by modeling the crystal as a set of discrete parallel planes separated by a constant parameter d as shown in figure 4.3.

A constructive interference occurs when the differences in the X-rays travel paths ABC and A'B'C' is an integer multiple of the wavelength. When this constructive interference

occurs, a diffracted beam of X-rays will leave the crystal at an angle equal to that of the incident beam. This condition can be expressed by Bragg's law [4]:

$$2d \sin\theta = n\lambda \quad (4.1)$$

where λ is the wavelength of the X-ray, d is the spacing of the crystal layers; θ is the incident angle (the angle between incident ray and the diffracted ray) and n is an integer representing the order of the diffraction peak.

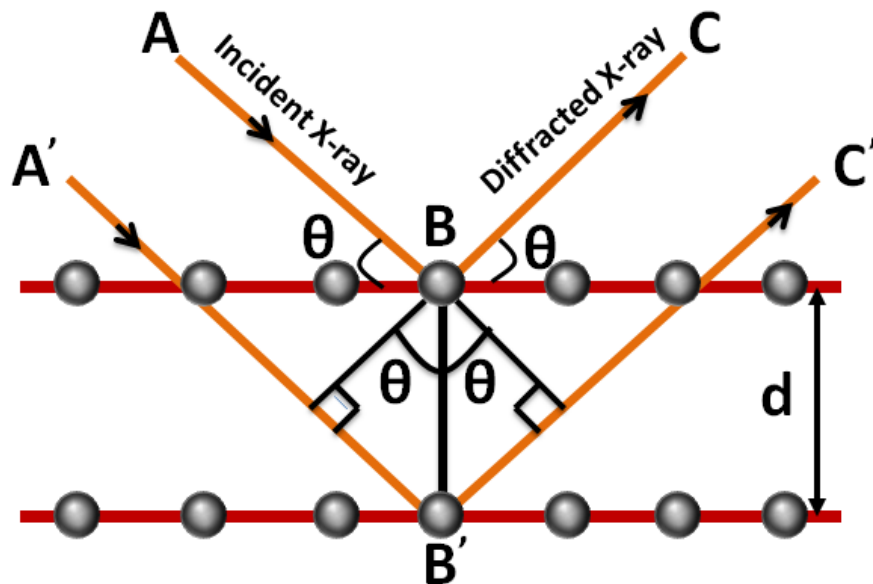


Figure 4.3: Schematic diagram of Bragg diffraction from a set of atoms.

4.2.3 X-ray diffractometer

An X-ray diffractometer consist of three basic elements: an X-ray source, a sample holder and an X-ray detector as schematically presented in figure 4.4. In a typical experiment, the sample rotates in the path of the collimated X-ray beam at an angle θ while the X-ray detector is collect the diffracted X-rays and rotates at an angle of 2θ . The typical patterns data is collected as function of 2θ .

The main objective of using XRD in this study is to identify the phase of our phosphors as well as the crystalline size particularly for Ag NPs. For phase identification, the Bragg law (equation 4.1) is used to calculate the d spacing and then compare the data with known standards in the Powder Diffraction File (PDF). The mean crystallite size can be obtained by Paul Scherrer's equation, who investigated the effect of small and spherical particles on X-ray diffraction patterns [5]:

$$\tau = \frac{K\lambda}{\beta \cos\theta} \quad (4.2)$$

where τ is the mean size of the crystallites, K is the shape factor, λ is the X-ray wavelength, β is the full-width-at-half-maximum (FWHM) in radians and θ is the Bragg angle.

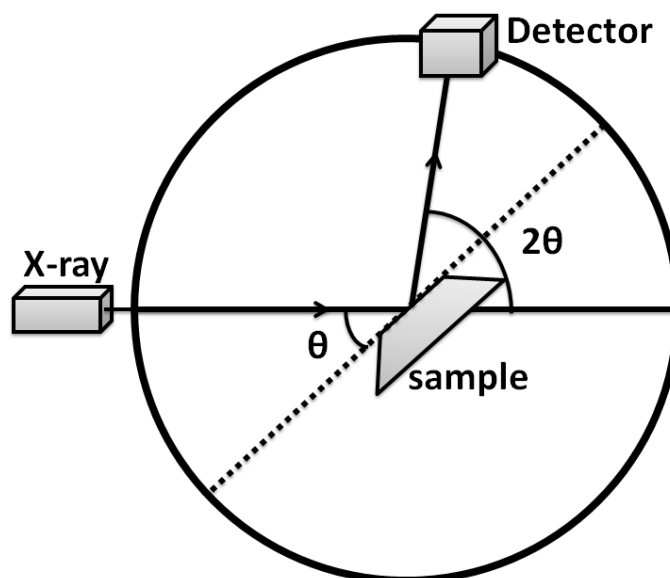


Figure 4.4: X-ray diffractometer.

The XRD data of this work were collected by a Bruker D8 diffractometer (figure 4.5) using $\text{CuK}\alpha$ ($\lambda=1.5405 \text{ \AA}$) radiation in the 2θ scan range of $15\text{-}90^\circ$ and the X-rays were generated by applying 40 kV voltage on Cu anode material at a current of 40 mA.



Figure 4.5: Bruker D8 Advance X-ray diffractometer.

4.3 Ultraviolet-visible spectroscopy

The UV-vis spectrometer is one of the oldest instrumental techniques used to identify the number of absorbing species in a sample. The UV-vis spectrophotometer is commonly used to analyze compounds (molecules, ions and complexes) of organic, inorganic and biochemical in the ultraviolet (UV) and visible regions of the electromagnetic spectrum. UV-vis spectrometers find a wide range of applications in research, industry, clinical laboratories, chemistry etc. [6]. In most previous mentioned applications other techniques could have been used but none replace UV-vis spectroscopy for its simplicity, versatility, speed, accuracy and cost-effectiveness. The measured UV-vis spectrum can be obtained as absorption, transmission and reflection spectrum [7]. Absorption and transmission apply for gas and solution or transparent glass samples, while reflection applies only for solid samples. All these different spectra give the same information, but show a different interpretation of the data.

4.3.1 Basic theory

The interaction of light with matter causes a number of process including reflection, scattering, absorbance, fluorescence/phosphorescence and photochemical reaction [8]. In general, when measuring UV-vis spectra, one only wants absorbance to occur. The absorption of light is dependant on the electronic structure of species (molecules, ions and complexes). A given electronic energy level contains a number of vibration energy levels and each of these vibration energy levels has a number of rotational energy levels. When photon of a given energy interacts with these species, it may cause a transition amongst the electronic energy levels if it is energy satisfy the following relation [7]:

$$E_{\text{photon}} = E_1 - E_2 = h\nu \quad (4.3)$$

where E_1 and E_2 are the ground state and excited state of species respectively, h is Planck's constant and ν is the frequency of the photon.

When light passes through a sample (figure 4.6), the amount of light absorbed by the sample is the difference between the incident radiation (I_0) and the transmitted radiation (I). The amount of light absorbed is expressed as either transmittance or absorbance. Transmittance is defined as [8]:

$$T = I/I_0 \quad (4.4)$$

while absorbance A is defined as

$$A = -\log T. \quad (4.5)$$

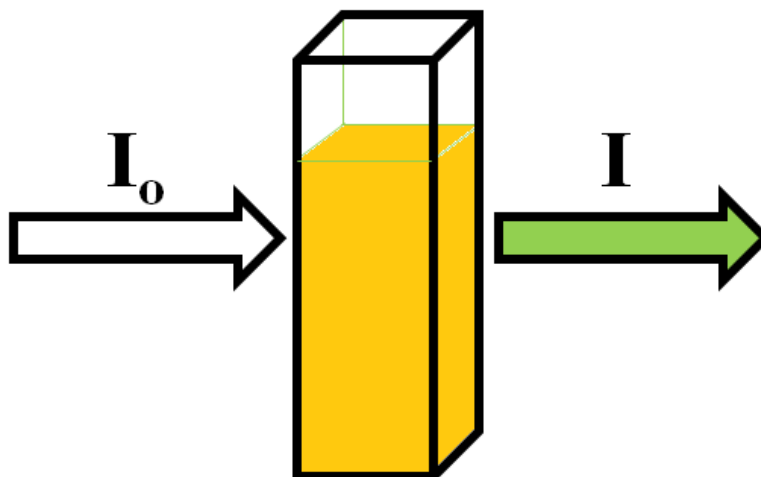


Figure 4.6: Incident and transmitted light.

4.3.2 Sample preparation

4.3.2.1 Solution phase

For diffuse absorption and transmission measurements, samples were ground to fine powder and suspended into water or ethanol, sonicated for several minutes. Then two cuvettes were half filled, one with only solvent (water or ethanol) used as reference and the other mixed with sample. Both cuvettes were placed into sample holder. The data were collected at room temperature.

4.3.2.2 Solid phase

For diffuse reflectance measurements, the powder samples were ground to fine powder and placed into sample holder. The standard used was spectralon which exhibits near 100% reflectance in the wavelength range from the near UV to the near-infrared (NIR). For accurate measurement the powder sample has to be sufficiently thick so that all incident light is absorbed or scattered before reaching the back surface of the holder.

4.3.3 Determination of the energy band gap

4.3.3.1 Energy band gap from absorption spectra

The optical band gap energy can be calculated from the UV-vis absorption edge using the well-known Tauc law relation [9]:

$$\alpha h\nu = C_1(h\nu - E_g)^m \quad (4.6)$$

where α is the absorption coefficient, $h\nu$ is the incident photon energy, C_1 is constant, E_g is the optical gap energy, and the exponent m is a parameter which depends on the type of electronic transition responsible for absorption. For direct band gap m equal $1/2$ and $1/3$ for allowed transition and forbidden transition respectively, while for indirect band gap m equal 2 and 3 for allowed transition and forbidden transition respectively. By plotting $[\alpha h\nu]^2$ against $h\nu$ and fit the linear region with a line and extend it to the energy axis, then one can easily obtained E_g by extrapolating the linear fitted regions to $[\alpha h\nu]^2 = 0$.

4.3.3.2 Energy band gap from reflectance spectra

In case of reflectance spectra, both Tauc law relation (equation 4.6) and the following Kubelka-Munk relation (equation 4.7) [9] can be used to calculate the E_g .

$$F(R_\infty) = (1 - R_\infty)^2 / 2R_\infty = K/S \quad (4.7)$$

where $R_\infty = R_{\text{sample}}/R_{\text{reference}}$, K is absorption coefficient and S is scattering coefficient. If the material scatters light perfectly, the absorption coefficient K becomes equal to 2α [9]. Considering the scattering coefficient S as constant with respect to wavelength, and using equations 4.6 and 4.7, the following expression can be written:

$$[F(R_\infty) * h\nu]^m = C_2(h\nu - E_g) \quad (4.8)$$

and by plotting $[F(R_\infty)*h\nu]^m$ against $h\nu$ and fitting the linear region with a line and extending this to the energy axis one can easily obtain E_g .

4.3.4 Instrumentation

Figure 4.7 shows a dual-beam UV-vis spectrophotometer. Inside this instrument there are usually two light sources, a tungsten lamp which gives visible light and a deuterium lamp which gives ultraviolet light. Mirror 1 directs light from the appropriate source through

an entrance slit into a monochromator which contains a diffraction grating to split the light into its constituent wavelengths. A single wavelength passes through the filter to minimize signal noise into the modulator which contains a beamsplitter (half-mirror) to divide the light into two beams: one passes through the sample cell while other passes through the reference cell. Both sample and reference beams are directed into detectors after being focussed by lenses.

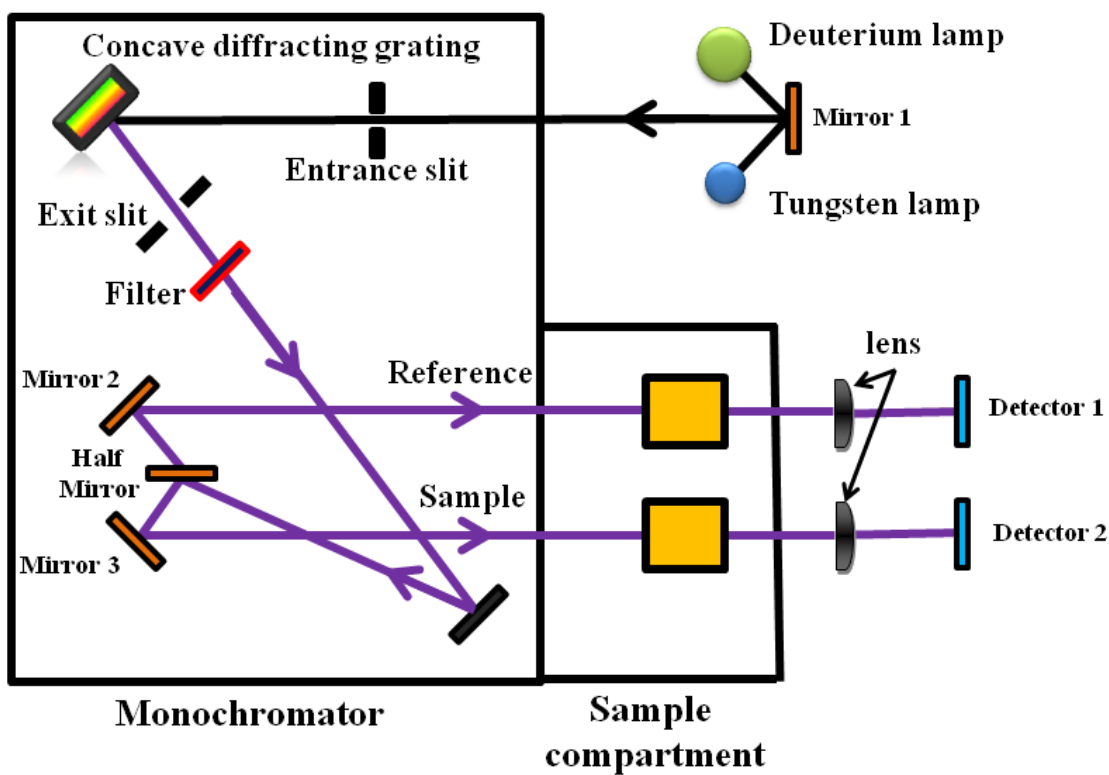


Figure 4.7: A dual-beam UV-vis spectrophotometer. Adapted from [10].

The detectors send the signal to the computer, which compares the intensities of two beams and calculated the ratio of their intensities. The logarithm of this ratio gives the quantity called absorbance which measure of how much light has been absorbed by the sample at that particular wave length.

For diffuse reflectance measurements, the UV-vis spectrophotometer equipped with an integrating sphere coated with a white standard, intended to collect the light reflected by the standard and the sample. For measurements, an integrating sphere which contains collection port and detector was used. Diffuse reflectance spectra were recorded by a Lambda 950 UV-vis spectrophotometer with an integrating sphere (figure 4.8). The standard used was spectralon.

The main objective of this instrument in this work is to determine the energy band gap of the host materials and the absorption band of LSPR.



Figure 4.8: Lambda 950 UV-Vis spectrophotometer.

4.4 Transmission electron microscopy

In 1925, De Broglie discovered that the electrons had wave-like characteristics, which was a breakthrough in understanding many physical phenomena and led to many applications, particularly electron microscopes. In 1927 Bush showed that a magnetic coil can be used to focus an electron beam in the same way of using lenses glass for focusing the light. A few years later regular production of commercial TEMs was begun [11].

TEMs use electromagnetic lenses to focus a high energy (100-300 kV) beam of electrons through a very thin sample (<100 nm). One of the best advantages of using electron microscopes is that the interaction of the electron beam with the sample produces a wide range of secondary signals which are very useful in analytical electron microscopy, providing one with a lot of information about the sample (see figure 4.9). Most of these signals are presented in the TEMs, namely unscattered electrons (transmitted beam), elastically scattered electrons (diffracted beam), inelastically scattered electrons and X-rays which are used to generate both imaging and spectrum modes which will be discussed in detail below.

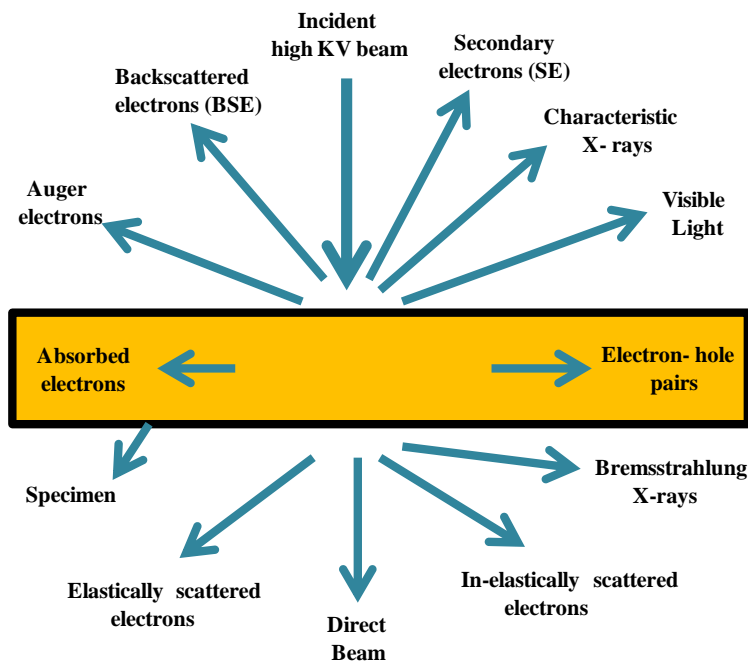


Figure 4.9: Secondary signals generated when a high-energy beam of electrons interacts with a thin sample. The signals direction shown here is not always represent the physical direction of the signal. Adapted from [11].

4.4.1 Elastic Scattering

Elastic scattering is the process in which the incident electrons beam deflected from the sample without losing its energy. The origin of this scattering is due to the Coulomb interaction of the electrons with the atomic nuclei in the sample. Because of the small mass of electrons compared to the atomic nuclei, little or no energy is lost [11]. In this type of scattering the majority of incident electrons are forward scattered (by a few degrees) and contribute to TEM image formation.

4.4.1.1 Bright field and dark field images

Actually there are two types of image which can be extracted from TEM, namely bright field and dark field images. The first one is formed by selecting the direct electron beam (transmitted beam) while the other is formed by selecting only electrons that are not in the direct beam [11] (see figure 4.10). Selection of bright field or dark field electrons results in contrast variations that provide crystallographic information.

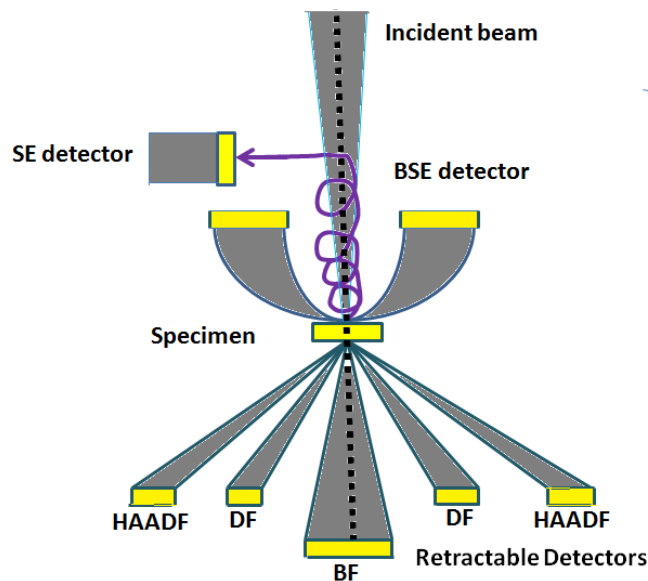


Figure 4.10: The various electron detectors used in electron microscopes, namely high angle annular dark field (HAADF), Dark field (DF), Bright field (BF), secondary electron (SE) and backscattered electron (BSE) detectors. Adapted from [11].

4.4.1.2 Diffraction patterns

Diffraction pattern image is generated due to diffracted waves scattered by a plane of atoms. Every atom acts as a new secondary wave source with the same wavelength as the incident wave. These secondary waves interfere constructively to produce a direct beam and a series of diffracted beams. The electromagnetic lenses in TEM are used to focus these diffracted electrons beam into a regular arrangement of diffraction spots to form the electron diffraction pattern. The main used of diffraction pattern is to solve crystallographic problems [12].

4.4.2 Inelastic Scattering

Elastic scattering is used only in the conventional TEMs as discussed above, for imaging samples and obtaining information about the crystal structure from diffraction pattern. Inelastic scattering occurs as a result of Coulomb interaction between a fast incident electron and the atomic electrons that surround each nucleus, results in these fast electrons losing a characteristic amount of energy [13], results in a collective oscillation of free electron gas (bulk plasmons) in the material which is discussed earlier in section 3.2.1. Electron Energy Loss Spectroscopy (EELS) is concerned with the study of these inelastic interactions. By using a high-resolution electron spectrometer the transmitted electron beam in TEMs can be separated according to their kinetic energy and produces an electron energy-loss spectrum showing scattered intensity as a function of their decrease in kinetic energy (figure 4.11).

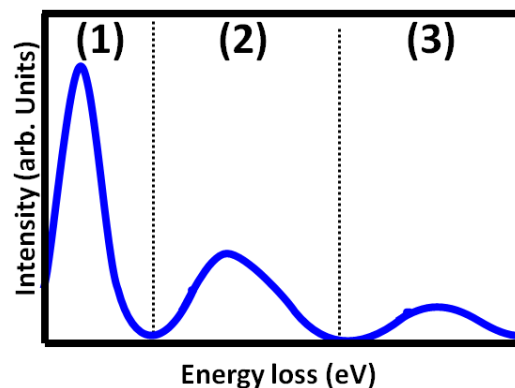


Figure 4.11: Diagram of an EELS spectrum.

As can be seen from [figure 4.11](#), the EELS spectrum is divided into three regions, namely zero loss, low loss (< 100 eV) and high loss (>100 eV) regions. The peak appearing in the zero loss region is due to elastic scattering of electron with the sample which gives only information about the resolution of this particular spectrum. Region two (low loss) shows peak related to plasmon oscillations which provides data about the composition or the dielectric nature of the material, while region three (high loss) depends on the bonding or the ionization spectra of the particular material.

4.4.3 Energy dispersive X-ray spectroscopy

X-ray microanalysis [\[11\]](#) is achieved using energy dispersive X-ray spectroscopy (EDS) to detect a characteristic X-ray signal. In TEMs the X-rays are generated when the primary electron beam interacts with the sample, given sufficient energy, inner shell electrons will be ejected and the atoms will be left in excited state. These excited atoms will relax by emitting their excess energy in the form of a characteristic X-ray. The energy of the emitted X-ray will be the energy difference between the two level and therefore specific to the particular excited atom. Therefore, the energy of the emitted X-ray can be related to a particular element.

4.4.4 Instrumentation

TEMs can be divided into three components: the illumination system, the objective lens/sample holder system, and the imaging system. The illumination system composes the electron gun and condenser lenses, which it is responsible to take the electrons from the source and transfer them to the sample. The second part acts as the heart of the TEM because all the beam-sample interactions take place there. The third part is comprised of several lenses to magnify the images or to focus this images and diffraction pattern produced by the objective lens on the viewing screen or computer display via a charged coupled device (CCD) camera [\[11\]](#) ([figure 4.12\(b\)](#)). It is important to note that the whole system requires high vacuum to avoid scattering of electrons.

In this study the images, particle sizes and the diffraction pattern were obtained using a Philips CM100 TEM. [Figure 4.12](#) showed its photograph and a schematic diagram of a TEM.

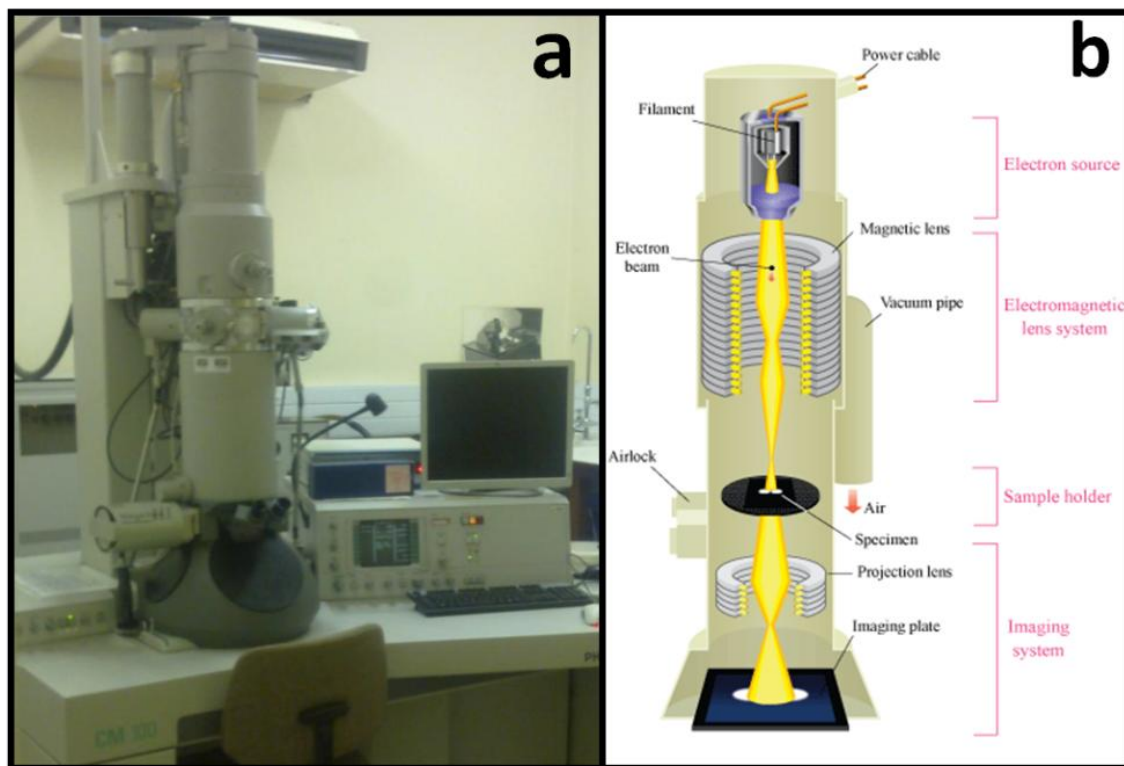


Figure 4.12: (a) Photograph of the Philips CM100 TEM and (b) a schematic outline of a TEM [14].

4.5 Fourier transform infrared spectroscopy

FTIR spectroscopy was discovered in 1887 by Michelson [15]. It is an important technique in organic chemistry which can be used to identify the presence of certain functional groups in a molecule. In addition it can be used to confirm the identity of a pure compound or to detect the presence of specific impurities [16]. It offers some advantages such as low maintenance, low cost and specificity compared with other methods such as chromatography and mass spectroscopy [17].

The infrared is part of electromagnetic spectrum is usually divided into three parts, namely NIR from 0.8-2.5 μm ($4000\text{-}12500\text{ cm}^{-1}$), mid-infrared from 2.5-50 μm ($200\text{-}4000\text{ cm}^{-1}$) and far-infrared from 50-1000 μm ($10\text{-}200\text{ cm}^{-1}$). The mid-infrared range is

very important and commonly used for chemical analysis because the most molecular vibrations occur in this region.

4.5.1 Physical principles

When a material is irradiated with infrared radiation, specific wavelengths will be absorbed by molecules, causing changes in their dipole moment and consequently exciting molecules into higher vibrational states. The wavelength absorbed by a particular molecule is a function of the energy difference between the ground and excited vibrational states. Thus infrared radiation can only be absorbed by molecules vibration when the frequencies of the radiation match the vibrational frequencies of these molecules. Absorption probability and the vibration frequency depend on the strength and polarity of the vibrating bonds and can be influenced by intra- and intermolecular effects [18]. Therefore, the absorbed wavelengths provide fingerprint-like information on the chemical composition of the sample.

There are different modes of vibration which can be divided into the two main modes as follows [19]: Firstly stretching vibration modes, which one or more bond lengths change – these are classified into two other terms related to the symmetry: symmetric vibrations, which the symmetry of the molecules is maintained during vibration while in asymmetric stretching, one or more of the symmetries of the molecule vanish during vibration (see figure 4.13(a)). Secondly, bending or deformation vibration modes, in which the bond length remains constant while one or more bond angles change. This may also be classified into two types, namely in-plane (such as scissoring and rocking) and out-of-plane (such as wagging and twisting) as shown in figure 4.13(b).

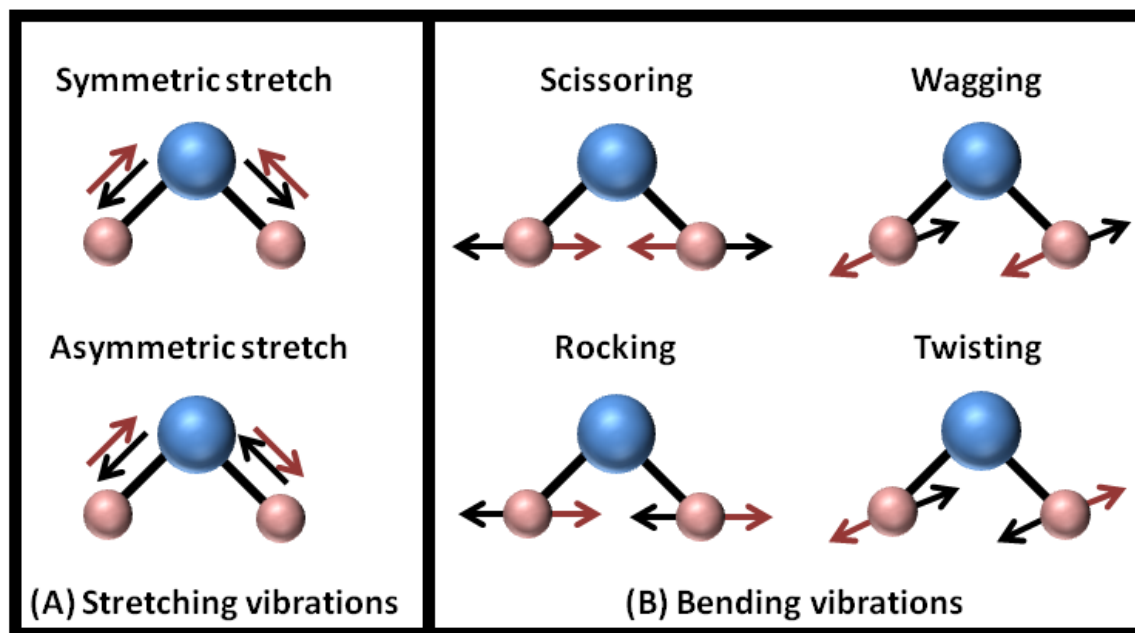


Figure 4.13: Schematic diagram for the IR active fundamental vibration modes. Adapted from [19].

4.5.2 Sample preparation

All samples in this thesis were prepared by the following steps shown [figure 4.14](#): in the first step the KBr powder was placed into an oven at 60 °C overnight for drying. Then 200 mg of KBr and 1mg of samples were weighted by using a sensitive balance (step 2). The weighed KBr and sample were mixed together, ground for 20 seconds using a grinder machine (step 3). Due to hygroscopicity of KBr, the mixture was placed again into oven at 60 °C for 30 min (step 4). Finally a transparent pellet was obtained by pressing the mixture under 9 tons for 10 min (steps 5 and 6).

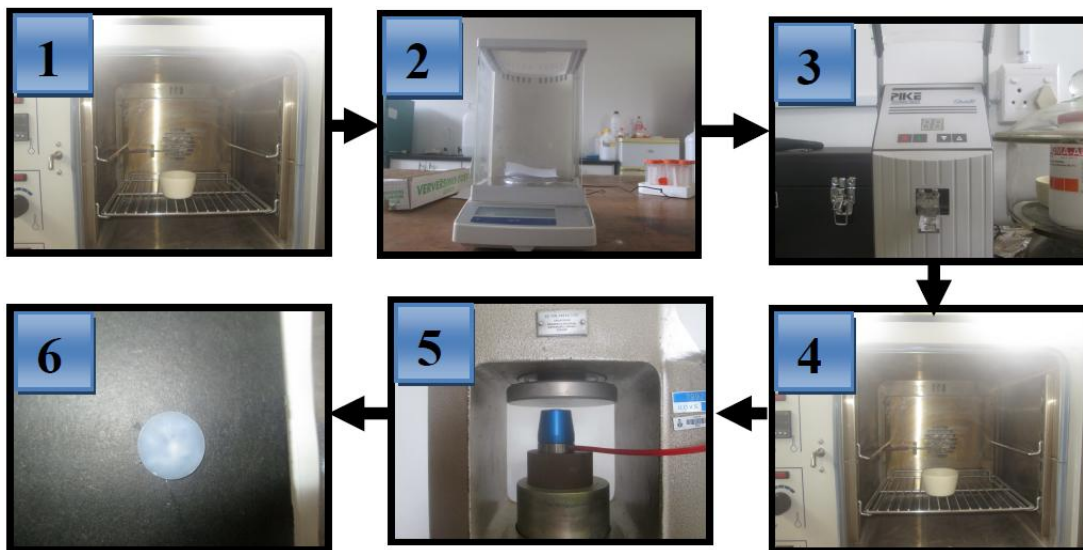


Figure 4.14: Schematic diagram for the FTIR sample preparation steps.

4.5.3 Instrumentation

There are a number of interferometer designs used by FTIR manufacturers. But the most common type of interferometer in use today is the Michelson interferometer. The basic components of a Michelson interferometer are a broad light source covering the mid-IR, a beam splitter, two front mirrors - one moving and one fixed - and a detector as shown schematically in [figure 4.15](#).

The light from source enters the spectrometer and is split by the beamsplitter. Half of the beam is reflected and half is transmitted. The reflected beam goes to the fixed mirror and reflected back to the beamsplitter while the transmitted beam is sent to the moving mirror and is also reflected back towards the mirror. The both reflected beams from fixed and moving mirrors are split again into two beams by the beamsplitter: one goes back to the source (not reaching the detector) and the other goes towards the detector. Thus, the detector detects two beams: one from the moving mirror and the other from the fixed mirror. Due to the optical path difference of these two beams which is determined by the positions of the two mirrors, the two beams are interfere by either constructively or destructively for a particular frequency by positioning the moving mirror.

If the moving mirror is scanned over a range, then the intensity of the signal should be between maximum and minimum which gives rise to a cosine wave. The plot is defined as an interferogram. Once an interferogram spectrum is collected, it needs to be translated into a spectrum (absorption or transmission). The process of conversion is through the Fast Fourier Transform algorithm which can be done by computer programme.

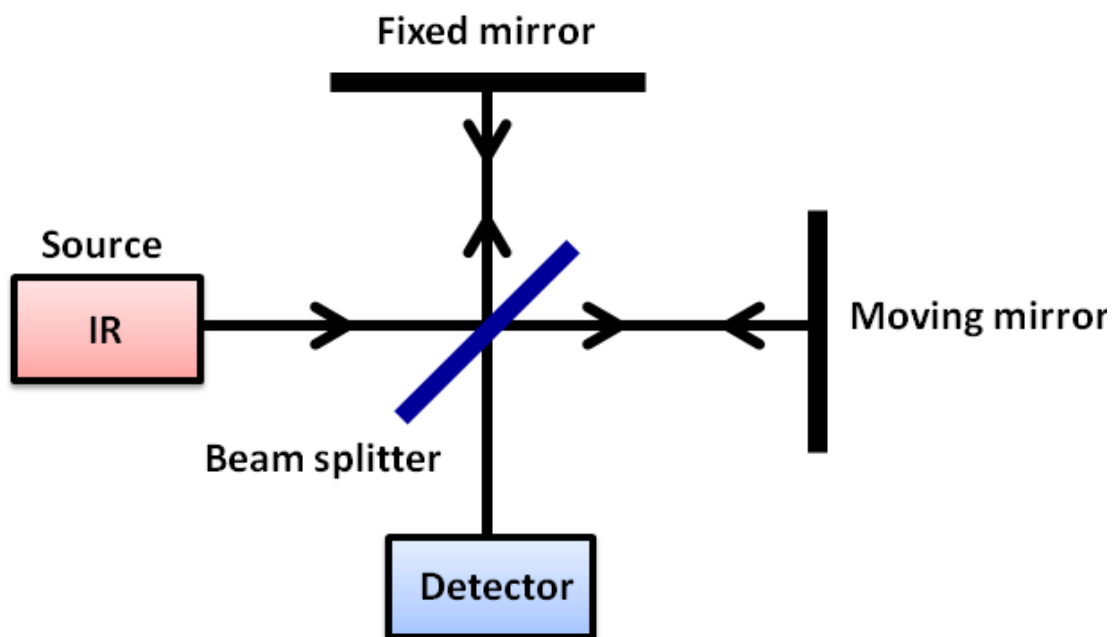


Figure 4.15: Schematic diagram of a Michelson Interferometer.

The purpose of technique in this work is to identify the purity, phase change and to confirm the presence of specific impurities of SiO_2 powder before and after heat treatment. [Figure 4.16](#) showed a photo of a typical Bruker Tensor 27 FTIR spectrometer used in this work.

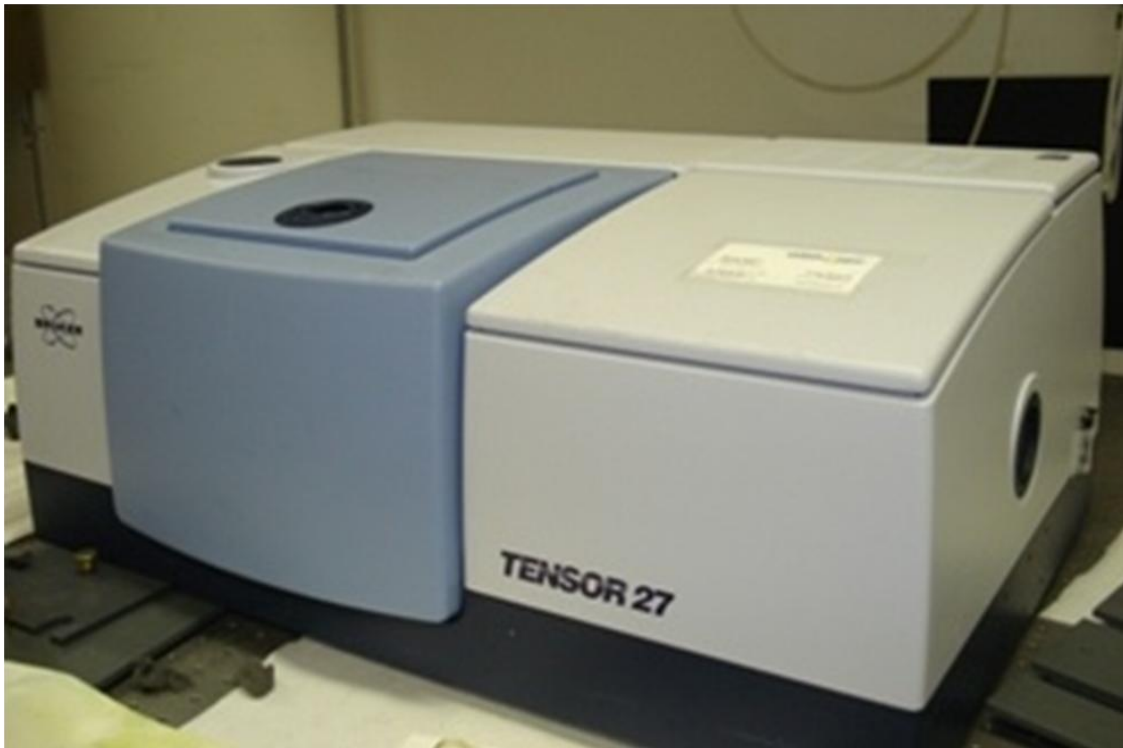


Figure 4.16: Bruker Tensor 27 FTIR spectrometer.

4.6 Photoluminescence spectroscopy

PL spectroscopy is an analytical technique used to measure the fluorescence or phosphorescence emitted by a substance when excited by photons (UV, visible or other electromagnetic radiation) [20]. This technique is very efficient, contactless and non-destructive. It is widely used to understand recombination mechanisms, determination of band gap, estimation of the material quality, detection of impurity and defect levels. After excitation of the sample to an excited state, it returns to the lower energy state which results in the emission of photons. Normally, emission and excitation spectroscopy are performed in one setup, which is require a broadband excitation source (particularly xenon lamp because it has an energy continuum extending from the UV into the NIR [20, 21]. In emission spectroscopy, the excitation source remains fixed during scanning of the emitted light while in excitation spectroscopy, the emission monochromator is set at a

wavelength corresponding to a strong emission line and the excitation (the specific range of electromagnetic radiation where the emitters have a good absorption) light is scanned.

Figure 4.17 shows a schematic diagram of a PL spectrophotometer with general basic equipment. In this instrument various sources may be used as an excitation source, namely lasers, photodiodes, and lamps. It is also provided with two monochromators to select both the excitation and emission.

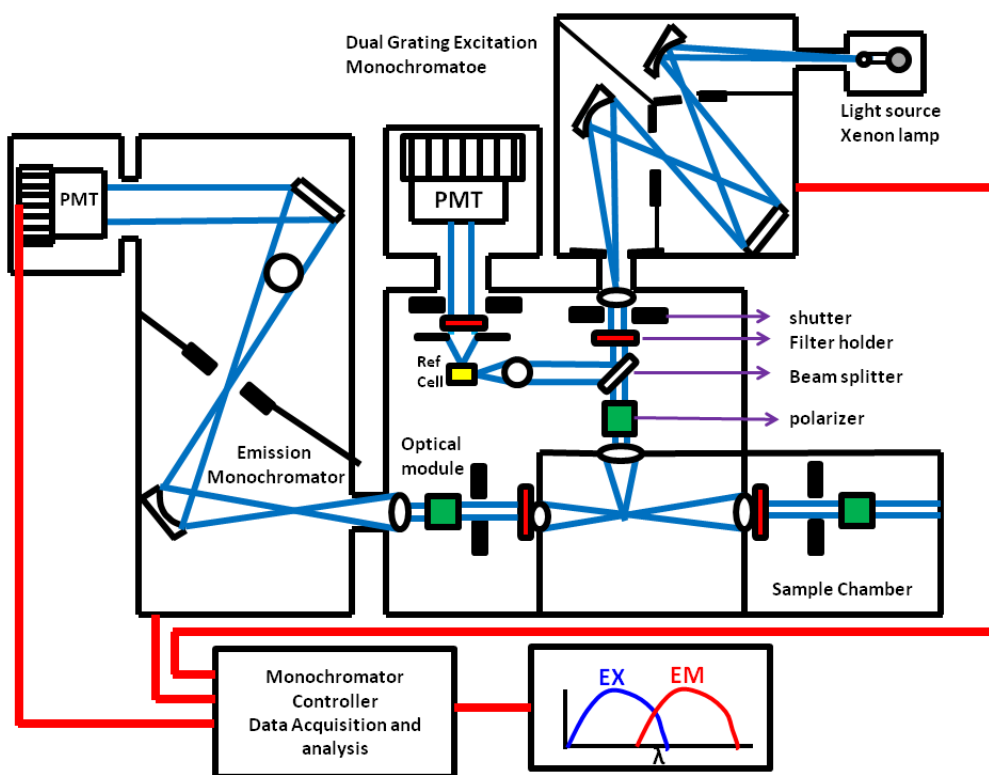


Figure 4.17: Schematic diagram of a spectrofluorometer. Adapted from [20].

These two monochromators are motorized to allow automatic scanning of wavelength. Photomultiplier tubes (PMTs) are used to detect luminescent samples and quantified with the appropriate electronic devices. The output is normally presented on a wavelength scale in graphical form which is recorded and stored with the computer. For ideal measurements, the spectrofluorometer must have the following criteria [20]: (a) the

light source must yield a constant photon output at all wavelengths. (b) The monochromator must pass photons of all wavelengths with equal efficiency. (c) The monochromator efficiency must be independent of polarization. (d) The detector must detect photons of all wavelengths with equal efficiency.

In this study, the PL measurements as well as exponential decay times of the rare-earth (RE) ion (i.e. Tb^{3+}) were done using either a Cary Eclipse fluorescence spectrophotometer with xenon lamp shown in [figure 4.18\(a\)](#) or alternatively with a 325 nm He-Cd laser as an excitation source and Horiba iHR320 monochromator attached with an PMT detector ([figure 4.18\(b\)](#)). All measurements were collected in air at room temperature.

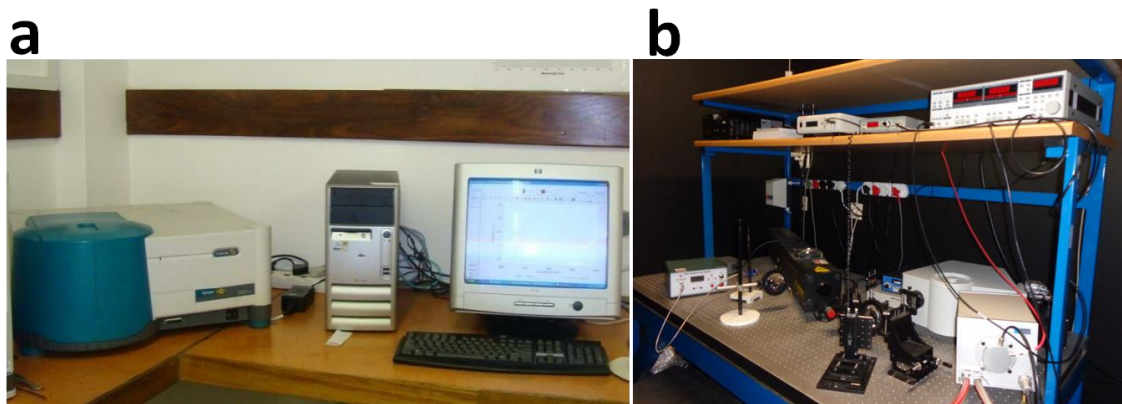


Figure 4.18: Schematic representation of (a) the Cary Eclipse fluorescence spectrophotometer (b) The 325 nm He-Cd laser PL system.

4.7 X-ray photoelectron spectroscopy

XPS was developed in mid of 1960's as a practical technique by Siegbahn and his group in Sweden at University of Uppsala (Nobel Prize 1981) [22]. XPS is also known as Electron Spectroscopy for Chemical Analysis (ESCA). This technique provides qualitative and quantitative information on all the elements in the periodic table (except hydrogen and helium) present at concentrations >0.1 at%. Due to the short free mean path

of the photoelectrons in the solid, this technique provides information from only the top 1-5 nm of a sample surface [23]. Due to its wide range of applications, this technique is considered as the one of the most powerful analytical tools available. The most important information provided by this technique is the information about the molecular environment (oxidation state and bonding strength). The peak position in the XPS spectrum provides information about the atomic composition of the sample surface while the measurement of relative area of the peaks allows the composition of the sample to be determined quantitatively.

4.7.1 Basic theory

The XPS technique is based on the photoelectric effect in which the energetic photon (X-ray) interacts with the solid sample and produces an emission of electrons from its surface (see figure 4.20 (a)). The kinetic energy (KE) of the ejected photoelectrons is given by the Einstein equation [23]:

$$KE = h\nu - E_B \quad (4.9)$$

where $h\nu$ is the energy of the photon, E_B is the binding energy which is the energy required to completely remove an electron from an atom or a molecule. The binding energy can be calculated by measuring the kinetic energy of the photoelectron ejected from the sample. To measure KE (and therefore determine E_B) a calibrated and suitably referenced XPS spectrometer is required [22]. To do this properly, the sample is placed in electrical contact with the spectrometer, and both the sample and the spectrometer are grounded. This makes the Fermi level (E_F) of both the sample and spectrometer at the same energy level. Then the KE of photoelectron can be measured as shown in figure 4.19.

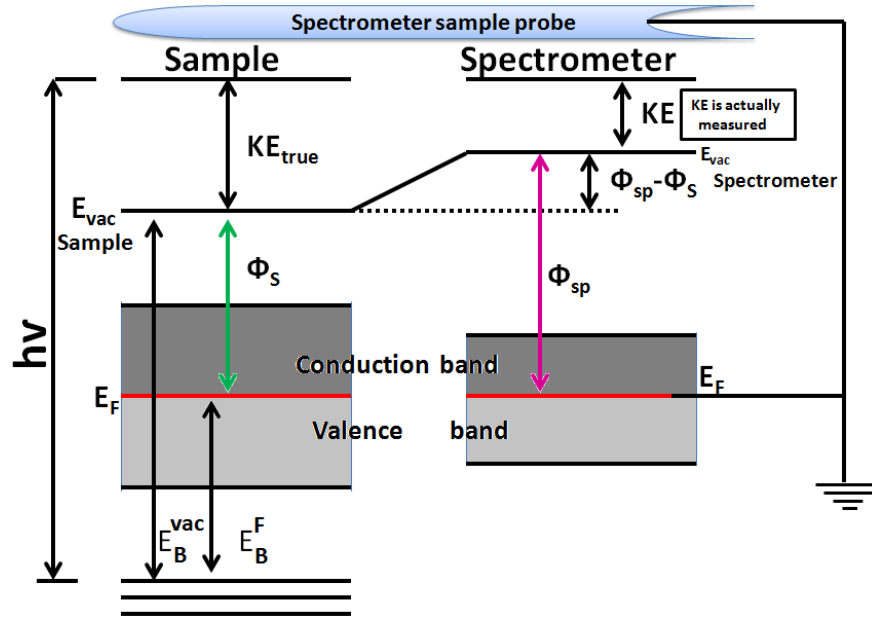


Figure 4.19: The energy level diagram for grounded sample and spectrometer. The Fermi levels of both sample and spectrometer are aligned, so that E_B is referenced to E_F . Adapted from [20].

Considering figure 4.19, after alignment, the X-ray energy does not equal exactly the sum of KE and E_B as shown in equation 4.9. The difference is the work function of the spectrometer (ϕ_{sp}). However, the work function ϕ is defined as the distance between the Fermi level (E_F) and the vacuum level (E_{vac}) as follows:

$$\phi = E_F - E_{vac} \quad (4.10)$$

Then after alignment, equation 4.9 can be written as

$$E_B^F = h\nu - KE - \phi_{sp} \quad (4.11)$$

In order to determine the binding energy E_B^F , both KE and ϕ_{sp} must be measured. The superscript F means that E_B is referenced to E_F . Then the photoelectron spectrum of

different binding energies can be recorded by scanning the kinetic energies using an electron analyzer. XPS spectra are generally accompanied by Auger peaks which result from relaxation of the excited ions remaining after photoemission. In typical process, the K-shell vacancy left behind by the initially ejected electron as in figure 4.20 (a) may be filled by an electron from higher energy level i.e. $L_{2,3}$ (see figure 4.20 (b)). As the result of conservation energy, another electron must be emitted from the same energy level ($L_{2,3}$). This electron is the so-called Auger electron [24]. Thus the photoionization may be associated with the emission of two electrons, a photoelectron and an Auger electron. Note that instead of emitting an Auger electron, the photoionized atom may also relax by emitting a characteristic X-ray, which occurs more readily for atoms with greater atomic number (heavier atoms). Although XPS and Auger electron spectroscopy (AES) are similar in the sense that both of them are use of a spectrometer to measure electron with relatively low energy, the main difference between them is the source of the primary radiation, which is necessary to induce ionization of the atoms. The primary radiation in the AES is the electron gun while for XPS is the soft X-ray. Moreover, the energy of photoelectron depends on the primary excitation source while the energy of Auger electron it does not.

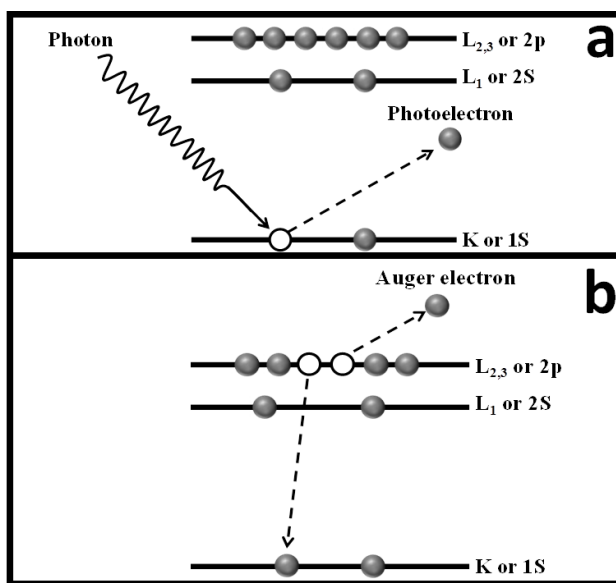


Figure 4.20: (a) The XPS process and (b) the Auger process. Adapted from [25].

4.7.2 Instrumentation

The main components of XPS system include a source of X-rays, an ultra-high vacuum chamber and electron energy analyzer. Figure 4.21 shows a schematic diagram of an XPS spectrometer. A description detail of the main components of XPS spectrometer is given in [22].

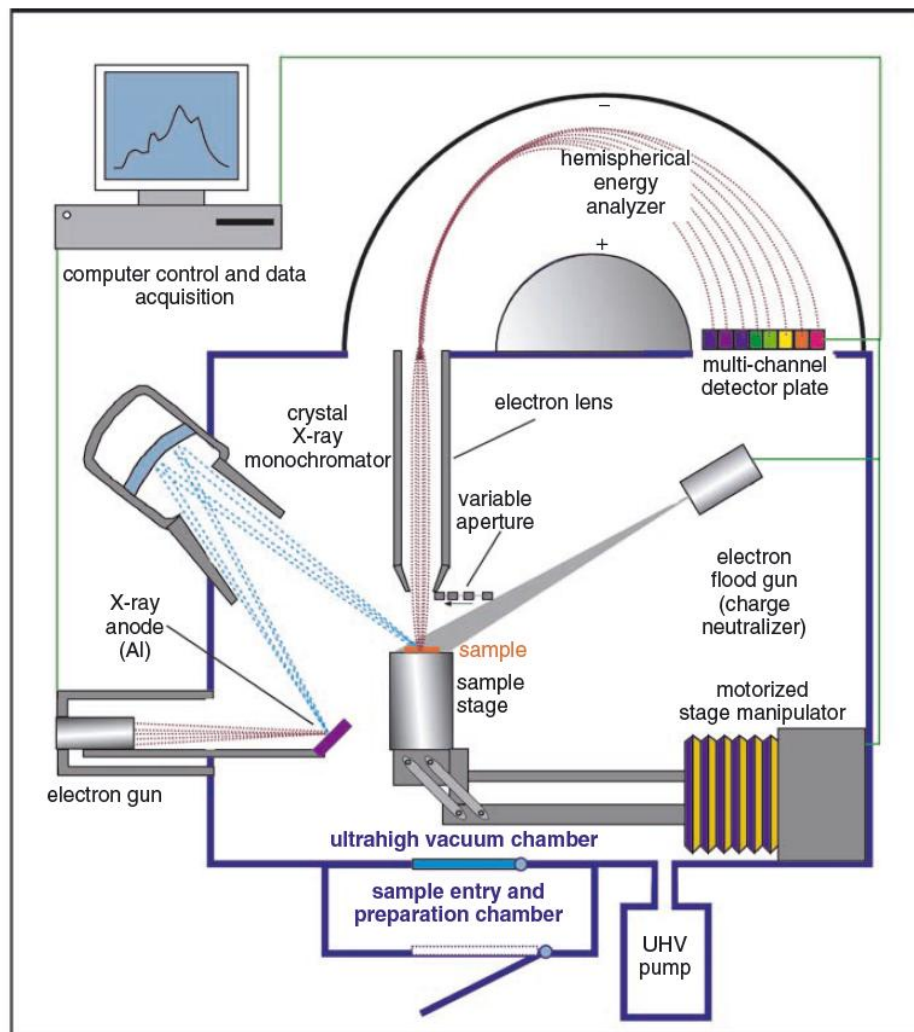


Figure 4.21: The XPS spectrometer [22].

4.7.3 Interpretation of spectra

The photoelectrons are emitted from all energy orbitals of the target atom of a particular element and therefore the electron energy spectrum is characteristic of the emitting atom type. Consequently, the existence of lines in the XPS spectrum indicates the presence of a specific element in the sample under investigation. The intensity of these lines also indicates the relative concentration of a particular element in the sample. Therefore the XPS technique can be used for quantitative analysis as well. Actually there are two ways to collect photoelectron spectra, survey and high resolution scans. A survey scan is acquired at high pass energy (pass energy is the energy which control the count rate and therefore the resolution, i.e. high pass energy means high count rate but low resolution and vice versa) while high resolution scans are collected at low pass energy. A survey scan can be used to identify the composition of the sample and the determination of each element depends on its core electrons. Figure 4.22 shows an example of the survey scan spectrum of SiO₂:Ag, obtained with pass energy of 187 eV. Elements can be identified with the help of an XPS database of binding energies.

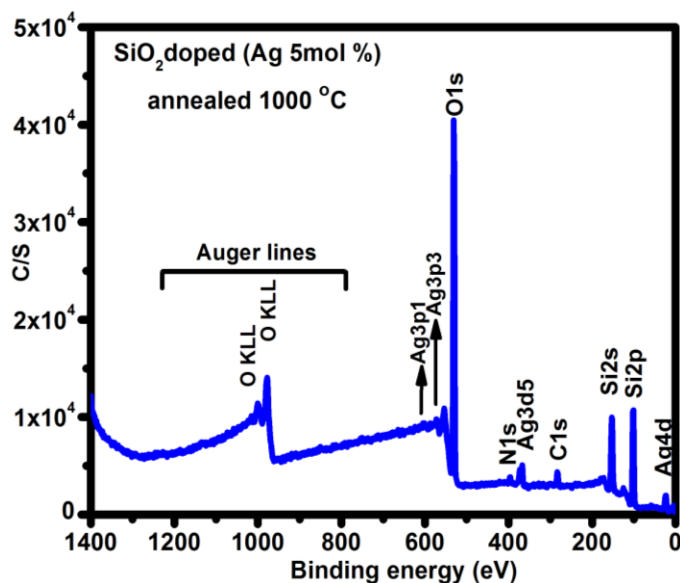


Figure 4.22: XPS survey scan of SiO₂ doped with Ag (5 mol%).

High resolution scans for the same sample mentioned in [figure 4.22](#) are collected at low pass energy of 58.7 eV. The detailed line shape allows individual chemical shifts to be determined. [Figure 4.23](#) shows an example of a high resolution scan spectrum of SiO₂:Ag sample. The peaks were scanned within the range of 360-385 eV and are associated with Ag 3d photoelectrons. By using MultiPak software, the spectrum can be fitted with 4 peaks. Details analysis about this sample is given in [chapter 7](#).

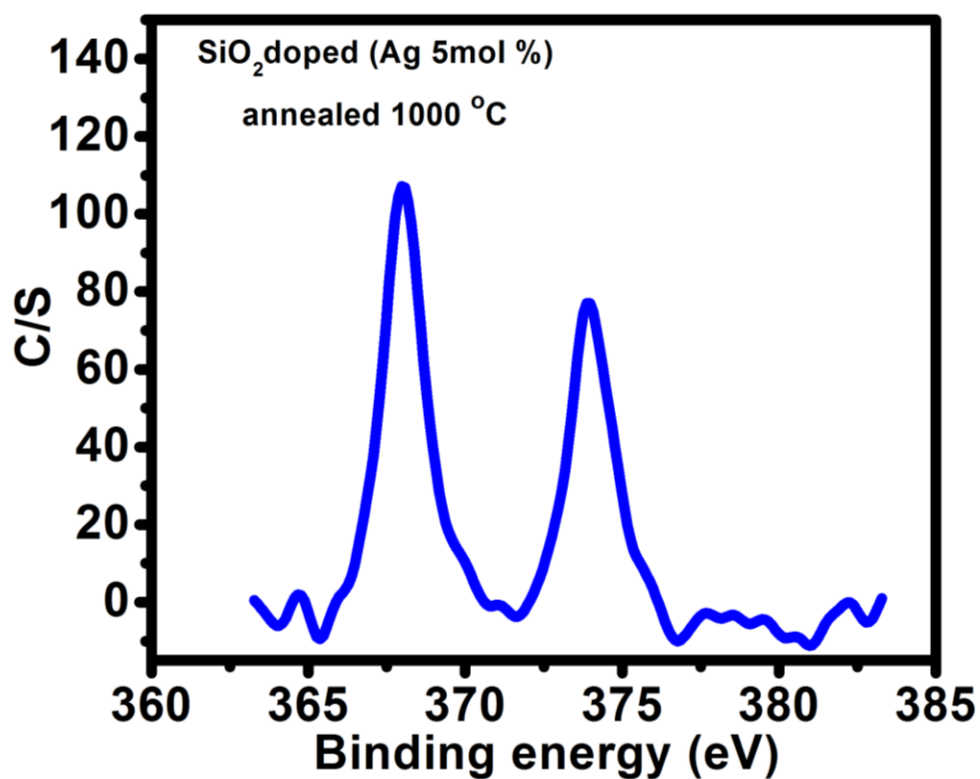


Figure 4.23: XPS high resolution scan of SiO₂ doped with Ag (5 mol%).

The XPS spectrometer used in this study was the PHI 5000 Versaprobe, shown in [figure 4.24](#).

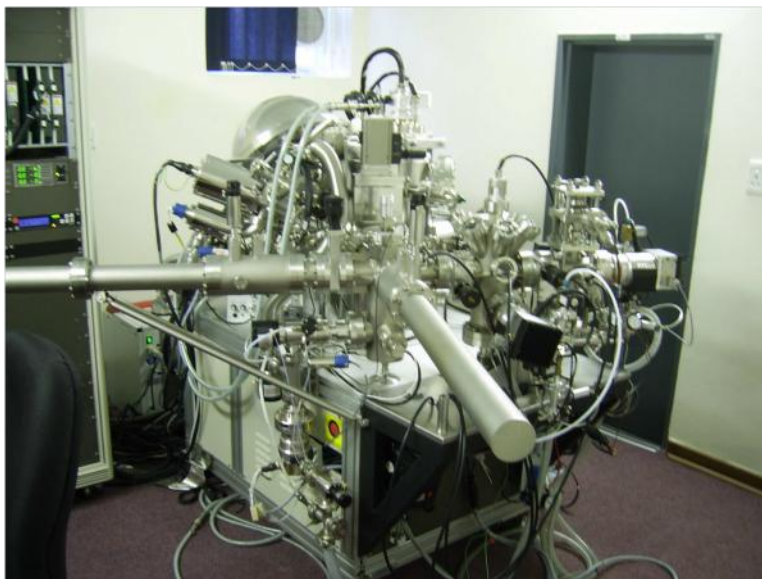


Figure 4.24: PHI 5000 Versaprobe scanning XPS.

4.8 References

- [1] B. D. Cullity, Elements of X-ray diffraction, *Addison-Wesley Publishing Company Inc.*, USA, (1956) (510 pages).
- [2] S. Shanmugan, D. Mutharasu and A. H. Haslan, Structural Analysis of RF Sputtered TiO₂ Thin Film on Cu Substrate for Various Annealing Temperatures, *Int. J. Eng. Trend. Technol.* **14** (2014) 57-60.
- [3] X Ray Generation, [online]. Available from: <http://xrayweb.chem.ou.edu/notes/xray.html> [Accessed 01 October 2015]
- [4] W. H. Bragg and W. L. Bragg, The Reflection of X-rays by Crystal, *Nature* **17** (1913) 428-438.
- [5] R. E. Kroon, Nanoscience and the Scherrer equation versus the ‘Scherrer-Gottingen equation’, *S. Afr. J. Sci.* **109** (2013) (2 pages).
- [6] S. Skujins, A. G. Varian, Applications of UV-Visible DerivativeSpectrophotometry, *Agilent Technologies*, Switzerland, (1986).
- [7] H. Förster, UV/VIS Spectroscopy, *Mol. Sieves* **4** (2004) 337-426.

- [8] T. Owen, Fundamentals of modern UV-visible spectroscopy, *Agilent Technologies*, Germany (2000) (135 pages).
- [9] E. Morales, E. S. Mora and U. Pal, Use of diffuse reflectance spectroscopy for optical characterization of un-supported nanostructures, *Rev. Mex. Fis.* **53** (2007) 18-22.
- [10] Double Beam Spectrophotometer [online]. Available from http://www.hitachi-hightech.com/global/product_detail/?pn=ana-u2900 [Accessed 21 May 2015].
- [11] D. B. Williams and C. B. Carter, Transmission Electron Microscopy, *Springer Science +Business Media*, USA (1996) (737 pages).
- [12] L. A. Bendersky and F. W. Gayle, Electron Diffraction Using Transmission Electron Microscopy, *J. Res. Natl. Inst. Stand. Technol.* **106** (2001) 997-1012.
- [13] R. F. Egerton, Electron Energy-Loss Spectroscopy in the Electron Microscope, *Springer Science+Business Media*, USA (2011) (491 pages).
- [14] Basic principle of transmission electron microscope [online]. Available from http://www.hk-phy.org/atomic_world/tem/tem02_e.html [Accessed 21 May 2015].
- [15] S. D. Sawanta, A. A. Baravkar and R. N. Kale, FT-IR Spectroscopy: principle, technique and mathematics, *Int. J. Pharma and BioSci.* **2** (2011) 513-519.
- [16] G. E. A. Swann and S. V. Patwardhan, Application of Fourier Transform Infrared Spectroscopy (FTIR) for assessing biogenic silica sample purity in geochemical analyses and palaeoenvironmental research, *Clim. Past* **7** (2011) 65-74.
- [17] W. M. Doyle, Principles and applications of Fourier transform infrared (FTIR) process analysis, *Process control and quality* **2** (1992) 11-41.
- [18] A. Barth and C. Zscherp, What vibrations tell about proteins, *Q. Rev. Biophys.* **35** (2002) 369-430.
- [19] B. H. Stuart, Infrared spectroscopy: fundamentals and applications, *John Wiley & Sons Ltd*, England (2004) (223 pages).
- [20] J. R. Lakowicz, Principles of Fluorescence Spectroscopy, *Kluwer Academic/Plenum Publishers*, New York (1999) (697 pages).

- [21] C. R. Ronda, Emission and Excitation Mechanisms of Phosphors, In: Luminescence: From Theory to Applications, edited by C. Ronda, *WILEY-VCH Verlag GmbH & Co. KGaA*, Germany (2008) 219-260.
- [22] B. D. Ratner and D. G. Castner, Electron Spectroscopy for Chemical Analysis, In: Surface Analysis -The Principal Techniques, edited by J. C. Vickerman, *John Wiley & Sons Ltd*, United Kingdom (2009) 47-112.
- [23] B. D. Fahlman, Materials Chemistry, *Springer* (2007) 485pp.
- [24] J. F. Watts and J. Wolstenholme, An Introduction to Surface Analysis by XPS and AES, *John Wiley & Sons Ltd*, England (2003) (212 pages).
- [25] F. Moulder, W. F. Stickle, P. E. Sobol and K. D. Bomben, Handbook of X-ray Photoelectron Spectroscopy, *Physical electronics Inc.*, USA (1995) (261 pages).

Chapter 5

White luminescence from sol-gel silica doped with silver

5.1 Introduction

Many researchers have recently been attracted to research white phosphors for applications in solid state lighting with the goal to replace fluorescent lamps by creating sources with improved lifetime, efficiency and reliability [1-4]. Phosphor-converted white light emitting diodes (pcW-LEDs) generate white light using phosphors together with a short-wavelength excitation source in the visible and/or ultraviolet spectral regime and now play an important role in modern lighting due to their high efficiency, relatively low cost, compact structure and simple driving circuitry [5, 6].

Sol-gel silica (SiO_2) is a potential candidate material for optoelectronic applications because it is environmental friendly, low-cost, easy to fabricate and has good thermal and chemical stability. It can emit light in the ultraviolet, blue and red spectral regions and this is dependent on the type of defects in its structural network. Different synthesis methods, thermal treatment or dopants can create different types of defects in the network structure and then new luminescent centres may be observed [7]. Much research has been done to control the photoluminescence (PL) associated with such defects during synthesis by either changing the reaction medium using different parameters, such as solvents, pH and precursors [7, 8], or by adding some impurities i.e. dopants [9]. For instance, Kachurin *et al.* observed a new optical active centre in SiO_2 implanted by Ge ions during thermal treatment [10] while Komarov *et al.* showed that the implantation of Sn ions in SiO_2 formed a large number of radiative centres after heat treatment [11].

Recently, active research has been focused on Ag doped SiO_2 for different applications [12, 13]. Most of the work related to phosphors has been done to investigate the possible enhancement of the luminescence of other dopants (e.g. RE ions) in the silica co-doped with Ag as a result of plasmonic effects related to metallic Ag nanoparticles (NPs) [14].

However, the luminescent properties of silica doped only with Ag have not been the focus of any studies. In the present work we report on the influence of the addition of Ag on the luminescence properties of sol-gel SiO₂. The effects of Ag ions and Ag NPs on the optical properties of SiO₂ are considered in detail and possible mechanisms for the emission are proposed. Near white light from the SiO₂ sample doped only with 1 mol% Ag annealed at 1000 °C was observed.

5.2 Experimental

Undoped and Ag doped SiO₂ were prepared by the sol-gel method [15]. Tetraethylorthosilicate (TEOS, 99.7%), ethanol (C₂H₅OH, 99.0%) and water were used as starting materials and nitric acid (HNO₃) was used as the catalyst. The molar ratio was taken as 1:5:10 for TEOS:ethanol:water [16]. Silver nitrate (AgNO₃, 99.9%) was used as the source of Ag. All samples were prepared by first dissolving TEOS in ethanol by magnetic stirring for 30 min. Then dilute (0.15 M) HNO₃, instead of pure water, was added to the solution in order to catalyze the hydrolysis/condensation reaction. The mixture was stirred continuously for another 30 min. To dope the silica, different amounts of AgNO₃ were first dissolved ultrasonically in a small amount of the dilute HNO₃ taken from total amount. Then the solution containing this dopant was added to the mixture which was stirred for a further 5 h. A gel was produced after about 20 h when storing the solutions in closed containers placed in a water bath at 50 °C. These gels were dried in open containers in air for 24 h and then ground to fine powders, which were further dried in an oven at 50 °C for a 20 h and finally annealed in air at different temperatures for 2 h.

Samples were analyzed at room temperature. X-ray diffraction (XRD) patterns were recorded with a Bruker D8 diffractometer. The morphology and size of Ag NPs were obtained from transmission electron microscope (TEM) images recorded with a Philips CM 100 instrument. Diffuse powder absorption spectra were measured using a Perkin Elmer Lambda 950 UV-vis spectrophotometer with integrating sphere while

luminescence emission properties and the degradation process were measured using a 325 nm He-Cd laser.

5.3 Results and discussion

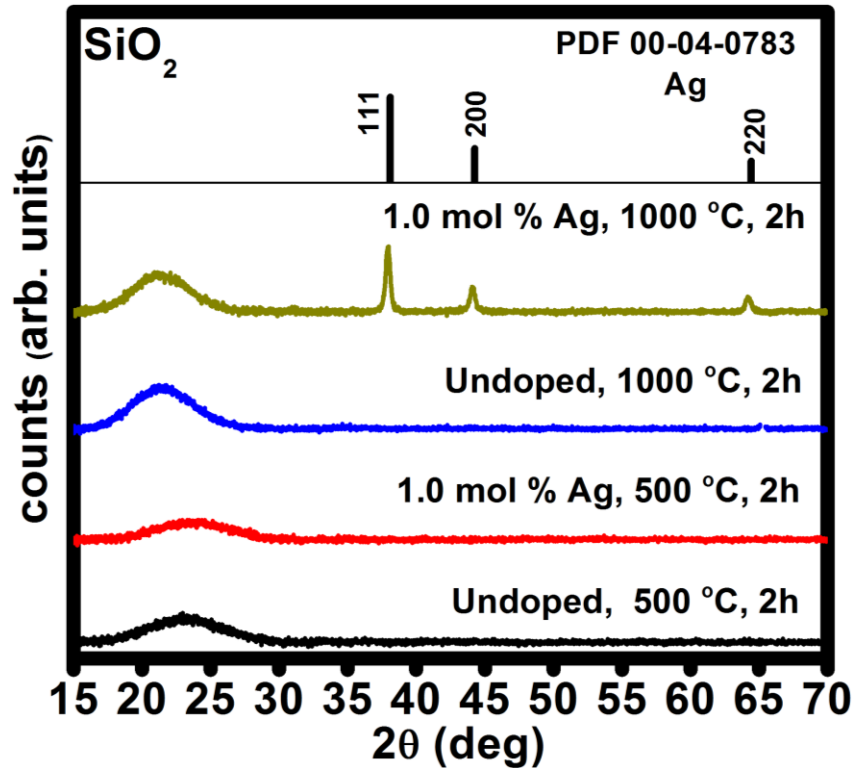


Figure 5.1: XRD patterns of undoped and 1 mol% Ag doped SiO₂ annealed at 500 °C and 1000 °C in air for 2 h.

Figure 5.1 shows the XRD patterns of powder samples of undoped SiO₂ and 1 mol% Ag doped SiO₂ prepared by the sol-gel method. These samples were annealed in air at different temperatures for 2 h. The samples annealed at the lower temperature (500 °C), both with or without Ag, showed a broad peak centred at $2\theta \sim 23^\circ$ indicating the amorphous structure of the silica. This peak became narrower and shifted to $2\theta \sim 21^\circ$ for the samples annealed at 1000 °C, corresponding to an increase in the structural order of

the amorphous silica towards the cristobalite phase, which is one of the crystalline forms of silica [12]. Of interest is that the addition of 1 mol% Ag did not change the phase of the amorphous structure of silica, even after annealed at 1000 °C. This is contrary to previous reports which suggested that the addition of Ag to amorphous SiO₂ promoted partial crystallization of the cristobalite phase [17, 18].

The average size of these Ag NPs was calculated by Scherrer's equation $D = 0.9\lambda/(\beta \cos\theta)$, where β is the full width at half maximum of a diffraction peak in radians, θ is the corresponding Bragg angle and λ is the wavelength of the X-rays. The diameter obtained using different diffraction planes was found to be in the range of 18-25 nm.

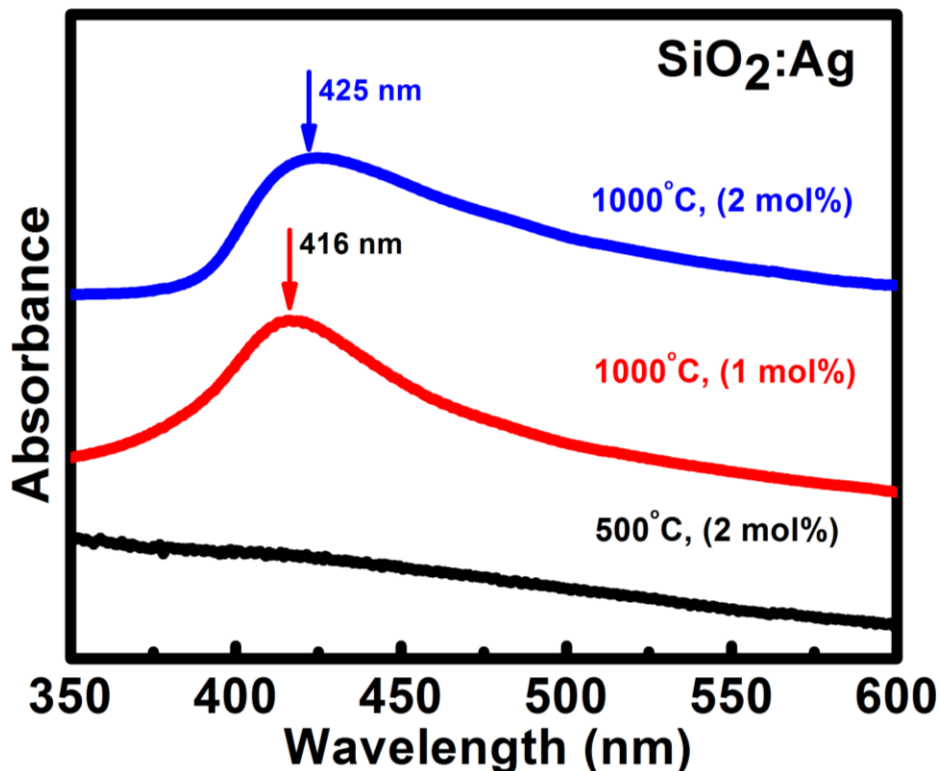


Figure 5.2: Diffuse absorbance curve of SiO₂ doped with different concentrations of Ag annealed at different temperature in air for 2 h.

Figure 5.2 shows diffuse absorbance spectra of two silica samples doped with 2 mol% Ag annealed at different temperatures in air for 2 h. The sample annealed at 500 °C shows no obvious absorption band from the localized surface plasmon resonance associated with Ag NPs, indicating that the Ag ions are not reduced to metallic NPs in the silica glass of this sample. However, for the sample annealed at 1000 °C there is a broad peak centred at 425 nm corresponding to plasmonic absorption, confirming the formation of Ag NPs in agreement with the XRD results.

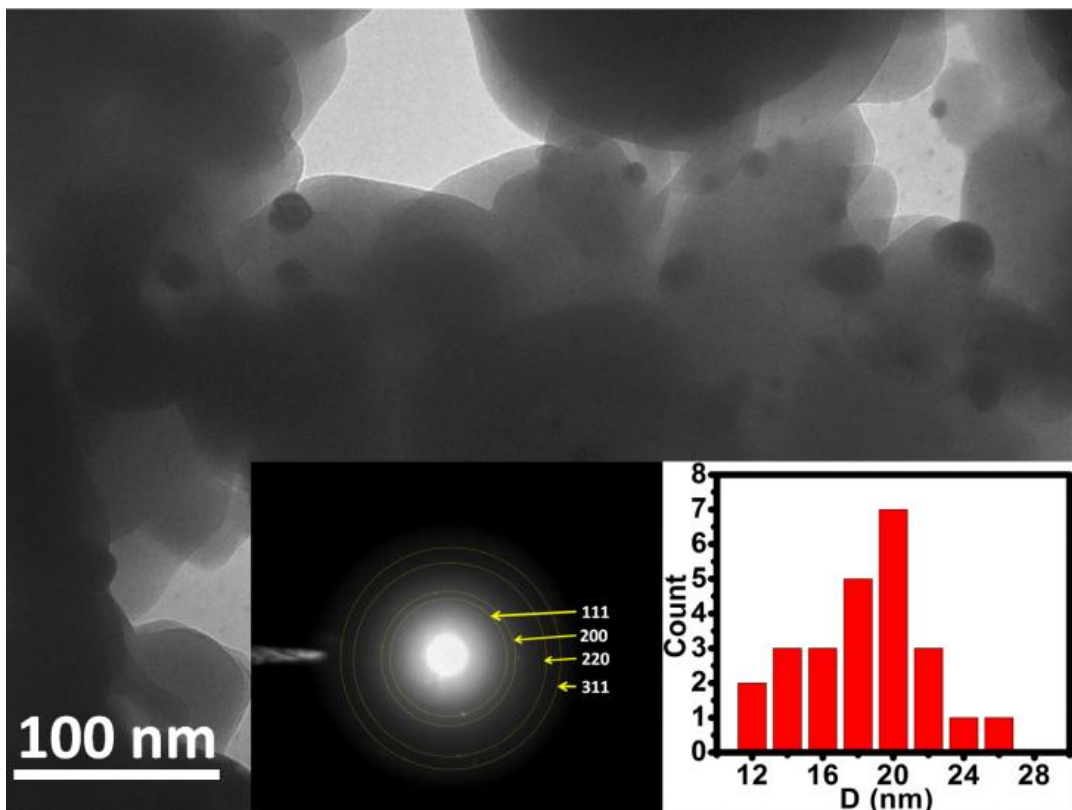


Figure 5.3: TEM image of SiO₂ doped with 5 mol% Ag annealed at 1000 °C for 2 h. The insets show the selected area diffraction pattern with several bright spots at radii consistent with electron diffraction from metallic Ag NPs and the size distribution of the observed NPs.

Figure 5.3 is a TEM image of SiO₂ doped with 5 mol% Ag annealed at 1000 °C in air for 2 h. This micrograph image shows Ag NPs which are almost spherical in shape in an amorphous matrix of SiO₂. The right-side inset shows the size distribution of these NPs and the modal size is found to be 20 nm, which is close to the average size calculated using the XRD pattern and Scherrer's equation despite the concentration of Ag in the TEM sample being substantially higher. The crystallinity of these Ag NPs is apparent from electron diffraction of the particles in the amorphous SiO₂ host (left-side inset), which is a further confirmation for the formation of Ag NPs in SiO₂, in agreement with the XRD and diffuse absorbance results.

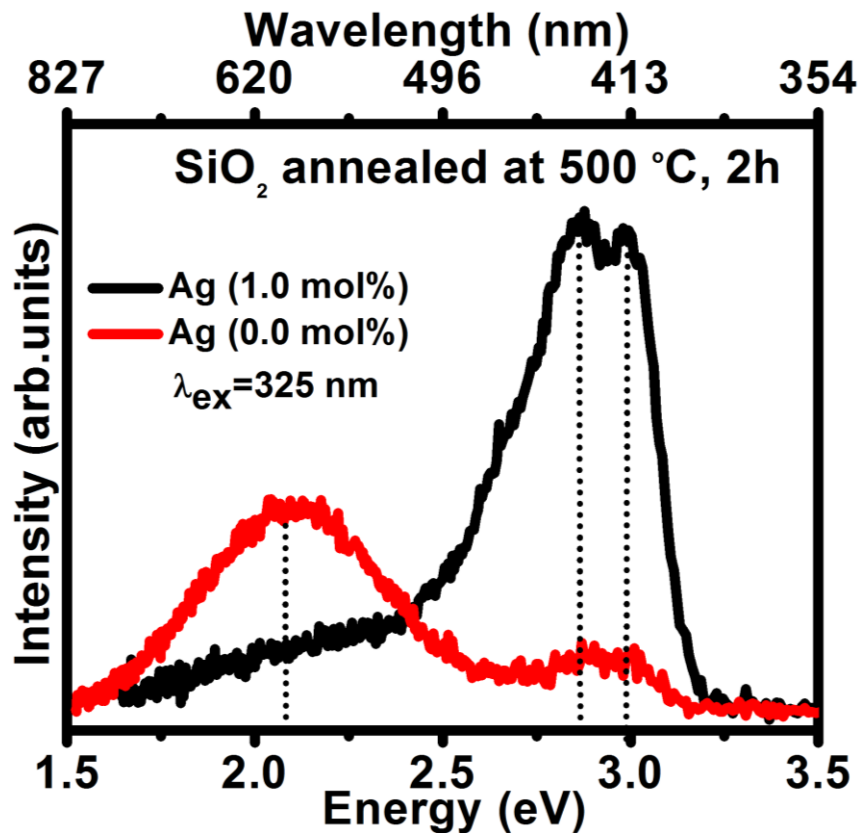


Figure 5.4: Emission spectra for undoped silica and silica doped with 1 mol% Ag annealed at 500 °C in air for 2 h.

Figure 5.4 shows the PL emission spectra of undoped and 1 mol% Ag doped SiO₂ samples annealed at 500 °C for 2 h. The spectrum of the undoped sample consists of a small peak centred at 420 nm, which is a well-known emission region in SiO₂ attributed to oxygen deficiency centres (ODCs) [7, 19], and a larger broad emission band centred near 590 nm which is attributed to carbon impurities [14]. The addition of 1 mol% Ag caused significant change in the luminescence: there is a strong enhancement of the emission centred at 420 nm associated with ODCs while the peak at 590 nm associated with carbon impurities has decreased. The enhancement of the peak at 420 nm is associated with the decrease in oxygen content in the silica network due to the formation of Ag₂O in the doped sample, which will be discussed in chapter 7 [14]. The Ag dopant in this sample has not coalesced into NPs to the extent that diffraction peaks in the XRD patterns (figure 5.1) or a plasmonic absorption band in the diffuse reflectance measurements (figure 5.2) can be observed, and it is therefore present as individual ions or small clusters. These are known to be luminescent, and fluorescent Ag nanoclusters stabilized in different scaffolds were reviewed by Díez and Ras [20] while Dubrovin *et al.* [21] considered the many Ag-related species that may occur in photo-thermo-refractive glasses. The optical properties of these luminescent species are dependent on their environment and may therefore vary significantly. According to Valotto *et al.* [22], Ag ions in silicate glasses give rise to a UV band at about 330 nm from isolated Ag⁺ ions at low concentrations, a blue band at about 450 nm due to Ag⁺ in higher concentrated systems, a green band at about 530 nm which is likely due to Ag⁺-Ag⁺ pairs and an orange band at about 600-650 nm due to Ag₃²⁺. Li *et al.* [23] summarize the literature for Ag ion-exchange glasses and identify four main features: a UV band around 350 nm and a violet band around 420 nm (attributed to transitions from the ¹D₂ and the ³D_J (*J* = 1,2,3) states of Ag⁺ to the ¹S₀ ground state, respectively, under about 250 nm excitation), as well as a deep-blue band at about 450 nm and a green band at about 525 nm (attributed to Ag₂⁺ species and Ag⁺-Ag⁺ pairs, respectively, and excited effectively at about 350 nm). Lai *et al.* [24] have recently considered the enhancement of Eu³⁺ luminescence due to Ag species in macroporous sol-gel silica and provide a simplified energy structure diagram

indicating the emission from Ag^+ ions at 396 nm when excited at 245 nm and the emission of Ag^+-Ag^+ ion pairs at 540 nm when excited at 345 nm. Since the material considered in this study is sol-gel silica, these results are most relevant. The wavelength of the He-Cd laser used in this study (325 nm) is not of short enough wavelength to excite Ag^+ ions, but may excite Ag^+-Ag^+ ion pairs. Their emission at 540 nm (2.3 eV) would then form part of the prominent low energy shoulder of the emission peak of the Ag doped sample in [figure 5.4](#).

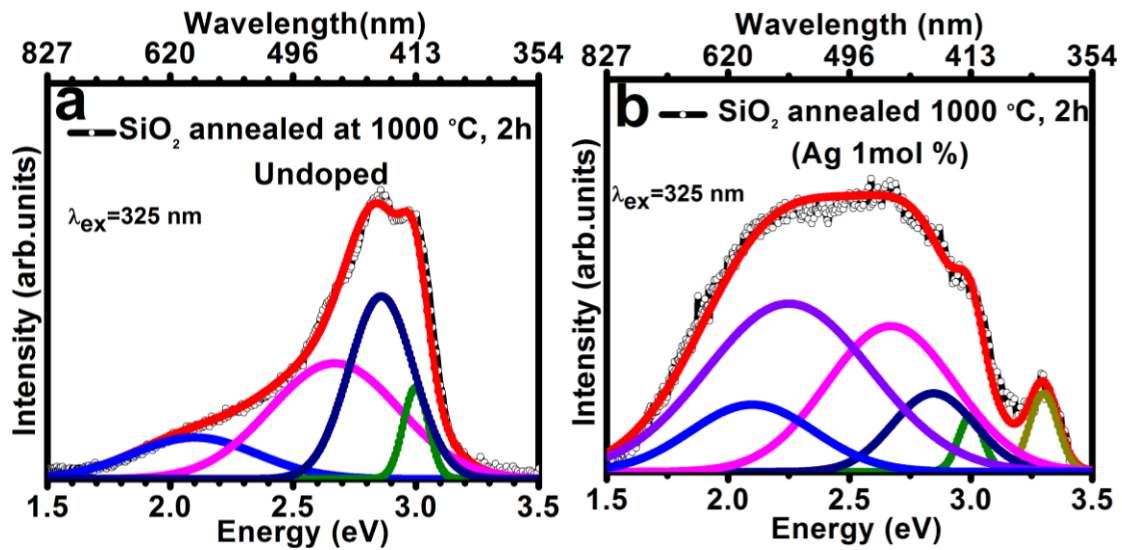


Figure 5.5: Emission spectra of SiO_2 samples (a) undoped and (b) doped with 1 mol% Ag, annealed at 1000 °C for 2 h. These spectra have been fitted with Gaussian peaks on the energy scale.

[Figure 5.5](#) show the emission spectra of the undoped and Ag doped SiO_2 samples after annealing at the higher temperature of 1000 °C. The emission spectrum of the undoped sample shown in [figure 5.5\(a\)](#) is similar to that of the Ag doped sample annealed at 500 °C, being dominated by ODC defects and indicating that while doping with Ag may lead to the formation of these defects for lower temperature annealing, they also form in pure SiO_2 after annealing at higher temperature. The sample doped with 1 mol% Ag and

annealed at the higher temperature (1000 °C) showed significant broadening of its emission spectrum as seen in [figure 5.5\(b\)](#). Under such conditions the Ag ions are also converted to metallic Ag NPs as confirmed by the XRD, diffuse absorbance and TEM measurements presented here, as well as X-ray photoelectron spectroscopy (XPS) results reported in chapter 7 [\[14\]](#). To study the broadening of the emission spectrum associated with the addition of Ag and its possible relation to the formation of the Ag NPs, the emission spectra of [figure 5.5](#) were deconvoluted into separate Gaussian peaks on the energy scale. The emission of [figure 5.5\(a\)](#) corresponding to the undoped sample could be composed of four peaks, three located in the range 2.5-3.1 eV (400-500 nm) together attributed to ODCs and the fourth one at 2.1 eV (590 nm) attributed to carbon impurities, as already discussed. Peaks with the same positions and widths were used to deconvolute the emission spectrum of the Ag doped sample in [figure 5.5\(b\)](#), which could be fit fairly well with the addition of only two additional peaks. One of these was in the ultraviolet region centred at 3.26 eV (380 nm) while the second, much larger, additional peak dominating the broadening process was centred at 2.25 eV (550 nm). Although these two additional peaks in the Ag doped sample correspond remarkably well with the emission wavelengths given earlier from Lai *et al.* [\[24\]](#) for Ag⁺ ions (396 nm) and Ag⁺-Ag⁺ ion pairs (540 nm), we do not attribute them to Ag species. It has already been mentioned that the excitation wavelength used in this study is not short enough to excite the isolated Ag⁺ ions (if present) to produce the 396 nm emission. The high temperature used for annealing the samples (1000 °C for 2 h) was effective in producing Ag NPs. The formation mechanism of Ag NPs in ion-exchange glass has been considered by Simo *et al.* [\[25\]](#) and occurs above a critical temperature of 410 °C. Although the Ag NP formation process may differ significantly in sol-gel silica glass, it is believed that the annealing conditions that were used resulted in most of the Ag diffusing into NPs and leaving an insignificant amount as ions or clusters. The high temperature annealing condition (1000 °C) and the formation of NPs do not suggest that the concentration of Ag⁺-Ag⁺ ion pairs should have increased substantially compared to the sample annealed at 500 °C, for which only weak luminescence could be attributed to the Ag⁺-Ag⁺ ion pairs near 540 nm.

In their study of macroporous sol-gel silica, Lai *et al.* [24] found that the excitation peak corresponding to Ag^+-Ag^+ no longer occurred when samples were sintered at 750 °C and suggested that the Ag^+-Ag^+ is transformed into Ag NPs under such annealing conditions. Since the two new luminescence peaks at 380 nm and 550 nm in the Ag doped sample annealed at 1000 °C cannot be attributed to Ag species, alternative possibilities must be considered. The peak for the fitting of the spectra in figure 5.5 at 2.1 eV (590 nm) has already been attributed to carbon impurities. Although carbon impurities have also been reported to be associated with emission in the blue and green-red regions [2], the appearance of the two additional peaks in figure 5.5(b) when the sample is doped with Ag are not thought to be associated with carbon impurities. The charge transfer mechanism between O and Si occurs only in the blue region [26] and therefore also cannot account for the new peaks. Even emission from nanocrystalline silicon [27] has been considered, but since the XPS in chapter 7 [14] does not show a peak related to pure Si, this is ruled out. What remains is emission due to defects, suggesting that the presence of Ag creates new optically active defects in the SiO_2 network which may be responsible for these new peaks. PL emission close to 380 nm has been attributed to surface defects formed after exposure to an abundant oxygen environment [27]. In our case the Ag ions (in Ag_2O) convert to metallic Ag (in the form of NPs) at high temperature and during this process oxygen is released, suggesting an abundant oxygen environment suitable for the formation of these defects. This is also confirmed by the XPS results in chapter 7 [14] which showed that the O/Si ratio has increased in samples annealed at high temperature. Therefore the presence of Ag plays a role in the formation of these new optically active centres which does not occur in the undoped SiO_2 samples. The origin of the other new peak centred at 2.25 eV (550 nm) could be due to luminescence from oxygen interstitials or self-trapped exciton defects which have been reported to form an emission band in SiO_2 with a peak in the 2.2-2.5 eV range [28]. In our case oxygen interstitials are considered to be responsible for the new emission peak because this is consistent with the release of oxygen as part of the decomposition of Ag_2O and the formation of Ag NPs. Therefore both new peaks in the Ag doped sample annealed at 1000 °C were formed due

to a surplus of oxygen which occurs at high temperature because of the Ag doping. Despite the presence of this excess oxygen, the ODCs responsible for the blue luminescence of undoped SiO_2 were not annihilated (although their emission may be reduced), but instead these additional oxygen excess defects are formed together with the ODCs and the result is a very broad band of luminescence close to white light.

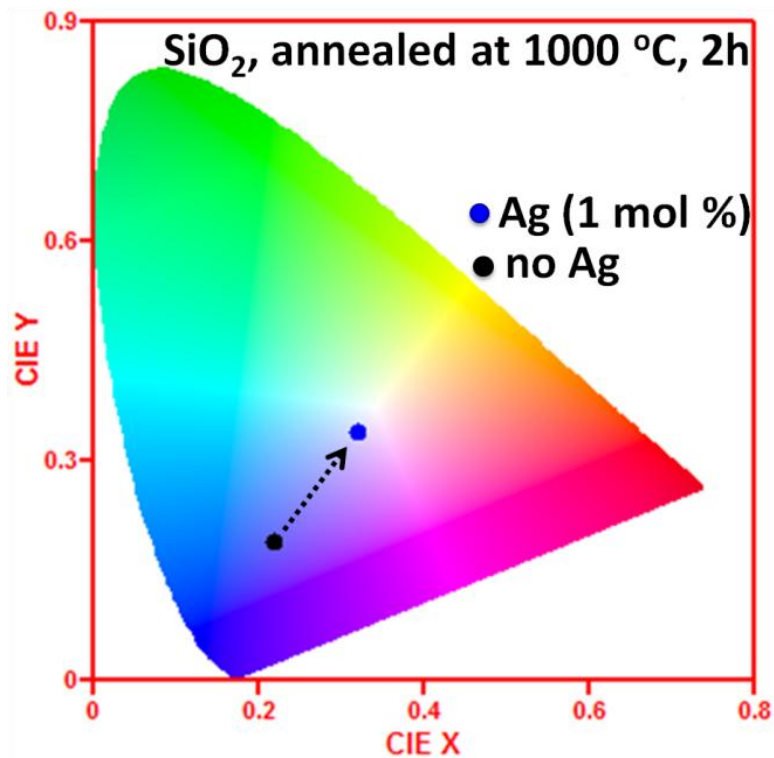


Figure 5.6: CIE coordinates for undoped and 1 mol% Ag doped SiO_2 .

The Commission Internationale de l'Eclairage (CIE) parameters such as colour coordinates and colour correlated temperature (CCT) were calculated in order to know the change in the photometric characteristics of our samples. As can be seen in the CIE diagram plotted in [figure 5.6](#), the broadening of the luminescence emission associated with the addition of Ag changed the emission of the pure SiO_2 from blue with CIE coordinates (0.22, 0.19) to emission with CIE coordinates (0.32, 0.34) which is very close

to pure white light having CIE coordinates (0.33, 0.33) [3]. The CCT values were calculated using the McCamy equation [1]:

$$CCT = -437n^3 + 3601n^2 - 6861n + 5514 \quad (5.1)$$

where $n = (x - x_e)/(y - y_e)$ and the chromaticity epicentre is $x_e = 0.332$ and $y_e = 0.186$, yielding 6070 K for the Ag doped SiO₂ which is close to the value of standard daylight at noon (D65, 6500 K) suitable for cold white light emission [6], suggesting it may have potential for solid state lighting applications.

To study the stability of this phosphor under ultraviolet radiation, the sample SiO₂:Ag (1 mol%) was irradiated by a 325 nm He-Cd laser for 22 h in air at room temperature and the emission spectrum was recorded every 5 min. The power of laser was measured to be 14 mW and the diameter of laser spot was measured to be 1.0 mm, giving an area of 0.79 mm² and an intensity of 18 mW/mm². During the degradation study no change in the shape of the emission spectrum was observed although the intensity was observed to decrease. Figure 5.7 shows the variation of the PL intensity at 520 nm as a function of time and shows relatively fast degradation. Rowland *et al.* [29] considered that excitation by a laser with small spot size accelerates the degradation compared to using a UV LED chip, which in their case had a power of 12 mW and area of 787 mm², giving an intensity of 15 μW/mm². The ratio of the intensities is about 1200 times, suggesting the degradation time used (22 hours) would be equivalent to almost 3 years under the conditions of the UV LED described by Rowland *et al.* [29]. Since during this time the sample shows considerable degradation, this would be a problem for its application for LEDs. Although the main objective of the present work is to study different kind of defects in sol-gel silica after the addition of Ag, the significant change in the emission spectrum after addition of Ag suggests its possible applications in lighting if the degradation could be inhibited.

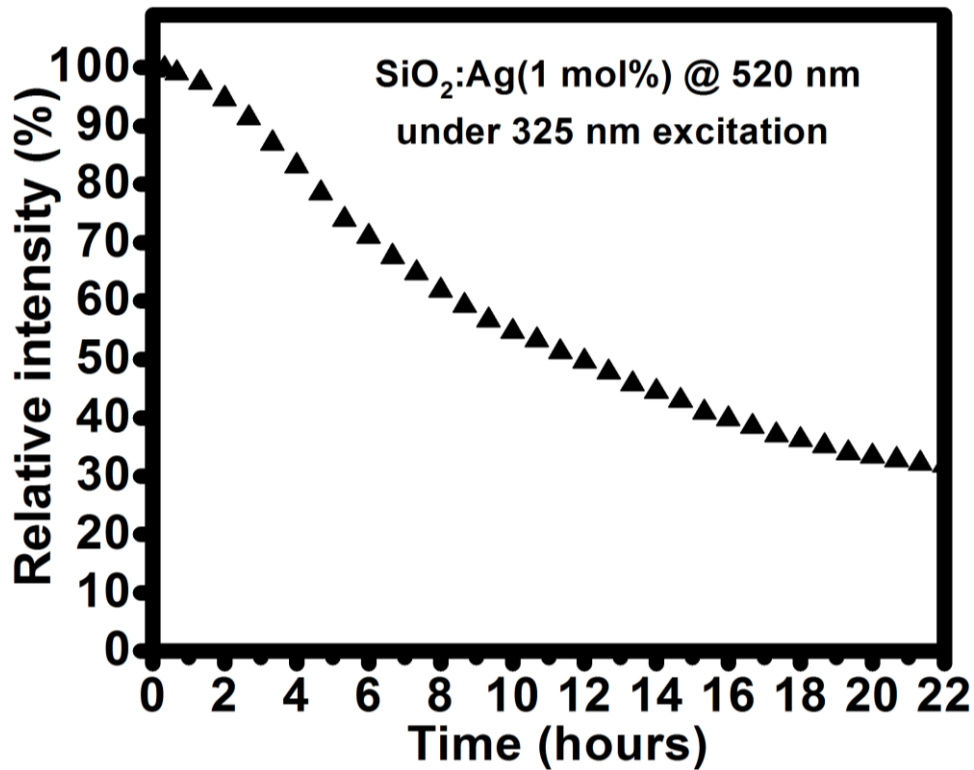


Figure 5.7: Degradation of the emission intensity of SiO₂:Ag(1 mol%) white phosphor under continuous He-Cd laser irradiation (intensity of 18 mW/mm²) in air at room temperature.

5.4 Conclusion

Undoped and Ag doped SiO₂ were prepared by sol-gel method. The influence of the Ag on the luminescence emission of the SiO₂ was investigated. The chemical state of Ag as function of annealing temperature was investigated by XRD, diffuse absorbance and TEM, while optical emission properties were investigated using a 325 nm He-Cd laser. The results indicate that the significant broadening of the luminescence of SiO₂ when doped with Ag and annealed at 1000 °C may be attributed to formation of new optical active centres associated with the decomposition of Ag₂O. Of interest is that two different defects have been revealed after addition of Ag which are attributed to oxygen interstitials and surface related defects. The additional new emission bands change the

luminescence from blue for undoped SiO₂ to white light emission for the Ag doped sample, although degradation limits the use of this phosphor for LED applications.

5.5 References

- [1] V. Kumar, S. Som, V. Kumar, V. Kumar, O. M. Ntwaeaborwa, E. Coetsee and H. C. Swart, Tunable and white emission from ZnO:Tb³⁺ nanophosphors for solid state lighting applications, *J. Chem. Eng.* **255** (2014) 541-552
- [2] S. Gallis, V. Nikas, H. Suhag, M. Huang and A. E. Kaloyeros, White light emission from amorphous silicon oxycarbide (a-SiC_xO_y) thin films: Role of composition and postdeposition annealing, *Appl. Phys. Lett.* **97** (2010) 081905 (3 pages).
- [3] J. X. Jiang, Y. H. Xu, W. Yang, R. Guan, Z. Q. Liu, H. Y. Zhen and Y. Cao, High-Efficiency White-Light-Emitting Devices from a Single Polymer by Mixing Singlet and Triplet Emission, *Adv. Mater.* **18** (2006) 1769-1773.
- [4] V. Nikas, S. Gallis, M. Huang, A. E. Kaloyeros, A. P. D. Nguyen, A. Stesmans and V. V. Afanas'ev, The origin of white luminescence from silicon oxycarbide thin films, *Appl. Phys. Lett.* **104** (2014) 061906 (4 pages).
- [5] C. Tsai, Color Rendering Index Thermal Stability Improvement of Glass-Based Phosphor-Converted White Light-Emitting Diodes for Solid-State Lighting, *Int. J. Photoenergy* **2014** (2014) 1-6.
- [6] C. Lorbeer and A. Mudring, White-Light-Emitting Single Phosphors via Triply Doped LaF₃ Nanoparticles, *J. Phys. Chem. C* **117** (2013) 12229-12238.
- [7] J. Lin and K. Baerner, Tunable photoluminescence in sol-gel derived silica xerogels, *Mater. Lett.* **46** (2000) 86-92.
- [8] M. A. García, S. E. Paje, M. A. Villegas and J. Llopis, Characteristic UV luminescence from sol-gel silica coatings, *Mater. Lett.* **43** (2000) 23-26.
- [9] P. K. Giri, S. Bhattacharyya, R. Kesavamoorthy, B. K. Panigrahi and K. G. M. Nair, Intense Ultraviolet-Blue Photoluminescence from SiO₂ Embedded Ge Nanocrystals Prepared by Different Techniques, *J. Nanosci. Nanotechnol.* **9** (2009) 5389-5395.

- [10] G. A. Kachurin, L. Rebohle, I. E. Tyschenko, V. A. Volodin, M. Voelskow, W. Skorupa and H. Froeb, Formation of Photoluminescence Centers During Annealing of SiO₂ Layers Implanted with Ge Ions, *J. Semicond.* **34** (2000) 21-26.
- [11] F. F. Komarov, L. A. Vlasukova, O. V. Milchanin, M. A. Makhavikou, I. N. Parkhomenko, E. Wendler, W. Wesch, A.V. Mudryi and G.A. Ismailova, Structural and luminescent properties of Sn doped SiO₂ layers, *J. Appl. Spectrosc.* **80** (2013) 855-860.
- [12] S. Duhan, N. Kishore, P. Aghamkar and S. Devi, Preparation and characterization of sol-gel derived silver-silica nanocomposite, *J. Alloys. Compd.* **507** (2010) 101-104.
- [13] E. Sumesh, M. S. Bootharaju, Anshup and T. Pradeep, A practical silver nanoparticle-based adsorbent for the removal of Hg²⁺ from water, *J. Hazard Mater.* **189** (2011) 450-457.
- [14] A. E. Abbass, H. C. Swart, R. E. Kroon, Effect of silver ions on the energy transfer from host defects to Tb ions in sol-gel silica glass, *J. Lumin.* **160** (2015) 22-26.
- [15] F. J García-Rodríguez, J. González-Hernández, F. Pérez-Robles, Y. V. Vorobiev, A. Manzano-Ramírez, S. Jiménez-Sandoval and B. S. Chao, Sol-Gel Films Containing Colloidal Copper Particles for Surface-enhanced Raman Scattering of Graphite SiO₂, *J. Raman Spectrosc.* **29** (1998) 763-771.
- [16] H. A. A. Seed Ahmed, O. M. Ntwaeaborwa and R. E. Kroon, High efficiency energy transfer in Ce,Tb co-doped silica prepared by sol-gel method, *J. Lumin.* **135**(2013)15-19.
- [17] M. G. Garnica-Romo, J. M. Yañez-Limón, M. Villicaña, J. F. Pérez-Robles, R. Zamorano-Ulloa and J. González-Hernandez, Structural evolution of sol-gel SiO₂ heated glasses containing silver particles, *J. Phys. Chem. Solids* **65** (2004) 1045-1052.
- [18] D. C. Altamirano-Juárez, C. Carrera-Figueiras, M. G. Garnica-Romo, M. L. Mendoza-López, M. B. Ortuño-López, M. E. Pérez-Ramos, A. Ramos-Mendoza, C. Rivera-Rodríguez, H. Tototzintle-Huitle, J. J. Valenzuela-Jáuregi, M. A. Vidales-Hurtado, M. A. Hernández-Landaverde and J. González-Hernández, Effects of metals on the structure of heat-treated sol-gel SiO₂ glasses, *J. Phys. Chem. Solids* **62** (2001) 1911-1917.

- [19] L. Skuja, Optically active oxygen-deficiency-related centers in amorphous silicon dioxide, *J. Non-Cryst. Solids* **239** (1998) 16-48.
- [20] I. Díez and R. H. A. Ras, Fluorescent silver nanoclusters, *Nanoscale* **3** (2011)1963-1970.
- [21] V. D. Dubrovin, A. I. Ignatiev, N. V. Nikonorov, A. I. Sidorov, T. A. Shakhverdov and D. S. Agafonova, Luminescence of silver molecular clusters in photo-thermo-refractive glasses, *Opt. Mater.* **36** (2014) 753-759.
- [22] G. Valotto, A. Quaranta, E. Cattaruzza, F. Gonella and G. Rampazzo, Multivariate analysis of Ion Beam Induced Luminescence spectra of irradiated silver ion-exchanged silicate glasses, *Spectrochim. Acta A: Mol. Biomol. Spectrosc.* **95** (2012) 533-539.
- [23] J. Li, Y. Yang, D. Zhou, Z. Yang, X. Xu and J. Qiu, Investigation of the role of silver species on spectroscopic features of Sm³⁺-activated sodium-aluminosilicate glasses via Ag⁺-Na⁺ ion exchange, *J. Appl. Phys.* **113** (2013) 193103 (5 pages).
- [24] S. Lai, Z. Yang, J. Li, B. Shao, J. Yang, Y. Wang, J. Qiu and Z. Song, Photoluminescence enhancement of Eu³⁺ ions by Ag species in SiO₂ three-dimensionally ordered macroporous materials, *J. Mater. Chem. C* **3** (2015)7699-7708.
- [25] A. Simo, J. Polte, N. Pfänder, U. Vainio, F. Emmerling and K. Rademann, Formation Mechanism of Silver Nanoparticles Stabilized in Glassy Matrices, *J. Am. Chem. Soc.* **134** (2012) 18824-18833.
- [26] J. García, M. A. Mondragón, C. Téllez, A. Camper and V. M. Castaño, Blue emission in tetraethoxysilane and silica gels, *Mater. Chem. Phys.* **41** (1995) 15-17.
- [27] J. Joo, S. Jang, K. Jung, C. Ko and M. Han, Strong Luminescence and Easy Color Control for SiO_x Thin Films by Using RF Magnetron Sputtering, *J. Korean. Phys. Soc.* **53** (2008) 1685-1689.
- [28] A. J. Miller, R.G. Leisure, V. A. Mashkov and F. L. Galeener, Dominant role of E' centers in X-ray-induced, visible luminescence in high-purity amorphous silicas, *Phys. Rev. B* **53** (1996)8818-8820.

[29] J. Rowland, G. Hong, W. Yoo, J. S. Yoo and P. H. Holloway, (2003) Abstract 1166 of *204th meeting of the electrochemical society* (12-16 October, Orlando FL) <https://www.electrochem.org/dl/ma/204/pdfs/1166.PDF>. Accessed 6 July 2015

Chapter 6

Effect of Ag nanoparticles on the luminescence of Tb doped sol-gel silica

6.1 Introduction

Nanomaterials are of importance for science and technology, due to their small size and large surface areas. Noble metal nanoparticles (NPs) are particularly interesting due to their plasmonic effects [1-2]. The study of the interaction of lanthanide ions with metal NPs has been paid much attention [3-9] because of their unique luminescent behaviours and potential applications. The interaction between Ag NPs and lanthanide ions, both dispersed in a host material, can result in enhanced luminescence from the lanthanide ions. This occurs when the excitation or emission wavelength of the lanthanide ions are close to the LSPR wavelength of the NPs [7]. Ag NPs is known to give more pronounced near-field effects than Au due to less pronounced resonance damping by interband electron transitions, as it is known to have a higher energy separation between localized surface plasmon resonance (LSPR) and interband absorption [10]. Ag NPs can be incorporated into silica using a sol-gel process [11], which is attractive due to its low cost, low temperature operation and environmental friendliness.

Among the lanthanides, the green luminescence of Tb^{3+} ions finds many uses for light emitting devices and display applications. However, Tb^{3+} ions have a small absorption cross-section due to parity forbidden $f-f$ transitions, which mean that they cannot be efficiently excited directly by long wavelength ultraviolet (UV) light longer than 300 nm. Researchers have used different approaches, particularly exciting the strong $f-d$ transitions of Tb^{3+} at shorter wavelengths or employing energy transfer (ET) from a sensitizer such as Ce^{3+} , to enhance the excitation efficiency of Tb^{3+} ions. In the present work, Ag NPs have been incorporated together with Tb^{3+} ions in silica, with the aim to

enhance the *f-f* absorption of Tb³⁺ ions due to the strong electric field associated with the LSPR of the metal NPs. The effect of the Ag NPs on the luminescent properties of the Tb³⁺ ions in amorphous silica is reported.

6.2 Experimental

All the chemicals were purchased from Sigma Aldrich and used without further purification. The reagents for the sol-gel process to make silica were tetraethoxysilane (TEOS) (99.0%), ethanol (99.7%) and water [12]. The molar ratio of the starting solution was taken as 1:5:10 for TEOS: ethanol: water. For all samples the TEOS was dissolved in the ethanol and stirred for 30 min. Dilute HNO₃ (0.15 M) was then added to the solution instead of the water, to catalyse the reaction, followed by stirring for a further 30 min. To dope the silica samples, Tb(NO₃)₃ (99.999%) and/or AgNO₃ (99.9%) were dissolved ultrasonically in a small amount of ethanol and added to the mixture, which was stirred for another 5 h. All solutions were then stored in closed containers in a water bath at 50 °C until a gel was formed. For drying, gels were placed in open containers in air for 22 h, ground to fine powder and transferred to a drying oven at 50 °C for a further 20 h. Each sample was divided into two parts, one annealed at 500 °C and the other annealed at 1000 °C for 2 h. Samples were analysed at room temperature. X-ray diffraction (XRD) patterns were recorded with a Bruker D8 diffractometer. Morphology and size of the Ag NPs were obtained from transmission electron microscope (TEM) images recorded with a Philips CM 100. Diffuse reflection spectra were obtained using a PerkinElmer Lambda 950 UV-vis spectrophotometer with spectralon as a standard, while phosphorescence emission and excitation spectra were measured using a Cary Eclipse fluorescence spectrophotometer.

6.3 Results and discussion

6.3.1 Structural and morphological characterization

Figure 6.1 shows the XRD patterns of several samples prepared during the study. The as-prepared samples (before annealing) showed only a broad amorphous diffraction band centred at $2\theta \sim 23^\circ$, even when doped with 5 mol% Ag (figure 6.1(a)).

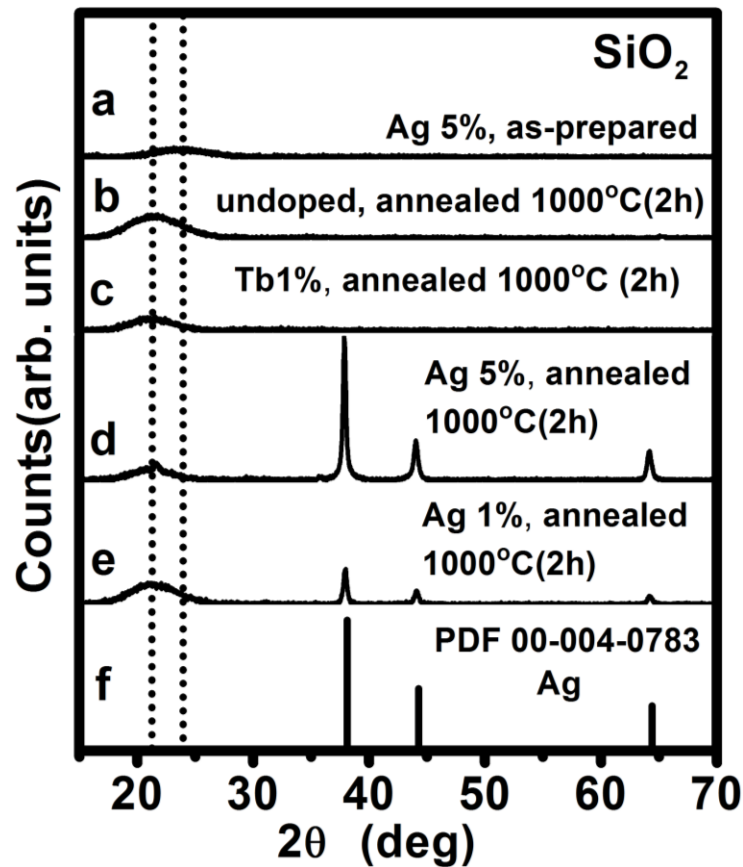


Figure 6.1: XRD patterns of (a) as-prepared silica with 5 mol% Ag, (b) pure silica annealed at 1000 °C (2 h), (c) silica with 1 mol% Tb^{3+} annealed at 1000 °C (2 h), (d) silica with 5 mol% Ag annealed at 1000 °C (2 h), (e) silica with 1 mol% Ag annealed at 1000 °C (2 h) and (f) PDF 00-004-0783 file for Ag.

In the undoped sample annealed at 1000 °C for 2 h (figure 6.1(b)) this peak shifted to $2\theta \sim 21^\circ$, corresponding to an increase in the structural order of the amorphous silica towards the cristobalite phase, which is one of the crystalline forms of silica [11]. The addition of 1 mol% Tb^{3+} did not produce any additional peaks in the XRD pattern, even after annealing (figure 6.1(c)), but when the sample containing 5 mol% Ag was annealed (figure 6.1(d)) peaks corresponding to crystalline Ag appeared, as confirmed by comparison with the Powder Diffraction File (PDF 00-004-0783, figure 6.1(e)). In addition, a small peak on the amorphous silica band near $2\theta \sim 21^\circ$ indicates that some of the amorphous silica converts to the crystalline phase due to the Ag doping. The average size of Ag NPs was calculated by Scherrer's equation $D = 0.9\lambda/(\beta \cos\theta)$ where β is the full width at half maximum of a diffraction peak in radians, θ is the corresponding Bragg angle and λ is the wavelength of the X-rays (154 pm). The average diameter of the NPs obtained using the different Ag diffraction peaks was in the range of 20-30 nm.

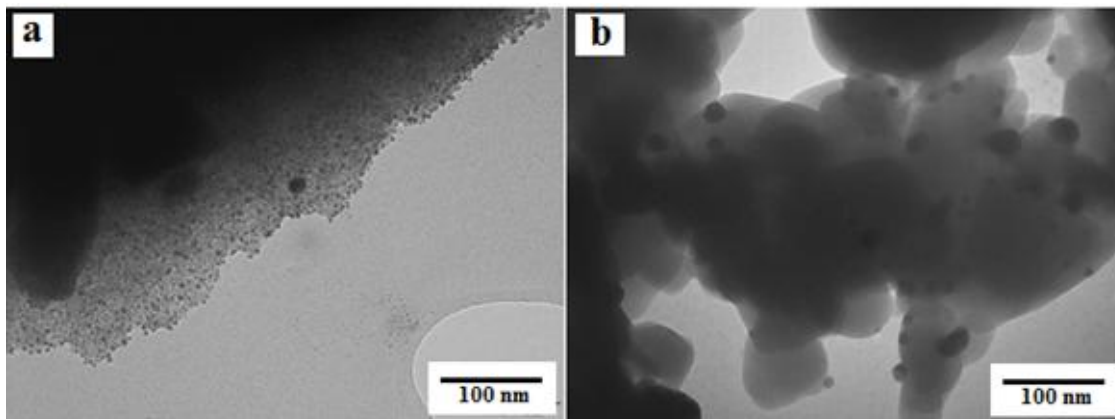


Figure 6.2: TEM results for two silica samples doped with 5 mol% Ag (a) annealed at 500 °C for 2 h, (b) annealed at 1000 °C for 2 h.

Figure 6.2 shows TEM images of silica doped with 5 mol% Ag annealed at (a) 500 °C and (b) 1000 °C for 2 h. The sample annealed at 500 °C shows a fine distribution of a large number of Ag NPs in the silica matrix, which appear spherical in shape and about

5-10 nm in diameter. In the sample annealed at 1000 °C the Ag NP density was much lower and the NPs were much larger in size (20-33 nm in diameter, in agreement with the mean size calculated by Scherrer's equation) and not perfectly spherical in shape. This is attributed to aggregation of the Ag NPs during the high temperature treatment. This means that the thermal treatment can affect the size and shape of the Ag NPs. The phenomenon of aggregation is controlled by the Gibbs-Thomson effect, where the chemical potential is inversely proportional to the particle size [13].

6.3.2 Optical characterization

Figure 6.3 shows diffuse reflectance spectra of three silica samples annealed at different temperatures for 2 h: (a) pure silica annealed at 1000 °C (b) 1 mol% Ag doped silica annealed at 500 °C and (c) 1 mol% Ag doped silica annealed at 1000 °C. The broad absorption peak in the doped sample annealed at 1000 °C near 405 nm corresponds to the LSPR peak of Ag NPs and confirms the formation of Ag NPs in the silica matrix, in agreement with the XRD and TEM measurements.

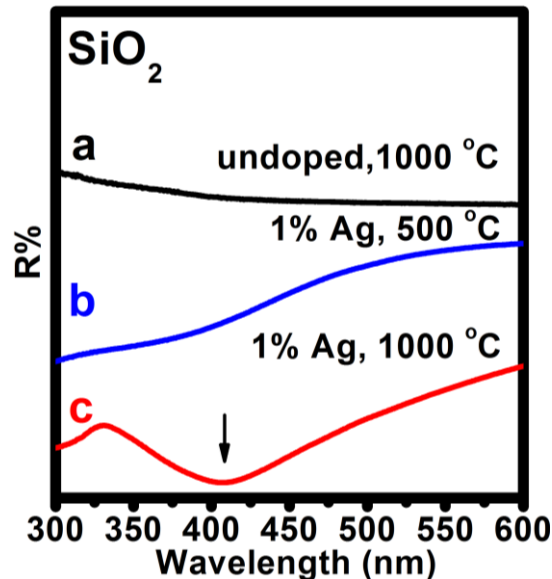


Figure 6.3: UV-vis diffuse reflectance spectra of (a) pure silica annealed at 1000 °C for 2 h, (b) silica doped with 1 mol% Ag, annealed at 500 °C for 2 h and (c) silica doped with 1 mol% Ag, annealed at 1000 °C for 2 h.

For silica samples doped only with Tb^{3+} , the green emission from the Tb^{3+} ions at 544 nm increased in intensity with the doping concentration up to 7 mol%, which was the highest concentration considered. However, due to the high cost of terbium nitrate it was decided to work with further samples doped with 5 mol% Tb^{3+} . Figure 6.4(a) shows the excitation spectra for the 544 nm emission of Tb^{3+} for sol-gel silica samples with 5 mol% Tb^{3+} in the presence of different amounts of Ag, where the samples have been annealed at 500 °C for 2 h. For the sample with no Ag added, we observed six peaks at 485, 377, 369, 351, 340, and 318 nm and assigned them to the electronic transitions of Tb^{3+} ions from the ground state $^7\text{F}_6$ to the $^5\text{D}_4$, $^5\text{D}_3$, $^5\text{L}_{10}$, $^5\text{D}_2$, $^5\text{G}_4$, and $^5\text{D}_1$ excited states, respectively. As the amount of Ag increased, the excitation peaks below 400 nm become less distinct, although the $^7\text{F}_6$ to $^5\text{D}_4$ transition near 485 nm is little affected. It is clear that the shorter wavelength f - f transitions are highly affected by the addition of Ag. Depending on the excitation wavelength, there can be considerable enhancement of the Tb^{3+} emission. The emission intensity of all samples at 544 nm excited by 325 nm as the function of Ag load is shown in figure 6.4(b). The intensity increases with increasing Ag load from 0 to 1 mol%, whereas further increasing of Ag concentration decreases the intensity. The inset shows the relation between Ag load and enhancement factor (the Tb^{3+} emission intensity relative to the sample without Ag) and it can be seen that the maximum enhancement factor is 8.8. This enhancement factor is particularly high because the wavelength of 325 nm does not correspond to one of the Tb^{3+} f - f transition wavelengths. However, even for those wavelengths some enhancement does occur, e.g. for the $^7\text{F}_6$ to $^5\text{D}_3$ transition near 377 nm the peak height is increased by the addition of some Ag and the maximum occurs for Ag load of 0.3 mol%. For simple plasmonic enhancement of the Tb^{3+} f - f levels, it was expected that the excitation bands would retain their positions and that the peaks closest to the LSPR of the Ag NPs would increase in height. Clearly the experimental results are different to this, with the f - f excitation bands becoming less distinct. Stark splitting of the energy levels could be the reason for this, but is not considered to be the case since the $4f$ levels are well shielded and stark splitting would also result in a broadening of the emission bands, which is not observed. So although we have achieved some enhancement

of the green Tb^{3+} emission by the addition of Ag, the mechanism does not appear to be simple plasmonic enhancement, but is unclear and requires further study. One possibility is the interaction of Tb^{3+} ions with Ag^+ ions, instead of Ag NPs, and ET from the Ag^+ ions instead of a plasmonic enhancement [14].

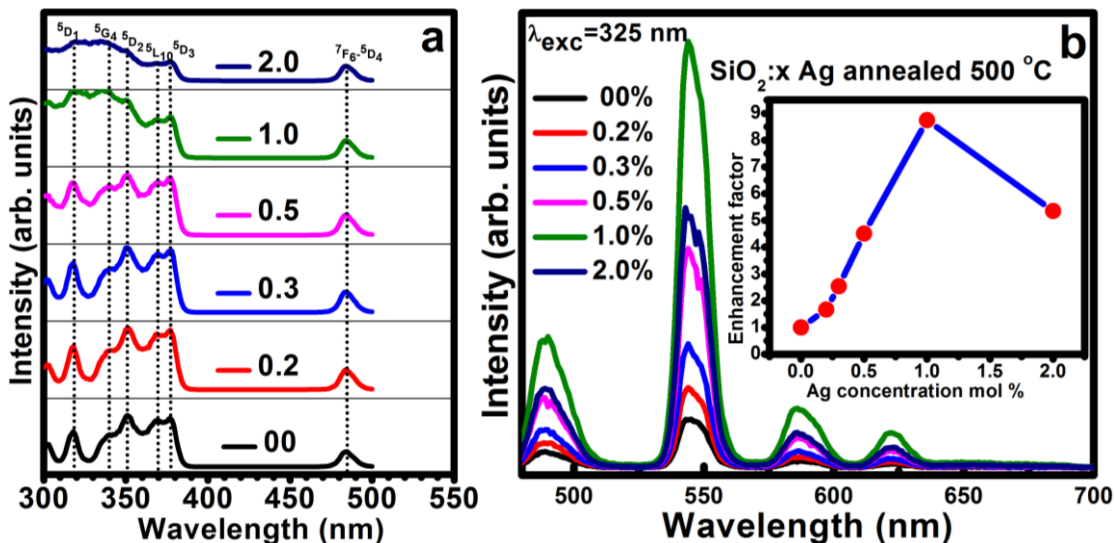


Figure 6.4: Luminescence spectra of silica samples doped with 5 mol% Tb^{3+} and various concentrations of Ag (a) excitation ($\lambda_{\text{em}} = 544 \text{ nm}$) (b) emission ($\lambda_{\text{exc}} = 325 \text{ nm}$), after annealing at 500 °C for 2 h.

The photoluminescence data of the sample annealed at 1000 °C did not show any enhancement and is discussed further in the next chapter.

6.4 Conclusion

Tb^{3+} and Ag co-doped silica samples have been successfully synthesized using the sol-gel method. XRD, TEM and UV-vis diffuse reflectance results confirmed the formation of Ag NPs in the silica matrix. The results showed that the annealing temperature can be used as mechanism to control the shape and size of the Ag NPs in amorphous silica. For an excitation wavelength of 325 nm, the highest intensity of the green emission of Tb^{3+}

ions at 544 nm is obtained when the doping concentration of Ag was 1 mol%. The change in the Tb^{3+} $f-f$ excitation spectrum is not merely an increase in the $f-f$ excitation peaks closest to the LSPR wavelength of the Ag NPs, as expected for simple plasmonic enhancement, but instead the peaks merge into a broad excitation band. This may be evidence that ET from Ag^+ ions also plays a role in the luminescence enhancement.

6.5 References

- [1] K. A. Willets and R. P. Van Duyne, Localized Surface Plasmon Resonance Spectroscopy and Sensing, *Annu. Rev. Phys. Chem.* **58** (2007) 267-297.
- [2] S. Hayashi and T. Okamoto, Plasmonics: visit the past to know the future, *J. Phys. D: Appl. Phys.* **45** (2012) 433001 (24 pages).
- [3] O. L. Malta, P. A. Santa-Cruz, G. F. Desa and F. Auzel, Fluorescence enhancement induced by the presence of small silver particles in Eu^{3+} doped materials, *J. Lumin.* **33** (19985) 261-272.
- [4] O. L. Malta and M. A. Couto dos Santos, Theoretical analysis of the fluorescence yield of rare earth ions in glasses containing small metallic particles, *Chem. Phys. Lett.* **174** (1990) 13-18.
- [5] B. Lipowska and A. M. Kłonkowski, Energy transfer and surface plasmon resonance in luminescent materials based on Tb(III) and Ag or Au nanoparticles in silica xerogels, *J. Non-Cryst. Solids* **354** (2008) 4383-4387.
- [6] P. Piasecki, A. Piasecki, Z. Pan, R. Mu and S. H. Morgan, Formation of Ag nanoparticles and enhancement of Tb^{3+} luminescence in Tb and Ag codoped lithium-lanthanum aluminosilicate glass, *J. Nanophotonics* **4** (2010) 043522 (9 pages).
- [7] Z. Pan, A. Ueda, R. Aga, A. Burger, R. Mu and S. H Morgan, Spectroscopic studies of Er^{3+} doped Ge-Ga-S glass containing silver nanoparticles, *J. Non-Cryst. Solids* **356** (2010) 1097-1101.
- [8] R. K. Verma, K. Kumar and S. B. Rai, Pulsed laser ablation synthesis of silver nanoparticles and their use in fluorescence enhancement of Tb^{3+} C-doped aluminosilicate glass, *Solid State Commun.* **150** (2010) 1947-1950.

- [9] D. Zhang, X. Hu, R. Ji, S. Zhan, J. Gao, Z. Yan, E. Liu, J. Fan and X. Hou, Influence of Ag nanoparticles on luminescent performance of $\text{SiO}_2:\text{Tb}^{3+}$ nanomaterials, *J. Non-Cryst. Solids* **358** (2012) 2788-2792.
- [10] K. Drozdowicz-Tomsia and E. M. Goldys, Gold and silver nanowires for fluorescence enhancement, In: Nanowires - Fundamental Research edited by ed A. Hashim, *InTech* (2011) 309-332.
- [11] S. Duhan, N. Kishore, P. Aghamkar and S.Devi, Preparation and characterization of sol-gel derived silver-silica nanocomposite, *J. Alloys Compd.* **507** (2010) 101-104.
- [12] H. A. A. Seed Ahmed, O. M. Ntwaeaborwa, R. E. Kroon, High efficiency energy transfer in Ce,Tb co-doped silica prepared by sol-gel method, *J. Lumin.* **135** (2013)15-19.
- [13] G. De Marchi, Mattei, P. Mazzoldi, C. Sada and A. Miotello, Two stages in the kinetics of gold cluster growth in ion-implanted silica during isothermal annealing in oxidizing atmosphere, *J. Appl. Phys.* **92** (2002) 4249-4254.
- [14] M. Eichelbaum and K. Rademann, Plasmonic Enhancement or Energy Transfer? On the Luminescence of Gold-, Silver-, and Lanthanide-Doped Silicate Glasses and Its Potential for Light-Emitting Devices, *Adv. Funct. Mater.* **19** (2009) 2045-2052.

Chapter 7

Effect of silver ions on the energy transfer from host defects to Tb ions in sol-gel silica glass

7.1 Introduction

Glasses doped with RE ions have become increasingly important during the past fifty years due to their unique luminescence properties and wide applications [1, 2]. RE ions can exhibit three types of excitation transitions, namely $4f-4f$ transitions, $4f-5d$ transitions and charge-transfer transitions. Although $4f-4f$ transitions are very important, for example in lighting applications, they are theoretically forbidden by the parity rule which leads to low absorption cross-sections [1, 3]. Researchers have used alternative approaches, particularly exciting the strong (parity allowed) $4f-5d$ transitions of RE ions at shorter wavelengths or employing energy transfer (ET) from a sensitizer to enhance the excitation efficiency [4].

More recently noble metals nanoparticles (NPs) have been used in order to improve the absorption cross-section of RE ions [5-7]. Noble metal NPs may be effective due to localized surface plasmon resonance (LSPR) effects. While a plasmon refers to a quantum of the collective oscillation of free electrons in a bulk metal, surface plasmons correspond to charge oscillations at the extended interface of a metal (e.g. with a dielectric) and localized surface plasmons are associated with charge oscillations in small metallic NPs. These oscillations have particular natural frequencies which can lead to resonance effects when they are excited by electromagnetic radiation. This phenomenon occurs in Ag and Au NPs in the 10-200 nm size range and can result in amplification of the electric field near the NP surfaces more than thousand times greater than the incident field [8]. Due to these properties, NPs exhibiting LSPR have become more attractive in different research fields such as physics, chemistry, medicine and biology [9, 10].

For phosphors the first report of the use of noble metal NPs as a means for improving the luminescence properties of RE ions was that of Malta *et al.* [3] who found enhanced fluorescence for Eu^{3+} ions doped in glass containing Ag NPs and attributed this to LSPR effects. Further research has been done regarding the effect of Ag NPs on the luminescence of RE ions in glass and the general conclusion of these studies is that the enhancement may be due to two effects: plasmonic enhancement due to the Ag NPs or ET from Ag ions inadvertently also incorporated in the host. The differentiation between these different luminescence enhancement mechanisms has remained a challenge [11]. In this paper we have investigated the effects of the addition of Ag on the optical properties of Tb ions in silica. Our results suggest an additional complexity in understanding the enhancement, namely that Ag ions can affect the defects in the silica host and therefore the luminescence which results from ET from these host defects to Tb ions.

7.2 Experimental

Pure silica and silica doped with Tb and/or Ag were prepared by the sol-gel technique [4]. The starting materials were TEOS (99.7%), ethanol (99.0%) and distilled water. The molar ratio was taken as 1:5:10 for TEOS:ethanol:water [4]. Silver nitrate (AgNO_3 , 99.9%) and terbium nitrate ($\text{Tb}(\text{NO}_3)_3$, 99.999%) were used as the source of dopants. For all samples TEOS was first dissolved in ethanol by magnetic stirring for 30 min. To catalyze the hydrolysis/condensation reaction, dilute HNO_3 (0.15 M) instead of water was added to solution and stirring continued for another 30 min. To dope the silica, AgNO_3 and/or $\text{Tb}(\text{NO}_3)_3$ was firstly dissolved in small amount of dilute HNO_3 taken from the total amount. This solution was added to the mixture and stirred for further 5 h. The gel was produced in about 20 h by storing the solutions in closed containers placed in a water bath at 50 °C. The gel was then dried in an open container in air for 24 h and ground to a fine powder. This powder was further dried in an oven at 50 °C for a further 20 h and finally annealed at different temperatures in air for 2 h.

Samples were analyzed at room temperature. X-ray diffraction (XRD) patterns were recorded with a Bruker D8 diffractometer using $\text{Cu K}\alpha$ X-rays. Morphology and size of

the Ag NPs were obtained from transmission electron microscope (TEM) images recorded with a Philips CM 100 instrument. X-ray photoelectron spectroscopy (XPS) measurements were made using a PHI 5000 Versaprobe utilizing Al X-rays. Absorption and diffuse reflectance spectra were measured using a Perkin Elmer Lambda 950 UV-vis spectrophotometer, while luminescence properties were measured using a Cary Eclipse fluorescence spectrophotometer (using a monochromatized xenon lamp as its tuneable excitation source) and also with a 325 nm He-Cd laser photoluminescence system.

7.3 Results and discussion

Figure 7.1 shows the XRD patterns of silica doped with 2 mol% Ag annealed in air at different temperatures for 2 h. There is a broad peak centred at $2\theta \approx 23^\circ$ for the sample annealed at 500 °C, indicating the amorphous (glass) structure of the silica. The crystalline (metallic) phase of Ag did not form in the samples annealed at 500 °C and 700 °C, but increasing the annealing temperature to 800 °C and higher converts Ag ions to Ag NPs which are indicated by the appearance of peaks related to metallic Ag (PDF 04-0783). The average crystallite size of the Ag NPs was calculated with Scherrer's equation $D = 0.9\lambda/(\beta \cos \theta)$ where β is the full-width-at-half-maximum of a diffraction peak in radians, θ is the corresponding Bragg angle and λ is the wavelength of the X-rays. Using the (111) diffraction peaks this was found to be 18 nm, 21 nm, 23 nm and 30 nm after annealing at 800 °C, 900 °C, 1000 °C and 1200 °C respectively.

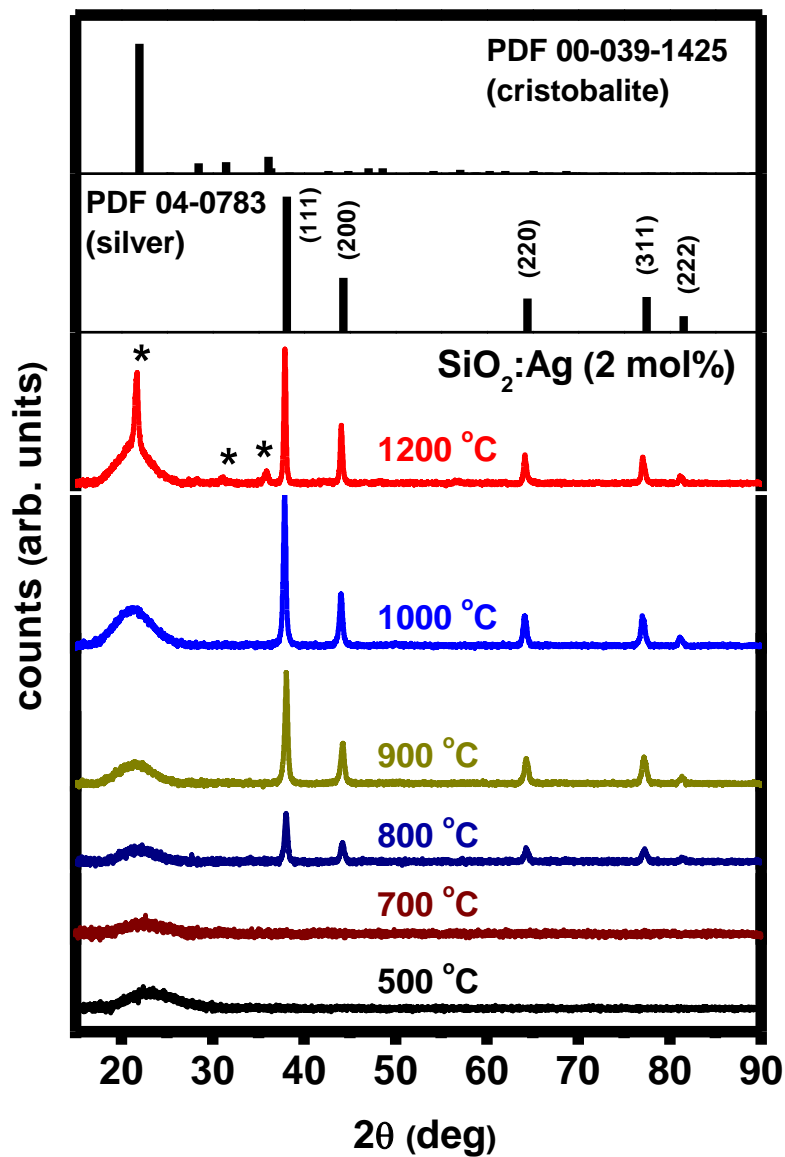


Figure 7.1: XRD patterns of silica doped with 2 mol% Ag annealed at different temperatures for 2 h. Peaks marked with an asterisk (*) correspond to the cristobalite phase of silica.

The broad peak related to amorphous silica shifted to slightly lower angles with increasing annealing temperature and for the sample annealed at 1200 °C it has a sharp peak at 21.7° superimposed on it. This and some additional small peaks marked with asterisks (*) correspond to the cristobalite phase of silica (PDF 00-039-1425).

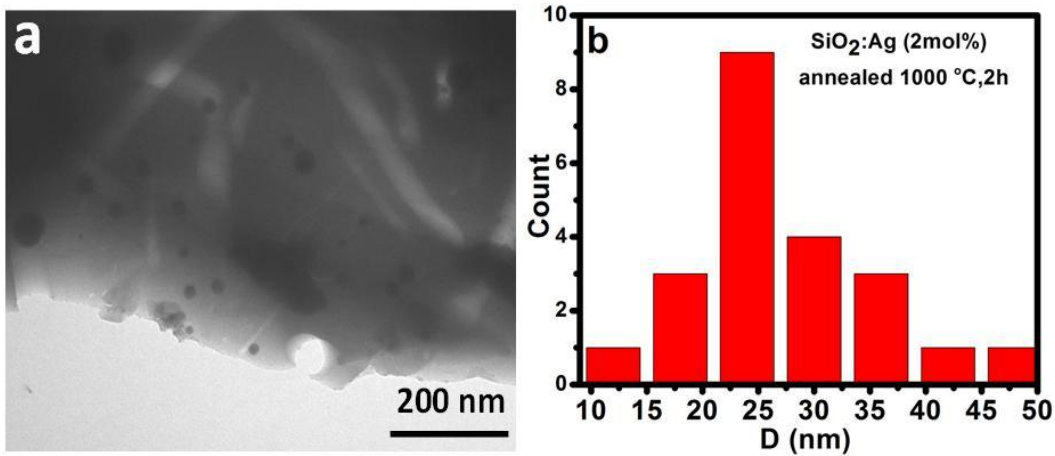


Figure 7.2: (a) TEM image and (b) size distribution of Ag NPs for silica doped with 2 mol% Ag annealed at 1000 °C for 2 h.

Figure 7.2(a) shows a TEM image of a silica sample doped with 2 mol% Ag annealed at 1000 °C for 2 h. Embedded in the silica are Ag NPs, most of which are roughly spherical in shape. This confirms the formation of Ag NPs inside the silica network in agreement with the XRD data. Figure 7.2(b) shows the Ag NP diameter distribution of 25 ± 5 nm, in agreement with the average crystallite size of Ag NPs calculated by Scherrer's equation.

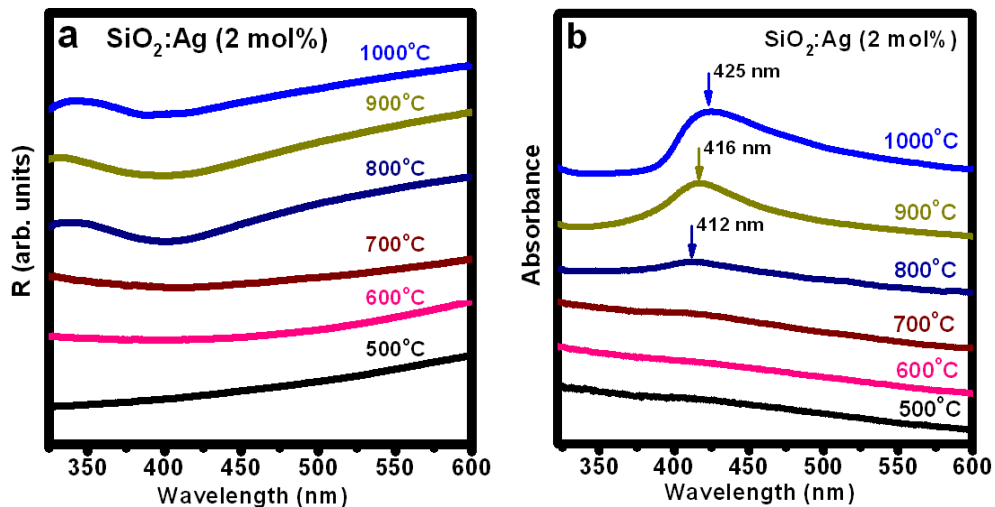


Figure 7.3: UV-vis spectra of silica samples doped with 2 mol% Ag annealed at different temperatures for 2 h: (a) diffuse reflectance of powder and (b) absorbance of powder suspended in ethanol.

Figure 7.3(a) shows diffuse reflectance spectra from the powder samples of silica doped with 2 mol% Ag annealed in air at different temperatures for 2 h. The samples annealed below 700 °C show no obvious absorption band from the LSPR of Ag NPs, indicating that the Ag ions are not reduced to metallic NPs in the silica glass, which is in agreement with the XRD results. Higher annealing temperatures produced a broad peak corresponding to LSPR absorption, with no obvious shift in position as a function of annealing temperature. Figure 7.3(b) shows absorption spectra of the same samples suspended in ethanol. Measured in this manner, the absorption band is narrower and shows a clear shift to longer wavelengths with increasing annealing temperature, being centred at 412 nm, 416 nm and 425 nm for samples annealed at 800 °C, 900 °C and 1000 °C respectively. The shift of the absorption band with increasing annealing temperature can be attributed to the changing average size of the Ag NPs, since the LSPR wavelength is known to increase with increasing NP size [12].

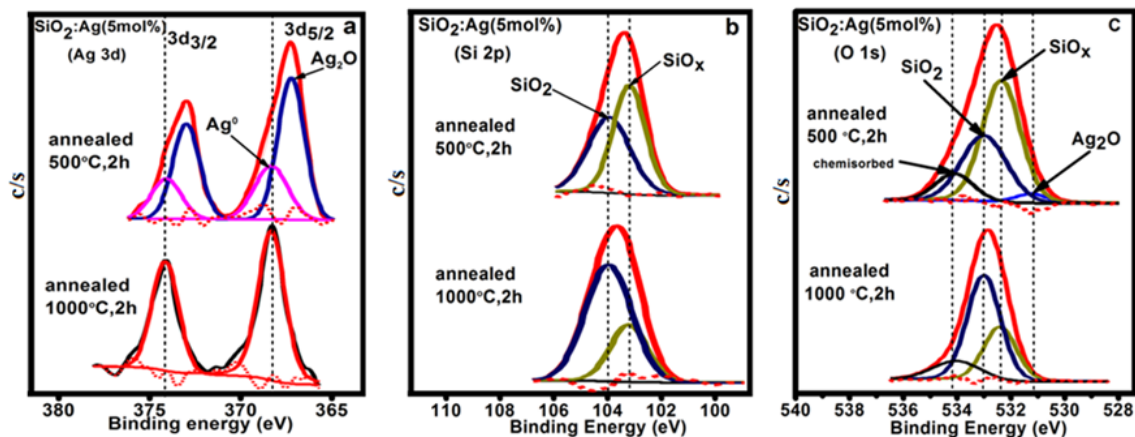


Figure 7.4: High resolution XPS spectra for (a) Ag 3d (b) Si 2p and (c) O 1s binding energy regions of silica samples doped with 5 mol% Ag annealed at 500 °C and 1000 °C for 2 h.

Figure 7.4(a) shows high resolution XPS spectra for the Ag 3d binding energy region for samples annealed for 2 h at 500 °C (above) and 1000 °C (below). A concentration of 5 mol% Ag as was used because XPS requires concentrations of few percent for easy

detection. For the sample annealed at 500 °C the spectrum can be fitted in terms of two different chemical species, namely metallic silver (Ag^0) and silver ions in Ag_2O (Ag^+) with Ag $3d_{5/2}$ binding energies at 368.2 and 367.7 eV respectively, in good agreement with literature values [13]. The Ag $3d_{3/2}$ peaks occur at higher binding energies due to a spin-orbit splitting of 6 eV with an intensity ratio of 2:3 compared to the Ag $3d_{5/2}$ peaks. The Ag XPS peaks for the sample annealed at 1000 °C are shifted towards higher binding energy values. These peaks can be fitted using only a contribution from metallic Ag and not from the Ag ions, suggesting that almost all of the Ag ions have moved out of the silica host to form metallic Ag NPs. Although the XRD and UV-vis absorption results indicated that no Ag NPs had formed after annealing at 500 °C, the XPS shows a significant peak corresponding to metallic Ag for this sample. Unlike XRD and UV-vis absorption which analyse the bulk material, XPS is surface sensitive and it is therefore possible that some Ag NPs are formed at low annealing temperature (500 °C) on the surface. Annealing the sample at the high annealing temperature (1000 °C) produces material where the surface has Ag only in the metallic state and there are no Ag ions. The reduction of Ag ions to Ag NPs therefore takes place during the decomposition of Ag oxide (Ag_2O). Figure 7.4(b) shows the high resolution XPS spectra for the Si $2p$ binding energy region. For both annealing temperatures the Si $2p$ peak was fitted with two peaks, attributed to Si in SiO_x and SiO_2 with binding energies of 103.3 and 104.0 eV respectively [14, 15]. For the sample annealed at the lower temperature SiO_x is dominant, whereas the SiO_2 contribution is larger for the sample annealed at 1000 °C. This corresponds with an increase of the O/Si ratio with an increase of annealing temperature. The XPS data therefore shows that as the annealing temperature increases, Ag ions are reduced to metallic Ag while the released oxygen bond to Si and therefore increases the O/Si ratio, increasing the amount of SiO_2 in the material compared to SiO_x . Figure 7.4(c) shows the high resolution XPS spectra for the O $1s$ binding energy region, with the separation between the O $1s$ and Si $2p$ binding energies in SiO_2 taken as 429 eV [16]. This data is consistent with the interpretation of the other XPS peaks, indicating that Ag^+ ions are present in the sample annealed at 500 °C but do not occur after annealing at 1000

°C and that the relative amount of SiO_x compared to SiO_2 is higher for the sample annealed at 500 °C than at 1000 °C.

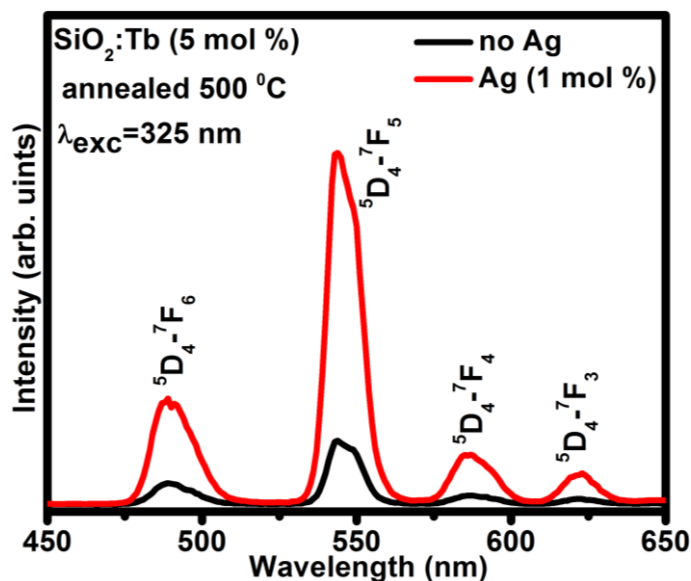


Figure 7.5: Emission spectra for Tb^{3+} ions excited at 325 nm in silica doped with 5 mol% Tb only, or with 5 mol% Tb and 1 mol% Ag, after annealing at 500 °C for 2 h.

To investigate the influence of the addition of Ag on the Tb emission in sol-gel silica, 5 mol% Tb doped silica samples were prepared with and without the addition of 1 mol% Ag. These samples emitted the well-known green luminescence of Tb^{3+} ions (figure 7.5) with the maximum corresponding to the ${}^5\text{D}_{4-7}\text{F}_5$ transition at 544 nm. The XRD and XPS results of the co-doped samples were not significantly different to those shown for the samples only doped for Ag already discussed. Figure 7.6 shows the excitation spectra for the Tb^{3+} ions in the singly Tb doped samples compared to those also co-doped with Ag after annealing at (a) 500 °C and (b) 1000 °C for 2 h. For the sample annealed at 500 °C, with the addition of Ag there is a significant enhancement of the excitation band centred around 325 nm compared to the sample only containing Tb. For the sample annealed at 1000 °C and only containing Tb, the excitation peaks are stronger than for the samples annealed at 500 °C, which could be due to the better elimination of quenching centres

such as hydroxyl groups at the higher temperature. Of particular interest is the fact that at this higher annealing temperature there is no enhancement of the Tb excitation spectrum when Ag is added.

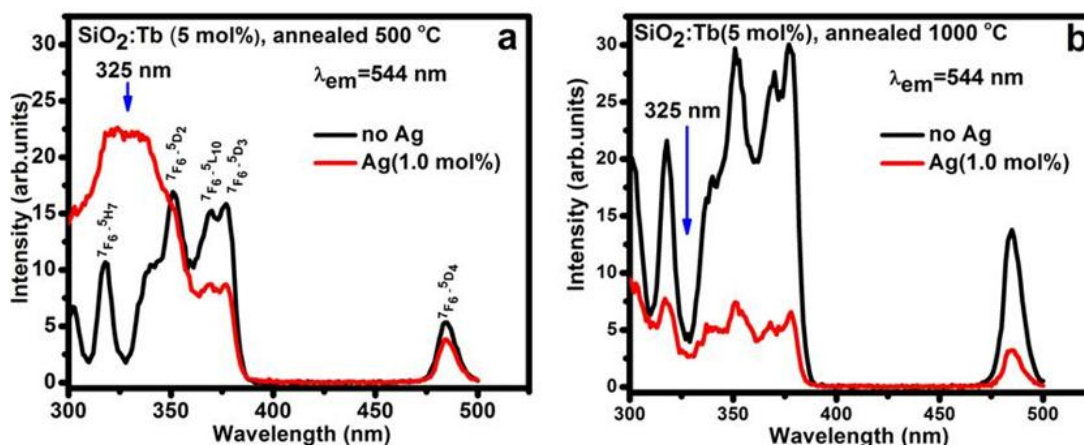


Figure 7.6: Excitation spectra for Tb³⁺ ions emitting at 544 nm in silica doped with 5 mol% Tb only, or with 5 mol% Tb and 1 mol% Ag, after annealing at (a) 500 °C and (b) 1000 °C for 2 h, measured with the Cary Eclipse fluorescence spectrophotometer.

Several possible explanations for the enhancement for the Tb excitation spectrum after the addition of Ag for annealing at 500 °C have been considered. Even if the addition of Ag caused a change in the local environment of the Tb³⁺ ions, the f-levels of Tb are shielded and insensitive to the host and therefore should not produce such a change. Additionally the emission spectrum of the Tb³⁺ ions would then be affected, but had the same form with or without the addition of Ag (see [figure 7.5](#)). A second possibility is that it could be due to plasmonic enhancement, but since the XRD and absorption measurements show that Ag NPs do not form after annealing at 500 °C, this is unlikely. Furthermore the position of the LSPR absorption peak for small Ag NPs in silica near 420 nm ([figure 7.3\(b\)](#)) does not match the wavelength where enhancement of the Tb³⁺ excitation spectrum occurs (about 325 nm, [figure 7.6\(a\)](#)). Thirdly, ET effects are considered. ET from Ag NPs to RE ions in general is not expected due to very short

lifetime of the plasmons [3], and is not possible here since the Ag NPs only form at higher annealing temperatures than 500 °C. ET from Ag ions to RE ions has been suggested in the past to be responsible for enhancement of the RE ion fluorescence. Ag ions incorporated in silica glass have a reported excitation range of 200-250 nm [1, 17, 18] which does not match the enhanced excitation around 325 nm observed in figure 7.6(a). Also our measurements did not show any luminescence related to Ag ions when excited at 325 nm, meaning that ET from Ag ions to Tb ions is not responsible for the enhancement. The final possibility considered was ET from host defects of the silica to the Tb ions in the presence of Ag ions.

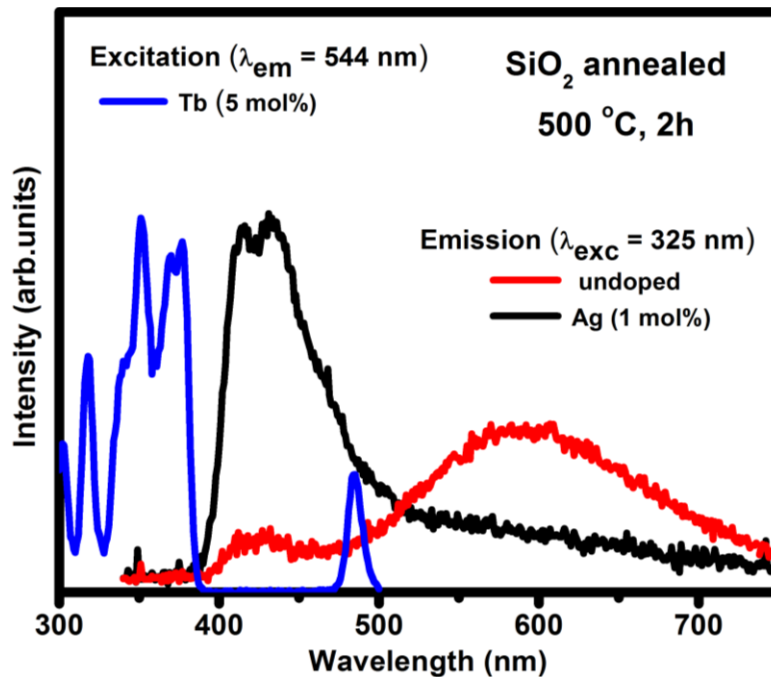


Figure 7.7: Overlap between the excitation spectrum of Tb^{3+} ions and the host defect emission spectrum of an undoped silica, as well as silica doped with 1 mol% Ag, both excited at 325 nm.

Figure 7.7 shows the luminescence of undoped and Ag doped silica annealed at 500 °C when excited by a He-Cd laser at 325 nm. For the undoped sample the origin of the broad

band centred at 590 nm is attributed to carbon impurities [19, 20] which may come from the organic precursors, while the smaller peak at 420 nm is attributed to oxygen deficiency centres (ODCs) which are well-known defects in silica [21]. For a sample doped with Ag, the luminescence peak at 420 nm associated with ODCs is greatly increased, while the peak at 590 nm associated with C impurities is decreased. The addition of Ag in the silica produces mainly Ag ions which compete with the silicon for the available oxygen atoms, creating a large number of ODCs in the silica network (in a similar way that the addition of Na affects the silica network as described by Kahnt [22]). We consider the possibility that these ODC defects transfer energy to Tb ions. The excitation spectrum of Tb from figure 7.6(a) is redrawn on figure 7.7 and shows that the ODC defect emission peak around 420 nm, with its shoulder at longer wavelengths, overlaps the 7F_6 - 5D_4 excitation transition of Tb^{3+} at 490 nm. This suggests that ET from the ODC defects to the Tb^{3+} ions is indeed possible, which could then account for the enhancement of the Tb excitation spectra of figure 7.6(a) near 325 nm.

For higher annealing temperatures the Ag ions coalesce to form metallic Ag NPs and in the process oxygen is released from the Ag_2O , so the O/Si ratio is increased with a corresponding decrease in the ODCs. This decrease in the ODC defect concentration after annealing at high temperature (1000 °C) therefore means that the Tb ions cannot be excited strongly through ET from these defects and the Tb excitation spectrum does not show enhancement near 325 nm in figure 7.6(b) as it did in the case of the sample annealed at 500 °C (figure 7.6(a)). The luminescence of the Tb ions is therefore affected indirectly by the addition of Ag through the influence this has on the host defect concentration in the silica. In a similar way, Zhang *et al.* [23] have suggested that the luminescence from Yb in SiO_2 thin films was enhanced by ET from non-bridging oxygen hole defects influenced by the addition of Al in the SiO_2 network.

The enhancement of RE ion emission by the addition of noble metals to phosphor materials is an interesting possibility which has received some study in the past but which has not yet produced systematic results and requires further study. Although the main idea is that the fluorescence may be enhanced by plasmonic effects due to noble metal

NPs, in the case where Ag is added the cause of the enhancement has been debated and suggested to be due to ET from Ag ions to the RE ions. This work has shown that the addition of Ag in silica can also affect the host defect concentrations and therefore the ET from these host defects to Tb ions, adding to the complexity in the interpretation of the enhancement affects when noble metals are added to phosphor materials.

7.4 Conclusion

Tb and Ag co-doped silica samples have been synthesized using the sol-gel method. For annealing below 700 °C the Ag was incorporated as ions, while XRD, TEM, UV-vis and XPS results confirmed the formation of metallic Ag NPs at higher temperatures following decomposition of the Ag₂O. The results showed that the Ag ions influence host defects in the silica which, through ET, can enhance the luminescence of Tb ions for an excitation wavelength around 325 nm.

7.5 References

- [1] J. Li, R. Wei, X. Liu and H. Guo, Enhanced luminescence via energy transfer from Ag⁺ to RE ions (Dy³⁺, Sm³⁺, Tb³⁺) in glasses, *Opt. Express* **20** (2012) 1-6.
- [2] L. Li, Y. Yang, D. Zhou, Z. Yang, X. Xu and J. Qiu, Investigation of the interaction between different types of Ag species and europium ions in Ag⁺-Na⁺ ion-exchange glass, *Opt. Express* **3** (2013) 806-812.
- [3] O. L. Malta, P. A. Santa-Cruz, G. F. Desa and F. Auzel, Fluorescence enhancement induced by the presence of small silver particles in Eu³⁺ doped materials, *J. Lumin.* **33** (1985) 261-272.
- [4] H. A. A. Seed Ahmed, O. M. Ntwaeaborwa and R. E. Kroon, High efficiency energy transfer in Ce,Tb co-doped silica prepared by sol-gel method, *J. Lumin.* **135** (2013) 15-19.
- [5] S. M. Lee and K. C. Choi, Enhanced emission from BaMgAl₁₀O₁₇:Eu²⁺ by localized surface plasmon resonance of silver particles, *Opt. Express* **18** (2010) 12144-12152.

- [6] H. Guo, X. Wang, J. Chen and F. Li, Ultraviolet light induced white light emission in Ag and Eu³⁺ co-doped oxyfluoride glasses, *Opt. Express* **18** (2010) 18900-18905.
- [7] P. Piasecki, A. Piasecki, Z. Pan, R. Mu and S. H. Morgan, Formation of Ag nanoparticles and enhancement of Tb³⁺ luminescence in Tb and Ag co-doped lithium-lanthanum-aluminosilicate glass, *J. Nanophotonics* **4** (2010) 043522.
- [8] A. J. Haes, C. L. Haynes, A. D. McFarland, G. C. Schatz, R. P. Van Duyne and S. Zou, Plasmonic materials for surface-enhanced sensing and spectroscopy, *MRS Bull.* **30** (2005) 368-375.
- [9] K. Y. Yang, K. C. Choi and C. W. Ahn, Surface plasmon-enhanced energy transfer in an organic light-emitting device structure, *Opt. Express* **17** (2009) 11495-11504.
- [10] N. G. Khlebtsov and L. Dykman, Optical properties and biomedical applications of plasmonic nanoparticles, *J. Quant. Spectrosc. Radiat. Transfer* **111** (2010) 1-35.
- [11] M. Eichelbaum and K. Rademann, Plasmonic enhancement or energy transfer? On the luminescence of gold, silver, and lanthanide-doped silicate glasses and its potential for light-emitting devices, *Adv. Funct. Mater.* **19** (2009) 2045-2052.
- [12] M. Eichelbaum, K. Rademann, R. Müller, M. Radtke, H. Riesemeier and W. Güner. On the chemistry of gold in silicate glasses: studies on a nonthermally activated growth of gold nanoparticles, *Angew. Chem. Int. Ed.* **44** (2005) 7905-7909.
- [13] E. Sumesh, M. S. Bootharaju, Anshup and T. Pradeep, A practical silver nanoparticle-based adsorbent for the removal of Hg²⁺ from water, *J. Hazard. Mater.* **189** (2011) 450-457.
- [14] W. A. M. Aarnink, A. Weishaupt and A. van Silfhout, Angle-resolved X-ray photoelectron spectroscopy (ARXPS) and a modified Levenberg-Marquardt fit procedure: a new combination for modeling thin layers, *Appl. Surf. Sci.* **45** (1990) 37-48.
- [15] F. G. Bell and L. Ley, Photoemission study of SiO_x (0 ≤ x ≤ 2) alloys, *Phys. Rev. B: Condens. Matter.* **37** (1988) 8383-8393.
- [16] T. Schroeder, M. Adelt, B. Richter, M. Naschitzki, M. Bäumer and H.-J. Freund, Growth of well-ordered silicon dioxide films on Mo (1 1 2), *Microelectron. Reliab.* **40** (2000) 841-844.

- [17] M. A. Villegas, Optical spectroscopy of hybrid sol-gel coatings doped with noble metals, *J. Sol-Gel Sci. Technol.* **11** (1998) 251-265.
- [18] G. E. Malashkevich, A. V. Semchenko, A. A. Sukhodola, A. P. Stupak, A. V. Sukhodolov, B. V. Plyushch, V. V. Sidskioe and G. A. Denisenko, Influence of silver on the Sm^{3+} luminescence in “aerosil” silica glasses, *Phys. Solid State* **50** (2008) 1464-1472.
- [19] V. Nikas, S. Gallis, M. Huang, A. E. Kaloyeros, A. P. D. Nguyen, A. Stesmans and V. V. Afanas'ev, The origin of white luminescence from silicon oxycarbide thin films, *Appl. Phys. Lett.* **104** (2014) 1-4.
- [20] S. Gallis, V. Nikas, H. Suhag, M. Huang and A. E. Kaloyeros, White light emission from amorphous silicon oxycarbide ($\text{a-SiC}_x\text{O}_y$) thin films: Role of composition and postdeposition annealing, *Appl. Phys. Lett.* **97** (2010) 1-3.
- [21] J. Lin and K. Baerner, Tunable photoluminescence in sol-gel derived silica xerogels, *Mater. Lett.* **46** (2000) 86-92.
- [22] H. Kahnt, Ionic transport in glasses, *J. Non-Cryst. Solids* **203** (1996) 225-231.
- [23] J. Zhang, X. Wang, B. Cheng, J. Yu and Q. Wang, Near infrared photoluminescence from Yb, Al co-implanted SiO_2 films on silicon, *Chin. Phys. Lett.* **23** (2006) 2183-2186.

Chapter 8

Non-plasmonic enhancement of the near band edge luminescence from ZnO using Ag nanoparticles

8.1 Introduction

ZnO has attracted considerable attention as a low cost, environmentally friendly photonic material because of its direct band gap (3.37 eV at room temperature) and large exciton binding energy (60 meV) [1-4]. It generally has two photoluminescence (PL) emission regions, namely near band edge (NBE) emission in the ultraviolet (UV) due to the recombination of excitons and visible emission due to the recombination of carriers trapped at deep level defects. Doping ZnO with impurities has been investigated in order to improve its optical properties for white light applications [2, 3], as well as for enhancing the NBE emission for UV applications [4] where it is reported that incorporation of Ag nanoparticles (NPs) in ZnO significantly improved the NBE emission efficiency as a result of the resonant coupling between the ZnO excitons and Ag NP localized surface plasmons. Localized surface plasmon resonance (LSPR) describes the large collective oscillation of the conduction electrons in small metallic NPs [5] and can amplify the electric field of incident electromagnetic radiation near the metallic NPs by two orders of magnitude [6]. Enhancement of the NBE emission of ZnO nanorods has been reported when Au NPs have been sputtered onto their surface. Because the enhancement factor varied considerably with coating time, Lin *et al.* [7] suggested that simple surface passivation could not account for the effect. To explain the enhancement of the NBE as well as suppression of the visible luminescence, it was proposed that the visible emission from ZnO was absorbed by the Au NPs due to surface plasmon resonance (of almost matching wavelength) and that energetic electrons resulting from non-radiative decay of the plasmons were able to transfer from the Au NPs to the

conduction band of the ZnO. Similar experimental results were obtained by C. W. Cheng *et al.* [8] and although possible contributions from the surface passivation effect and the mechanism previously explained were considered, two additional mechanisms were proposed to account for the NBE emission enhancement and visible emission quenching. Firstly it was suggested that electrons normally trapped at the defect level of ZnO responsible for the visible luminescence are able to transfer directly to the Au NPs (having lower Fermi energy) and consequently hot electrons are created in high energy states which can transfer back to the conduction band of the ZnO nanorods. Secondly, it was suggested that the presence of Au NPs creates a new recombination path for ZnO excitons via coupling to surface plasmons, which results in efficient energy transfer (ET). This Purcell enhancement mechanism would rely on a subsequent radiative emission mechanism from the surface plasmons as explained by Lai *et al.* [9], who reported a negligible enhancement of NBE emission for ZnO films coated by Au but a large enhancement for coating by Ag and attributed this difference to the better match of the ZnO NBE luminescence energy with that of the Ag surface plasmons. The effect of sputtering Ag on ZnO thin films was studied by Peihong Cheng *et al.* [10]. The Ag islands on the ZnO surface were considered as oblate spheroids having LSPR modes associated with directions normal and parallel to the surface which were found to be close to the wavelengths of the NBE and visible emissions from ZnO, respectively. They noted that luminescence enhancement of the ZnO is possible due to the Ag NPs as a result of enhancement of the electric field and radiative decay rates, but that damping induced by non-radiative ET may also occur. For their samples the NBE emission was strongly enhanced while the visible luminescence could be slightly enhanced or suppressed depending on the experiment details. The effect of Ag NPs embedded in ZnO films grown by magnetron sputtering was reported by Liu *et al.* [11] who found that the absorption of the Ag NPs covered a wide spectrum, which was attributed to a broad distribution in their size and shape. The NBE emission of the ZnO was enhanced by a factor which correlated well with the density of Ag NPs and was attributed to the effect

of LSPR, while a similar enhancement of the weak visible emission was also found because of the broad range of the plasmon resonance wavelengths.

In this paper, undoped and Ag doped ZnO were prepared by the combustion method with the aim to further understand the interaction mechanism between the NBE emission of ZnO and the Ag NPs. Despite the number of existing models dealing with the enhancement of the NBE emission of ZnO, we do not find a satisfactory explanation for the phenomenon, which we also observe, within the parameters of our experiment and therefore present an additional model. Despite the enhancement being as a result of the Ag NPs incorporated in the ZnO, it does not rely on their plasmonic nature.

8.2 Experimental

All chemicals were purchased from the market and used as received. Undoped and 1 mol% Ag doped ZnO were prepared by the combustion method. Silver nitrate (AgNO_3 , 99.9%) was used as the source of dopant. Zinc nitrate tetrahydrate ($\text{Zn}(\text{NO}_3)_2 \cdot 4\text{H}_2\text{O}$, 98.5%) was used as a precursor and urea ($\text{CO}(\text{NH}_2)_2$, 99%) was used as a fuel. In a typical synthesis the Zn nitrate and urea mixed in the stoichiometric ratio of 2:7 were dissolved in a small amount of distilled water and a homogenous solution was obtained after stirring for 20 min. For doping, the necessary amount of AgNO_3 was added to the mixture before stirring began. The resulting solution was transferred to a muffle furnace which was maintained at a temperature of 500 °C. In a few minutes all the water evaporated, followed by decomposition and generation of a large amount of gases. These combustible gases ignite and burn with a flame, yielding a large amount of foamy solid. The resulting material was allowed to cool down to room temperature outside the furnace and then ground to fine powder. The colour of the samples changed from white to light grey when doped with Ag.

The structural properties were studied with a Bruker D8 X-ray diffractometer using $\text{CuK}\alpha$ radiation generated by an accelerating voltage of 40 kV and a current of 40 mA. The morphology and size of the Ag NPs were obtained from transmission electron microscope (TEM) images recorded with a Philips CM 100 instrument working at 60 kV

and the samples were produced by the dipping amorphous carbon support grids into a dilute ethanol suspension of the powder samples. Diffuse reflectance spectra were measured using a Perkin Elmer Lambda 950 UV-vis spectrophotometer, while luminescence properties were measured using a 325 nm He-Cd laser PL system.

8.3 Results and discussion

Figure 8.1 compares the X-ray diffraction (XRD) pattern of the undoped ZnO with that of the 1 mol% Ag doped ZnO. For the pure sample all the diffraction peaks can be matched to the Miller indices of planes for the hexagonal wurtzite structure of ZnO as given in the Powder Diffraction File (PDF 079-0208). For the doped sample additional peaks marked with asterisk (*) are observed. Their relative size is exaggerated by plotting the square root of the counts on the vertical axis. These additional peaks match the expected positions for face centred cubic Ag (PDF 04-0783). No additional diffraction peaks were observed, indicating only the formation of metallic Ag NPs in the ZnO matrix and no silver oxide (Ag_2O , AgO) phases.

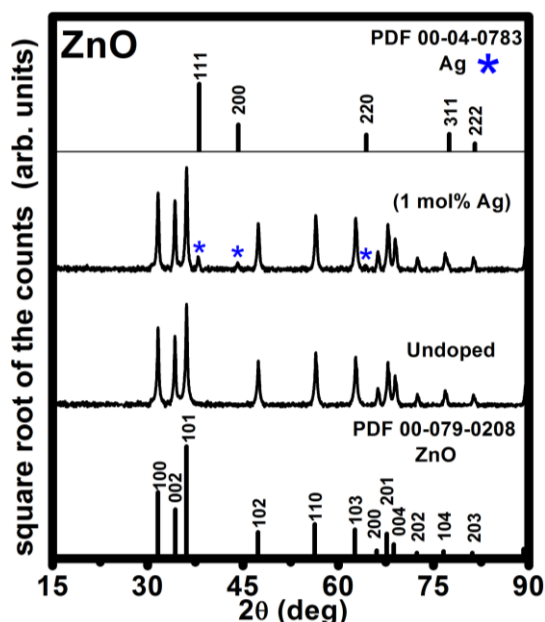


Figure 8.1: XRD patterns of pure and Ag doped ZnO compared to standard patterns from the Powder Diffraction File. The square root of the counts is plotted on the vertical axis to emphasize the small peaks of the metallic Ag NPs (stars).

No slight shift of the ZnO peaks to smaller angles in the doped samples was detected, which has previously been reported when larger Ag^+ ions substitute Zn^{2+} ions in the lattice [4]. The crystallite size of the undoped ZnO host particles was estimated using the well known Scherrer formula [12] and found to be about 30 nm. Since the XRD peaks related to the Ag NPs are small, their size was rather determined by TEM measurements instead of the Scherrer formula.

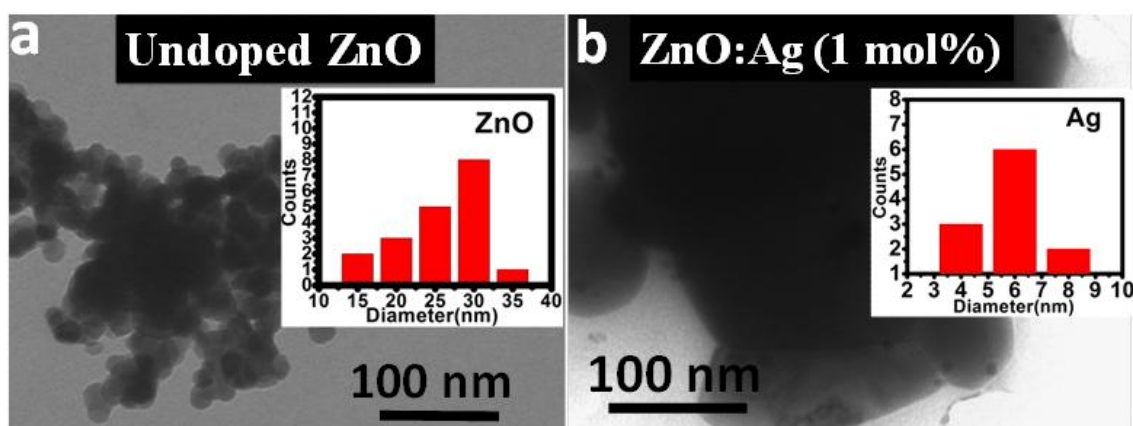


Figure 8.2: TEM images of (a) undoped ZnO and (b) ZnO doped with 1 mol% Ag.

Figure 8.2 shows TEM images of (a) undoped ZnO and (b) ZnO doped with 1 mol% Ag. As can be seen from figure 8.2(a) the ZnO nanocrystals are irregularly spherical with an average diameter of 30 nm, which is similar to the calculated crystallite size from the XRD data. Figure 8.2(b) shows additional small spherical Ag NPs of diameter about 6 nm present in the Ag doped sample. The grain structure of the ZnO host material is clearly affected by the addition of the Ag dopant, although there is not a significant difference in the width of the ZnO XRD peaks between the doped and pure sample in figure 8.1.

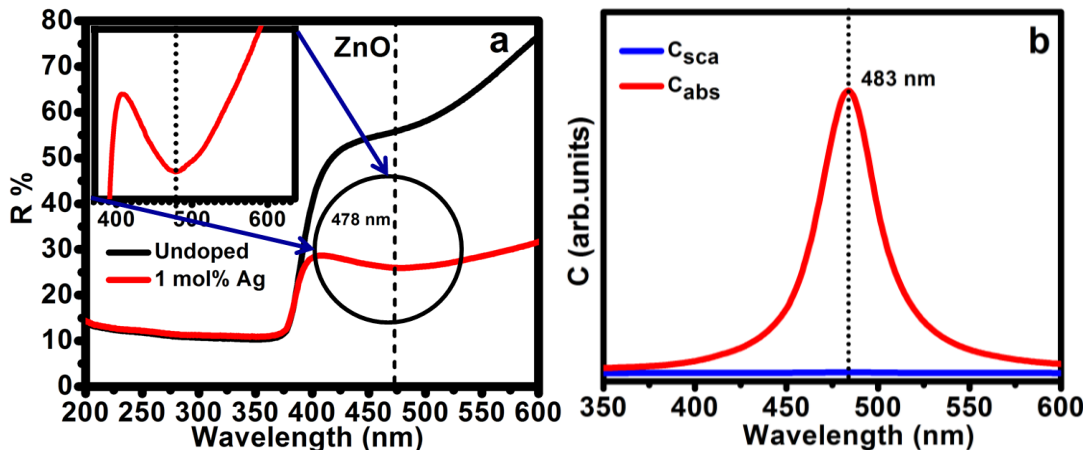


Figure 8.3: (a) Diffuse reflectance curve of pure ZnO and Ag doped ZnO doped. (b) Calculated scattering and absorption cross-sections for an isolated 6 nm Ag NP embedded in a ZnO matrix.

Figure 8.3(a) shows diffuse reflectance spectra of pure and 1 mol% Ag doped ZnO. The sharp decline in reflectance as the wavelength decreases into the UV below 400 nm is associated with the NBE excitonic and band-to-band absorption of the ZnO. For the doped samples there is a dip in the reflectance spectra centred at 478 nm (see the inset) which is attributed to LSPR absorption of the Ag NPs. This confirms the formation of metallic Ag NPs in the ZnO in agreement with the XRD and TEM measurements. Figure 8.3(b) shows the extinction cross-section components (scattering and absorption) for a 6 nm diameter Ag NP in a ZnO matrix calculated using the software MiePlot v4.2.11 [13]. The refractive index of the host material is assumed to be constant and a value of 2.1 was used as an average for ZnO in the wavelength range of interest [14]. The default dielectric constant data (i.e. refractive index) used in the MiePlot software is for bulk Ag [15], but was corrected for the enhanced electron scattering in a small (6 nm) Ag NP [16]. As expected for very small metallic NPs, the scattering is negligible compared to the absorption. The experimental and theoretical absorption results match well and the small variation may be due to the dispersion of shapes and particle sizes in the sample or the estimation of the refractive index data, but confirm that most of the Ag NPs are embedded within the ZnO host material as it appears from the TEM data (figure 8.2(b)).

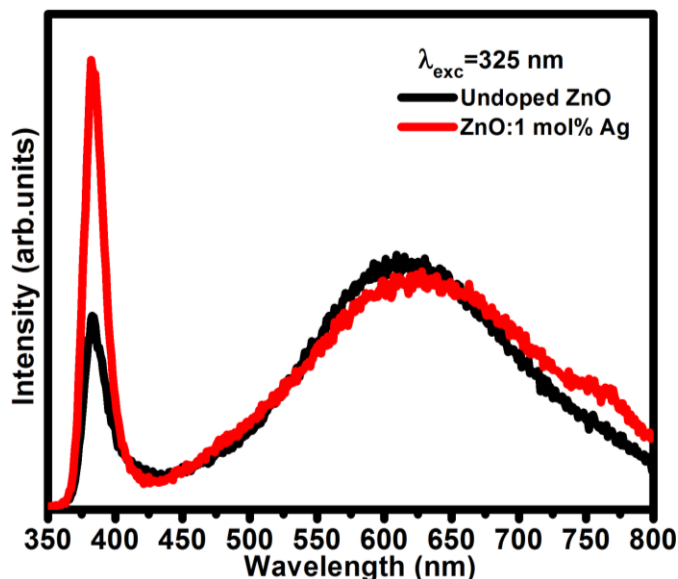


Figure 8.4: Emission spectra of pure and Ag doped ZnO excited at 325 nm by He-Cd laser.

Figure 8.4 shows the luminescence spectra of the undoped and 1 mol% Ag doped ZnO excited by a He-Cd laser at 325 nm. These spectra both have a sharp peak near 390 nm due to NBE emission and a broad visible emission band centred near 610 nm. The red visible emission which was observed, rather than the generally reported green defect emission, is characteristic of ZnO prepared by the combustion method and is attributed to oxygen-related defect [17]. The addition of 1 mol% Ag caused more than a twofold increase in the NBE emission while the visible emission band was almost unchanged. The weak emission feature near 780 nm is due to the second order of the strong NBE emission. The data did not show any luminescence from Ag_2O [18], Ag nanoclusters [19] or Ag ions [20], showing that the Ag is located only within the metallic NPs which were observed using XRD, TEM and diffuse reflectance.

An enhancement of the NBE emission (i.e. radiative exciton recombination) could result from an increase in the number of excited carriers, an enhancement of the radiative recombination rate or a decrease in some non-radiative recombination pathway. In the latter case, improving the crystal quality, decreasing the concentration of defects and passivating the surface are therefore expected to enhance the NBE emission of ZnO.

Although the TEM results showed a change in the morphology of the ZnO matrix when Ag was added, no significant change to the crystal structure or crystallite size can be deduced from the XRD data. In addition, there is no significant change to the visible defect emission from the ZnO after doping. Therefore it appears unlikely that there was an improvement in the crystal quality or a reduction in defect concentration in the Ag doped sample sufficient to explain the large enhancement of the NBE emission. Any possible reduction of surface traps or surface passivation related to the addition of Ag is expected to be small (especially since the Ag is located mainly in the NPs) and this alone is not considered sufficient to explain the change in the luminescence. We therefore consider further either an enhancement of the radiative recombination rate or an increase in the number of excited carriers.

Plasmonic enhancement (metal enhanced fluorescence) of a luminescent centre may occur when the LSPR band of a nearly metallic NP overlaps either with its excitation band (as a result of an enhancement of the local electric field) or its emission band (as a result of enhancement of its radiative decay rate) [21, 22]. A good match is a key factor when trying to achieve a large plasmonic enhancement and this allowed Chen *et al.* to obtain a 40-fold NBE emission enhancement in $\text{Mg}_{0.2}\text{Zn}_{0.8}\text{O}$ by utilizing the quadrupole mode of plasmon resonance of Ag nanostructures which occurred in the UV close to the emission wavelength [23], as well as accounting for the slightly varied enhancement of the visible luminescence from ZnO utilizing the LSPR of Ag and Au NPs by Lawrie *et al.* [24]. In the case of our experiment, the LSPR of the Ag NPs was centred at 478 nm (figure 8.3(a)) which is not close to either the narrow NBE emission wavelength of 390 nm or the broad red visible luminescence centred at 610 nm (figure 8.4), meaning that the condition for effective plasmonic enhancement is not realized, neither via an increase in the NBE emission recombination rate nor via effective local field enhancement which might have excited more carriers. Because of the mismatch of the excitation wavelength and both the NBE emission and red visible defect luminescence with the LSPR wavelength in this study, plasmons are not effectively excited in the sample and the enhancement mechanism whereby hot carriers resulting from plasmon decay [25, 26] are

transferred to the ZnO conduction band to enhance the NBE emission cannot be invoked in this case. Other reported mechanisms which have been shown to be important in other studies, such as unintentional H doping, metal-induced gap states and metal diffusion [27] are not considered to be of relevance for our experimental conditions. Considering the possibilities, it is concluded that the enhancement is most likely due to an increase in the number of excited carriers, although this increase is not due to plasmonic effects.

We therefore propose a new model that may contribute to the enhancement of the NBE emission of ZnO. Existing models include the injection of hot electrons created by plasmon decay from the Ag NPs to the conduction band of ZnO. Plasmons are not effectively excited in our sample, but we propose that hot electrons are created by direct absorption of the UV excitation photons of the He-Cd laser by the Ag NPs and transferred to the ZnO in a process similar to the well known phenomenon of photoemission. This charge transfer then leads to enhanced NBE emission in a similar way as if the electrons had originated due to plasmon decay i.e. an increase of the excited electron density in the conduction band of ZnO and leads to more emission. Figure 8.5 illustrates the proposed mechanism in terms of the energy level structures of Ag and ZnO, assuming the formation of a Schottky barrier between them and taking the ZnO to be n-type. As-prepared undoped ZnO is typically n-type and even though doping it with Ag is often done in the expectation of making it p-type, this has generally proved challenging [28, 29] and in this experiment the Ag is located in the metallic NPs rather than substitutional sites, so it is not expected to change the ZnO from the typical n-type. From the diagram it is seen that photo-excited electrons in the Ag can pass over the relatively small Schottky barrier into the ZnO. The charge transfer is not unique to our model, being often considered in other models as well [27].

The essential difference is the origin of the electron i.e. photo-excited carriers in our case rather than hot carriers induced by plasmon decay. The Ag 4d band lies relatively deep below the Fermi level for Ag [30] and the energy of the 325 nm He-Cd laser (3.82 eV) would not be sufficient for electrons excited by interband transitions to overcome the Schottky barrier. However, intraband transitions may still account for the effect. Note

that this mechanism is not in opposition to others, but provides an additional manner in which the NBE emission of ZnO may be enhanced by doping with Ag. Although figure 8.5 illustrates the essential features of the new model, the size of the Schottky barrier (ϕ_{SB}) is not accurately known. It can be estimated from the simplistic formula $\phi_{SB} = \phi_M - \chi_S$ neglecting surface states [31] where ϕ_M is the work function of Ag and χ_S is the electron affinity of ZnO, which using the values from Fang *et al.* [32] gives ϕ_{SB} in the range 0.17 eV to 0.39 eV. This can be contrasted to actual values quoted by Fang *et al.* [32] of 0.68 eV to 0.84 eV, and the experimental values of 0.908 eV and 0.988 eV [33]. The higher experimental values have been attributed to oxidation of the Ag [34]. Despite the variation in reported values, the Schottky barrier is much smaller than the laser excitation energy.

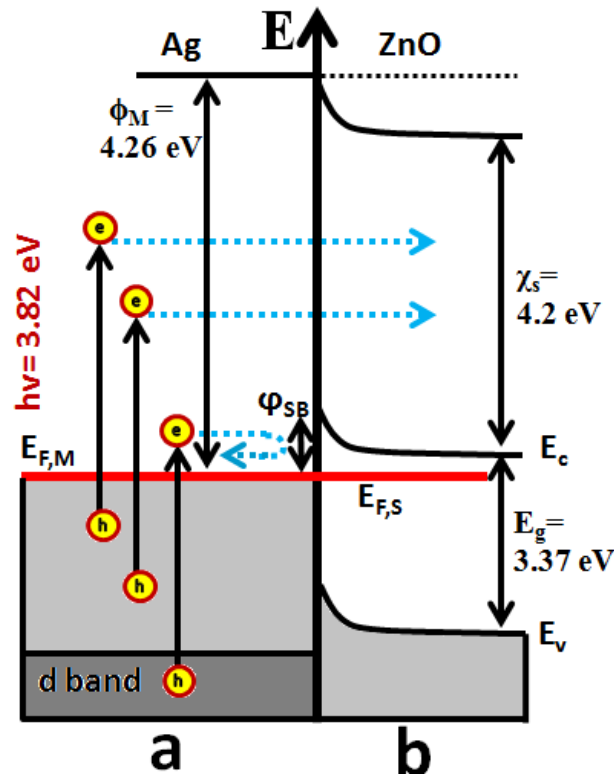


Figure 8.5: Simplified representation of (a) e-h pairs in Ag NPs excited directly by a He-Cd laser at 325 nm, (b) excited electrons with energies high enough to overcome the Schottky barrier $\phi_{SB} = \phi_M - \chi_S$ are injected into the conduction band E_c of ZnO, where ϕ_M is the work function of the Ag and χ_S is the electron affinity of the ZnO.

Of interest is that Fang *et al.* [32] suggest that the ZnO NBE emission enhancement caused by Ag is much less than that for Zn, which has a lower work function and forms an ohmic contact with the ZnO, allowing easy transfer of electrons from the metal to the ZnO. The fact that such an electron transfer leads to enhancement of the NBE emission of ZnO is a key aspect of our mechanism. Despite the Schottky barrier that is normally assumed to form between metals such as Ag and Au, they are still widely reported to enhance the NBE emission and the transfer of energetic electrons from the metal to the ZnO is attributed to plasmonic effects [35]. In our case where plasmonic enhancement is not possible, we ascribe the origin of the energetic electrons to absorption of the excitation laser photons. Finally, it can be noted that the contact between Ag and ZnO has been reported to be ohmic in an electrical study [36] and this possibility has also been considered in explaining the photocatalytic properties of Ag doped ZnO [37, 38] which has led to some confusion on the nature of the interface [39]. Recent first principles calculations have given the interesting prediction that Ag deposited on the O-terminated c-plane of ZnO gives a Schottky barrier of 1.11 eV while Ag deposited on the Zn-terminated c-plane results in an ohmic contact [40]. In the model for the enhancement of the NBE emission presented here the size of the Schottky barrier is not critical, but the process is expected to be more efficient if the Schottky barrier is smaller.

8.4 Conclusion

The formation of ~6 nm diameter NPs in Ag doped ZnO prepared by the combustion method was confirmed by XRD, TEM and diffuse reflectance measurements. PL excited by a 325 nm He-Cd laser showed a more than two-fold enhancement in the intensity of the NBE emission of the doped sample compared to the pure ZnO, while the red visible emission band was similar for both samples. The results suggest that this enhancement is not due to LSPR associated with metallic NPs as may have been expected, but instead it is proposed that photoemission transfer of electrons occurs from the Ag NPs into the conduction band of ZnO and results in the enhancement. This model adds to the variety

of ways in which doping or coating ZnO with noble metals can enhance its NBE emission for possible UV optoelectronics applications.

8.5 References

- [1] A. Janotti and C. G. Van de Walle, Fundamentals of zinc oxide as a semiconductor, *Rep. Prog. Phys.* **72** (2009) 126501 (29 pp).
- [2] G. L. Kabongo, G. H. Mhlongo, T. Malwela, B. M. Mothudi, K. T. Hillie and M. S. Dhlamini, Microstructural and photoluminescence properties of sol-gel derived Tb³⁺ doped ZnO nanocrystals, *J. Alloys Compd.* **591** (2014) 156-163
- [3] V. Kumar, S. Som, V. Kumar, V. Kumar, O. M. Ntwaeaborwa, E. Coetsee and H. C. Swart, Tunable and white emission from ZnO:Tb³⁺ nanophosphors for solid state lighting applications, *Chem. Eng. J.* **255** (2014) 541-552.
- [4] L. Xu, G. Zheng, L. Zhao and S. Pei, Two different mechanisms on UV emission enhancement in Ag-doped ZnO thin films, *J. Lumin.* **158** (2015) 396-400.
- [5] A. E. Abbass, H. C. Swart and R. E. Kroon, Effect of silver ions on the energy transfer from host defects to Tb ions in sol-gel silica glass *J. Lumin.* **160** (2015) 22-26.
- [6] M. Eichelbaum and K. Rademann, Plasmonic Enhancement or Energy Transfer? On the Luminescence of Gold-, Silver-, and Lanthanide-Doped Silicate Glasses and its Potential for Light-Emitting Devices, *Adv. Funct. Mater.* **19** (2009) 2045-2052.
- [7] H. Y. Lin, C. L. Cheng, Y. Y. Chou, L. L. Huang and Y. F. Chen, Enhancement of band gap emission stimulated by defect loss, *Opt. Express* **14** (2006) 2372-2379.
- [8] C. W. Cheng, E. J. Sie, B. Liu, C. H. A. Huan, T. C. Sum, H. D. Sun and H. J. Fana, Surface plasmon enhanced band edge luminescence of ZnO nanorods by capping Au nanoparticles, *Appl. Phys. Lett.* **96** (2010) 071107 (3 pages).
- [9] C. W. Lai, J. An and H. C. Ong, Surface-plasmon-mediated emission from metal-capped ZnO thin films, *Appl. Phys. Lett.* **86** (2005) 251105 (3 pp).
- [10] P. Cheng, D. Li, X. Li, T. Liu and D. Yang, Localized surface plasmon enhanced photoluminescence from ZnO films: Extraction direction and emitting layer thickness *J. Appl. Phys.* **106** (2009) 063120 (4 pp).

- [11] M. Liu, S. W. Qu, W. W. Yu, S. Y. Bao, C. Y. Ma, Q. Y. Zhang, J. He, J. C. Jiang, E. I. Meletis and C. L. Chen, Photoluminescence and extinction enhancement from ZnO films embedded with Ag nanoparticles, *Appl. Phys. Lett.* **97** (2010) 231906 (3 pp).
- [12] R. E. Kroon, Nanoscience and the Scherrer equation versus the ‘Scherrer-Gottingen equation’, *S. Afr. J. Sci.* **109** (2013) (2pp).
- [13] P. Laven, MiePlot: A Computer Program for Scattering of Light from a Sphere using Mie Theory & the Debye series. <http://www.philiplaven.com/mieplot.htm> (accessed 31 Mar 2015).
- [14] A. R. Goñi, F. Kaess, J. S. Reparaz, M. I. Alonso, M. Garriga, G. Callsen, M. R. Wagner, A. Hoffmann and Z. Sitar, Dependence on pressure of the refractive indices of wurtzite ZnO, GaN, and AlN, *Phys. Rev. B* **90** (2014) 045208 (11 pp).
- [15] P. B. Johnson and R. W. Christy, Optical constant of noble metal, *Phys. Rev. B* **6** (1972) 4370-4379.
- [16] V. Amendola, O. M. Bakr and F. Stellacci, A Study of the Surface Plasmon Resonance of Silver Nanoparticles by the Discrete Dipole Approximation Method: Effect of Shape, Size, Structure, and Assembly, *Plasmonics* **5** (2010) 85-97.
- [17] V. Kumar, H. C. Swart, O. M. Ntwaeaborwa, R. E. Kroon, J. J. Terblans, S. K. K. Shaat, A. Yousif and M. M. Duvenhage, Origin of the red emission in zinc oxide nanophosphors, *Mater. Lett.* **101** (2013) 57-60.
- [18] E. Lund, A. Galeckas, A. Azarov, E. V. Monakhov and B. G. Svensson, Photoluminescence of reactively sputtered Ag₂O films, *Thin Solid Films* **536** (2013) 156-159.
- [19] A. S. Kuznetsov, Y-G. Lu, S. Turner, M. V. Shestakov, V. K. Tikhomirov, D. Kirilenko, J. Verbeeck, A. N. Baranov and V. V. Moshchalkov, Preparation, structural and optical characterization of nanocrystalline ZnO doped with luminescent Ag-nanoclusters, *Opt. Mater. Express* **2** (2012) 725-734.
- [20] A. E. Abbass, H. C. Swart and R. E. Kroon, White luminescence from sol-gel silica doped with silver, *J. Sol-Gel Sci. Technol.* **75** (2015) 708-714.

- [21] X. D. Zhou, X. H. Xiao, J. X. Xu, G. X. Cai, F. Ren and C. Z. Jiang, Mechanism of the enhancement and quenching of ZnO photoluminescence by ZnO-Ag coupling, *A letters journal exploring the frontiers of physics* **93** (2011) 57009 (6 pp).
- [22] R. Das, P. Phadke, N. Khichar and S. Chawla, Plasmonic enhancement of dual mode fluorescence in a silver nano-antenna-ZnO:Er³⁺ hybrid nanostructure, *J. Mater. Chem. C* **2** (2014) 8880-8885.
- [23] H. Chen, K. Liu, M. Jiang, Z. Zhang, X. Xie, D. Wang, L. Liu, B. Li, D. Zhao, C. Shan and D. Shen, Tunable enhancement of exciton emission from MgZnO by hybridized quadrupole plasmons in Ag nanoparticle aggregation, *Appl. Phys. Lett.* **104** (2014) 091119 (4 pp).
- [24] B. J. Lawrie, R. Mu and R. F. Haglund, Coupling dynamics between photoluminescent centers in ZnO and surface plasmons, *Proc. of SPIE* **7394** (2009) (8 pp).
- [25] C. Clavero, Plasmon-induced hot-electron generation at nanoparticle/metal-oxide interfaces for photovoltaic and photocatalytic devices, *Nature Photonics* **8** (2014) 95-103.
- [26] R. Sundararaman, P. Narang, A. S. Jermyn, W. A. Goddard and H. A. Atwate, Theoretical predictions for hot-carrier generation from surface plasmon decay, *Nat. commun.* **5** (2014) 5788 (8 pp).
- [27] M. Liu, R. Chen, G. Adamo, K. F. MacDonald, E. J. Sie, T. Sum, N. I. Zheludev, H. Sun and H. Jin Fan, Tuning the influence of metal nanoparticles on ZnO photoluminescence by atomic-layer-deposited dielectric spacer, *Nanophotonics* **2** (2013) 153-160.
- [28] O. Volnianska, P. Boguslawski, J. Kaczkowski, P. Jakubas, A. Jezierski and E. Kaminska, Theory of doping properties of Ag acceptors in ZnO, *Phys. Rev. B* **80** (2009) 245212 (8 pp).
- [29] M. A. Thomas, W. W. Sun and J. B. Cui, Mechanism of Ag Doping in ZnO Nanowires by Electrodeposition: Experimental and Theoretical Insights, *J. Phys. Chem.C* **116** (2012) 6383-6391.

- [30] G. Fuster, J. M. Tyler, N. E. Brener and J. Callaway, Electronic structure and related properties of silver, *Phys. Rev. B* **42** (1990) 7322-7329.
- [31] J. L. Freeouf and J. M. Woodall, Schottky barriers: An effective work function model, *Appl. Phys. Lett.* **39** (1981)727-729.
- [32] Y. J. Fang, J. Sha, Z. L. Wang, Y. T. Wan, W. W. Xia and Y. W. Wang, Behind the change of the photoluminescence property of metal-coated ZnO nanowire arrays, *Appl. Phys. Lett.* **98** (2011) 033103 (3 pp).
- [33] L. Xin-kun, L. Qing-shan, L. De-chun and X. Yan-dong, Electrical properties of silver Schottky contacts to ZnO thin films, *Optoelectron. Lett.* **5** (2009) 0216-0219.
- [34] L. J. Brillson and Y. Lu, ZnO Schottky barriers and Ohmic contacts, *J. Appl. Phys.* **109** (2011) 121301(33 pp).
- [35] T. Singh, D. K. Pandya and R. Singh, Surface plasmon enhanced bandgap emission of electrochemically grown ZnO nanorods using Au nanoparticles, *Thin Solid Films* **520** (2012) 4646-4649.
- [36] S. J. Ikhmayies, N. M. Abu El-Haija and R.N. Ahmad-Bitar, A comparison between different ohmic contacts for ZnO thin films, *J. Semicond.* **36** (2015) 033005 (5 pp).
- [37] F. Yan, Y. Wang, J. Zhang, Z. Lin, J. Zheng and F. Huang, Schottky or ohmic metal-semiconductor contact: influence on photocatalytic efficiency of Ag/ZnO and Pt/ZnO modelsystem, *ChemSusChem.* **7** (2014) 101-104.
- [38] Y. Zheng, C. Chen, Y. Zhan, X. Lin, Q. Zheng, K. Wei and J. Zhu, Photocatalytic Activity of Ag/ZnO Heterostructure Nanocatalyst: Correlation between Structure and Property, *J. Phys. Chem. C* **112** (2008) 10773-10777.
- [39] W. He, H. Wu, W. G. Wamer, H. Kim, J. Zheng, H. Jia, Z. Zheng and J. Yin, Unraveling the Enhanced Photocatalytic Activity and Phototoxicity of ZnO/Metal Hybrid Nanostructures from Generation of Reactive Oxygen Species and Charge Carriers, *Appl. Mater. Interfaces* **6** (2014) 15527-15535.
- [40] N. R. D'Amico, G. Cantele, C. A. Perroni and D. Ninno, Electronic properties and Schottky barriers at ZnO-Metal interfaces from first principles *J. Phys. Condens. Matter.* **27** (2014) (21 pp).

Chapter 9

Use of ZnO:Tb down-conversion phosphor for Ag nanoparticle plasmon absorption using a He-Cd ultraviolet laser

9.1 Introduction

Noble metal nanoparticles (NPs) have attracted particular interest because of their unique properties associated with localized surface plasmon resonance (LSPR) [1-4], which is defined as the collective oscillation of conduction electrons in small metal NPs [1]. The interaction of light with spherical metal NPs was explained a long time ago with Mie theory, showing that when NPs are exposed to light the electrons start to oscillate, particularly when driven at the LSPR frequency [5]. Some energy from the incident light wave is converted into thermal energy in an absorption process while the accelerated electrons can also re-radiate energy in a scattering process [6]. The sum of these two processes is the so-called extinction coefficient which can be expressed by $C_{\text{ext}} = C_{\text{abs}} + C_{\text{sca}}$. The absorption process is dominant for small NPs while the scattering process is dominant in larger NPs having a size comparable to the electron mean free path [7]. Although the former process is problematic for luminescence enhancement applications, it is very important and beneficial in a range of applications requiring localized heating [3, 8, 9].

The normal way to tune the LSPR of metal NPs is to change their size or shape, which may require special synthesis methods and equipment [10], or to change their dielectric environment (host or solvent) which may not be desired. Moreover, tuneable lasers have a limited wavelength range and can be extremely expensive. In this work we propose a new mechanism to resonantly excite the NPs without the need for changing the excitation source (laser) and the particle size, shape or environment by using the down-conversion

properties of an appropriate RE ion. ZnO has attracted considerable attention as a low-cost, environmentally-friendly and easy to synthesize material, and has been used in the medical field because of its biocompatibility, biodegradability and non-toxicity [11]. Although small Ag NPs in ZnO have a LSPR wavelength near 478 nm, it is demonstrated that they can be excited using a 325 nm He-Cd ultraviolet laser indirectly through the down-converting properties of Tb^{3+} ions doped in the ZnO host material. The radiative energy transfer (ET) from the Tb^{3+} ions to the Ag NPs was studied by means of spectral overlap and photoluminescence (PL) lifetime measurements in the presence and absence of the Ag NPs. The results show that the Ag NPs act as energy acceptors, having a quenching effect on the luminescence of the Tb^{3+} ion donors. The excited Ag NPs convert the light energy into heat during relaxation with possible applications for localized heating.

9.2 Experimental

Powder samples of ZnO and ZnO:Tb (5 mol%) were prepared by the combustion method. To some samples Ag was also added to form NPs. Zinc nitrate tetrahydrate ($Zn(NO_3)_2 \cdot 4H_2O$, 98.5%) was used as a precursor and urea ($CO(NH_2)_2$, 99%) was used as a fuel. These were mixed in a stoichiometric ratio of 2:7. For the doped samples 5 mol% of the Zn precursor was replaced with terbium nitrate pentahydrate ($Tb(NO_3)_3 \cdot 5H_2O$, 99.9%), while silver nitrate ($AgNO_3$, 99.9%) was also added to some samples. In a typical synthesis, the precursor nitrates and urea were dissolved in a small amount of distilled water and a homogenous solution was obtained after stirring for 20 min. The resulting solution was transferred to a muffle furnace maintained at temperature of 500 °C. In a few minutes all the water evaporated, followed by decomposition and the generation of a large amount of gases. These combustible gases ignite and burn with a flame, yielding a large amount of foamy solid. The resulting material was allowed to cool down to room temperature outside the furnace and then ground to fine powder.

The structural properties were studied with a Bruker D8 X-ray diffractometer (XRD) using $CuK\alpha$ radiation generated by an accelerating voltage of 40 kV and a current of 40

mA. The morphology and size of the Ag NPs were obtained from transmission electron microscope (TEM) images recorded with a Philips CM 100 instrument working at 60 kV and the samples were produced by the dipping amorphous carbon support grids into a dilute ethanol suspension of the powder sample. Diffuse reflectance spectra were measured using a Perkin Elmer Lambda 950 UV-vis spectrophotometer, while luminescence properties were measured using a 325 nm He-Cd laser photoluminescence system. The decay curve measurements were carried out with a Cary Eclipse fluorescence spectrophotometer having a xenon lamp as the excitation source.

9.3 Results and discussion

Figure 9.1(a) shows the XRD pattern of undoped ZnO. All of the peaks correspond to the hexagonal wurtzite structure of ZnO given in Powder Diffraction File (PDF) 079-0208. The average crystallite size was calculated from the Scherrer equation using each of the (100), (002) and (101) planes, giving an average diameter of 29 nm.

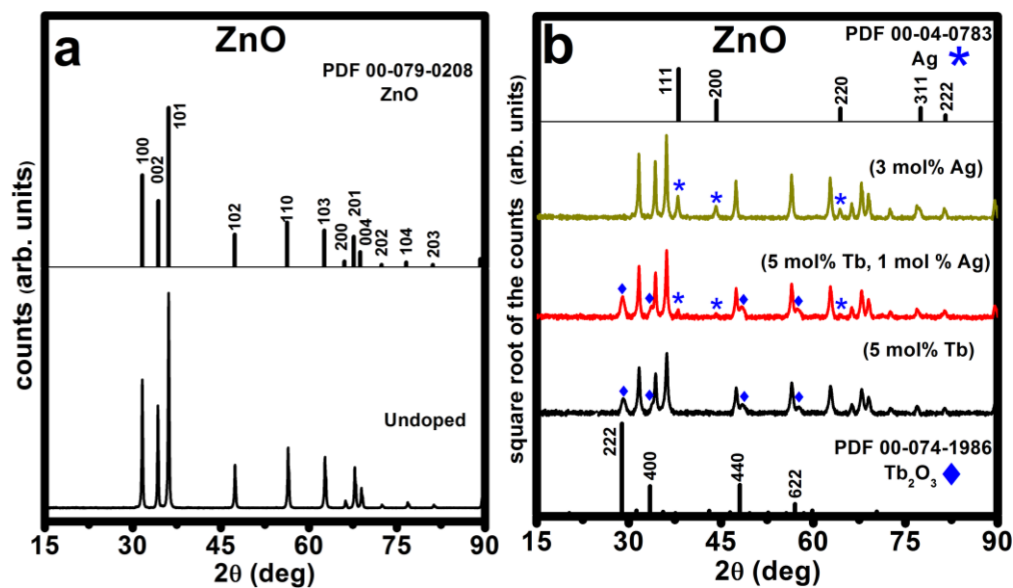


Figure 9.1: XRD patterns of (a) pure ZnO and (b) ZnO doped with Ag and/or Tb. Note that for (b) the square root of the counts is plotted on the vertical axis to emphasize the small peaks of the metallic Ag NPs (stars) and the Tb₂O₃ phase (diamonds).

Figure 9.1(b) shows the patterns of the ZnO samples either single doped, or co-doped, with Ag and Tb. A number of additional small diffraction peaks are present in these samples, which are attributed to face centred cubic (metallic) Ag (PDF file 04-0783) and body centred cubic Tb_2O_3 (PDF file 074-1986). Of interest is that no diffraction peaks from silver oxide phases (Ag_2O , AgO) were observed, indicating only the formation of metallic Ag NPs in the ZnO.

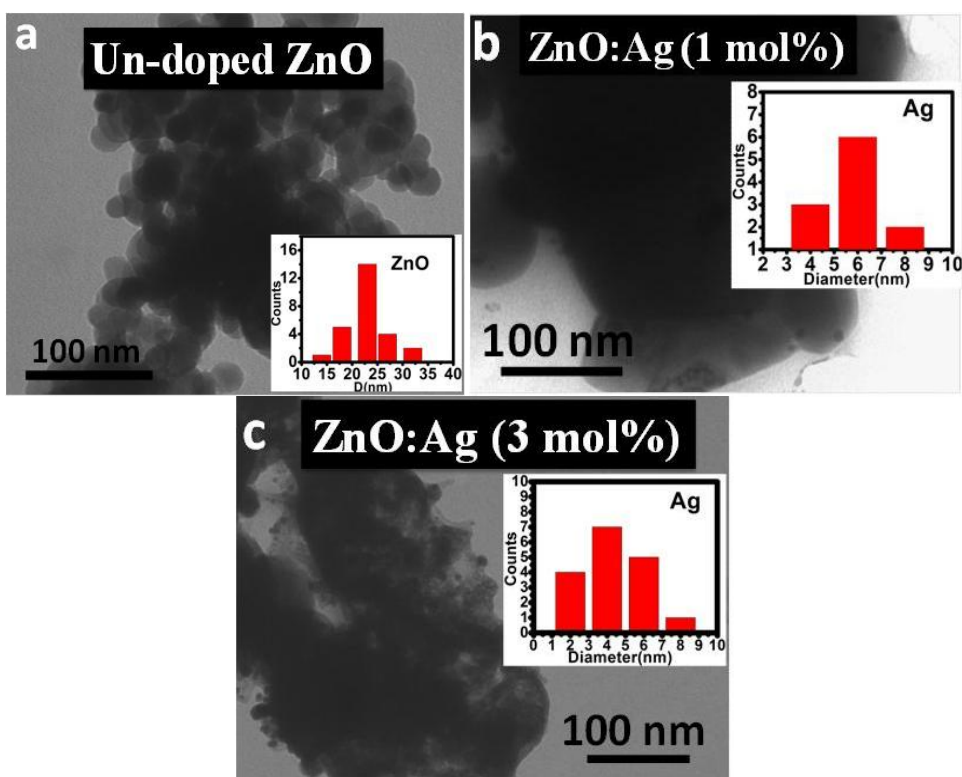


Figure 9.2: TEM image of (a) undoped ZnO. (b) ZnO doped with 1 mol% Ag. (c) ZnO doped with 3 mol% Ag.

Since the XRD peaks of the metallic Ag NPs are very small, rather than estimating their size using the Scherrer equation it was measured directly using TEM. Although the Scherrer equation has been applied extensively to calculate particle sizes from XRD data, it must still be considered as an approximate method since the effects of some parameters

such as shape of particles, distribution of particle sizes and the strain are not considered. Therefore, the calculation of the particle size from TEM images is more preferable. Figure 9.2(a) is an image of the undoped ZnO showing the nanocrystals were irregularly spherical with an average diameter of 30 nm, which is in agreement of the value of 29 nm calculated using the XRD data. Figure 9.2(b) and (c) correspond to ZnO doped with 1 mol% and 3 mol% Ag, respectively. Both images show small, near-spherical Ag NPs embedded in an irregular matrix of ZnO rather than the individual ZnO nanocrystals found in the undoped case. The average size of Ag NPs in the sample doped with 1 mol% is about 6 nm while for the sample doped with 3 mol% it is about 5 nm, which is almost the same if taking into account uncertainty of the measurement. As a result the absorption band of the LSPR is not expected to shift when the concentration of Ag increases from 1 to 3 mol%. Although some Ag NPs appear on the edges of the ZnO particles, most of them are located inside the ZnO.

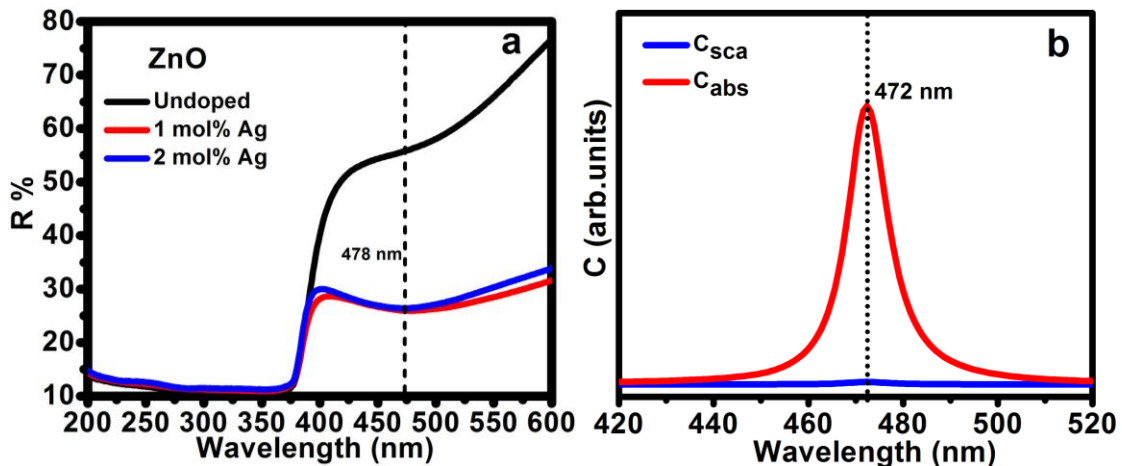


Figure 9.3: (a) Diffuse reflectance spectra of pure ZnO and ZnO with different concentrations of Ag added. (b) Calculated scattering and absorption cross-sections for a 5 nm Ag NP embedded in a ZnO matrix.

Figure 9.3(a) shows the diffuse reflectance spectra of pure ZnO and ZnO with different concentrations of Ag added. The colour of the samples changed from white to light-grey when Ag was added, corresponding to the measured decrease in reflectance over the

visible wavelength range from 400-600 nm. There is a dip in the reflectance spectra of the Ag doped samples near 478 nm. Figure 9.3(b) shows a calculation using MiePlot v4.2.11 of Philip Laven [12] for the extinction cross-section components (scattering and absorption) of a 5 nm diameter Ag NP in a ZnO matrix of refractive index 2.029 [13]. It is dominated by absorption, as expected for NPs having a size much smaller than the electron mean free path [7] i.e. 52 nm in Ag [14]. The wavelength of the maximum absorption, corresponding to LSPR, occurs at 472 nm, which is confirmation that the dip in the diffuse reflectance spectra of the Ag doped ZnO samples results from plasmonic effects of the very small metallic Ag NPs in these samples shown to be present by the XRD and TEM data. Of interest is that the matching between the experimentally observed and the theoretically calculated absorption band of the LSPR indicates that most of the Ag NPs are inside the ZnO in agreement with the TEM measurements. Moreover, due to a large variation between the refractive index of ZnO and air, a large shift in the LSPR absorption band is expected if most Ag NPs precipitated on the surface of the ZnO, which is not observed.

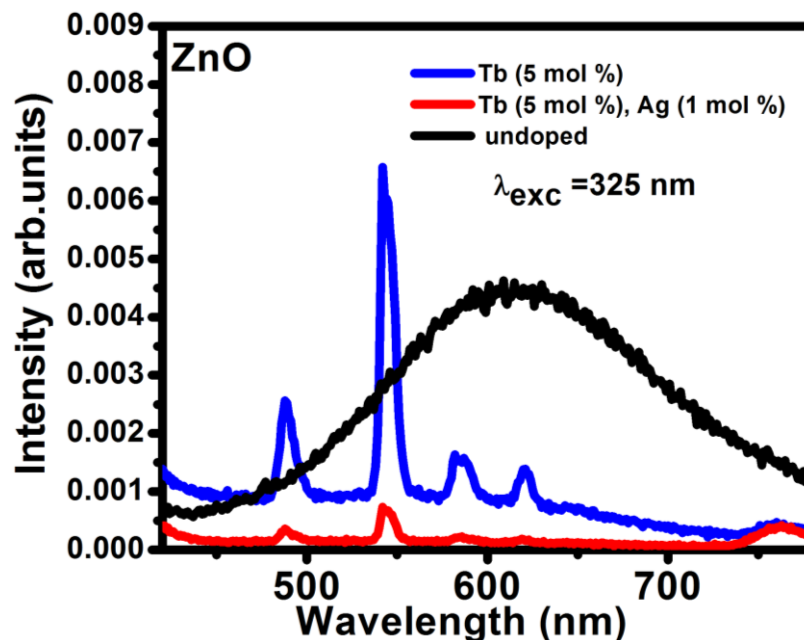


Figure 9.4: Emission spectra of undoped ZnO and Tb single doped as well as Tb,Ag co-doped ZnO excited at 325 nm by He-Cd laser.

Figure 9.4 shows the luminescence of pure ZnO and Tb doped ZnO as well as Tb doped ZnO with Ag added. The undoped ZnO shows a broad emission band centred near 610 nm, which is attributed to defect states related to oxygen in ZnO [15]. The addition of Ag to the ZnO sample did not change its emission spectrum significantly (not shown). The addition of Tb partially suppresses the broad deep-level emission while resulting in the characteristic luminescence of Tb^{3+} ions dominated by a green peak near 545 nm corresponding to the $^5D_4-^7F_5$ transition. In addition, several sharp emission peaks at 485, 590 and 621 nm were observed in the range of 450-650 nm, which are originated from the $4f-4f$ transitions assigned to $^5D_4-^7F_6$, $^5D_4-^7F_4$ and $^5D_4-^7F_3$, respectively. This indicates ET from these ZnO defects to the Tb ions [16, 17]. Adding 1 mol% Ag to the Tb (5 mol%) doped ZnO effectively quenches the ZnO deep level defect emission and reduces the Tb luminescence as well. It is well known that the presence of Ag NPs in the vicinity of emitters (e.g. Tb) can enhance or quench the emission intensity of these emitters depending on their distance from the Ag NPs. If the emitter is within about 5 nm of the surface of a Ag NPs then non-radiative ET occurs from the emitter to the Ag NP and this is accompanied by a decrease in emission intensity and lifetime of the emitters [18]. If the emitter is located within 10 to 50 nm, which is the spatial range of electric field associated with Ag NPs [2], then enhancement of emitter may be observed. At greater separations quenching of the emitters can again be observed due to re-absorption of light by Ag NPs (radiative ET), but in this case the emission lifetime remains unchanged [19]. A requirement for this ET is the overlap between the emission spectrum of the donor (Tb^{3+}) and the excitation of the acceptor (Ag NPs). From the UV-Vis absorption spectra (figure 9.3) and PL spectra (figure 9.4) it is clear that the plasmonic absorption band of Ag NPs at 478 nm shows considerable spectral overlap with the emission peak of Tb^{3+} 485 nm and is broad enough to possibly also overlap the main Tb^{3+} emission band at 545 nm. We believe that the LSPR in these samples can be excited by a broad wavelength range of light because the sizes and shapes of Ag NPs in the samples are dispersed (see figure 9.2(b) and (c)). Therefore, ET from the Tb^{3+} ions to Ag NPs may occur. Due to the very short lifetime of the plasmons, energy transfer from Ag NPs to Tb^{3+} ions is not

expected [20]. Moreover, if there is energy transfer from Ag NPs to Tb^{3+} ions then the intensity of Tb^{3+} emission should be increased, which is not observed.

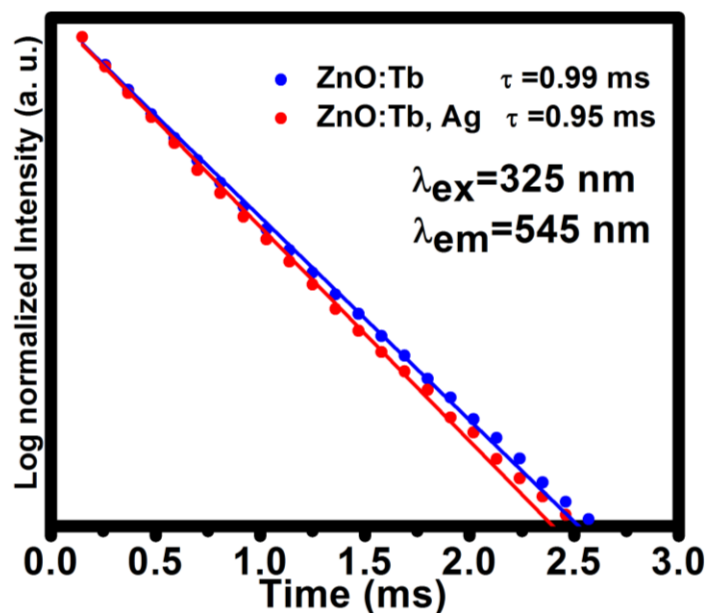


Figure 9.5: Luminescence decay curves for the ${}^5\text{D}_4\text{-}{}^7\text{F}_6$ transition of Tb^{3+} ions in ZnO in the presence and absence of Ag NPs.

To identify which type of the ET occurs, the luminescence decay curves for the ${}^5\text{D}_4\text{-}{}^7\text{F}_6$ transition of Tb^{3+} ions in ZnO in the presence and absence of Ag were measured (figure 9.5). Both decay curves are fitted well with a single exponential function of $I(t) = A \exp(-t/\tau)$ where τ is the lifetime of the Tb^{3+} transition. As can be seen from figure 9.5, the lifetime of the ${}^5\text{D}_4\text{-}{}^7\text{F}_6$ transition of Tb^{3+} changes very little in the presence of Ag, indicating that radiative ET from the donor (Tb^{3+} ions) to the acceptor (Ag NPs) occurs and corresponding to the situation where most Tb^{3+} ions are relatively far from the Ag NPs.

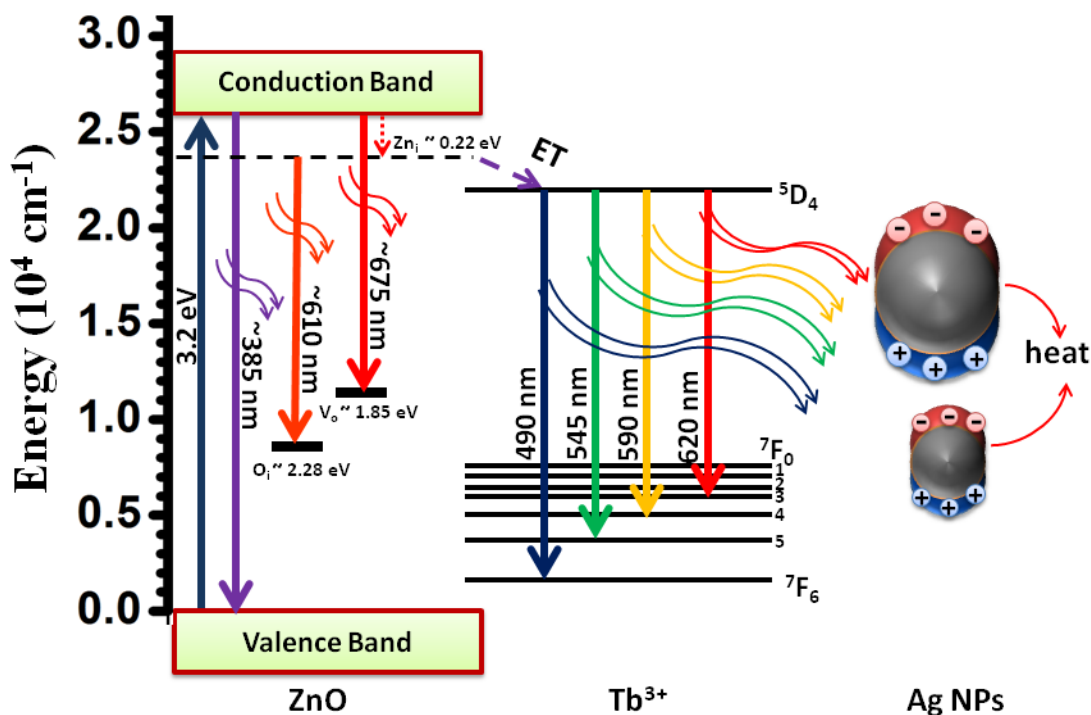


Figure 9.6: Energy level diagram showing non-radiative energy transfer from ZnO defects to Tb^{3+} ions and radiative energy transfer from Tb ion to Ag NPs.

Figure 9.6 illustrates the ET processes for excitation of Tb, Ag co-doped ZnO samples excited by a laser at 325 nm, showing non-radiative ET from ZnO defects to the $^5\text{D}_4$ level of Tb^{3+} and the subsequent radiative transfer of this energy to Ag NPs. The Ag NPs act as energy acceptors and convert the light energy into heat (scattering not being expected as discussed earlier), which may be useful in biological and polymer or other photothermal applications [3, 8]. The Tb^{3+} ions together with the ZnO host and its defects successfully act to indirectly couple the ultraviolet He-Cd laser wavelength of 325 nm to the Ag NP LSPR wavelength near 478 nm by down-conversion. This technique can be used to indirectly couple non-tuneable laser emissions to the LSPR wavelength of metallic NPs without changing their size or shape.

9.4 Conclusion

In this work, undoped ZnO and ZnO doped with only Tb, or co-doped with Tb and Ag, were synthesized by the combustion method. The formation of Ag NPs in the ZnO matrix was confirmed by X-ray diffraction, transmission electron microscopy and UV-vis diffuse reflectance measurements. The PL properties of ZnO:Tb system were studied before and after adding Ag by using a He-Cd laser. Radiative ET from Tb³⁺ ions to Ag NPs was observed and confirmed by mean of spectral overlap and lifetime measurements. Plasmons from 5 nm Ag NPs were excited indirectly through the down-conversion properties of Tb³⁺ ions. Consequently, it can be concluded that the use of a down-converting phosphor (containing, for example, RE ions) is an effective method to indirectly couple a laser to the plasmon resonance wavelength of metal NPs without need to change the particle size or shape of NPs. The obtained results suggest that the ZnO:RE,Ag system may be useful in applications that require local heating.

9.5 References

- [1] A. E. Abbass, H. C. Swart and R. E. Kroon, Effect of silver ions on the energy transfer from host defects to Tb ions in sol-gel silica glass, *J. Lumin.* **160** (2015) 22-26.
- [2] A. J. Haes, C. L. Haynes, A. D. McFarland, G. C. Schatz, R. P. Van Duyne and S. Zou, Plasmonic Materials for Surface-Enhanced Sensing and Spectroscopy, *MRS Bulletin.* **30** (2005) 368-375.
- [3] A. O. Govorov and H. H. Richardson, Generating heat with metal nanoparticles, *Nano Today* **2** (2007) 30-38.
- [4] P. K. Jain, X. Huang, I. H. El-Sayed and M. A. El-Sayed, Noble Metals on the Nanoscale: Optical and Photothermal Properties and Some Applications in Imaging, Sensing, Biology, and Medicine, *Acc. Chem. Res.* **41**(2008) 1578-1586.
- [5] V. A. G. Rivera, F. A. Ferri and E. Marega, Localized Surface Plasmon Resonances: Noble Metal Nanoparticle Interaction with Rare-Earth Ions, In: Plasmonics - Principles and Applications, edited by K. Y. Kim, *Intech.* (2012) 283-312.

- [6] H. Horvath, Gustav Mie and the scattering and absorption of light by particles: Historic developments and basics, *J. Quant. Spectrosc. Radiat. Transfer.* **110** (2009) 787-799.
- [7] C. Noguez, Surface Plasmons on Metal Nanoparticles: The Influence of Shape and Physical Environment, *J. Phys. Chem. C* **111** (2007) 3806-3819.
- [8] X. Huang and M. A. El-Sayed, Gold nanoparticles: Optical properties and implementations in cancer diagnosis and photothermal therapy, *J. adv. res.* **1** (2010) 13-28.
- [9] S. Maity, L. N. Downen, J. R. Bochinski and L. I. Clarke, Embedded metal nanoparticles as localized heat sources: An alternative processing approach for complex polymeric materials, *Polymer* **52** (2011) 1674-1685.
- [10] N. Cathcart, A. J. Frank and V. Kitaev, Silver nanoparticles with planar twinned defects: effect of halides for precise tuning of plasmon resonance maxima from 400 to >900 nm, *Chem. Commun.* (2009) 7170-7172.
- [11] T. Bora, K. K. Lakshman, S. Sarkar, A. Makhil, S. Sardar, S. K. Pal and J. Dutta, Modulation of defect-mediated energy transfer from ZnO nanoparticles for the photocatalytic degradation of bilirubin, *Beilstein J Nanotechnol.* **4** (2013) 714-725.
- [12] P. Laven, MiePlot: A Computer Program for Scattering of Light from a Sphere using MieTheory & the Debye series, [online]. Available from <http://www.philiplaven.com/mieplot.htm>.
- [13] I. A. Ezenwa, Synthesis and Optical Characterization of Zinc Oxide Thin Film, *Res. J. Chem. Sci.* **2** (2012) 26-30.
- [14] O. Veron, J. P. Blondeau, D. D. S. Meneses and C. A. Vignolle, Structural Changes of Ag⁺-Na⁺ Annealed Ion-Exchanged Silicate Glasses Scanning Electron Microscopy, Far-Infrared Reflectivity, UV-Visible Absorption, and TEM Investigation, *Plasmonics* **6** (2010) 137-148.
- [15] P. Cheng, D. Li, X. Li, T. Liu and D. Yang, Localized surface plasmon enhanced photoluminescence from ZnO films: Extraction direction and emitting layer thickness, *J. Appl. Phys.* **106** (2009) 063120 (4 pages).

- [16] Vinod Kumar, S. Som, Vijay Kumar, Vinay Kumar, O. M. Ntwaeaborwa, E. Coetsee and H. C. Swart, Tunable and white emission from ZnO:Tb³⁺ nanophosphors for solid state lighting applications, *Chem. Eng. J.* **255** (2014) 541-552.
- [17] G. L. Kabongo, G. H. Mhlongo, T. Malwela, B. M. Mothudi, K. T. Hillie and M. S. Dhlamini, Microstructural and photoluminescence properties of sol-gel derived Tb³⁺ doped ZnO nanocrystals. *J. Alloys. Compd.* **591**(2014) 156-163.
- [18] J. Qi, Y. Xu, F. Huang, L. Chen, Y. Han, B. Xue, S. Zhang, T. Xu, S. Dai and A. Srivastava, Photoluminescence of Ag Nanoparticles and Tm³⁺ Ions in the Bismuth Germanate Glasses for the Blue Light-Excited W-LED, *J. Am. Ceram. Soc.* **97** (2014) 1471-1474.
- [19] L. Rothberg and S. Pan, Plasmon-enhanced radiative rates and applications to organic electronics, In: Metal-enhanced fluorescence, edited by C. D. Geddes, *John Wiley & Sons*, USA, (2010) 543-567.
- [20] O. L Malta, P. A. Santa-Cruz, G. F. Desa and F. Auzel, Fluorescence enhancement induced by the presence of small silver particles in Eu³⁺ doped materials, *J. Lumin.* **33** (1985) 261-272.

Chapter 10

Enhanced terbium emission due to plasmonic silver nanoparticles in bismuth silicate

10.1 Introduction

The localized surface plasmon resonance (LSPR) associated with noble metal nanoparticles (NPs) has attracted much attention both theoretically and experimentally due to its applications in different fields [1]. Crystals doped with RE ions are well known as important phosphor materials, since quantum efficiencies are generally higher in crystals than in amorphous hosts [2]. Some further advantages of crystalline hosts is that they generally have greater hardness and higher thermal conductivity than amorphous materials, that they may inhibit the clustering of dopants (e.g. RE ions) because the doping is achieved by substitution of cations with similar size and valence in the crystal lattice and that the excitation and emission from activators is narrower and the distribution in lifetimes is smaller than for amorphous hosts due to the lack of substantial variation in the local environment of the activator sites. In addition to its crystalline nature, bismuth silicate has excellent physical, chemical and mechanical properties such as a high refractive index, high nonlinearity index, high mechanical strength, chemical inertness and a fast response to optical signals [3].

Incorporation of noble metal NPs in the vicinity of RE ions has been proposed as a strategy to enhance the f - f absorption cross-section of the RE ions by mean of plasmonic effects [4] since f - f electric dipole transitions are in theory forbidden by the parity rule, which in turn leads to a weak absorption cross-section. There continues to be significant interest in the luminescence enhancement of RE ions associated with Ag NPs [5-7]. Two possibilities have been given for the origin of the enhancement: plasmonic effects of metallic Ag NPs (electric field amplification) which are responsible for increasing the

effective excitation rate or increasing the radiative decay rate of RE ions, [8] or alternatively energy transfer (ET) from Ag ions to RE ions [9] or from host defects, influenced by the added Ag, to Tb^{3+} ions [10]. The differentiation between plasmonic and ET effects remains a challenge [11].

It is predicted that the emission of RE ions could be enhanced when the plasmon absorption band overlaps their $f-f$ absorption lines [12]. The LSPR absorption band can be tuned over a wide spectral range covering the near ultraviolet (UV), visible and near-infrared (NIR) regions by varying the choice of the dielectric matrix or by manipulation of the size and shape of the metal NPs [13, 14]. Controlling the LSPR absorption position by varying the size and shape of the NPs requires special synthesis and equipment [14] and therefore the appropriate choice of dielectric matrix is the easiest way to produce an overlap between the LSPR absorption band and the absorption lines of the selected RE ion.

In our case we have chosen the trivalent terbium ion (Tb^{3+}) as activator because it is known as an important RE ion for green phosphors, which has good photoluminescence (PL) characteristics from $^5D_4-^7F_J$ transitions in the visible range [7]. We have chosen bismuth silicate as the crystalline host because of its high refractive index of ~ 2 [15] that shifts the LSPR absorption band of small Ag NPs close to the Tb^{3+} $f-f$ excitation band corresponding to the $^7F_6-^5D_4$ transition near 485 nm. The objective of the present work is the study of the luminescence properties bismuth silicate co-doped with Tb^{3+} and Ag NPs in order to explore the role of the Ag NP plasmonic effect on the luminescence of the Tb^{3+} ions. Bismuth silicate doped with Tb^{3+} ions and Ag NPs has not yet been explored and a particular novelty of the present work is the use of a crystalline host instead of an amorphous host to study plasmonic enhancement as in previous studies.

10.2 Experimental

Powders of pure bismuth silicate, as well as bismuth silicate doped with either Tb or Ag (or co-doped with both) were prepared by the sol-gel method [16, 17]. Tetraethyl orthosilicate (TEOS, 99.7%) and bismuth nitrate hydrate ($Bi(NO_3)_3 \cdot 5H_2O$, 99.999%)

were used as sources of Si and Bi respectively, while silver nitrate (AgNO_3 , 99.9%) and terbium nitrate ($\text{Tb}(\text{NO}_3)_3$, 99.999%) were used as the source of dopants, to produce undoped $\text{Bi}_4\text{Si}_3\text{O}_{12}$ (sample BS), $\text{Bi}_{3.95}\text{Tb}_{0.05}\text{Si}_3\text{O}_{12}$ (sample BST), $\text{Bi}_4\text{Si}_3\text{O}_{12}:\text{Ag}_x$ (samples BS: Ag_x) and $\text{Bi}_{3.95}\text{Tb}_{0.05}\text{Si}_3\text{O}_{12}:\text{Ag}_x$ (samples BST: Ag_x). The TEOS was first dissolved in ethanol (99.0%) and stirred for 30 min at room temperature. Separately, the $\text{Bi}(\text{NO}_3)_3 \cdot 5\text{H}_2\text{O}$ was dissolved in dilute nitric acid (HNO_3 , 2 M) at 70 °C under vigorous stirring until completely dissolved. For doped samples the nitrate(s) of the dopant(s) were firstly dissolved in a small amount of the dilute HNO_3 taken from the total amount and then added to the TEOS mixture with magnetic stirring for a further 30 min. Finally the Bi and Si precursor solutions were combined under vigorous stirring at a constant temperature of 70 °C until a gel formed. This gel was kept at room temperature in air for one day, then dried in an oven at 70 °C, then ground to fine powder and finally annealed at 800 °C in air for 2 h.

Samples were analyzed at room temperature. X-ray diffraction (XRD) patterns were recorded for a 2θ scan range of 15° to 90° with a step of 0.02° using a diffractometer (model D8, from Bruker) with $\text{Cu K}\alpha$ X-rays of wavelength 0.1548 nm generated with an accelerating voltage of 40 kV and a current of 40 mA. Morphology and size of the Ag NPs were obtained from transmission electron microscope (TEM) images (model CM 100, from Philips) operating at 60 kV for which samples were prepared by dipping amorphous carbon support grids into a dilute ethanol suspension of the powders and allowing them to dry. Further investigation of the Ag NPs was performed with Auger electron spectroscopy (AES) scans (model PHI 700 scanning Auger nanoprobe from Physical Electronics). This instrument is also capable of scanning electron microscopy (SEM) measurements for imaging and accurate location of the electron beam position. Although charging of the sample made these measurements challenging, this was overcome by crushing the powder sample onto a rough copper sample holder and examining particles making good contact with this holder. Measurements were made using an accelerating voltage of 25 kV and a beam current of 5 nA, giving a spatial resolution of about 5 nm. Diffuse reflectance spectra were measured with an integrating

sphere in the range 200 nm to 700 nm (model Lambda 950 spectrophotometer, from Perkin Elmer) using spectralon as a standard, while photoluminescence (PL) properties were measured using a fluorescence spectrophotometer (model Cary Eclipse, from Varian) having a xenon lamp as its excitation source.

10.3 Results and discussion

Maximum luminescence enhancement is expected when the absorption band of the emitting RE ion overlaps well with the LSPR absorption band of the NPs [12]. Table 10.1 lists the positions of the LSPR absorption band of 30 nm diameter spherical Ag NPs as a function of the refractive index of some phosphor host materials, as calculated using the program MiePlot (v4.2.11) [18], and the information is represented graphically in figure 10.1. The value of 30 nm for the diameter used in the simulations was chosen based on our earlier experimental work on Ag NPs produced in amorphous SiO₂ [10, 19].

Table 10.1: Calculated position of the LSPR absorption band for 30 nm diameter Ag NPs in different materials.

Material	Refractive index	LSPR wavelength (nm)	Reference
Amorphous SiO ₂	1.46	396	24
LuSiO ₅	1.81	444	25
YAG	1.91	453	25
ZnO	2.02	466	26
SrGa ₂ S ₄	2.17	495	25

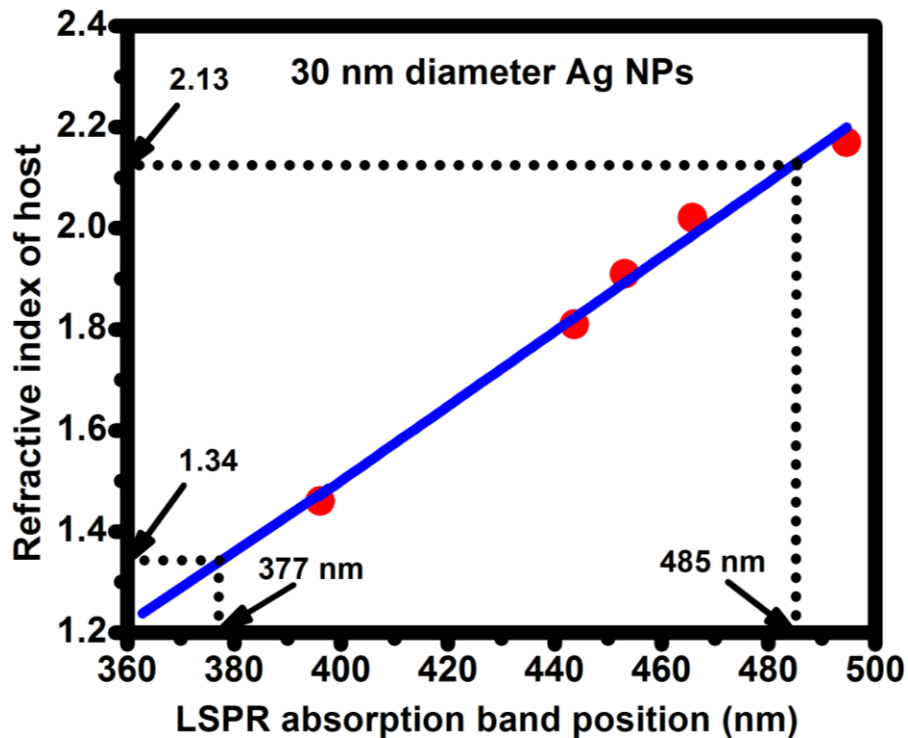


Figure 10.1: Position of the LSPR absorption band of 30 nm diameter Ag NPs as the function of the refractive index of the host. The line is a fit to show the trend of the data.

The Tb^{3+} ion has two absorption bands lying in the wavelength range shown in [figure 10.1](#), one in the near ultraviolet region at 377 nm (${}^7F_6-{}^5D_3$) and the other in the visible region at 485 nm (${}^7F_6-{}^5D_4$) [\[10\]](#). Therefore as illustrated in [figure 10.1](#) one can select a host with an appropriate refractive index to shift the LSPR absorption band to overlap with one of these Tb^{3+} absorption bands as having a refractive index of about 1.34 or 2.13. In this paper, bismuth silicate was selected as an interesting and appropriate crystalline host materials because it has a refractive index of ~ 2 [\[15\]](#) that should shift the LSPR band to overlap with the Tb^{3+} absorption band at 485 nm. In general this approach can be used to select appropriate hosts for different RE ions to adjust the LSPR of Ag NPs to overlap with the RE ion absorption bands.

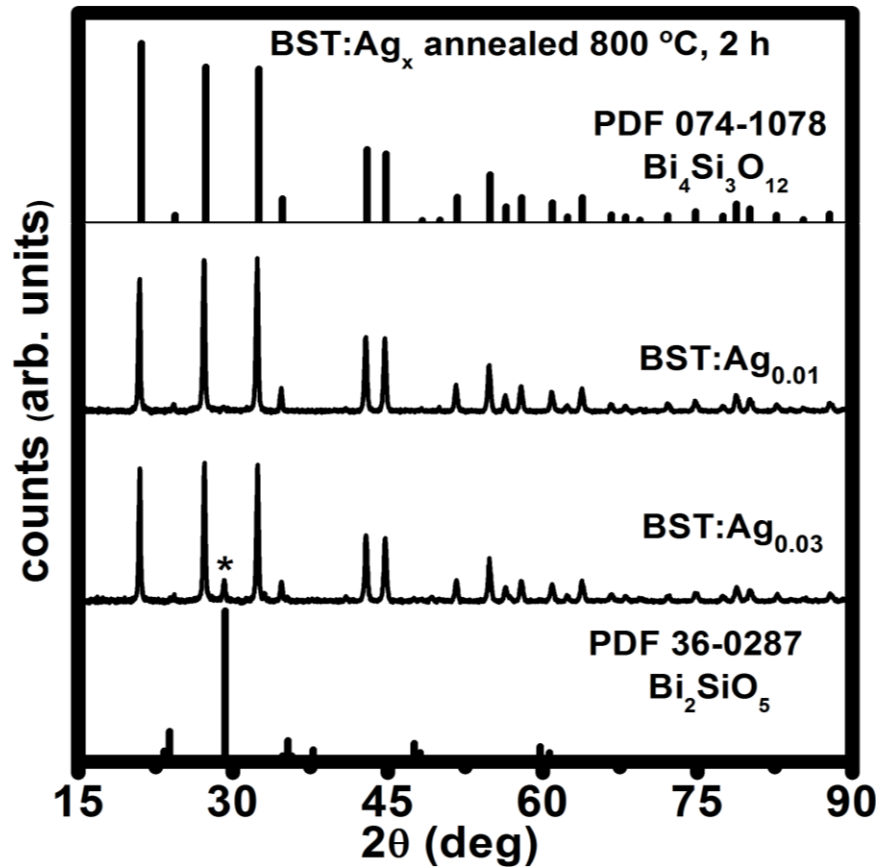


Figure 10.2: XRD patterns of BST:Ag_x samples doped with different concentrations of Ag compared to standard patterns of bismuth silicate phases from the Powder Diffraction File.

A set of samples doped with 5 mol% Tb^{3+} and different concentrations of Ag were prepared. Two of these samples were selected to investigate their structure by XRD, one with a low concentration of Ag ($\text{BST:Ag}_{0.01}$) and the other with higher concentration of Ag ($\text{BST:Ag}_{0.03}$), as shown in [figure 10.2](#). The diffraction pattern for $\text{BST:Ag}_{0.01}$ shows it is single phase crystalline $\text{Bi}_4\text{Si}_3\text{O}_{12}$ by comparison with the Powder Diffraction File (PDF 00-074-1078). This XRD pattern indicates that the Tb^{3+} was successfully incorporated in the lattice, substituting Bi^{3+} ions in the structure, but does not show any peaks corresponding to metallic Ag NPs. Note that deviating from the annealing temperature (800 °C) or time (2 h) used was found to affect the phase purity of the

resultant material. The sample with a higher Ag concentration (BST:Ag_{0.03}) prepared using the same procedure and conditions showed an additional small peak near $2\theta \approx 29^\circ$ which is related to the Bi₂SiO₅ phase, as confirmed by comparison with the Powder Diffraction File (PDF 00-36-0287). These two bismuth silicate phases have different structures and space groups, namely orthorhombic (*Cmc2₁*) for Bi₂SiO₅ and cubic (*I $\bar{4}$ 3d*) for Bi₄Si₃O₁₂. Investigation of bismuth silicate phases can be quite complicated since it is reported that Bi₂SiO₅, Bi₁₂SiO₂₀, Bi₄Si₃O₁₂ and Bi₂O₃ crystalline phases can be precipitated as a function of annealing temperature [3]. Our results show additional complexity where the phase transition is also influenced by the addition of dopants. Even in the BST:Ag_{0.03} sample with the higher Ag concentration the XRD pattern did not show any peaks related to metallic Ag NPs, which may be due to the small amount of Ag (~0.16 at%) which is probably below the detection limit.

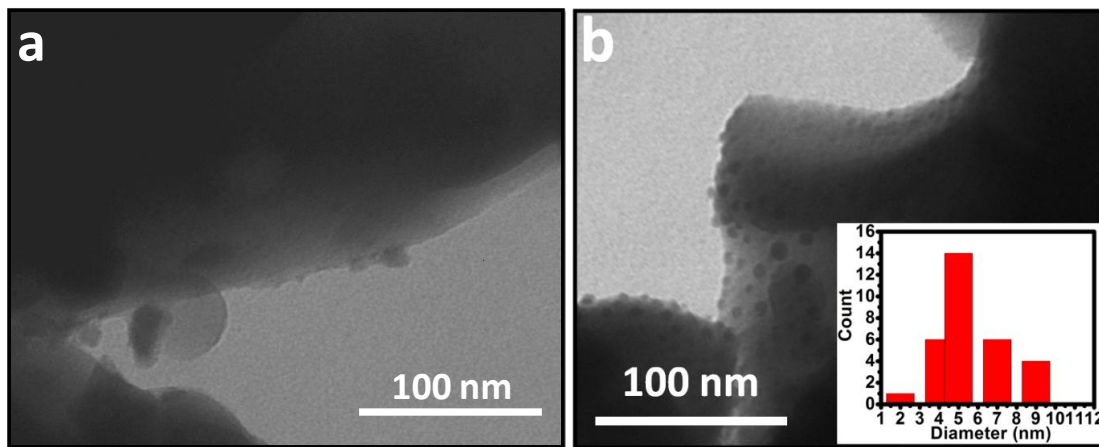


Figure 10.3: TEM images of (a) BS and (b) BS:Ag_{0.03} samples.

Therefore to confirm the formation of Ag NPs in the bismuth silicate matrix for a small concentration of Ag, samples were examined using TEM. Figure 10.3(a) shows a TEM image of the undoped bismuth silicate sample (BS) annealed at 800 °C for 2 h, while figure 10.3(b) shows bismuth silicate doped with 3 mol% Ag (BS:Ag_{0.03}) produced with the same annealing conditions. A comparison of the images shows that for the sample

doped with Ag there are additional small particles of dark contrast around 5 nm in size (see the inset of [figure 10.3\(b\)](#)) which were not found for the undoped sample. The difference is attributed to the doping with Ag and suggests that these small particles having dark contrast may show the formation of Ag NPs. Since it proved difficult to obtain clear electron diffraction patterns from such small particles, especially in the close vicinity to the crystalline bismuth silicate host material, the sample doped with 3 mol% Ag (BS:Ag_{0.03}) was further examined with nanoprobe AES to confirm the formation of Ag NPs.

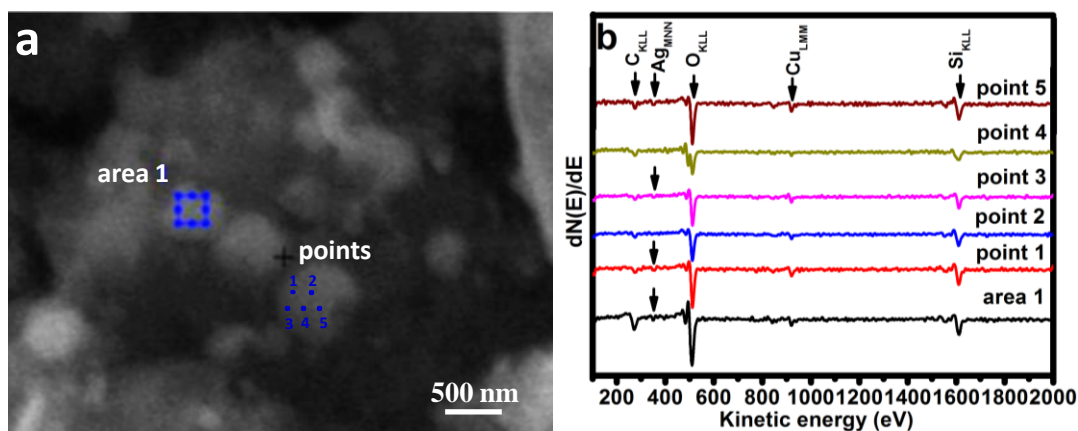
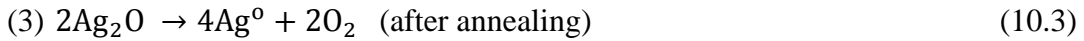
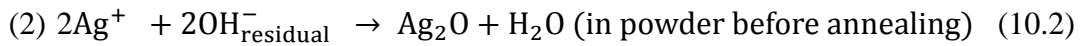
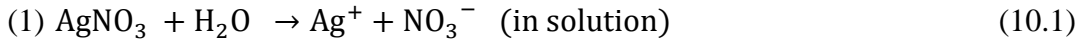


Figure 10.4: (a) SEM image and (b) AES spectra of BS:Ag_{0.03} sample.

[Figure 10.4\(a\)](#) shows a SEM image of some powder particles and [figure 10.4\(b\)](#) shows the AES spectrum averaged over a particle surface (area 1) as well as spectra at various positions (points 1-5) on a particle as marked in the SEM image. The small but significant Auger peak near 359 eV for the spectrum of area 1 corresponds to the MNN Auger transition of Ag. To determine whether the Ag is distributed homogeneously in the bismuth silicate or agglomerated into isolated NPs, Auger spectra were measured at various points on a particle. The Auger spectra at points 1, 3 and 5 showed small but clear bands related to Ag, while points 2 and 4 showed no obvious peak related to Ag. This demonstrates that the Ag is not homogeneously distributed, which is consistent with the formation of Ag NPs. Since Auger spectroscopy is a surface technique that only probes the first few nanometres of a sample, the data from [figure 10.4](#) shows that Ag NPs

occur on the surface of the particles. While AES cannot give any information about the inside of the particles, TEM gives information through the entire sample. Although some of the small particles with dark contrast in figure 10.3(b) may appear to be inside the sample, they could also be at the top or bottom surfaces and therefore there is no clear evidence that Ag NPs definitely occur within the bismuth silicate particles, but only on their surface. As no reducing agent was used during the synthesis, the formation of Ag NPs is believed to take place according to the following steps:



The formation of Ag NPs in Ag ion-exchanged glass [20] has been reported to proceed above a critical temperature of 410 °C, and although the host material may play an important role this temperature is substantially lower than the annealing temperature of 800 °C used in this study.

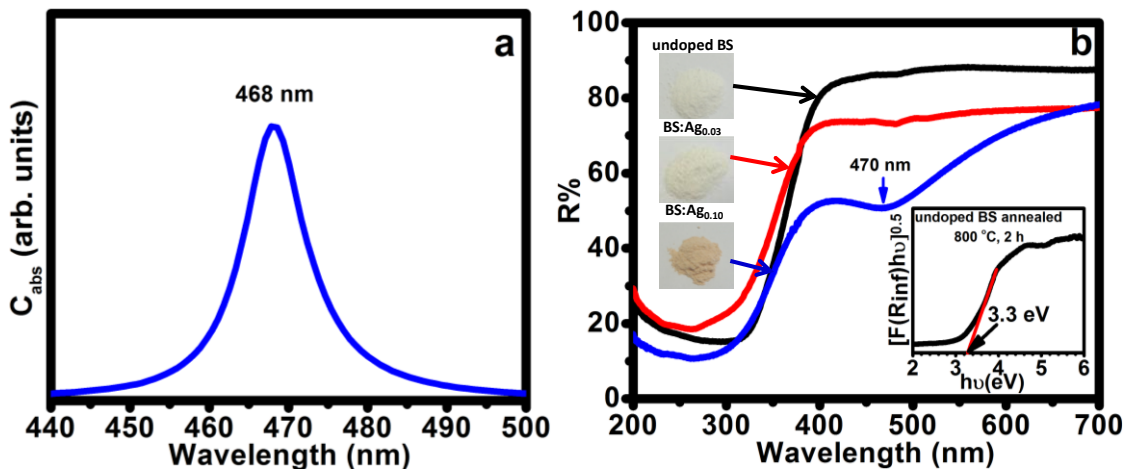


Figure 10.5: (a) Theoretical absorption cross-section for Ag NPs with diameter of 5 nm distributed in bismuth silicate with refractive index of 2. (b) Diffuse reflectance spectra of BS, BS:Ag_{0.03} and BS:Ag_{0.10} samples.

The fact that the Ag NPs found experimentally are much smaller than those used for the theoretical prediction in [figure 10.1](#) needs to be considered, but since the position of the LSPR band does not change quickly with decreasing size for small Ag NPs less than ~30 nm, it does not necessarily affect the choice of refractive index (and therefore host). This is confirmed by [figure 10.5\(a\)](#) showing the theoretical absorption cross-section calculated using MiePlot (v4.2.11) for Ag NPs with a diameter of 5 nm (the average size determined from the TEM data) distributed in a bismuth silicate matrix with a refractive index of 2. The LSPR absorption band for these small Ag NPs is predicted at 468 nm, which is 17 nm less than the 485 nm predicted for 30 nm diameter Ag NPs in order to perfectly overlap the Tb^{3+} excitation band. [Figure 10.5\(b\)](#) shows diffuse reflectance spectra of the undoped BS sample and two BS:Ag_x samples annealed at 800 °C for 2 h. Although there is no obvious LSPR absorption band of Ag NPs for the sample BS:Ag_{0.03}, probably because the doping level is low, there is a perceptible colour change compared to the undoped sample, and when the doping of Ag is increased (sample BS:Ag_{0.10}) there is a distinct colour change and the clear LSPR absorption band for Ag NPs in the bismuth silicate host is centred at 470 nm. The good correspondence between the measured and calculated absorption band positions suggests that most of the Ag NPs are in an environment where the refractive index matches that of bismuth silicate, i.e. as nano-precipitates inside the host particles, although the width of the measured absorption indicates that the Ag NPs exist in a distribution of environments. Of interest is that there is no additional LSPR absorption band related to Bi NPs in any samples observed. According to standard reduction potential values [\[5\]](#) Ag⁺ ions would reduce first rather than Bi³⁺. The indirect band gap energy of undoped bismuth silicate (sample BS) was determined to be 3.3 eV using the well-known Kubelka-Munk relation [\[21\]](#) (inset of [figure 10.5\(b\)](#)). It can be clearly seen there is a good match between the theoretical cross-section absorption wavelength of [figure 10.5\(a\)](#) and the experimental LSPR absorption band in [figure 10.5\(b\)](#).

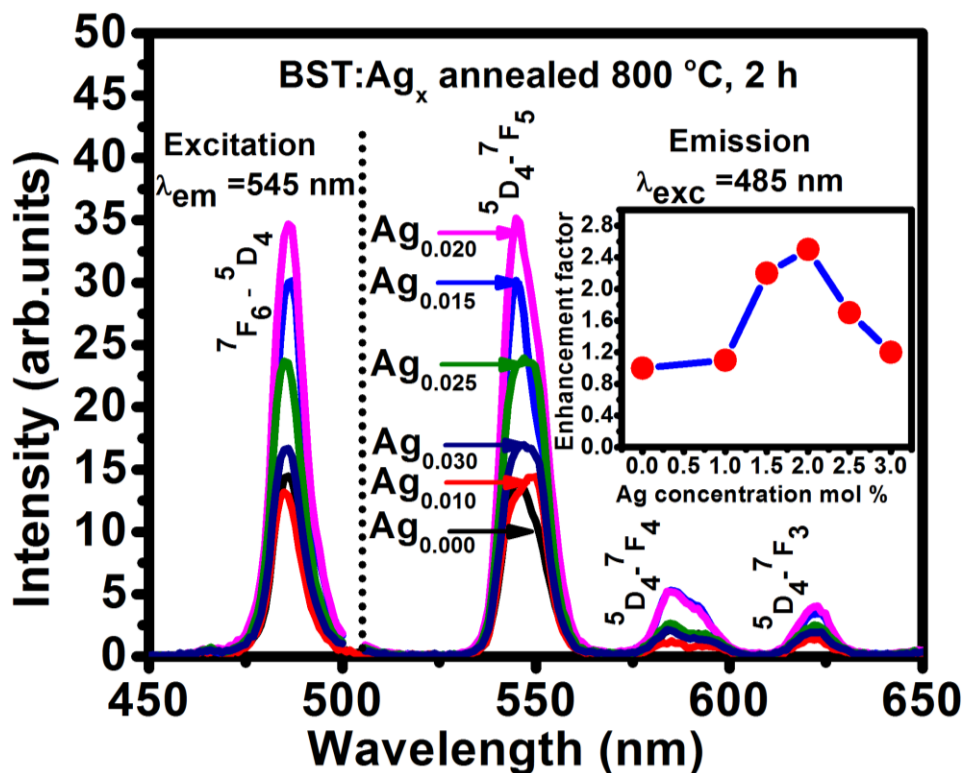


Figure 10.6: Excitation and emission luminescence spectra of BST and BST:Ag_x samples.

Several peaks were observed in the excitation spectrum of the bismuth silicate sample doped with Tb³⁺ ions (BST) when monitoring the well known green emission of Tb³⁺ corresponding to the ⁵D₄-⁷F₅ transition at 545 nm. The peak at 485 nm (figure 10.6) as well as others at 377 nm, 358 nm and 318 nm (not shown) were assigned to *f-f* transitions from the ⁷F₆ level to the ⁵D_{*J*} (*J* = 4, 3, 2, 1) levels respectively. To investigate the effect of co-doping with Ag on the Tb³⁺ luminescence, BST:Ag_x samples were prepared with various concentrations of Ag. The emission spectra of these samples excited at 485 nm are also shown in figure 10.6 and reveal three characteristic peaks of Tb³⁺ which are assigned to the ⁵D₄-⁷F_{*J*} (*J* = 3, 4, 5) transitions. It can be seen that the emission intensity depends on the Ag concentration, firstly increasing and then decreasing with increasing Ag concentration as shown in the inset of figure 10.6. The maximum enhancement factor

of about 2.5 times was obtained for the sample BST:Ag_{0.02}. The quenching of the Tb³⁺ emission for a high concentration of Ag has been previously reported as due to ET from Tb³⁺ ions to Ag NPs, since the distance between the RE ions and metallic NPs will become very small and then the dipole-dipole interaction will take place, leading to ET [4, 22, 23]. It is clear from figure 10.6 that the Tb³⁺ emissions at 585 nm and 621 nm have been enhanced similarly to that at 545 nm. This indicates that the emission enhancement is due to an increased excitation rate of electrons to the ⁵D₄ level of Tb³⁺, followed by their subsequent decay.

The cause of Tb³⁺ luminescence enhancement with co-doping of Ag has previously been attributed to two possible reasons: ET or plasmonic effects. ET could occur from Ag NPs, Ag clusters or Ag ions to the RE ions, but ET from NPs to RE ions is not expected in general due to the very short lifetime of the plasmons [4]. Also in the case of this study ET from Ag ions is not expected since the Ag has formed into metallic NPs and in addition, the excitation wavelength of both Ag ions and Ag clusters are below 300 nm [9]. Moreover, the increase of RE emission due to ET has normally been observed under non-resonant excitation of the NPs accompanied by changes in excitation shape [5, 9]. Therefore the luminescence enhancement in this system is attributed to plasmonic local field enhancement confined around the Ag NPs, which increases the excitation rate of the Tb³⁺ ions to the ⁵D₄ level due to the overlap between LSPR absorption band and the ⁷F₆-⁵D₄ excitation band of Tb³⁺. Some enhancement in the excitation band around 377 nm was also observed (not shown), although it does not overlap nearly as well with the LSPR absorption band of the NPs compared to the excitation band at 485 nm which have higher enhancement. The enhancement of about 2.5 times observed for the 485 nm excitation might be further improved by better overlap between the LSPR band and the Tb³⁺ excitation energy, which differed slightly in this study due to the small size of the Ag NPs produced, possibly due to more difficult growth of Ag NPs in a crystalline host than in amorphous hosts used before in such plasmonic enhancement studies or that the Ag NPs may occur predominantly on the surface of the phosphor particles.

10.4 Conclusion

In this work, we have presented a simple way to cause overlap between the LSPR absorption band of metallic NPs and the excitation band of a phosphor activator (e.g. Tb^{3+}) in a suitable host by using Mie theory calculations. In addition, we have succeeded in using a crystalline host instead of amorphous host to study plasmonic enhancement of phosphors for the first time. Tb^{3+} doped bismuth silicate with Ag NPs was successfully prepared using the sol-gel method and subsequent annealing. Formation of Ag NPs was confirmed by diffuse reflectance, TEM and AES measurements. The addition of Ag NPs led to an enhancement of the green Tb^{3+} emission at 545 nm of about 2.5 times when excited at 485 nm. This enhancement is attributed to the amplified local electric field associated with the Ag NPs. Our methodology for selecting the host and dopant was successfully applied and may be extended to other RE ions.

10.5 References

- [1] M. Rycenga, C. M. Cobley, J. Zeng, W. Li, C. H. Moran, Q. Zhang, D. Qin and Y. Xia, Controlling the Synthesis and Assembly of Silver Nanostructures for Plasmonic Applications, *Chem. Rev.* **111** (2011) 3669-3712.
- [2] J. W. M. Verwey and G. Blasse, Luminescence Efficiency of Ions with Broad-Band Excitation in Lithium Lanthanum Phosphate Glass, *Chem. Mater.* **2** (1990) 458-463.
- [3] H. W. Guo, X. F. Wang and D. N. Gao, Non-Isothermal Crystallization Kinetics and Phase Transformation of Bi_2O_3 - SiO_2 Glass-Ceramics, *Sci. Sintering* **3** (2011) 353-362.
- [4] O. L. Malta, P. A. Santa-Cruz, G. F. Desa and F. Auzel, Fluorescence Enhancement Induced by the Presence of Small Silver Particles in Eu^{3+} Doped Materials, *J. Lumin.* **33** (1985) 261-272.
- [5] J. Qi, Y. Xu, F. Huang, L. Chen, Y. Han, B. Xue, S. Zhang, T. Xu and S. Dai, Photoluminescence of Ag Nanoparticles and Tm^{3+} Ions in the Bismuth Germanate Glasses for the Blue Light-Excited W-LED, *J. Am. Ceram. Soc.* **97** (5) (2014) 1471-1474.
- [6] S. M. Lee and K. C. Choi, Enhanced Emission from $\text{BaMgAl}_{10}\text{O}_{17}:\text{Eu}^{2+}$ by Localized Surface Plasmon Resonance of Silver Particles, *Opt. Express* **18** (2010) 12144-12152.

- [7] P. Piasecki, A. Piasecki, Z. Pan, R. Mu and S. H. Morgan, Formation of Ag Nanoparticles and Enhancement of Tb³⁺ Luminescence in Tb and Ag Co-doped Lithium Lanthanum-Aluminosilicate Glass, *J. Nanophotonics* **4** (2010) 043522 9.
- [8] S. Lai, Z. Yang, J. Liao, J. Li, B. Shao, J. Qiu and Z. Song, Preparation and Photoluminescence Property of SiO₂:Tb³⁺ Three Dimensionally Ordered Macroporous Composites including Ag Nanoparticles, *J. Non-Cryst. Solids* **405** (2014) 176-179.
- [9] J. Li, R. Wei, X. Liu and H. Guo, Enhanced Luminescence via Energy Transfer from Ag⁺ to RE Ions (Dy³⁺, Sm³⁺, Tb³⁺) in Glasses, *Opt. Express* **20** (2012) 10122-10127.
- [10] A. E. Abbass, H. C. Swart and R. E. Kroon, Effect of Silver Ions on the Energy Transfer from Host Defects to Tb in Sol-gel Silica Glass, *J. Lumin.* **160** (2015) 22-26.
- [11] M. Eichelbaum and K. Rademann, Plasmonic Enhancement or Energy Transfer? On the Luminescence of Gold, Silver, and Lanthanide-doped Silicate Glasses and its Potential for Light-Emitting Devices, *Adv. Funct. Mater.* **19** (2009) 2045-2052.
- [12] Y. Chen, K. Munechika and D. S. Ginger, Dependence of Fluorescence Intensity on the Spectral Overlap between Fluorophores and Plasmon Resonant Single Silver Nanoparticles, *Nano Lett.* **7** (2007) 690-696.
- [13] K. L. Kelly, E. Coronado, L. L. Zhao, and G. C. Schatz, The Optical Properties of Metal Nanoparticles: The Influence of Size, Shape, and Dielectric Environment, *J. Phys. Chem. B.* **107** (2003) 668-677.
- [14] N. Cathcart, A. J. Frank and V. Kitaev, Silver Nanoparticles with Planar Twinned Defects: Effect of Halides for Precise Tuning of Plasmon Resonance Maxima from 400 to > 900 nm, *Chem. Commun.* **14** (2009) 7170-7172.
- [15] D. P. Bortfeld and H. Meier, Refractive Indices and Electro-optic Coefficients of the Eulities Bi₄Ge₃O₁₂ and Bi₄Si₃O₁₂, *J. Appl. Phys.* **43** (1972) 510-5111.
- [16] Y. Dimitriev, M. Krupchanska, Y. Ivanova and A. Staneva, Sol-gel Synthesis of Material in the System Bi₂O₃-SiO₂, *J. Univ. Chem. Technol. Metall.* **45** (2010) 39-42.
- [17] Z. Bai, X. Ba, R. Jia, B. Liu, Z. Xiao and X. Zhang, Preparation and Characterization of Bismuth Silicate Nanopowders, *Front. Chem. China* **2** (2007) 131-134.

- [18] P. Laven, MiePlot: A Computer Program for Scattering of Light from a Sphere using Mie Theory & the Debye series, [online]. Available from <http://www.philiplaven.com/mieplot.htm>.
- [19] A. E. Abbass, H. C. Swart and R. E. Kroon, Effect of Ag Nanoparticles on the Luminescence of Tb doped Sol-gel Silica, in *Proceedings of SAIP2013: 58th Annual Conference of the South African Institute of Physics*, edited by R. Botha and T. Jili (2014), pp. 2-7. ISBN: 978-0-620-62819-8 (available at <http://events.saip.org.za>).
- [20] A. Simo, J. Polte, N. Pfänder, U. Vainio, F. Emmerling and K. Rademann, Formation Mechanism of Silver Nanoparticles Stabilized in Glassy Matrices, *J. Am. Chem. Soc.* **134** (2012) 18824-18833.
- [21] A. E. Morales, E. S. Mora and U. Pal, Use of Diffuse Reflectance Spectroscopy for Optical Characterization of Un-supported Nanostructures, *Rev. Mex. Fís. S* **53** (2007) 18-22.
- [22] J. A. Jiménez, S. Lysenko and H. Liu, Enhanced UV-excited Luminescence of Europium Ions in Silver/Tin-doped Glass, *J. Lumin.* **128** (2008) 831-833.
- [23] L. R. P. Kassab, R. de Almeida, D. M. da Silva, T. A. A. de Assumpção and C. B. de Araújo, Enhanced Luminescence of Tb³⁺/Eu³⁺ Doped Tellurium Oxide Glass Containing Silver Nanostructures, *J. Appl. Phys.* **105** (2009) 103505.
- [24] J. Q. Xi, M. Ojha, W. Cho, J. L. Plawsky, W. N. Gill, Th. Gessmann and E. F. Schubert, Omnidirectional Reflector using Nanoporous SiO₂ as a Low Refractive-index Material, *Opt. Lett.* **30** (2005) 1518-1520.
- [25] C. K. Duan and M. F. Reid, Local Field Effects on the Radiative Lifetimes of Ce³⁺ in Different Hosts, *Curr. Appl. Phys.* **6** (2006) 348-350.
- [26] I. A. Ezenwa, Synthesis and Optical Characterization of Zinc Oxide Thin Film, *Res. J. Chem. Sci.* **2** (2012) 26-30.

Chapter 11

Summary and future work

11.1 Summary

The enhancement and quenching of phosphors when doped with Ag have been intensively studied in previous work. The enhancement is attributed to two possible mechanisms: plasmonic effect (enhancement of local electric field) associated with the Ag NPs or due to energy transfer (ET) from Ag ions to the emitters while the quenching is assigned to ET from Ag ions or Ag NPs to the emitters. Indeed, it is very difficult to differentiate the role of plasmonic and ET in the observed enhancement and also there is still lack of information about the interaction between the phosphor and different species of Ag (e.g., Ag^+ , Ag^+-Ag^+ , Ag^0), prompting a need for more study. Therefore, for further study, different phosphor hosts with and without dopants (Ag and/or Tb) were synthesised using different methods. SiO_2 and $\text{Bi}_4\text{Si}_3\text{O}_{12}$ were synthesized by sol-gel method while ZnO were synthesised by combustion method. XRD was successfully applied to investigate the structure and particle size of these hosts as well as the Ag NPs. The formation of Ag NPs into these hosts was confirmed by the XRD, UV-Vis, XPS, AES and TEM measurements while optical properties were investigated using a Cary Eclipse fluorescence spectrophotometer or by exciting samples with a 325 nm He-Cd laser.

SiO_2 doped only with Ag (1 mol%), shows enhancement of the emission from SiO_2 related to oxygen deficiency centres (ODCs) when the sample is annealed at low temperature (500 °C). XPS revealed that the addition of Ag creates more ODCs defects in the silica network due to formation of Ag_2O and therefore enhanced the emission. Increasing of annealing temperature to 1000 °C, produced significant broadening of the luminescence from SiO_2 . This is attributed to formation of new optical active centres associated with the decomposition of Ag_2O as investigated by XPS, UV-Vis, XRD and

TEM. Of interest is that two different defects have been revealed after addition of Ag which are attributed to oxygen interstitials and surface related defects. The additional new emission bands change the luminescence from blue for undoped SiO₂ to white light emission for the Ag doped sample. These results may be useful for solid state lighting applications. In addition, these results also show a new approach to understanding the interaction mechanism between Ag and phosphors.

The Tb, Ag co-doped SiO₂ show significant enhancement of Tb intensity at low temperature (500 °C) while increasing temperature to 1000 °C completely quenched the emission intensity of the Tb. Ag was incorporated as ions for annealing temperatures below 700 °C, while XRD, TEM, UV-vis and XPS results confirmed the formation of metallic Ag NPs at higher temperatures following decomposition of the Ag₂O. With the help of the discussion above for the sample doped only with Ag, this work has proved that the addition of Ag in silica affected the host defect concentrations which in turn led to ET from these host defects to Tb ions. This results added new complexity in the interpretation of the enhancement effects when noble metals are added to phosphor materials.

ZnO has been used as phosphor material and as a host for Tb and Ag as well. Firstly, the effect of Ag on the luminescence of ZnO has been discussed in detail. The obtained results showed more than two times increase in the intensity of near band edge emission of ZnO in the presence of Ag NPs. Our results strongly suggest that this enhancement is not due to LSPR effect as we expected, but instead due to transfer of electrons from the Ag NPs into the conduction band of ZnO. Our results suggest also that e-h pairs in Ag NPs can be excited directly by high energy photon instead of plasmon decay as previously reported. Our methodology reported here could be considered as additional possibility of interaction between metal NPs and phosphors.

Secondly, the effect of Ag on the luminescence of Tb both incorporated into ZnO was studied. The PL properties of ZnO:Tb system were studied before and after adding Ag by using a He-Cd laser. Radiative ET from Tb³⁺ ions to Ag NPs was observed and confirmed by means of spectral overlap and lifetime measurements. Plasmons from 5 nm

Ag NPs were excited indirectly through the down-conversion properties of Tb^{3+} ions. Consequently, it is concluded that the use of a down-converting phosphor (containing, for example, RE ions) is an effective method to indirectly couple a laser to the plasmon resonance wavelength of metal NPs without a need to change the particle size or shape of NPs. The obtained results suggest that the ZnO:RE, Ag system may be useful in applications that require local heating.

Crystalline $Bi_4Si_3O_{12}$ (BS) has been selected as appropriate host to study possible plasmonic enhancement using Mie theory calculations. Moreover, using these calculations, a simple way to cause overlap between the LSPR absorption band of metallic NPs and the excitation band of a phosphor activator (e.g. Tb^{3+}) is presented. In addition, we have succeeded in using a crystalline host instead of amorphous host to study plasmonic enhancement of phosphors for the first time. The effect of doping Ag on the luminescence of Tb^{3+} ions in this host was investigated. The obtained results showed an enhancement of the green Tb^{3+} emission at 545 nm of about 2.5 times when excited at 485 nm. This enhancement is attributed to the amplified local electric field associated with the Ag NPs. Our methodology for selecting the host and dopant was successfully applied and may be extended to other RE ions.

11.2 Future work

There is no limit that can be set to define a complete work since there is always interesting aspects that require further investigation to complement what has already been done. Therefore, for future work the following are suggested.

1. Only Tb is used to study possible plasmonic enhancement in this thesis. Research on the other RE ions should be done, especially for those with absorption energy in the visible range.
2. In this thesis, the reduction of Ag ions to Ag NPs has been done using heat treatment only, which also has an effect on the host structure. Moreover, it is very difficult to convert all Ag ions to Ag NPs using thermal method, and the shape, size and particle distribution cannot be well controlled as well. Therefore, commercial Ag NPs with

specific particle size should be used to avoid the effect of residual Ag ions and to use the correct size and shape of Ag NPs.

3. The methods used in this work (sol-gel and combustion method) are associated with a lot of defects which add another complexity to study plasmonic effect. Therefore, a method like ion exchange should be applied using commercial slide glass.

4. To apply our methodology used in [chapter 10](#) to select other appropriate hosts, especially polymers to further study plasmonic enhancement.

5. The effect of doping Ag on the luminescence of Tb has been studied only for powder samples. Further studies can be done on samples that are still in solution before and after doping with Ag NPs.

6. To control the distance between the Ag NPs and the emitters, core-shell of silica doped with Ag NPs (Ag@SiO_2) should be prepared to increase the enhancement of the emitters.

7. To enhance the spectral overlap between plasmonic NPs and the emitters, metal alloy nanoparticles should be used, especially the alloy of Ag and Au. The Ag NPs has LSPR absorption band about 420 nm while for Au NPs is about 500 nm. Therefore, the LSPR absorption band for Ag-Au alloy is expected to be very broad and it can overlap nicely with Tb excitation.

Appendix A

Publications

1. Abd Ellateef Abbass, H. C. Swart and R. E. Kroon, Effect of Ag nanoparticles on the luminescence of Tb doped sol-gel silica, in *Proceedings of SAIP 2013: 58th Annual Conference of the South African Institute of Physics*, edited by R. Botha and T. Jili (2014), pp. 2-7. ISBN: 978-0-620-62819-8 (available at <http://events.saip.org.za>).
2. Abd Ellateef Abbass, H. C. Swart and R. E. Kroon, Effect of silver ions on the energy transfer from host defects to Tb ions in sol-gel silica glass. *J. Lumin.* **160** (2015) 22-26.
3. Abd Ellateef Abbass, H. C. Swart and R. E. Kroon, White luminescence from sol-gel silica doped with silver. *J. Sol-Gel Sci. Technol.* **76** (2015) 708-714.
4. Abd Ellateef Abbass, H. C. Swart, E. Coetsee and R. E. Kroon, Enhanced terbium emission due to plasmonic silver nanoparticles in bismuth silicate. Accepted for *J. Am. Ceram. Soc.* (DOI: 10.1111/jace.14011)
5. Abd Ellateef Abbass, H. C. Swart and R. E. Kroon, Use of ZnO:Tb down-conversion phosphor for Ag nanoparticle plasmon absorption using a He-Cd ultraviolet laser. Accepted for *Luminescence: the journal of biological and chemical luminescence*.
6. Abd Ellateef Abbass, H. C. Swart and R. E. Kroon, Non-plasmonic enhancement of the near band edge luminescence from ZnO using Ag nanoparticles. (Submitted to *J. Lumin.*)

Conference presentations

1. Abd Ellateef Abbass, H.C. Swart and R.E. Kroon, Effect of Ag nanoparticles on the luminescence of Tb doped sol-gel silica. The 58th Annual conference of the South African Institute of Physics, Richards Bay, South Africa, 8-12 July 2013.
2. Abd Ellateef Abbass, H. C. Swart and RE Kroon, Formation of Silver nanoparticles in Sol-Gel Silica. Southern African Powder Diffraction Conference and Workshop, University of the Witwatersrand, Johannesburg, South Africa, 27-31 January 2014.
3. Abd Ellateef Abbass, H.C. Swart and R.E. Kroon, Formation, size and distribution Silver nanoparticles in Silica. The 52nd Annual MSSA conference, Stellenbosch, South Africa, 2-5 December 2014.
4. Abd Ellateef Abbass, H.C. Swart and R.E. Kroon, Effect of Ag doping on the luminescence of ZnO and ZnO:Tb. The 6th South African Conference on Photonic Materials, Mabula, South Africa, 5-7 May 2015.
5. Abd Ellateef Abbass, H.C. Swart and R.E. Kroon, White luminescence from sol-gel silica doped with silver. The 60th Annual conference of the South African Institute of Physics, Port Elizabeth, South Africa, 29 June - 3 July 2015.